Imperial College
London

Dynamic Response of Steel Monolithic Plated Structures Subjected to Localised Blast Loads

By

Navid Mehreganian

B. Eng. & Arch., MSc. (Eng. & Arch.), MSc.

A thesis submitted for the partial fulfilment of the requirements for the degree of Doctor of Philosophy (PhD) and the Diploma of Imperial College (DIC) to the Department of Civil and Environmental Engineering, Imperial College of Science, Technology and Medicine, London SW7 2AZ, United Kingdom

September 2018

DECLARATION OF ORIGINALITY

I confirm that this thesis is a result of my own work carried out in the department of Civil and Environmental Engineering at Imperial College London. Appropriate references and citations wherever I described, quoted from or referred to other works, whether published or unpublished, have been acknowledged and cited. The work in this thesis is not the same as any other work submitted in any institution for the award of my degree.

COPYRIGHT DECLARATION

Navid Mehreganian

ABSTRACT

This thesis investigates the nonlinear dynamic response of the steel monolithic square plated structures due to localised blast loads, such as those emanating from close-in charges. Such target plates are assumed to be made of novel high strength ARMOX steel material types manufactured by SSAB® as well as conventional mild steel.

A detailed review of earlier works in the literature is presented on the experimental, numerical and theoretical methods of analysis to predict the response of beams, circular and quadrangular plates subject to blast and impact loads. The large scatter of data from the above analyses has been cast in dimensionless forms to correlate between the methods of predicting the response. The review concludes that, the choice of material type as well as the intrinsic complexity associated with the load type make the response of the structure inherently different to those of plated elements made of more conventional grade metals.

Based on the state-of-the-art Digital Image Correlation experimental testing conducted in the Blast Impact and Survivability Research Unit in University of Cape Town, various proposed numerical models have been validated. These include advanced techniques to model the fluid structure interactions. This led to discerning the parameters that influence the plastic response. Empirical relations in dimensionless form have been proposed which pass through most scattered data from numerical and experimental results. A prompt observation is that assessing the plastic response of the structures to localised blasts necessitates understanding the underlying patterns and laws of plastic response. Such understanding is gained by theoretical methods with idealisations of the material or the structural response.

This leads to theoretical studies using the principles of virtual velocities assuming constitutive framework of limit analysis, i.e. rigid, perfectly plastic behaviour. While appreciating the limitations of current theoretical models, a comprehensive approach is undertaken to explore the response of the plates of various boundary conditions, distinguished in terms of their thicknesses, i.e. thick, moderately thick and thin plates. Furthermore, the nonlinear elastic response of the plates has been examined, leading to a unified theoretical solution of elastic-perfectly plastic systems.

On the basis of the existing work in the literature, a method to mathematically describe the parameters that characterise the blast load itself and the structure impacted whereupon with a given charge geometry, stand off and material type is presented and validated with numerical models. Based on the dimensionless study, single parameters to predict the rupture impulse has been determined.

ACKNOWLEDGEMENTS

I wish to express my sincerest appreciation to all who have been instrumental to the successful completion of this thesis. Indeed, this thesis would not have been completed by me alone.

First, I wish to express my great appreciation to my supervisor, Dr Luke. A. Louca, for the opportunity he provided for me to enroll on this project since summer 2014, his positive encouragement, patience and support helped me embark on a journey to scientific contributions, to its culmination summarised in this thesis. Indeed, his support exemplified Winston Churchill's quote '…it is the courage to continue that counts'

Further, I have been immensely fortunate to receive invaluable advice from Dr Arash Soleiman Fallah-my second supervisor, whom I am truly grateful for instructive comments, the vast knowledge he has shared with me as well as his useful instructions he has patiently offered.

I am grateful to my examiners, Dr Christian Malaga and Dr Andrew Tyas, for their insightful comments and positive criticism on this thesis. Truly, I had the priviledge of learning from their instructive feedbacks and advice. I deeply admired their interactive questions during my examination combined with their warm personality; not only did it helped me enhance the quality of this thesis, but it also improved my understandings in this field.

I am also grateful to my office-mates at room 429 Department of Civil and environmental engineering, as well as the staff member of the same department, especially Ms. Fionnuala Donavan, Sarah Willis, Prof. Ahmer Wadee and Dr Andrew Phillips, for their colourful company, sharing their knowledge and providing a professional environment.

I would like to express my thanks to the friends and family, my partner, Miss J Agwanda, as well as my best friends Mr Tim Cheux and Miss Niloufar Malik for their patience, consistent support, provision and maintaining stability to my life.

Vous tous, merci beaucoup à cœur; maintenant et toujours, puisse la paix de Dieu etre avec vous

You wote, asante sana kwa moyo; sasa na siku zote, amani ya Mungu iwe nanyi

صمیمانه از زخمات و همکاریهای شما سپاسگذارم، آرامش ایزد توانا با شما باشد.

TABLE OF CONTENTS

TABLE OF FIGURES

TABLE OF TABLES

Nomenclature

The following symbols are used throughout this thesis:

Latin Upper Case

$A_i - G_i$	Loading parameters, various
$\bar{A}$	Elemental area; $[L^2]$
B	Rectangular plate side width; $[L]$
$B_1{}'$	Johnson Cook hardening parameter; $[ML^{-1}T^{-2}]$
C_0	Dimensionless elastic load parameter; [1]
$\mathrm{C_p}$	ideal gas specific heat capacity at constant pressure; $[L^2T^{-2}K^{-1}]$
$\mathrm{C_v}$	ideal gas specific heat capacity at constant volume; $[L^2T^{-2}K^{-1}]$
D_e	Disc charge diameter; $[L]$
D_n	Johnson's damage number; [1]
D_r	Flexural rigidity; $[ML^2T^{-2}]$
$\dot{D}$	Internal Energy dissipation rate;$[ML^2T^{-3}]$
D	Cowper-Symonds coefficient; $[T^{-1}]$
$\dot{E}$	External Work rate; $[ML^2T^{-3}]$
H	Plate characteristic thickness; $[L]$
$\hat{I}, I^*$	Impulse density $[\mathrm{M}L^{-1}T^{-1}]$
I_i, i_s	Incident impulse $[\mathrm{M}LT^{-1}]$
I_p, I	Transmitted impulse to the plate $[\mathrm{M}LT^{-1}]$
I_r	Rotatory inertia; $ML^2]$
L	Plate characteristic side length; $[L]$
M_0	Maximum moment of the plate per unit length; $[MLT^{-2}]$
M	Plastic bending moment per unit length; $[MLT^{-2}]$

Greek Lower case

α_b	Boundary condition parameter; [1]
α	Exponential pulse shape decay constant; $[T^{-1}]$
α_e	Localised blast elastic parameter; [1]
$\propto$	Lower bound Static collapse coefficient; [1]
β	Upper bound Static collapse coefficient; [1]
β_0	Reflected impulse coefficient; $[L^3]$
γ_{xy}	Transverse shear strain [1]
γ'	Critical load parameter; [1]
$\bar{\gamma}$	Specific heat capacity ratio; [1]
δ_1	Dynamic blast load parameter;
δ'_{ij}	Kronecker Delta;
ϵ	Dimensionless perturbation parameter; [1]
ϵ_1	Localised impulsive velocity coefficient; $[L]$
ε_{ij}	Strain tensor; [1]
$\dot{\varepsilon}$	plate strain rate tensor; $[T^{-1}]$
ε	plate strain tensor; [1]
ε_f	strain at tensile fracture; [1]
$\dot{\varepsilon}_e$	Equivalent strain rate; $[T^{-1}]$
η	Dynamic load factor [1]
η_{crit}	Critical dynamic load factor; [1]
$\dot{\theta}_i$	Rotational (angular) velocity at the outer boundaries of zone i ($i = 1,2$); $[T^{-1}]$

M_e	mass of explosive, $[M]$	$\dot{\theta}_3$	Rotational velocity across the inclined plastic hinge; $[T^{-1}]$
N	Plastic membrane force per unit length; $[MT^{-2}]$	$\dot{k}_x$	Curvature rate in x direction; $[T^{-1}]$
Q_e	specific heat energy $[L^2T^{-2}]$	$\dot{k}_y$	Curvature rate in y direction; $[T^{-1}]$
N_0	Maximum plastic membrane force per unit length; $[MT^{-2}]$	$\dot{k}_{xy}$	Curvature rate in xy direction; $[T^{-1}]$
Γ	Elastic load parameter;	λ	Dimensionless kinetic energy; [1]
Q	Transverse shear force per unit length; $[MT^{-2}]$	$\bar{\lambda}$	Dimensionless kinetic energy; [1]
Q_0	Maximum transverse shear force per unit length; $[MT^{-2}]$	μ_k	Dynamic viscosity of air; $[ML^{-1}T^{-1}]$
P_0	Ambient pressure; $[ML^{-1}T^{-2}]$	μ	Areal density; $(= \rho H)$; $[ML^{-2}]$
P_r	Reflected overpressure; $[ML^{-1}T^{-2}]$	ν_e	Poisson's ratio [1]
R	Circular Plate radius $[L]$	ν	Inverse slenderness ratio (L/H) [1]
$\mathcal{R}_n$	Response number; [1]	$\xi(t)$	Active plastic hinge generalised coordinate; [1]
S_D, d	Stand-off distance; $[L]$	ξ_0	Stationery plastic hinge generalised coordinate; [1]
T_i	Duration of the i^{th} phase; $[T]$	ρ, ρ_p	Material (plate) density; $[ML^{-3}]$
T_f	End of motion time; $[T]$	ρ_s	Shock density; $[ML^{-3}]$
$\bar{T}_f$	dimensionless final time of motion	ρ_e	Explosive (initial) density; $[ML^{-3}]$
U_T	Specific energy to tensile fracture; $[ML^{-1}T^{-2}]$	ρ_0, ρ_a	Fluid (air) density; $[ML^{-3}]$
$U(i,j)$	Strain energy density; $[ML^{-1}T^{-2}]$	σ_0	Static plastic flow stress; $[ML^{-1}T^{-2}]$
V_1	Impulsive velocity of uniform blast; $[LT^{-1}]$		
V_0	Impulsive velocity of localised blast; $[LT^{-1}]$		
V_p	plate volume; $[L^3]$		
$\ddot{W}_i$	Maximum transverse acceleration at the i^{th} phase; $[LT^{-2}]$		
$\dot{W}_i$	Maximum transverse velocity at i^{th} phase; $[LT^{-1}]$		
W_f	Maximum permanent mid-point transverse displacement; $[L]$		

Latin Lower Case

f(z), g(z)	Moment parameter function; $[MLT^{-2}]$
a	Exponent (loading parameter); [1]
b	Loading Exponent; $[L^{-1}]$
d_i	Ordinary Differential Equation constant; $[MLT^{-2}]$
i	Dimensionless impulse; [1]
$\bar{m}_i$	dimensionless moment normal to i [1]
m_{TNT}	TNT equivalent mass; $[L]$
$p_1(r)$, $p(x,y)$	Spatial part of pressure pulse load; $[ML^{-1}T^{-2}]$
$p_2(t)$	Temporal part of pressure pulse load; [1]
p_c	Static plastic collapse pressure; $[ML^{-1}T^{-2}]$
p_0, p_s	Maximum plastic collapse overpressure; $[ML^{-1}T^{-2}]$
r_e	Loading constant (central) zone radius; $[L]$
r	characteristic radial distance from centre; $[L]$
t_A	Arrival time of the blast pressure; $[T]$
$\dot{w}_i$	Transverse velocity at i^{th} phase; $[LT^{-1}]$
$\ddot{w}_i$	Transverse acceleration at i^{th} phase; $[LT^{-2}]$
w_i	Generalised transverse displacement at i^{th} phase; $[L]$
$\bar{w}$	Dimensionless transverse displacement; $[L]$
$\bar{w}_f$	Dimensionless maximum final transverse displacement; [L]
z	Characteristic generalised coordinate; [1]

Greek lower case (Ctd.)

σ'_y	Dynamic flow stress; $[ML^{-1}T^{-2}]$
ς	normalised third deviatoric invariant;
t_d, τ	Duration of the pulse; $[T]$
τ^*	$\mu V_1 L^2/M_0$ $[T]$
ψ'_s	energy absorbing effectiveness factor; [1]
φ	Characteristic angle; [1]
ϕ_c, ϕ_{ql}	Non-dimensional impulse parameter [1]
ϕ	Airy stress function; $[MLT^{-2}]$
ζ	Stress triaxiality;
v_c	Shock propagation speed; $[ML^{-1}T^{-2}]$
v_0	Sound speed; $[ML^{-1}T^{-2}]$
ω_0	r_e/L ; [1]
ω_1	Pulse factor of pattern (A); $[T^{-1}]$
ω	Pulse factor of pattern (B); $[T^{-1}]$
ω_3	Elastic vibration frequency of phase 2 $[T^{-1}]$
$\overline{\omega_e}$	Pseudo vibration frequency; $[T^{-1}]$

CHAPTER 1

1.1 PREAMBLE

The main objective of this chapter is to provide a context for the objectives addressed and discussed throughout this thesis. It will outline the organisation of the thesis as well as the aspects investigated in each chapter.

1.2 BACKGROUND

In today's world, events such as 9/11, the recent European bombings (2015-2017) and Buncefield [1] have caused public awareness of explosive threats to increase dramatically. An explosion event, either accidental (Buncefield event) or deliberate (terrorist attacks) can cause catastrophic damage to structure and loss of life. Engineering structures are particularly vulnerable to extreme shock wave ensued by the blast, as these would induce large deformation and potentially rupture through the structural elements.

In response to the risk of explosions, efforts have been made to improve the response of civil infrastructures and transportation vehicles to air-blast loading. It is imperative to understand the loading arising from explosive detonations and the ensued damage sustained by the proximal structures.

1.3 BLAST LOAD

A blast load may occur due to several scenarios, terrorist attacks by means of conventional bombs concealed in trucks/vehicles, gas explosions from pressure vessels or Improvised Explosive Devices (IED), which can be sourced from proximal (near field) or distal (far field) charges. In the case of the former, the blast source, such as IED, is at proximity of the target which induces localised elastic and plastic floorboard deformation on, for example, a vehicle hull, transferring high axial loads to the occupants. The localised effects of the blast wave generate further failure modes in contradistinction to the blasts from distal charges [2]. The mechanical shock through the material due to the local effects of blasts is much higher than the global effects (5000m/s compared to 300m/s), highlighting the significance of the localised blast loads on structures and various other fields of engineering (i.e. aeronautics, forensics, military).

Close in charges from Anti-Vehicle and Anti-Personnel mines not only damage the infrastructures but also the vehicles and personnel. The military Mine Resistant Ambush Protected (MRAP) in Rhodesian war (1972-1980) sustained fatality rate of 1.2% compared to 11.4% from unprotected vehicles [3]. In Croatia war (1991-1995) an estimated 0.4 million AV mines laid [2]. An AV mine, apart from risk of injury or fatalities, can obstruct the movement transportation of goods, supplies and people. The mechanical shock and vertically channelled impulse would affect the occupants physically and psychologically. Furthermore, MRAP vehicles designed to shield the effects of blast are expensive and require maintenance. Thus, they need to be manufactured from materials with sufficient robustness, strength and durability.

Furthermore, in the case of shallow buried exploives, the blast phenomenon combined with the impact of the sand would add additional momentum to the target interface. The impact of the soild particles depends on the soil type, physical properties such as cohesion, moisture content, porosity, as well as the explosive size and shape. The combined influence of impact and localised blast loading of landmines is complex and entails soil-structure interaction, soil fragmentation and high velocity impacts. Thus, the scope of the thesis only entails the air-blast loads, with particulat focus on the localised blast loading and their impacts on the structures.

1.4 **MATERIAL TYPES**

Careful material selection can greatly assist in providing much needed blast protection for vulnerable structures. The designers are concerned with the choice of material on two *prima facie* factors: cost and weight. Conventional steel is still one of the most common materials used not only in structures but also on armoured vehicles, however, its low cost is offset by limited robustness as well as the increased weight. Heavy weight design poses challenges to the MRAP in terms of navigation due to high centre of gravity, while the weight of the vehicle inevitably imposes pressure on poor ground such as sand or mud one. Although the composites offer lightweight at the same robustness, the high cost associated with the manufacture and life-cycle of such materials limits their use.

With the recent advancement in production and tailored metallurgy of high strength armour graded steel, the demand for the design of blast and ballistic resistant armour vehicles is ever increasing. Modern armour graded steel panels, are a viable potential candidate, due to the offered cost-effectiveness, robustness and resilience at reduced thickness [4]. For example, an ARMOX 370T plate cost £18.7/kg compared to composites £272/kg [5]. Some military standards, such as US specifications [6]–[8] provide design guide for the blast protection of various grades of steel, with the basis of conventional design, unchanged since the World War II, on hardness and Charpy fracture toughness [9]. The stagnation of the design criteria fails the designer to effectively stipulate the appropriateness of these materials in the specifications.

1.4.1 Properties of Armour steel

- **Strength**

The relation between the armour steel strength and its penetration resistance is complex and not necessarily dependent on its yield strength. A complex relation exists between the yields tress, flow stress, strain rate and temperature due to the morphology of the carbide particles in the metal matrix.

Whittington examined the ductile fracture morphology of Rolled Homogenuous Armour (RHA) steel at 25 at $1ms^{-1}$ to $1000s^{-1}$ and showed that the increase of strain rate resulted in smaller ductile void formations at low temperatures. Conversely, the increase of temperature on tests of quasi static strain rate range resulted in higher void formation and growth. At high rates, the fracture surface exhibited larger voids than the low rate fracture surface, but the voids were smaller in size and depth [10]

- **Hardness**

Hardness is defined as the resistance of the solid to plastic flow deformation and depends on composite interactions of ductility, yield strength and flow stress. Material hardness is a quasi-static measure of yield pressure for specific indentor geometry, related to the initiation of the plastic flow. The flow stress of armour steel materials is impervious to the loading rate and the hardness does not mitigate fragmentation penetrations. The flow curve of armour steel is a combination of the flow stress and the thermal softening, the flow increase due to strain rate hardening is offset by the decrease due to thermal softening [11].

- **Toughness**

The utility of a material for resisting blast and ballistic applications depends on how it responds in presence of high three-dimensional local stresses. The fracture toughness of material depends also on ductility, which armour steel grades lack, resulting in rapid micro crack propagation.

1.5 AIMS AND OBJECTIVES

In light of the complexities associated with the localised blast type and the dearth in assessment of modern steel panels, this research aims to propose numerical and theoretical methods to delineate the response of ductile metallic plates, with the particular focus on armour steel and mild steel, to such pressure loads. The various methods of analyses in this thesis highlight a unified systematic approach on the method of design of plated system against localised blasts, which aids the designer on the choice of plate. Thus, the objectives of this research are set out as:

- To identify the key subjects of interest for further investigations in the scope of this thesis by a study of the literature related to the subject.
- To compare various numerical methods in terms of accuracy and practicability, to predict the response of monolithic steel square plates to range of blast loads from high explosives. The numerical models aim to correlate with the experimental models on the transient response of the monolithic plates subject to localised blast loads, as well as the theoretical models proposed in this thesis.
- To investigate the mechanism of fluid structure interaction in localised blasts and accordingly the parameters affecting such phenomenon and their reliability on estimating the blast response of the plates.
- To carry out rigorous analytical investigations on the performance of monolithic plates subjected to generic blast load which is predictive of the blast performance of such plates from uniform to localised blasts.
- To understand the mechanism behind the blast load and to develop a theoretical description of the blast load scenario involving the various parameters that characterise, with respect to the spatial and temporal sub-functions, of the localised blast load
- To propose a design criterion predictive of the minimum impulse that ensues rupture on the monolithic plates, using the proposed analytical and empirical relations, given *a priori* knowledge of load (charge mass, stand-off) and geometry of target.
- To compare the experimental, numerical and analytical models carried out in the research, thus to propose method which unifies these various models.

1.6 **ORGANISATION OF THE THESIS**

Following the introduction, a review of the existing work in the literature is discussed in Chapter 2, identifying the key aspects where dearth of research exists. The review structures a framework for the problems relevant to the objectives of this thesis, which are addressed in the subsequent chapters.

Chapter 3 examines the methodology of the numerical works as well as the small-scale experimental works conducted at BISRU.

In Chapter 4 the results of numerical and experimental results are presented. The proposed numerical models were verified against experimental models; together were cast in dimensionless form to correlate with the available theoretical models in the literature. Empirical ansatzes were proposed which circumscribed the large scatter of experimental/numerical data.

Chapter 5 describes a theoretical analysis for the blast assessment of monolithic, ductile metallic plates. The theoretical bounds of parameters and limitations were proposed using the constitutive framework of limit analysis. The static plastic collapse, static admissibility and the position of incipient plastic hinge were investigated.

A direct application of the rigid-perfectly plastic analysis in Chapter 5 is presented in Chapter 6. This chapter, in the first part, extends the limitations of plate response from the sole action of bending moments to the combined action of bending moments and membrane forces. Plates of various boundary conditions were investigated, the theoretical results, cast in dimensionless form, corroborated with the various experimental and numerical results from Chapter 4 as well as the results from the literature. The second part of this chapter examines the nonlinear elastic behaviour of steel plates in the circumstances the assumptions of rigid-perfectly plastic model are violated. The combined results of the two parts are capable of predicting the complex elastic-plastic behaviour of the plates while the nonlinearities brought about by the influence if geometry changes and material yielding were retained in the analysis.

Chapter 7 extends the theoretical model of chapter 5 to the cases of thick plates where the effects of transverse shear is considerably large. It is anticipated that the analytical models provide a platform for virtual testing of scenarios involving blast loads of different parameters to assess the critical scenarios suitable to be studied further using experimentations.

In Chapter 8 a generalised method to delineate the characteristics of the blast using the dimensional analysis has been examined. The rupture performance of the plates was discussed and a model to predict the rupture threshold of the plate, irrespective of the material type, was presented. The ductile damage model of armour steel plates is examined as supplementary data to the experimental studies on armour steel.

Finally, Chapter 9 presents a summary and conclusion of the thesis, followed by recommendations for future work relevant to the topics of this thesis.

1.7 DISSEMINATION

Significant portions of the results of this research were submitted for, or published in, peer-international conferences and peer- reviewed journals. Reference to the work whether submitted for publication or published, is made in appropriate parts of the relevant chapter.

- **Conferences**

19 Young Researcher's Conference, ISTRUCTE,

Thirteen International Conference of Multiphysics (MULTIPHYICS 2018),

SECED 2019 Conference

- **Journals**

International Journal of Impact Engineering (×2)

International Journal of Multiphysics

International Journal of Engineering Mechanics (ASCE)

International Journal of Mechanical Science

International Journal of Protective Structures

CHAPTER 2

Literature review

This chapter presents a review of the previous works in the literature which are of significance to the work of the thesis. The review stresses the aspects of the problems which are dealt with in the subsequent chapters to structure a context for the problems in this thesis. It should be noted that, it is not in the scope of this thesis to encompass an exhaustive and wide-ranging review of all the previous work of blast loads on structures, rather a critical and comprehensive overview of the previous studies most relevant to this work.

It bears emphasis that each of the subsequent chapters entail a brief review of the literature that is of primary use to that chapter and is disregarded here to avoid repetition. Thus, the main objectives of this chapter include:

- An introduction to the physics of the blast phenomenon and the parameters that affect the blast load accordingly.
- Effect of extreme blast and shock loads to the elementary structural systems, i.e. beams and plates.
- Failure mechanisms of isotropic, ductile materials due to the blast loads.
- An overview of the high strength steel materials and the preference of these materials over conventional steel.
- Dimensionless analysis of blast loaded parameters and structural response to impulsive load.

2.1 PHYSICS OF BLAST LOADING

A blast load is typically referred to three categories of explosion, namely as nuclear, physical or chemical events as follows [12].

1. Nuclear explosion: the energy released arises from nuclear interactions, the redistribution of protons and neutrons results in formation of different new nuclei, during either ‘fission’ or ‘fusion’ processes.
2. A physical explosion could arise in three ways, (i) catastrophic failure of compressed gas or pressure vessels, eruption of volcano or (iii) violent mixing of different substances at extreme temperature difference, e.g. hot liquid with cooled fluid, the explosion results from rapid conversion of states to vapour the cooled fluid.

3. The chemical explosion involves rapid oxidation of the fuel elements (i.e., carbon and hydrogen) which are already contained within the explosive compound. Chemical explosion can either be deflagration or detonation type, as follows.

During the deflagration process, the explosive compound consumes oxygen as it propagates (e.g. propagation of flame in a gas explosion) with subsonic speed. Due to the rather slower chemical reaction with oxygen, deflagration is characterised with much smaller pressure and flame propagation velocity than detonation.

In the event of detonation, (e.g. explosion of high explosives such as TNT), the explosive material will decompose violently rapidly, generating a substantial heat with supersonic exothermic front through the medium, which is driven by a shock front that propagates through the medium (viz. air or water). The presence of air is not necessary as the required oxygen is present within the explosive compound. The inertness and stability of the explosive compound determines its usefulness, e.g., high explosives such as composition-C4 (PE4) are more useful due to higher stability to friction at room temperature, while fulminated mercury is somewhat unstable and sensitive to friction. Furthermore, the duration of detonation is generally much lower than that of deflagration and the rise time to maximum pressure for detonation is virtually zero in contradistinction to the finite rise time for deflagration processes.

The detonation wavefront depends on many parameters characterised by the Rankine-Hugoniot relationships [12], [13], viz., the detonation velocity, the air density behind the wavefront and the maximum pressure. The potential heat and detonation pressure of high explosives may be estimated using Chapman-Jouguet conditions [14]. For example, the detonation pressure of TNT and Composition-B are $210kbar$ and $294kbar$, respectively, the detonation temperatures of $3511K$ and $3918K$, respectively, while the detonation velocities are $6930\ ms^{-1}$ and $7920ms^{-1}$, respectively [15]–[17]. A most prevalent expression to describe the state variables (energy, volume, temperature and pressure) of the detonation process is the Jones-Wilkins-Lee (JWL) equation of state (EOS). Further discussion is presented in Chapter 3.

The propagation of the blast wave depends on the medium the wave advection occurs. In air blast, the flow of gaseous products are assumed inviscid thus the viscous forces are not considered for explosive modelling [13]. In underwater explosion, high propagation velocity of water (due to instantaneous compression) levels off rapidly. In this study, only the air blast explosion is considered.

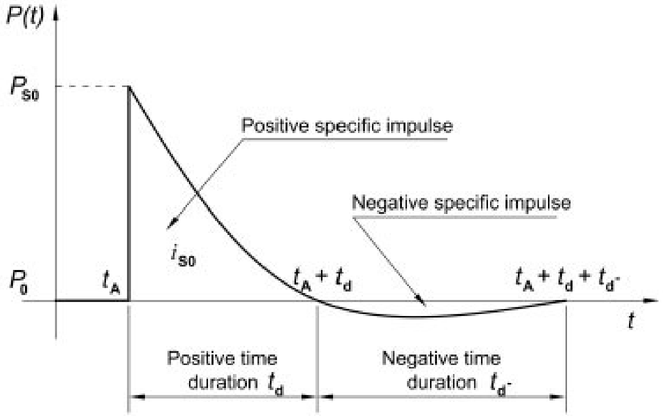

Figure 2-1- JWL EOS. P_0 and P_{so} represent the atmospheric pressure and the absolute pressure

A schematic of the pressure profile is defined by Friedlander Equation, as in Figure 2-1. The main characteristics of the blast are [18], [19]:

- The arrival time t_A, determined by the delay time from the beginning of detonation.
- Following the detonation of the explosive, the explosive products interact with fluid (air) particles, the air particles undergo instantaneous rise in the pressure above the ambient pressure. The gauge pressure $p_s = P_{so} - P_0$ is defined as the peak incident overpressure.
- Positive phase blast duration t_d, as the blast wave expands, the pressure decays exponentially, back to the ambient pressure P_0
- Beyond t_d, the pressure decays further to a negative pressure. The negative pressure is due to momentum conservation of air; the overexpansion of air causes the absolute pressure at the tail of blast fall below the atmospheric pressure. This reduction generates a reversed flow back towards the centre of detonation.

The idealised pressure wave is affected by the morphology of the medium through which the advection of wave occurs [19]. The negative phase depends on the stand-off, charge weight and the explosive topology. The negative phase is more significant for blasts from distal charges, as it gives rise to counter intuitive behaviour where the Reversed Snap Buckling (RSB) causes final configuration of the structure to be in opposite direction to the incident wave [20]. However, the negative phase becomes insignificant with the decrease in the proximity of blast which is not examined in this thesis.

Depending on the proximity of the blast source, the loading can be classified as global (e.g. far-field explosions) or localised (e.g. buried land mines). While researchers have proposed a few definitions for the sake of classification of loading depending on certain attributes [21], [22], the concern has been regarding the structural response rather than the definitions.

2.2 BLAST LOAD PARAMETERS AND SCALING LAWS

Whether the type of blast is localised, i.e., buried land mines, or globalised (far field explosions), the structure may either deflect some of the blast wave, or large inelastic deformation, partial or complete tearing and shear failure will occur. However, the damage of the structure would depend on a number of parameters, namely the impulse, the peak pressure load, the stand-off distance and the duration of the pressure. If the duration of blast is significantly less than the structures natural period, the structure's damage is directly dependent on the level of the impulse.

The positive phase of the blast pressure can be described with the Friedlander's expression as:

$$P(t) = P_0 + p_s\left(1 - \left(\frac{t - t_A}{t_d}\right) e^{-\frac{\alpha(t-t_A)}{t_d}}\right), \quad t_A \leq t \leq t_A + t_d \tag{2-1}$$

The waveform parameter α may be adjusted such that the overpressure time relationship provides convenient estimate for the blast impulse. The incident impulse per unit area of the positive phase is evaluated as $\hat{I}_i = \int_{t_a}^{t_d}(P(t) - P_0)dt$, or

$$\widehat{I_i} = p_s\left[\frac{t_d(\alpha + 1)(\alpha - 1 + e^{-\alpha})}{\alpha^2}\right] \tag{2-2}$$

Which leads to $\widehat{I_i} \cong 0.735 p_s t_d$ with $\alpha = 1$. When the pressure hits the target, it is normally reflected. The reflected pressure has the same profile, but higher magnitude, than the incident pressure. Thus, the total pressure transmitted to the structure is the algebraic sum of the reflected pressure and incident pressure. The fluid medium through which the explosive gas propagates may be assumed as ideal calorically perfect gas, and using the Rankine-Hugoniot relations, it is expressed as

$$\rho_s = \frac{\rho_0(\bar{\gamma} + 1)p_s + 2\bar{\gamma}p_0}{(\bar{\gamma} - 1)p_s + 2\bar{\gamma}p_0} \tag{2-3}$$

$$v_s = v_0\sqrt{\frac{p_s(\bar{\gamma} + 1)}{2\bar{\gamma}p_0} + 1} \tag{2-4}$$

where ρ_s and ρ_0 denote the shock density and initial density of propagating gas, respectively, while P_0 is the undisturbed gas pressure (ambient pressure). v_s and v_0 denote the shock propagating speed and sound speed, respectively. It is noted that in the fluids $v_0 = \sqrt{K_s/\rho} = \sqrt{\bar{\gamma} p_0/\rho_0}$ (K_s being the isentropic bulk modulus). The term $\bar{\gamma}$ is the specific gas constant, which is 1.4 in the case of free air blast, but it varies with the temperature. Hence, Eqn. (2-3) simplifies to the expression reported by Rajendran and Lee [13]:

$$P_r = 2p_s \frac{7P_0 + 4p_s}{7P_0 + p_s} \tag{2-5}$$

Where P_r represents the reflected overpressure pressure. The pressure reflection coefficient is given as the ratio of the reflected overpressure to incident overpressure, or

$$C_R = \frac{P}{p_s} = \frac{(3\bar{\gamma} - 1)p_s + 4\bar{\gamma}P_0}{(\bar{\gamma} - 1)p_s + 2\bar{\gamma}P_0} \tag{2-6}$$

The pressure coefficient is bound between $2 \leq C_R \leq (3\bar{\gamma} - 1)/(\bar{\gamma} - 1)$. Clearly, even for small incident overpressures, C_R departs from its acoustic limit (2) and approaches a value of (8) for very strong shock waves in air.

Referring back to Eqn. (2-1), an empirical relation of the peak overpressure reads[13]:

$$\frac{P_{so}}{P_0} = \frac{808\left\{1 + \left(\frac{Z}{4.5}\right)^2\right\}}{\sqrt{\left(1 + \left(\frac{Z}{0.048}\right)^2\right)\left(1 + \left(\frac{Z}{0.32}\right)^2\right)\left(1 + \left(\frac{Z}{1.35}\right)^2\right)}} \tag{2-7}$$

Where the scaling distance Z is given by

$$Z = \frac{S_D}{\sqrt[3]{m_{TNT}}} \tag{2-8}$$

This parameter was introduced by Hopkinson and Cranz [23], [24]; it is used as an index to be estimate the overpressure and impulse from TNT detonations (or TNT equivalent explosive mass, m_{TNT}). This parameter may be utilised as an index to gauge the blast type, i.e. far field or near field. The shock wave parameters according the scaled distance are given in Figure 2-2. In crude terms, the blast loads of $Z < 0.4$ may be assumed as localised.

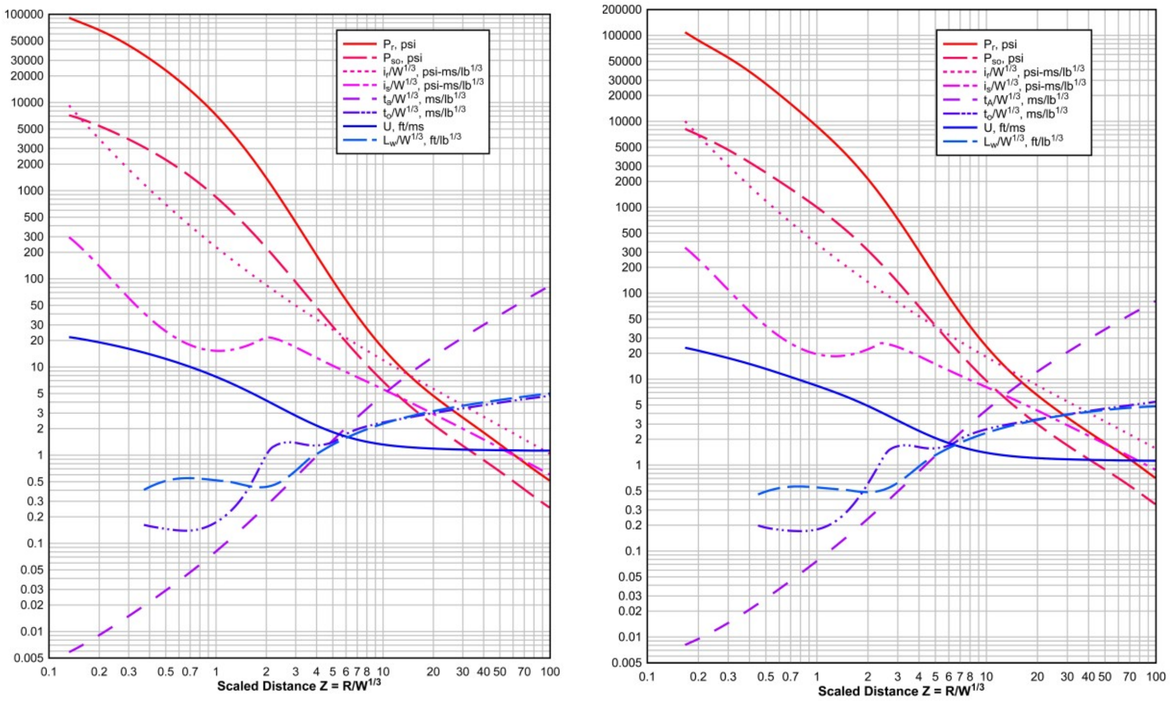

(a) (b)

Figure 2-2- Positive Shockwave parameters for a spherical (a) and hemispherical (b) free air TNT explosion [23]**.**

The scaling H.C scaling distance has been widely used by [23]–[26] to correlate the response of beams and plates in various load case scenarios. A dimensional study by [22], [27] highlighted the ratio of stand off distance to load radius as more theoretically sound scaling factor to gauge the loading nature. An extensive series of experimental data by Kingery and Bulmash [28] on TNT burst led to the idealisation of blast pressure with ConWep function (Conventional Weapons) in the UFC code [23]. Full discussion of the ConWep method is presented in Chapter 3.

A direct implication of the Eqn. (2-8) is for the blast scaling laws; in principle, two explosives of same geometry and same material would give rise to identical blast wave pressure, provided the same scaled distance. The blast curves hence developed by Kingery and Bulmash [28], [29] (Figure 2-2) enable the designer to find an estimate of the blast parameters which are related to the detonation of TNT charge.

For blast emanating from other high explosives, the concept of TNT equivalent mass factor is utilised. While the TNT equivalent mass factor enables the enables the designer to correlate between the incident and reflected overpressures and impulses of various explosive materials, these factors vary according to the blast type (i.e.) [30].

2.2.1 Fluid structure interaction

As the wavefront is transmitted onto the target, the plate gains instantaneous acceleration and departs from the interface of fluid. The pressure continues to decrease as the plate accelerates and vanishes at the time when the plate reaches the maximum velocity, so does the transferred momentum per unit area of the plate. Using the Buckingham's Π theorem, the transmitted impulse for exponentially decaying pressure is given by Taylor's [31] expression

$$\frac{I_p}{I_i} = 2\beta_0^{\frac{\beta_0}{1-\beta_0}} \tag{2-9}$$

where β_0 is the (non-dimensional) relative time constant of the fluid structure interaction and the incident wave, which is also interptreted as the relative ratio of the volume of compressed gas to the plate, i.e. $\beta_0 = \rho_0 H_f / \rho_p H$ where H_f and H are the depth of the compressed fluid and thickness of the plate, respectively. I_i and I_p represent the incident and the transmitted impulse, respectively. The degree of reflection depends on the rigidity of the target and the physics of fluid structure interaction. For example, in the circumstances where $\lim_{\beta \to 0} \frac{I_p}{I_i} = 2$, the target is assuemed rigid and incident wave is reflected completely of the rigid target plate. Thus, in the heavy plate limit the plate may be assumed as rigid body. In other words, as the limiting case of a plate with infinite mass is approached, the plate hardly moves and all of the incident pressure is reflected off the plate. Consequently, the impulse imparted to the plate reaches its maximum.

In contrast, in the case of thin plates, the plate equilibrates quickly and accelerates which relieves the reflected pressure, thus reducing the impulse. The theoretical work on the FSI effects by Taylor was extended by Kambouchev et al. [32], [33] to account for the fluid nonlinear compressibility effects. The transmitted impulse was given in terms of a single dimensionless parameter whereby the exact asymtotic limits for very light and very heavy plates were obtained.

Hutchinson [34] proposed an alternative FSI parameter (defined in terms of invariants of the incident wave) on Single Degree of Freedom (SDOF) rigid plate to delineanate the role of rigid backing to the adiabatically compressed air and stand off on the energy and momentum transfer of blast. The stand off was found to play a significant role to attenuate the momentum transfer to the plate.

2.3 LOCALISED BLAST LOAD

Analysing the blast effects requires a proper understanding of the phenomenon, the methods of blast modelling and the restrictions involved. In the sequel, there is a summary on different blast loads using associated characteristics for blast loading functions. The equations proposed by researchers [35]–[38] have been used to lift restrictions on temporal and spatial distributions of blast load function as well as providing a realistic yet accurate approximation of localised blast load which proves feasible for such types of loading.

2.3.1 Classification of structural failure modes

Depending on the load magnitude and profile, the structure responds in different failure modes. Early experimental works on uniformly blasted beam by Menkes and Opat [39] illustrated in Figure 2-3 led to a classification of the failure modes as large inelastic deformation (Mode I), large inelastic deformation with tensile tearing at supports (Mode II) and transverse shear failure at supports (Mode III), with Mode I and Mode II being the primary failure modes of for structures subject to most blast types [40].

This classification was further discussed and extended to mild steel circular and rectangular plates by Teeling Smith and Nurick [41] and Nurick and Shave [42], respectively, as presented in Table 2-1. Ref. [21], [42]–[45] also reported on a modified classification of failure modes associated with the localised blasts, while the permanent profile shape due to such phenomenon is generally characterised with a central bulged dome atop the global plate deformation. Mode II in locally blasted plates initiates with partial tearing at the central area, prior to tensile tearing in the boundaries. Transverse shear failure (mode III) is a phenomenon associated with the thick plates and is impertinent to the localised blast loads concentrated on the central portion of the plate.

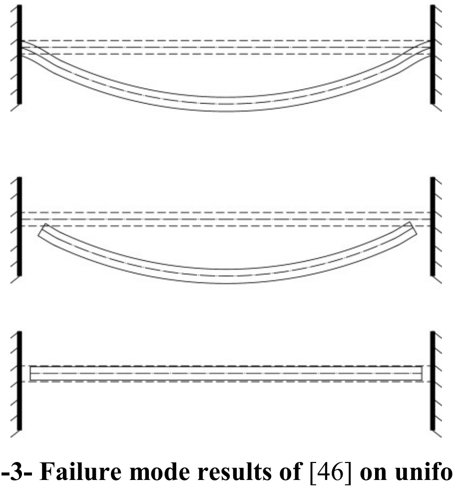

Figure 2-3- Failure mode results of [46] **on uniform blast load**

Langdon et al [47] observed that in mode I failure the thinning of the stiffened square plate is somewhat symmetrical along either side of the stiffener. The plate profile at either side of single stiffener panel shows a ‘double peak’. While introducing a single stiffener reduced deformation at similar impulse to the unstiffened plate, the tearing (Mode II*c) of the former plates occurred at lower impulse than the latter Figure 2-4. With the increase of impulse, the plate tore away from the stiffener, creating two symmetrical petals. Similar results were obtained by Ref. ‘s [46], [48]. For the blasts of sufficiently large magnitude, the boundary fixations are inconsequential in the permanent deformations in mode I, while they significantly affect the mode II response.

Rajendran and Lee [13] presented a detailed review of the pressure pulse from air and underwater explosions. The study included a description of blast wave detonation as well as shock wave propagation, various forms of pressure loads, and the plate wave interaction. Methods of calculating response to such shocks were proposed by researchers [49]–[51].

Table 2-1 Failure modes for plate subjected to localised and uniform blast load

Failure Mode	Description	Localised blast load	Uniform loading
Mode I	Large inelastic deformation	✓	✓
Mode Ia	Large inelastic response with necking around part of the boundary	-	✓
Mode Ib	Large inelastic response with necking around the boundaries	✓	✓
Mode Itc	Large inelastic response with thinning in the central area	✓	
*Mode II**	Large inelastic response with partial tearing around part of the boundary	-	✓
*Mode II*c*	Partial tearing in central area	✓	
Mode II	Tensile tearing at boundary	✓	✓
Mode IIc	Complete tearing in the central area with capping	✓	
Mode III	Transverse shear failure at the boundary	-	✓
Petalling	Tearing at the centre with petals of material folded back onto the plate	✓	

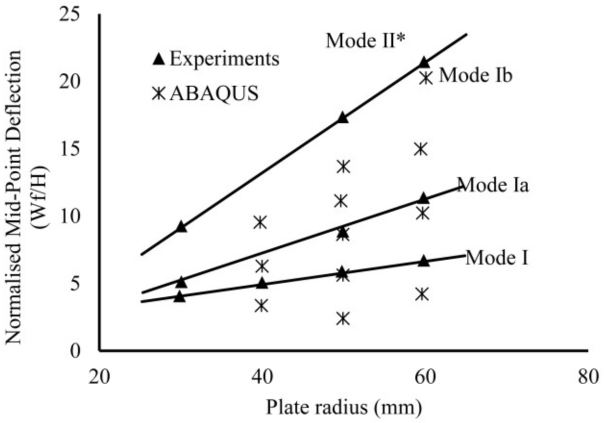

Figure 2-4- Failure mode results of [46]

Yuen and Nurick investigated the influence of plate thickness on the thinning and tearing impulse of impulsive loaded localised blast. The difference between the thinning impulse (mode Itc) and the rupture impulse decreased with the increase of the load diameter, as drawn in Figure 2-6, with the larger differences observed on thick plates (Figure 2-5-Figure 2-6).

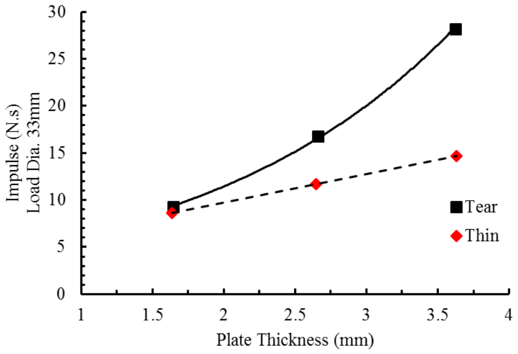

Figure 2-5- Experimental results [45]**-Tearing impulse of 33mm diameter plastic explosive**

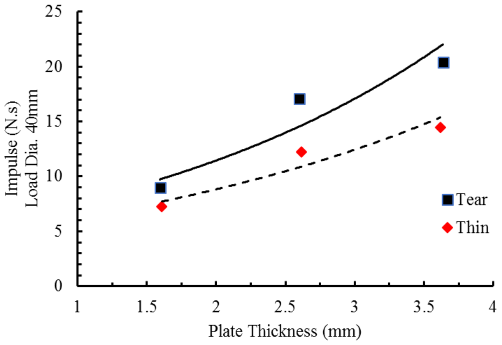

Figure 2-6- Experimental results [45]**-Tearing impulse of 40mm diameter plastic explosive**

The failure modes of localised blast initiate with large inelastic response at the central area. Thinning of the plate occurs in a narrow band along the circumference of the central bulge (mode Itc). With the increase of load magnitude, the localisation of material flow triggered by the tensile instability leads to tensile tearing and release of the central dome (mode IIc), a phenomenon referred to as capping [52] (Table 2-1). With further increase of the blast, the radial cracks continue to propagate at the fracture surface, several petals of material appear which curl back when the blast wave perforates through the material.

Following the classification response modes of plates, Nurick and co-authors [21], [25], [43], [46], [50], [51], [53]–[58] reported considerable experimental data on the response of steel plates to air-blast loading over the past three decades and developed a range of parameters, which are of practical significance in the study of dynamic response of plates subject to localised and global blast loads. Among these were the spatial loading distribution (localised versus uniform), explosive mass and shape, boundary conditions, plate characteristic dimensions and stand-off effects. A non-dimensional impulse parameter (NDIP), originally introduced by Nurick and Martin [59], [60], has been used to collapse the data into a single trend-line which allowed for the prediction of permanent displacement.

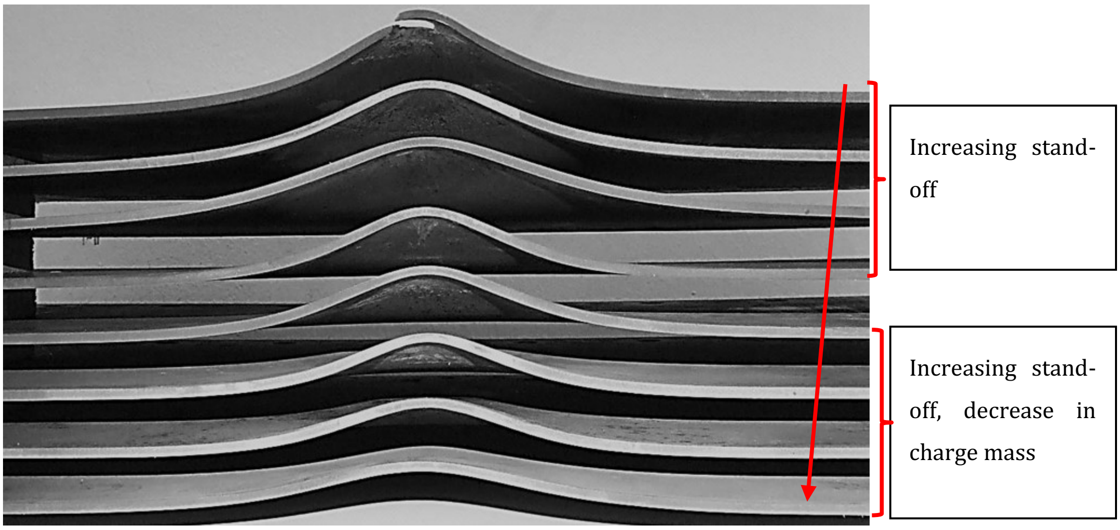

(a)

(b)

Figure 2-7- permanent deformation of ARMOX370T (a) and Mild steel (b), in order of increasing distance, courtesy of Langdon et al.[61] **M_e represents the charge mass.**

Recently, the research into the high strength armour steel has attracted attention as the high yield strength, hardness and toughness and consequently reduced structural deformation against intensive shock loads make them a potential candidate. Among these are the RHA ARMOX steel and High Hardness steel (HHA). While numerous military standards stipulate the hardness and Charpy fracture toughness as the design criteria, the limited ductility associated with the high strength of these materials may impede their protection capacity due to the brittle failure. In an experimental study by Langdon et al [61], only a marginal decrease in the thickness reduction was observed on ARMOX 370T steel type, suggesting the brittle tearing failure. The permanent deformation results of Ref. [61] is shown in Figure 2-7. Furthermore, the experimental results showed the two steel types ruptured at the same impulse, despite the higher strength of

ARMOX370Tthan Mild steel (Figure 2-8). Thus, the failure modes of the high strength steels may differ from those of conventional structural ductile materials and thus require particular attention.

Due to the high strain rates, the heat generated due to the plastic work is usually contained within the deforming material as it has no time to transfer and the process is considered adiabatic. The temperature rise due to the adiabatic process leads to local softening while the rest of the material strain hardens. provided the rate of thermal softening exceeds the work hardening in the surrounding area, the deformation occurs in bands of intense plastic shear , referred to as adiabatic shear localisation [11], [62]–[65]. In some cases, the localised temperature rise leads to instability within the microstructure of the material as narrow white etching bands of deformed martensite appear in carbon steel. These bands are referred to as the transformed adiabatic shear bands. In armour steel material, for example, the increase in static yield is accompanied by the reduction in penetration resistance over a certain hardness range. Materials with less strain rate dependence would encourage the adiabatic shear failure [11], [66].

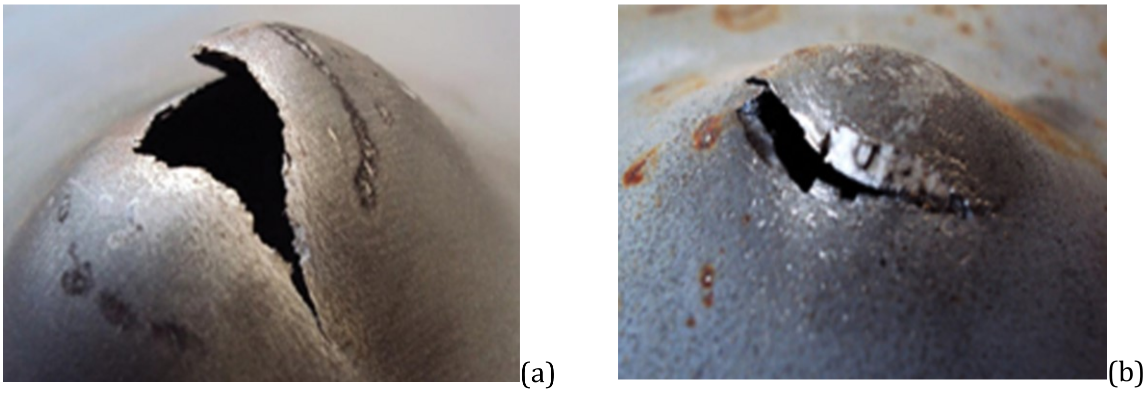
(a) (b)

Figure 2-8- Rupture of Mild steel (a) and armour steel 370T (b) under same loading configurations [61]

2.3.2 Numerical analyses

The boundary conditions significantly affect the onset of shearing and tearing afailure due to the variation of in-plane strains. Bonorchis et al. [67]–[69] conducted a numerical and experimental studies on the effects of boundary conditions and clamp heights on the localised blast response of rigid and deformable plates. They investigated the impulse generated by 8g, 12g and 15g PE4 explosive of 40mm diameter, blasted on rigid and deformable rectangular plates of 120mm ×200mm exposed area, but modified the clamp heights by according to the number of clamps involved. An essential observation of their work was that for rigid plates, the increase in the clamp height brought about an increase in the transfer of impulse recorded by the ballistic pendulum. However, even though the transferred impulse increased due to the presence of the clamps, the mid-point deformation was impervious to the clamp height. This indicates that the clamps absorb a portion of impulse recorded by the ballistic pendulum and the total impulse absorbed by the plate is reduced due to the presence of the clamps. The impulse recorded for the two clamps providing total 32mm clamp height was 18% higher than that with no clamps. The results of Bonorchis et al. on clamp type effects are illustrated in Figure 2-9.

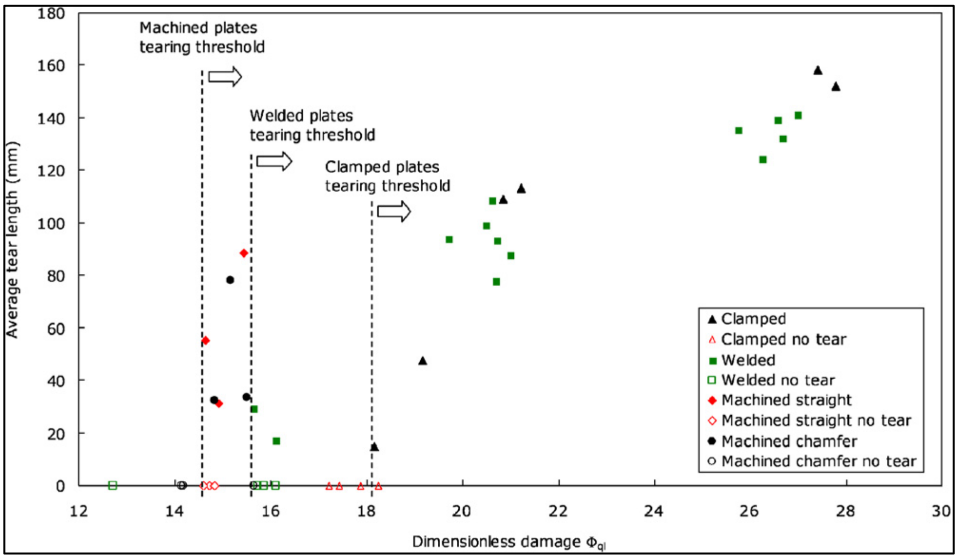

Figure 2-9- Threshold of impulse for locally blasted hot rolled steel plates with welded boundaries [69]

Advancements in numerical simulations have made it possible to observe the blast wave effects and its interactions with structures, using a Multi Material Eulerian approach. This approach incorporates the governing physics of FSI and was studied by [1], [25], [57], [70].

Børvik et al [70] presented numerical and experimental response of $6 \times 2.5 \times 2.5\ m^3$ unprotected corrugated steel containers due to 4000kg TNT at stand-off 120m. ConWep was used to calculate the peak pressure, impulse and the load duration. The pressure time history was also idealised with Eulerian Lagrangian methods as comparison to determine the efficacy of each numerical model. Detains of the Eulerian Lagrangian methods are given in the next chapter.

2.4 NON-DIMENSIONAL PARAMETERS

Dimensionless analysis provides a useful tool to corroborate between the blast load effects and the structural response in order to avoid unnecessary repetition of, experiments or numerical simulations. While the symbols for physical quantities have been devised in the past, it was Buckingham who devised a theorem-Buckingham Π theorem, to extract a complete set of dimensionless quantities, which interrelation within each set defines a unique physical problem.

A conventional non-dimensional parameter to describe the damage of metals is of Johnson's, described as

$$\mathrm{D_n} = \frac{\rho_p V_0^2}{\sigma_0} \tag{2-10}$$

This parameter has been altered and further modified by many researchers, for example, Nurick and Martin extended Johnson's damage number to incorporate the influence of the target geometry and aspect ratio, defined as the NDIP:

$$\Phi_{ql} = \frac{I}{2H^2\left(4LB\rho_p\sigma_0\right)^{\frac{1}{2}}} \tag{2-11}$$

Nurick and Martin [59], [60] then developed a simple empirical prediction of the permanent displacement of blast loaded quadrangular and circular plates. The NDIP introduced by Nurick and Martin [59] allowed for the impulse imparted to the plate to be scaled by several parameters such as the plate dimensions, material properties and explosive dimensions. This parameter has been used extensively by the researchers to predict the response of various metallic plate types as well as composites [36], [71], while extended to account for the stand-off distance by [21], [72] and plate slenderness ratio parameters [36].

A similar expression of Johnson's damage number was proposed by Jones, defined as a dimensionless initial kinetic energy, λ, in terms of the flow stress of perfectly plastic material, σ_0, the uniform impulsive velocity V_1, material geometry and density ρ. The expression of λ was proposed for mass impact and impulsive loading of either quadrangular or circular plates (Eqns. (2-12)and (2-13), respectively).

$$\lambda = \frac{4\rho_p V_1^2 LB}{\sigma_0 H^2} \tag{2-12}$$

$$\lambda = \frac{4\rho_p V_1^2 R^2}{\sigma_0 H^2} \tag{2-13}$$

Zhao [73] modified Johnson's damage number as :

$$\mathcal{R}_n = D_n\left(\frac{L}{H}\right)^2 \tag{2-14}$$

However, Li and Jones [74] questioned the validity of Zhao's response number where the transverse shear, strain rate and temperature effects become significant.

The uniform velocity of the blast phenomenon is related to the impulse as $I^* = \frac{\hat{I}}{h\sqrt{\sigma_0\rho}} = \frac{V_1}{\sqrt{\sigma_0/\rho}}$, where $\hat{I}$ and I^* are the impulse density and dimensionless impulse [75], respectively. As reported by [75] most blast load scenarios are, in fact, non-impulsive and the validity of such idealisation depends on the blast duration being shorter than the structural response time.

For impulsively localised blast loaded plates, Eqn. (2-12) can be modified empirically as in Eqn.(2-15), where A_0 is the burn area. This is attributed to the discolouration of the central plate area by the explosive particles. The expression of the burn radius R_b, defined by [45], is given in Eqn. (2-16), where h_e is the (disc explosive) charge height.

$$\lambda_1 = \frac{4I^2L^2}{\rho\sigma_0{A_0}^2H^4} \tag{2-15}$$

$$\frac{R_b}{R_e} = 0.9h_e^{0.3} \tag{2-16}$$

Jones' dimensionless kinetic energy [35] can be related to the NDIP originally defined by Nurick and Martin. The NDIP originally reported by Nurick and co-authors [43], [60], defined also as damage number $\phi_q = \frac{1}{2}\sqrt{\lambda_1/\beta}$, where $\beta = L/B$, did not incorporate the influence of geometry for quadrangular plates. However, Nurick and martin [59] later modified the NDIP as $\phi_{ql} = \left(1 + \ln\left(\frac{LB}{\pi R_e^2}\right)\right)\phi_q$ hence obtained Eqn. (2-17). The two expressions of (2-18) and (2-19) by the authors predict the normalised deflections empirically by the NDIP. Thus, the dimensionless kinetic energy is obtained $\lambda_s = 4\beta\phi_{ql}^2$, by replacing ϕ_q with ϕ_{ql} in the associated expressions.

$$\emptyset_{ql} = \frac{I\left(1 + \ln\left(\frac{4LB}{\pi{R_e}^2}\right)\right)}{2H^2(4LB\rho\sigma_0)^{1/2}} \tag{2-17}$$

$$\frac{w_f}{H} = 0.48\emptyset_{ql} \tag{2-18}$$

$$\frac{w_f}{H} = 0.47\emptyset_{ql} + 0.001 \tag{2-19}$$

Nurick and Martin's estimate for the permanent deformation (Eqn.s' (2-18)(2-19)) are widely accepted expressions to estimate the permanent deformation of most fully-clamped, protective plated systems against various blast scenarios of distal charges. Eqn. (2-17) is similar to the quotient of the kinetic energy to membrane resistance of the target in impulsive loading regime asymptotes. The relationship between the normalised deflection and NDIP has been modified by [21], [76] and [67] to account for the stand off distance in localised blast scenarios. It should be mentioned that, the above expressions have been modified in this thesis, in the context of problem, to obtain a better fit to the large scatter of data from the experimental and numerical results of armour and mild steel plates, discussed in Section 4.5.

2.4.1 Transient response of the structure

Measuring the transient deformation history of plates (prior to failure) provides valuable information that improves our understanding of the mechanisms which influence and control the deformation and rupture of plates. This is particularly of practical convenience in high strength armour steels where the elastic energy stored during deformation is of relatively high proportion of the total deformation energy, compared to mild steel. On the other hand, armour steels have limited ductility compared to mild steel plates which dissipate energy in plastic strain.

Neuberger et al [24], [26] conducted experimental studies on the 0.5m and 1m diameter circular steel plate made of Rolled Homogeneous Armour (RHA) subject to air blast and buried charge loading from spherical TNT charges (TNT mass was varying from 486g to 8.75kg), at varying -off distance (65-200mm). The scaling distance was $Z{\sim}0.143$ and the ConWep method was used. The objective was to investigate the scaling aspects of the blast test as well as the spring-back phenomenon. The deformation combs such as used by Neuberger [24] provides information about the maximum transient displacement of a plate (usually at the mid-point) but cannot give details regarding the time to peak of the deformation profile across the plate. There is also the possibility of contact measurement techniques influencing the response of the plates, a drawback that can be overcome by using non-contact measurement techniques such as high-speed imaging.

Fourney et al [77] and Spranghers et al [78] used high speed photography and a 3D digital image correlation (DIC) to measure the transient response of plates subjected to low charge mass explosive detonations. Small apertures on the lenses were used to ensure sufficient depth of field for tracking the plate motion, and challenges of changing light conditions on the specimen as it moved were also reported [77]. Aune et al [79] used high speed photography to film the motion of a blast loaded plate mounted in a stationary rigid clamp frame. The cameras were placed in the same room at the blast event and were unfortunately affected by the blast wave. The correlation of images reduced accuracy after the blast wave had impinged on the cameras, limiting the duration of the data capture. Aune et al [79] also reported inconsistencies in the trigger system and difficulties with the painted speckle pattern peeling from the plates. Zhu [80] investigated the plate profile based on numerical and experimental work on transient deformation of aluminium alloy and mild steel plate using a one camera system.

The DIC technique has also been proved a useful tool to capture the strain distribution and localisation of plates at different strain rates. Hooper monitored the deformed shape, strain rate and of PVB laminated glass panes subjected to air blasts of scaled distances $Z = 3.65$-5.3 [81]. At this distance, the strains were localised to the window edge while the central region was relatively unstrained. The piezoelectric pressure gauges were used to measure the pressure distribution on the panels. Sato et al. [82] captured the distribution and localisation behaviour of strain of various steel grades, having yield stresses 165MPa-1256MPa, at quasi-static strain rate $(10^{-3}s^{-1})$ to dynamic strain rates $(100s^{-1})$. To capture the mechanical properties at different strain rates, the authors used one camera and two cameras on their DIC test setup, adjusted with electro-mechanical tensile test, hydraulic tensile test and Hopkinson bar test machines. The calculated ratio of dynamic stress to static stress decreased exponentially with the increase of yield strength. Further, inhomogeneous strain distribution was observed at the nominal strain of 0.2. Similar have been carried out to measure the effect of strain rate on necking and fracture behaviour [83]–[86].

Børvik et al [70] observed the uncoupled Eulerian Lagrangian and fully coupled Eulerian Lagrangian gave the same results on the stiffened structure (Figure 2-10). This is because the impulse due to the fluid structure interaction is reduced. The structural rigidity increases the pressure impulse [87], [88] and thus increases the permanent magnitude of the structural response. uncoupled Eulerian Lagrangian approach A significant difference between the transient profiles of box containers due to the difference in the numerical techniques when modelling the pressure time history, despite the same total impulse.

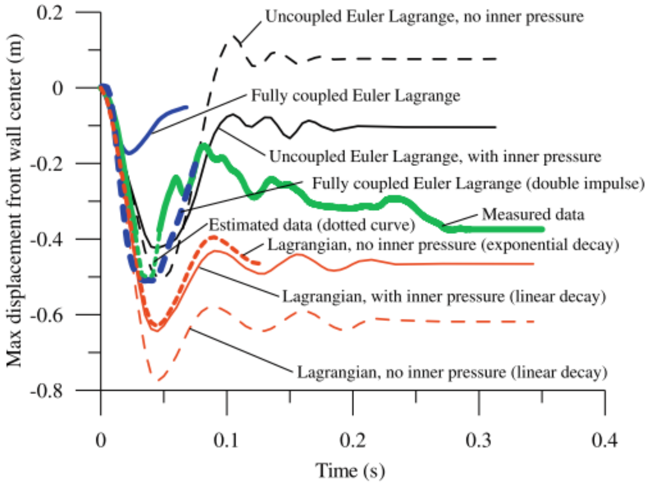

Figure 2-10- Transient mid-point displacement of the front wall of container by [70]

Much of the past work on blast loaded plates has concentrated on relatively ductile steels, which exhibit large plastic deformations and then ductile tensile tearing at high charge masses. Very few researchers have published work on the transient deformation, localised response and failure of high strength steels, such as the ARMOX armour steels. Among those, Langdon et al [61] reported the results of localised blast tests on mild steel, ARMOX 370T, aluminium alloy and fibre reinforced polymer composite plates. Permanent mid-point displacement increased linearly with increasing impulse for each material type, up to rupture. At higher charge masses, the mild steel plates exhibited ductile tensile rupture, while the armour steel plates (which ruptured at the same impulse) exhibited a more brittle type of failure. Non-dimensional impulse at rupture was observed to increase with increasing SETF (Specific Energy to Tensile Fracture), which was obtained by directly integrating the stress-strain curve obtained from uniaxial quasi-static tensile tests [61].

2.5 THEORETICAL ANALYSIS OF MONOLITHIC PLATES

The theoretical analysis of monolithic plates has been explored by means of constitutive models for many years. A constitutive model defines a set of relations that characterise the physical response of a material when subjected to external loading. Most commonly model of this kind is the constitutive framework of limit analysis which assumes the material as rigid, perfectly plastic.

2.5.1 Dynamic plastic behaviour of thin plates

The first study on static collapse of plates was conducted by Hopkins and Prager [89] who implemented the limit analysis theorems to determine the load carrying capacity of simply supported rigid-perfectly plastic circular plates. The quasi-static model response by Hopkins and Prager was extended to the dynamic loads having rectangular pulse pressure[75], [90]. Such a response is pertinent to the impulsive regime, where the ratio of the blast duration to the total plate response time is pivotal in idealisation of the blast with zero period, i.e. uniform momentum impulse. Youngdahl [37] discussed the strong dependence of the dynamic plastic deformation of plated structures on the pulse shape. An empirical relationship was proposed to eliminate the pulse shape effect which was incorporated in the design and analysis of two-dimensional structural members. He proposed a relationship which linked the maximum plastic deformation to square of effective impulse multiplied by a function of effective pressure. This relationship was widely used for decades prior to being theoretically established by researchers as the upper bound for the actual displacement while the response time was found to be the lower bound on the actual response time (Li and Jones [91]).

Cox and Morland [92] obtained theoretical solutions for dynamic plastic response of simply supported square plates as well as the response of n-sided polygonal plates subjected to uniform dynamic load. Jones with co-authors presented an extensive series of theoretical and experimental research on various structural elements subject to spatially uniform pressure loads of rectangular temporal pulse shape [93], [74], [94]–[97]. In most cases, Jones' analytical models for impulsive loading offered solutions concurrent with experimental works, provided the ratio of kinetic energy to maximum strain energy stored elastically remained more than ten [98]. Komarov and Nemirovskii [99] further extended the analyses of Jones [35] to the dynamic case with travelling plastic hinges to obtain the incipient plastic deformation in each of the two stages of motion.

The previous studies investigated the infinitesimal deformation of plates, where bending moment predominate the overall response. In the event of blasts having high magnitude impulses, large deformations are expected and for thin shells the membrane forces dominate the structural behaviour. Yuan et al [100] proposed an analytical model to calculate the large deformation of elastic-perfectly plastic beam systems. They studied the influence of catenary (membrane) forces, bending moment and transverse shear forces alone or in joint actions considering three distinct failure mode deformations. The effect of membrane action was similarly studied by [35], [101], [102] for blast loaded plates and for plates struck by single and repeated masses, the latter being a phenomenon called pseudo-shakedown. Chen and Yu [103] investigated the membrane effects on beams with inclusion of transient state in the velocity profile. Other researchers[104] extended analysis of Komarov and Nemirovskii [99] to include the effect of catenary action on circular panels. It was shown, theoretically, that the inclusion of transient phase-in which the velocity profile is time dependent- in analysis gave better agreement with experimental results than analysis of Jones [35]. Jones [105] later presented a mathematical procedure for the strain rate sensitive ductile plate under impact and explosive loading. His equations to predict the strain rate behaviour of plates were not only dependent on the material constants D and q (from Cowper Symonds equation), but also on the flow stress and density of the plate material.

Zheng et al [98] discussed the strain energy of a stiffened plate subject to uniform pressure load in terms of bending strain energy, elastic-plastic membrane strain energy in plastic zones and strain energy of the stiffeners. The plate deformation was represented by a piecewise function of cosine shape to represent the global deformation of central zone as well as a linear shape used for simplified rigid-plastic model in the surroundings parts. The generalised displacements were obtained numerically and used to determine the deflection time history.

Langdon and Schleyer [106], [107] presented a series of numerical, analytical and experimental studies on the connection characterization and linear decay pressure pulse response of the corrugated stainless-steel blast walls with welded angle section. They found that the yield pressure, i.e. the pressure to cause inelastic strains at the mid-point of corrugation, was reduced by increasing the flexibility of the angle length connections, which was influenced by loading direction. Buckling capacity was also influenced by load direction because of non-symmetry of the profile. Nwankwo et al. [108] extended the theoretical analysis of the former authors to the CFRP (carbon fibre reinforced polymer) retrofitted blast walls using the elastic-perfectly plastic beam spring system with stationery bending hinges.

2.5.2 Dynamic plastic behaviour of thick plates

The transverse shear response is an important concept during the early stage response of the structural elements [74], [109], [110]. The influence of transverse shear on uniformly impulsively loaded beams and circular plates have been examined by Jones and co-authors [111]–[116] who have classified the thick circular plates and shells according to the ratio of static plastic shear to bending moment ($\nu = \mathrm{Q_0R/2M_0}$), with R being the radius of the plate. With the increase in plate thickness, the plastic work rate due to bending transcends that of the membrane [117]. Further increase in thickness renders the effects of rotatory inertia and shear significant, although the effect of the former is not nearly as important as the effect of the latter. Rotatory inertia effects would contribute toward the moment for moderately-stocky circular plates ($L/H > 3/2$) or beams subjected to uniform blasts [111], [112]. However, the theoretical study sought in the case of class II (moderate stocky) circular plates-where ν is in the range of $\nu =\ 1.5 < \mathrm{Q_0R/2M_0} < 2$- showed that combined effect of the rotatory inertia and transverse shear effect would only improve the accuracy of maximum permanent displacement by only 11% 14% compared to the transverse shear effect alone [111]. Li [109] investigated the continuity conditions of shearing interface and bending interface of stationery and moving hinge and discussed that the localised shear response becomes the dominant mode when the transverse shear conditions are satisfied. Li and Huang [118] showed that while the inner plastic region undergoes a small transverse shear force, the transverse shear deformation increases rapidly in the outer plastic region. On the other hand, the bending moment is large throughout the plate and decreases only rapidly near the supports. It follows that the transverse shear forces induce shear sliding at the support at the interface of which the deformation profile is discontinuous.

The previous studies on rectangular plates have focused on temporally rectangular pulse loads of a spatially uniform pressure loading profile. These are often accompanied by simplifications in the mathematical treatments, which reduce the accuracy of the results. Thus, there is a paucity of theoretical analysis on the plates subjected to localised blasts.

2.6 SUMMARY AND CONCLUDING REMARKS

In this chapter, a detailed review has been presented on the performance of beams, quadrangular and circular metallic plates. It transpires that, while many researchers have examined the blast and impact behaviour of the monolithic plates, there is a paucity of systematic experimental, numerical and theoretical analysis which unifies the methods to describe the effect of localised blasts on modern armour steel materials. Thus, the presentation of work in this thesis consists of:

- A methodology for the advanced experimental and numerical studies, as presented in chapter 3. The numerical studies employ the fluid structure interaction phenomenon to simulate the blast.
- The results of Numerical methods and validations with experimental studies, presented in Chapter 4.
- Theoretical analysis on nonlinear dynamic response of thin ductile metallic plates with various boundary conditions, using the Kirchhoff Love plate theory, this is presented in Chapter 5.
- A rigorous study on the non-linear performance of square membranes subject to such blast loads, assuming the panels are made of elastic-perfectly plastic material. This is presented in Chapter 6.
- A theoretical study on the influence of transverse shear on the inelastic response of square plates, presented in Chapter 7.
- Dimensional analysis to describe the blast load and its effects on the structures to aid the designer to predict the localised blast load parameters, this is presented in Chapter 8.
- Based on the comprehensive theoretical, experimental and numerical models employed in the thesis, a unified design procedure is set out, as follows, to delineate the localised balst response of ductile, isotropic square panels encompassing wide range of blast load scenarios independent of the material type.

i. Assume a blast load scenario generated from cylindrical charge of certain mass M_e and geometry, say 40g PE4 of 50mm diameter. For the blast loads brought about by charges of other geometry/explosive type, the approximate charge equivalencies may be used. For example, assuming the spherical and cylindrical charges of identical masses to exert the same impulse, the radius of the spherical charges may be evaluated as $M_e = \rho V_p$. Regarding the different charge types, the TNT equivalencies may be utilised [30]. Further discussion is presented in Section 3.4.3.

ii. Estimate the pressure from Figure 8-8 (for localised blasts, (i.e. Z<0.4)) or from Figure 2-2 (for more global blast loads). Alternatively, for impulsive blasts, the pressure may be estimated directly from the known impulse.

iii. Determine the blast load parameters b, r_e, τ from Figure 8-15, Figure 8-12 and Figure 8-10 respectively.

iv. Using the empirical models, estimate the NDIP, assuming the quotient of the deformation to plate length is inconsequential, (e.g. ${}^{W_f}/_{2L} \leq 0.1$).

v. Estimate the NDIP using Eqn. (4-8) or Figure 4-16.

vi. Estimate the desired plate thickness. Using Eqn.(4-7)or Eqn. (4-8).

vii. Calculate the dimensionless initial kinetic energy λ

viii. Calculate the permanent deflection of the plates

ix. Calculate the energy effectiveness as a criterion for rupture impulse

This procedure is set out in Figure 2-11. Further details about the rupture impulse and the load parameters are set out in Chapter 8.

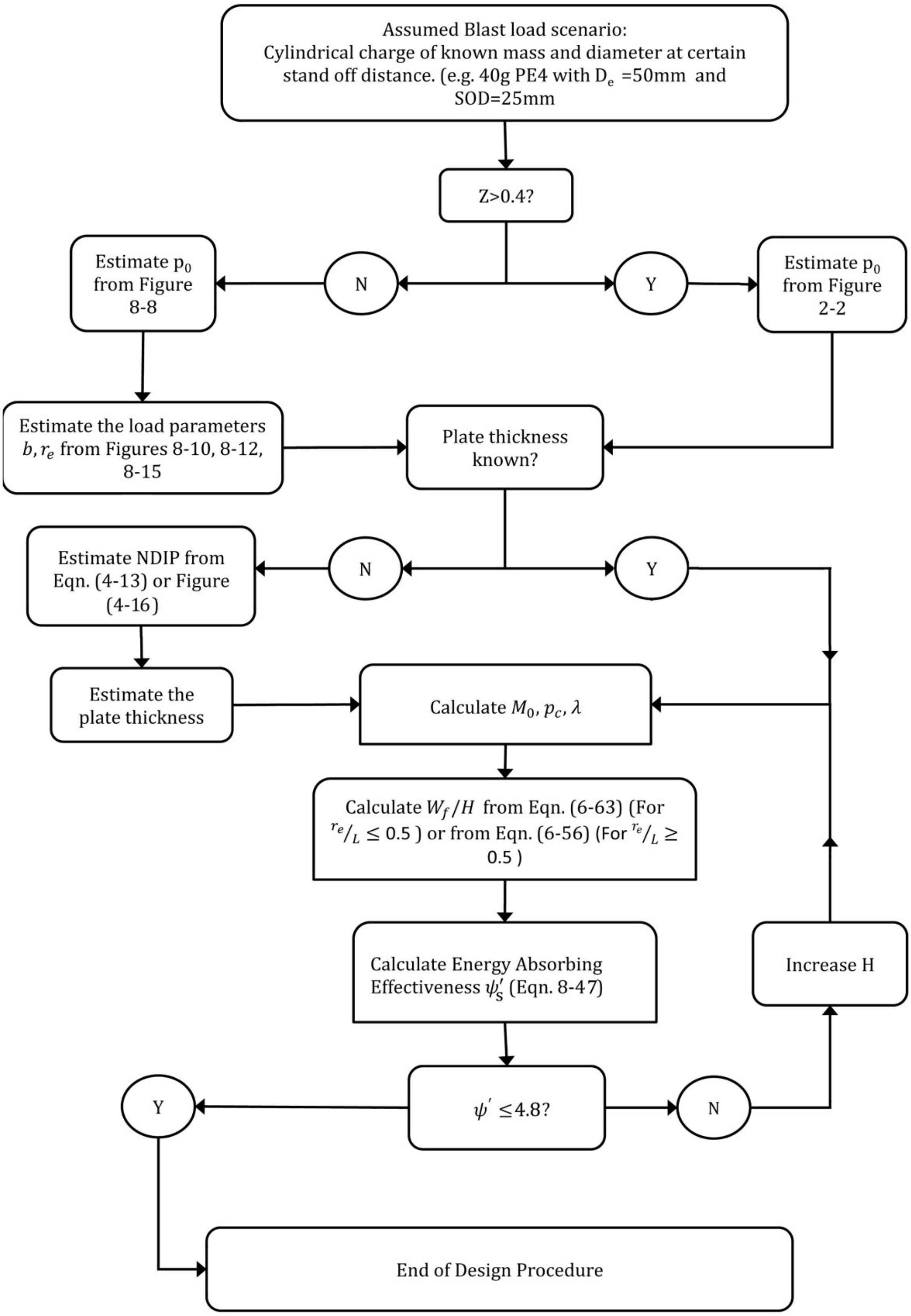

Figure 2-11- Preliminary Design procedure of membrane/plated structures against blast load.

CHAPTER 3

Methodology

3.1 BACKGROUND

This chapter explores the methodology of the numerical and experimental studies. It investigates the experimental and numerical models to capture the transient deformation and transmitted impulse of the plates. These numerical models were investigated to supplement the results of [61] on AR370T and mild steel, as well as further experimental setup on higher strength martensitic armour graded plates.

The dissemination of this chapter is as follows. First, the material properties and the constitutive models are presented, followed by the experimental studies on square plate steel graded materials in Section 3.3. Finally, in Section 3.4, the methodology of the numerical models is presented. The content of experimental and numerical methods described herein is published in [119]

3.2 MATERIAL PROPERTIES

3.2.1 Constitutive models

Most structural systems are made of ductile steel, or alloys of steel metals with isotropic behaviour, high strength and post yielding resilience. These metals undergo elastic-plastic behaviour with the associated post hardening effects of the yield strength. Beyond the ultimate tensile strength, ductile damage-necking and then tearing of the material will occur. Cowper and Symonds [120] proposed a phenomenological constitutive material model to describe the rate sensitivity dependence of the flow stress due to dynamic loads. The model by Cowper Symonds is prevalently utilised in the theoretical as well as the numerical models in the literature[40], [78], [121]–[123]. This constitutive equation defines dynamic plastic stress as a function of static yield stress and strain rate as in Eqn. (3-1).

$$\sigma'_y = \sigma_0 \left(1 + \left(\frac{\dot{\varepsilon}}{D} \right)^{1/q} \right) \tag{3-1}$$

where σ'_y and σ_0 are the dynamic and static yield stresses, respectively, and $\dot{\varepsilon}$ is the uniaxial strain rate. This expression is a highly nonlinear equation as the material constant q is usually large. This material model scales the initial yield stress by strain rate factor as well as the strain factor (as $\sigma_0 = f(\varepsilon)\sigma_y$ accounts for the work hardening, with σ_y being the initial static yield stress)[124]. Eqn. (3-1) requires the *priori* knowledge of strain hardening behaviour through uniaxial static tests. The material constants D and q for mild steel are commonly 40.4 (s^{-1}) and 5 [26], [35], [40], [43], [76], [78], [105], [125] although higher values of D (e.g. $D = 6500$) are proposed such that the C.S model predicted curve passes through widely scattered experimental data [96]. While Cowper Symonds parameters give satisfactory results in low strain rates, they are not independent of temperature. In high strain rates, the flow stresses increase rapidly, and the viscous drag controls the dislocation movement. However, high strength steel such as RHA and Ultra Hard Armour steel are less dependent on the strain rate, for the former the parameter $D = 300$ (s^{-1}) is proposed herein [26].

The Ramberg-Osgood constitutive model [126], [127] is given by

$$\mathrm{\varepsilon} = \frac{\sigma}{\mathrm{E}}\left(1 + \alpha\left(\frac{\sigma}{\sigma_y}\right)^{n-1}\right) = \frac{\sigma}{\mathrm{E}} + \varepsilon_0\left(\frac{3}{2(1+\nu)}\right)^{\frac{n+1}{2}}\left(\frac{\sigma}{\sigma_y}\right)^{n} \qquad \textbf{(3-2)}$$

Where the parameter α is the yield offset. This model does not account for strain rate effects but obeys the power law relations between the strain tensor and associated stress tensor.

Johnson & Cook [128] put forth an alternative model (Eqn. (3-3)) which includes the work hardening effect. The Johnson-Cook model is a multiplicative model, where the work hardening increases with the increase in strain rates. The model estimates the dynamic flow as a function of the strain hardening, the strain rate effects with change of temperature:

$$\sigma'_y = \left[\sigma_y + B_1{}'\varepsilon^n\right]\left[1 + C ln\dot{\varepsilon}^*\right]\left[1 - \hat{\theta}^m\right] \qquad \textbf{(3-3)}$$

$$\hat{\theta} = \left[\frac{T - 300}{T_{melt} - 300}\right] \qquad \textbf{(3-4)}$$

where $B_1{}'$ and n are the hardening constant and exponent, respectively, $\dot{\varepsilon}^* = \dot{\varepsilon}/\dot{\varepsilon}_0$ is the dimensionless plastic strain rate and the reference strain rate $\dot{\varepsilon}_0 = 1s^{-1}$, while C is the strain rate constant. The homologous temperature $\hat{\theta}$ is given by Eqn. (3-4), where T is the temperature in Kelvin and $T_{melt} = 1800K$ was assumed as the melting temperature. The J.C parameters for armour steel are obtained by the method discussed in [129]. While the herein numerical approach utilises the J.C material model, the results with C.S model are also investigated in parts for comparison.

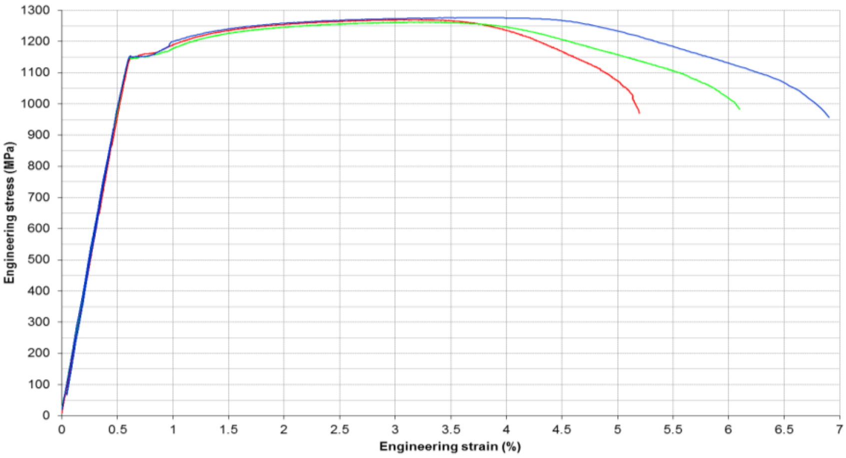

Figure 3-1- Uniaxial strain stress curve of AR370T, courtesy of Ref. [61]

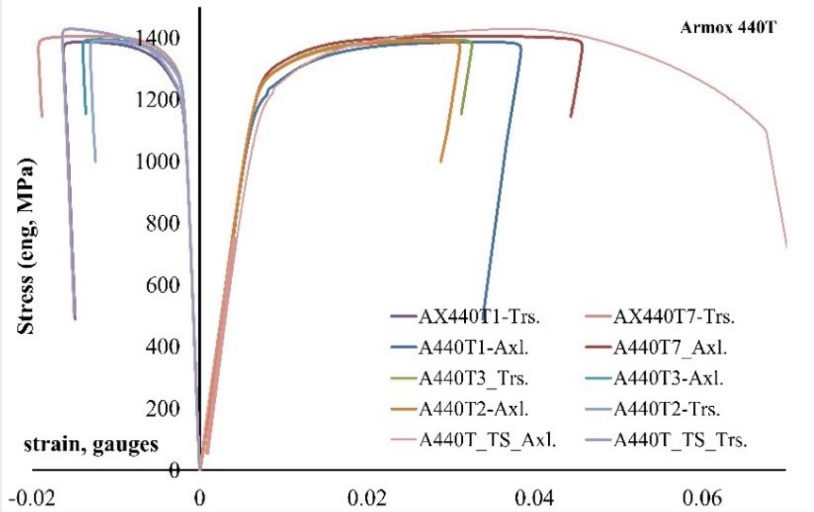

Figure 3-2 Quasi-static plot of axial (Axl0 and transverse (Trs) engineering stress curves for ARMOX 440T, compared against the true stress (TS) curves

Based on the uniaxial static test results at Imperial College laboratory and the material data sheet of ARMOX steel, the percentage elongation to rupture of AR440T is 8% and those of AR 370T and mild steel are 6% and 40%, respectively [61], [130], [131]. The Young modulus and Poisson ratio of all of these panels was taken as 200GPa $\upsilon_e = 0.3$, respectively. The yield strength of the panels is presented in Table 3-1 and a plot of engineering stress vs strain given in Figure 3-1-Figure 3-2 for AR370T and AR440T, respectively. To obtain the JC parameters for armour steel, the quasi-static tensile test data from [61] were adjusted to the line of best fit (Figure 3-3). These parameters are shown in Table 3-2. The material properties used for armour 500T were taken from [132]. The armour 500T had identical configurations to other panels except that H=4.16mm, $\sigma_0 = 1470$ MPa and $S_D = 38mm$ were used.

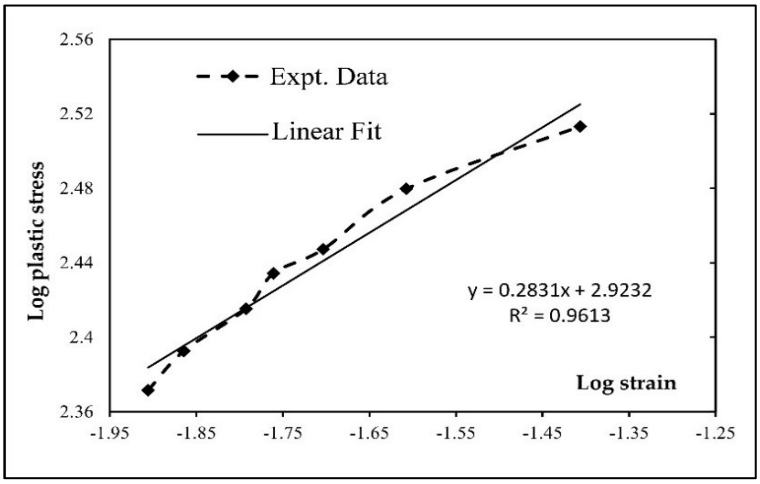

Figure 3-3 Log plastic strain vs log plastic stress curve. Notes: The values of B_1' and n are the 10(y intercept) and the slope of the log (plastic stress) vs log (plastic strain) plot. Constant C is found from the plot of high strain rate sensitivity vs dynamic stress plots [129]**. All materials were assumed to have the melting temp and transition temp of 1800 and 293 K respectively**

Table 3-1- Engineering yield and ultimate stress of the panels

Plate	**Thickness (mm)**	σ_0 (MPa)	σ_{UT} (MPa)	**Hardness (HBW)**
ARMOX 370T	3.8	1150	1250	380-430
ARMOX 440T	4.6	1210	1400	420-480
Mild Steel	4	330	400	120
AR500T	4.16	1470	1750	480-540

Table 3-2- JC and Cowper Symonds (C.S) material parameters

Material	**Johnson Cook**					**C.S**	
	σ_y (MPa)	B_1' (MPa	C	n	m	D	q
AR370T	1157	837.92	0.015	0.283	0.897	300	5
AR440 T	1210						
Mild steel MS4	325	275	0.076	0.36	1	40.4	5
AR500T	1470	837.92	0.005	0.36	0.897	300	5

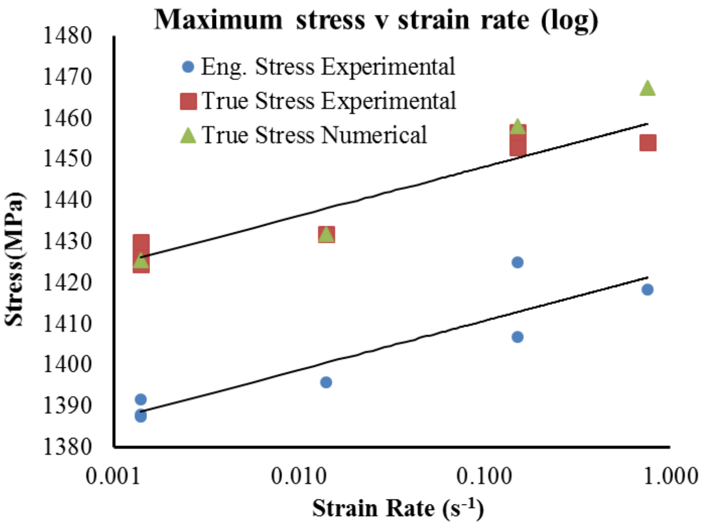

Figure 3-4 log plot of the ultimate tensile strength of ARMOX440T at various strain rates

Regarding the numerical studies, adiabatic heating condition was assumed. The temperature change due to such a condition is given as:

$$\Delta T = \int_0^{\varepsilon_{eq}} \chi \frac{\sigma_{eq} d\varepsilon_{eq}}{\rho C_p} \tag{3-5}$$

where ε_{eq} and σ_{eq} are the equivalent plastic strain and equivalent stress, respectively, ρ the material density, C_p is the specific capacity at constant pressure (defined in Table 3-7). The Taylor-Quinney coefficient χ was taken as 0.9 and represents the fraction of the plastic work converted to heat.

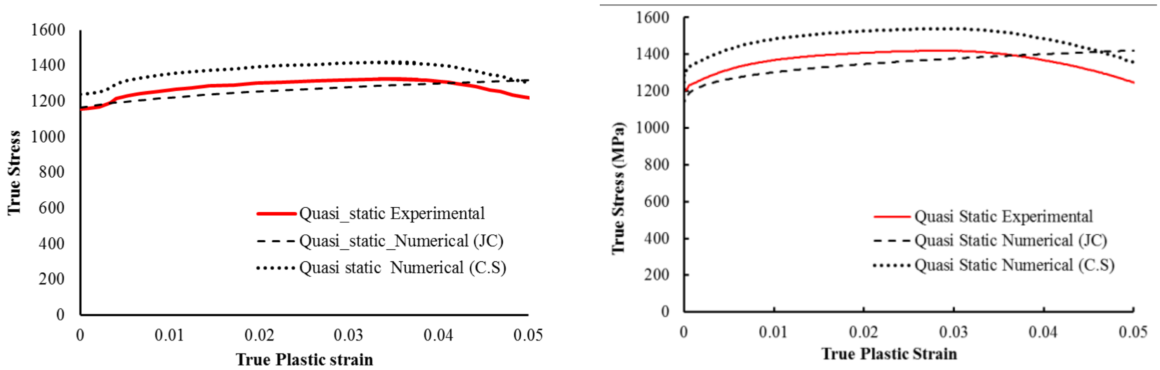

(a) (b)

Figure 3-5 Quasi-static strain hardening (8×10^{-4}s^{-1})-Numerical fit vs experimental data for armour 370T (a) and armour 440T (b). The temperature effects from JC model have been disregarded

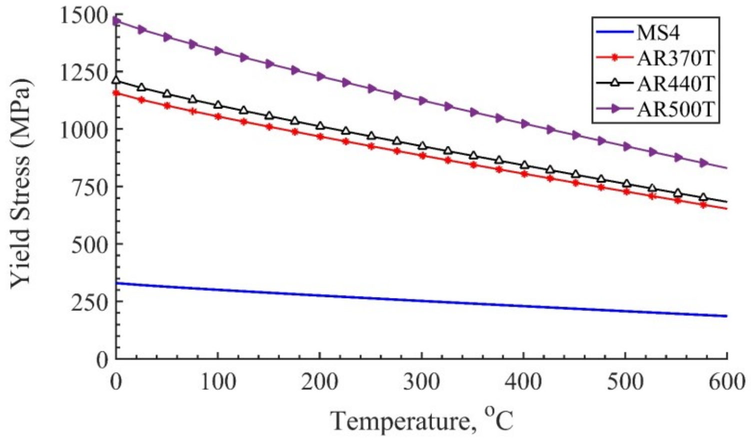

(a)

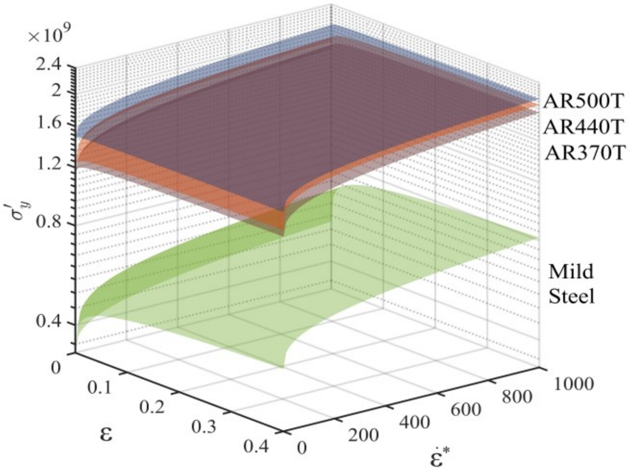

(b)

Figure 3-6 Influence of elevated temperature on predicted JC model yield stress (a) Influence of strain rate snd strain hardening on the dynamic flow stress

The predicted true stress –strain curves of the panels were calculated from the engineering stress strain curves provided by Ref. [61], [131] . The ultimate true stress of armour 440T is compared at different strain rates in Figure 3-4, while a plot of quasi- static strain hardening characteristics is presented in Figure 3-5. The specific heat capacity of the steel panels was assumed as $452kJ/kgK$. In Figure 3-6 the influence of temperature softening and strain rate on the material models are illustrated.

3.3 DESCRIPTION OF PHYSICAL EXPERIMENTS

In this work, the experimental studies and methods have been conducted by Langdon et al [61], [133] as well as those conducted by L.A. Louca is reported and compared against the numerical models.

Measuring the transient deformation history of plates prior to failure is of practical importance as well as intrinsic interest as it adds insight into the deformation modes and determination of the maximum displacement. However, placing instrumentation on or in proximity to the test plate poses damage to the instrumentation while affecting the plate response. Non-contact measurement techniques such as high-speed filming and 3D digital image correlation are more convenient to extract richer data and are used in many applications [134].

Curry et al. [133] recently reported results from tests on 3mm thick Domex 355MC steel plates subjected to air-blast loading. Curry et al. [133] also reported an improved technique for measuring transient deformation via high speed photography. The cameras and test plates were mounted onto a newly designed pendulum system. The camera section of the pendulum was covered by a shroud to protect the cameras from the light flash (causing saturation of the CCD) and blast wave impingement. Mid-point transient deformation-time histories and deformation profiles across the plate mid-lines at various discrete times were both reported.

3.3.1 Blast test Specimens

Several panels were tested in a specially built blast facility at the Department of Mechanical Engineering at the University of Cape Town (Figure 3-7). The test panels were made from two high strength steels with the properties described in Table 3-1. Each test plate was bolted into the clamps with 12 evenly spaced bolts. The plates were clamped along the periphery between two square clamp frames, leaving a square exposed area of 400 mm by 400 mm and areal density of 31kg/m^2. The AR440T panels incorporate higher mass with average nominal thickness of 4.6 mm and areal density of 37kg/m^2). As a comparison, mild steel panels with same dimensions were also tested.

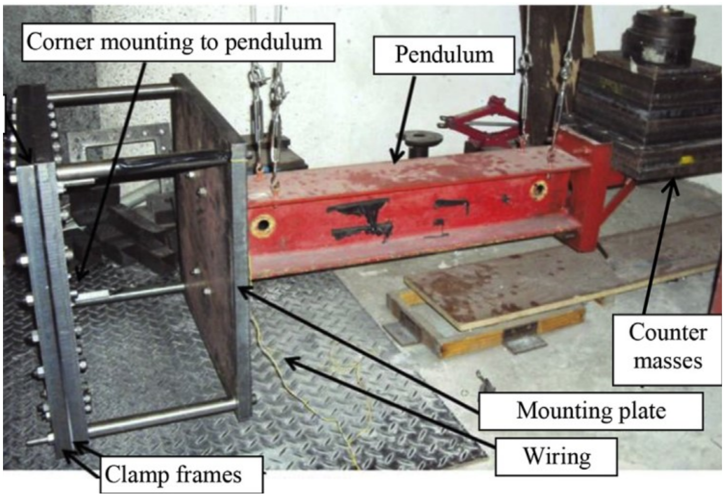

Figure 3-7 Experimental test arrangement with horizontal pendulum. Courtesy of [61]**.**

Figure 3-8- Photograph showing the inside of the modified, DIC pendulum, set up for filming the rear surface of the plates

The clamp frames were mounted to a pendulum so that the total impulse imparted to the system could be calculated from the pendulum swing. M2A3 instantaneous electrical detonators were used to generate the air-blast loading, by detonating circular disks of composition C4 (PE4) plastic explosive at a predetermined stand-off distance. The PE4 discs were adjusted at the centre of the test plates using a polystyrene bridge arrangement, as illustrated in Figure 3-9. Stand-off distances of 25 mm 38 mm and 50mm were used, as presented in Table 3-4, which were specified by varying the lengths of the bridge legs. The bridge arrangement of polystyrene is more practical method to provide the stand-off as it does not affect the blast wave pressure compared to the polystyrene buffer in [135] or mild steel tubes [21]. Only the specimen MSP1 and MSP2 configurations had the charge diameter $D_e = 75\text{mm}$, whereas the load diameter for the rest of mild steel models as well as all the armour steel models is 50mm, except for ASP7 and ASP8 which was 40mm. Thus, the charge mass could be varied only by changing the height of the explosive, and ranged from 24 g to 70 g. The general experimental arrangement is shown in Figure 3-7-Figure 3-8. Further details of the test arrangement are discussed in Ref. [60].

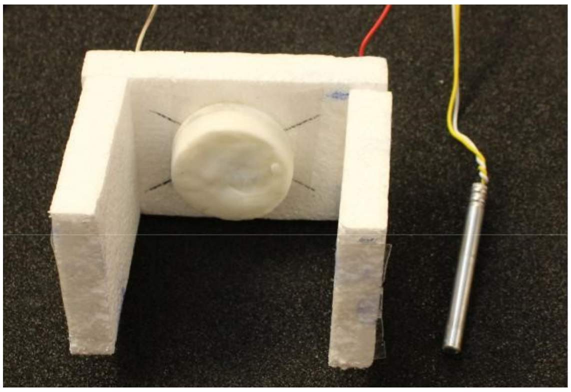

Figure 3-9- Photograph of the loading arrangement

Table 3-3 Chemical composition of the armour steel panels [131] *** intentional alloying element**

Chemical composition(%max)		C^*	Si^*	Mn^*	P	S	Cr^*	Ni^*	Mo^*	B^*
Panels	AR370T	0.32	0.4	1.2	0.010	0.003	1.0	1.8	0.7	0.005
	AR440T	0.21	0.5							
	AR500T	0.32	0.4							

A small number of the test plates (tested at charge masses to ensure that no fracture of the plates would occur) were mounted to the modified pendulum system described by Curry and Langdon [133] which was used to determine the impulse and house the cameras used for transient measurements. The new pendulum provided protection for the cameras from the intense light burst and the ensuing blast wave (Figure 3-8). Two IDT vision NR4 S3 high speed cameras were mounted to a vibration isolated aluminium rail system to prevent independent movement during the testing. The two cameras were oriented to face the rear of the test plate and separated by an approximate 30° included angle on a rail system to isolate them from the relative vibrations. The synchronised images from the two cameras were triggered with a custom built TTL trigger circuit that was activated by the detonation. A full width strip along the mid-line was filmed by both cameras at a frame rate of 30 000 Fps with the exposure set at 33 μs, adjusted due to the amount of light needed to illuminate the specimen.

Each test plate was bolted into the clamp frames with 12 bolts, the frames were chamfered to prevent pressure recirculation. The rear surfaces of the panels were cleaned, abraded and then painted with a random speckle pattern which was used in the DIC procedure to determine the spatial deformation of the plate. Full details of the specimen preparation procedure are found in Reference [133].

Table 3-4- Steel panels' configurations and load parameters

Configurations			M_e (g)	h_e. (mm)	Configurations			M_e (g)	h_e (mm)
Mat.	S_D (mm)	**Model**			**Mat.**	S_D (mm)	**Model**		
Mild Steel	25	MS-P1	25	3.53	**AMX 370T**	38	AS-P5	40	12.72
		MS-P6	40	12.72			AS-P6	50	15.91
		MS-P8	33	10.50			AS-P7	40	19.88
		MS-P10	40	12.72			AS-P8	50	24.85
AMX 370T	25	AS-P1	40	12.72	**AMX 440T**	25	B3	33	10.50
		AS-P2	33	10.50			B6	50	15.91
	50	AS-P3	40	12.72		38	AX24	24	7.3
		AS-P4	70	22.27			B4	33	10.49
							B7	70	10.50

3.4 METHODOLOGY OF NUMERICAL STUDIES

3.4.1 Choice of FE mesh

The complex nature of the localised blast phenomenon renders a precise prediction of the fluid structure interaction response and the associated damage modes in FE analyses intrinsically difficult. Accurate prediction of the structural response in FE models depends, firstly, on the accuracy of the mesh type to trace the solutions for local forces and bending moments along its section; and secondly, on the credibility of the input parameters utilised in the continuum mechanics equations incorporated in the FE computer programme. Unfortunately, more often than not, the coefficients are obtained empirically and vary in the literature. The plethora of values necessitate applying the consistency tests and validation of numerical models with experiments.

The numerical simulations were performed in the ABAQUS 6.13® Explicit Finite Element commercial software. This hydrocode specially designed to deal with the non-linear dynamic problems with varying degrees of complexity such as dynamic response of structures subject to blast loads.

A preliminary numerical analysis was set up to specify the convenient element type. The panels in each set of simulations were discretised with five element types, namely S4(R) conventional shells, SC8R continuum shells, M3D8R membrane and C3D8R continuum (solid homogeneous) elements, but with the same degree of refinement as 5mm element length (which satisfied the convergence). Further discussion on mesh convergence is discussed in Chapter 4. S4R elements are general purpose, uniformly reduced integration elements with hourglass control to avoid spurious zero energy modes. These elements allow for the finite membrane strains and arbitrary large rotations. The continuum shell elements on the other hand, are 8 noded hexahedral elements for general shell-like structures with continuum topology, adaptable to thick and thin shells, which permits for large strains and accuracy for contact pairs investigations.

The C3D8R continuum elements are a class of solid elements with reduced integration also known as 'brick' elements. These elements require refinement to capture stress components at boundary but are not stiff enough in bending unless a sufficient number of them are employed through the thickness of the plate. The choice of 5 elements through thickness, in combination with enhanced hourglass control, is presumed to give reasonable estimate to capture the local bending moments.

Membrane elements (M3D8R) are 8 node quadrilateral elements with reduced integration and hourglass control, which conform to simplified shell theory in which internal bending moments are neglected [136].

The element size in each model was kept constant at 5mm. Table 3-5 shows the percentage of error in maximum deflections against experiment. The MMALE models were carried out on a cluster of 16 High Performance CPU's each having 1600MB memory.

The membrane elements experienced large out-of-plane deformations compared to all other element types. Due to the membrane element's paucity of bending stiffness perpendicular to its plane; the element convergence is fraught with difficulty due to excessive lateral deformations. It transpires from Table 3-5 that the conventional and continuum shell elements incur less computational cost than the membrane or continuum elements. Thus, the conventional shell elements can be used throughout the study.

The preliminary analysis illustrated in Figure 3-10 and Table 3-5 showed the shell elements offered reduced computational time while maintaining the accuracy of the results. These elements provided more concurrent estimation of transient deformation history with the experiments [27] in terms of first peak and permanent deflection, thus, unless otherwise stated, the conventional shells are used throughout this thesis. The increased number of continuum (brick) elements through the thickness to capture the local bending moments significantly increased the computational time.

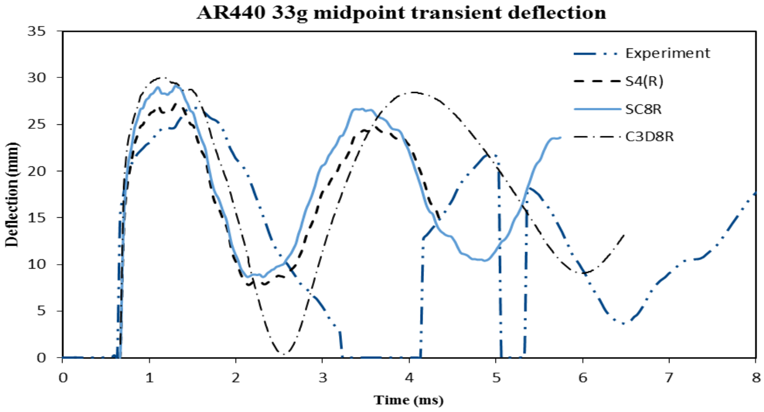

Figure 3-10- Transient deformation of the panel (d=38mm, De=50mm, Me=33gr)

Table 3-5- permanent and maximum transverse deformation of ARMOX Model ($M_e = 33gr, d = 38mm$)

Element type	W_f (mm)	W (mm)	% Error		CPU Time (min)
			W_f	W	
C3D8R	18.73	30.98	28.53	12.3	173
S4(R)	16.10	27.27	10.47	1.83	63
SC8R	17.64	29.11	20.11	8.67	53
Experiment	13.5	26.78	NA	NA	NA

3.4.2 Finite Element mesh models

The Numerical models are replicas of the experiments described hereabove and also those reported by Langdon et al [61]. All models were fit with two upper and lower clamps along the periphery of the plate designated with rigid body elements. At the contact interface of each clamp and the plate surface a penalty contact with friction coefficient 0.3 was assigned. An additional width of 20mm on each side of the plate was included for the contact interface. Due to symmetry, only a quarter of the plate was modelled.

Three types of numerical simulations were performed: (i) a full 3D Uncoupled Eulerian Lagrangian method, to register the pressure time history and thus obtain the impulse, (ii) a full Coupled Eulerian Lagrangian analysis and (iii) for the sake of comparison, a simple pressure-time Lagrangian analysis was performed for MSP8, B3 and ASP2 (same load parameters) having a rectangular pulse load, and load shape localised to the burn area as per Eqn. (2-16). The magnitude of the load was approximated from the experiment impulse over a presumed $20\mu s$ time duration.

3.4.3 ConWep method

Empirical blast load ConWep, based on the work of Randers-Pehrson and Bannister [137], provides an opportunity to simulate the blast load on a Lagrangian structure. In the Lagrangian reference frame, the mesh follows the material movement, which has the advantage of reduced computational time, but the mesh is prone to element distortions due to excessive deformations and possible solution failure [1], [138].

ConWep accounts for a collection of conventional weapons calculations which was developed empirically by Kingery and Bulmash[28], [139], from a large scatter of experimental data which calls the ConWep function. The total pressure function relies upon the incident pressure, the reflected pressure and the angle of incidence (Eqn. (3-6))

$$\mathrm{P(t) = P_i(t)[1 + cos\alpha - 2cos^2\alpha\,] + P_r(t)cos^2\alpha} \tag{3-6}$$

where $\alpha \geq 0$ is the angle of incidence, P_i and P_r are the incident pressure the reflected pressure from the surface, respectively.

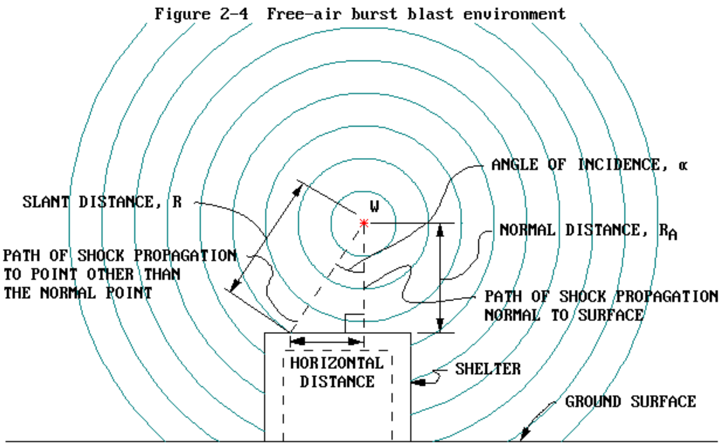

Figure 3-11- Air blast wave propagation [140]

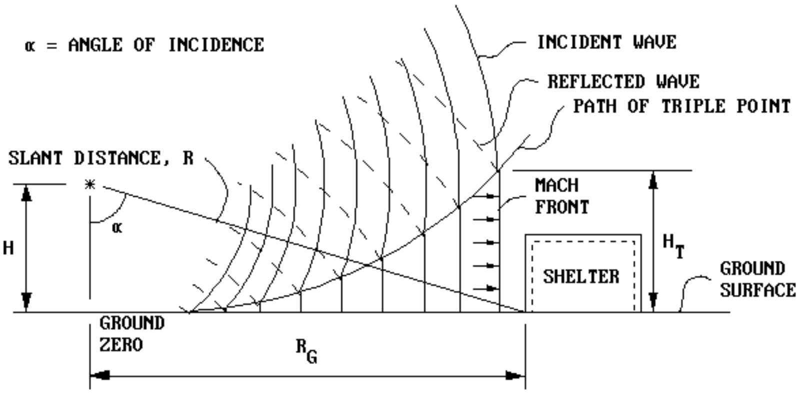

Figure 3-12- Path of ground blast wave propagation [23]

The ConWep function is already implemented hydrocodes such as LS-DYNA and ABAQUS can describe the close to ground or air blast explosions [136], [140]. For example, the computation of the blast pressure/impulse in the ABAQUS hydrocode depends merely on the specified equivalent TNT mass and stand-off distance. In the case of the ground blast, the initial wave burst is reflected from the ground surface which merges with and escalates the blast wave pressure. The representation of the air blast propagation and ground surface blasts are given in Figure 3-11-Figure 3-12, respetively. The interaction of the incident pressure and reflected pressure forms the Mach front which is a single wave and depends on the angle of incidence, as illustrated in Figure 3-13-Figure 3-14. The critical angle of incidence is between 40°-55°. The height of Mach front increases as the wave propagates away from the detonation source. The increase in height is due to the formation of the path of triple points (Figure 3-12), which emerges from the interaction of the incident, reflected and Mach waves [23].

Using the Hopkinson Cranz scaling law (Eqn. (2-8)), The small-scale models can represent the various threat scenarios of TNT landmine or IED detonations (Improvised Explosive Device) with 30cm stand-off distance from the full-scale prototype in Table 3-6. Further details on scaling laws is presented in Chapter 8.

Table 3-6- Scaling effects of some configurations.

Full scale Prototype threat		Z(m/kg$^{1/3}$)	Small scale model	
S_D (mm)	m_T (kg)		S_D (mm)	m_e (g)
300	11.22	0.1336	50	40
300	21.25	0.1083	38	33
300	25.82	0.1015	38	40
300	32.19	0.0943	38	50

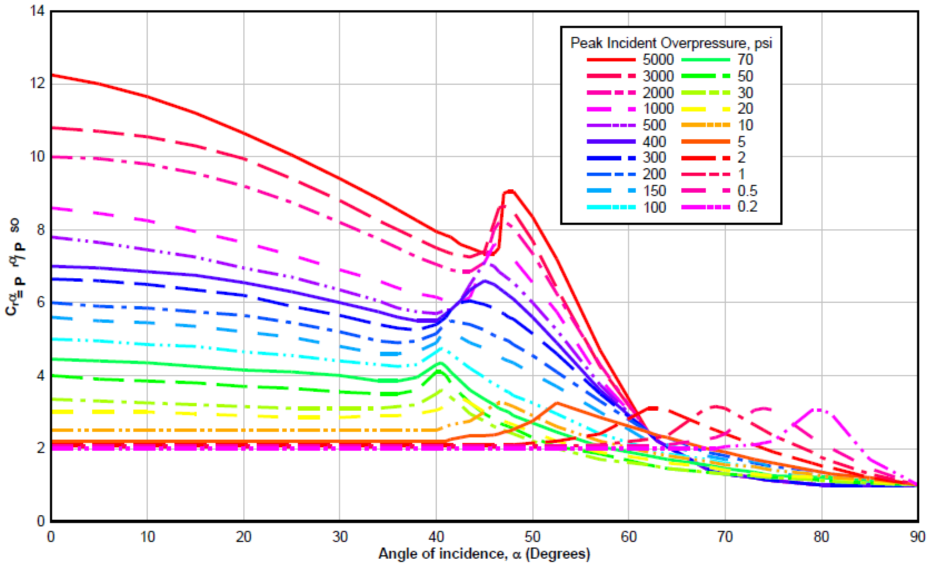

Figure 3-13- reflected pressure Coefficient versus Angle of incidence [23]

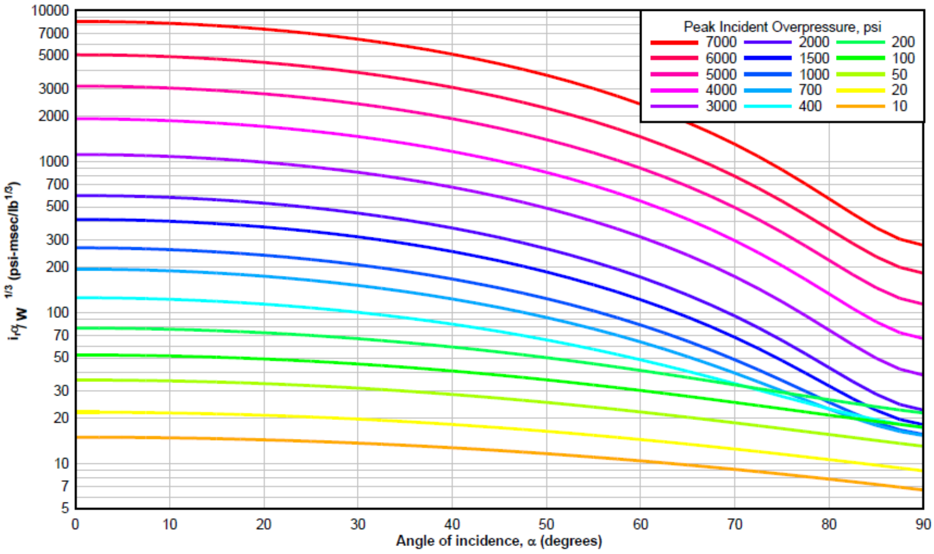

Figure 3-14- Reflected Scaled Impulse versus Angle of Incidence [23]

Various TNT mass equivalency values have been used in the literature [30], [141] to account relative effectiveness factor of the explosives, however a multiplier of 1.31 was commonly employed which assumes the same detonation energy. The stand-off distance is adjusted by considering spherical–cylindrical charge equivalency, which gives $r_{sphr} = \left(\frac{3}{4}h_e r_{cylnd}^2\right)^{1/3}$ assuming the spherical and disc explosives should have the same mass to exert the same impulse. As the stand- off distances decreases and the blast wave types become increasingly proximal, the target may be located inside the fireball, leading to the interaction between the expanding fireball and the overpressure. It must therefore be recognised that the ConWep approach will be approximate and that it predicts the response based on empirical pressure; however, it offers the possibility of simulating the blast load based on spherical and hemispherical charges with reasonable computational effort. It is also a useful baseline approach for comparing the more sophisticated and computationally more expensive approaches. Thus, the ConWep results herein are used as the first estimate to adjust the parameters of Arbitrary Lagrangien Eulerian (ALE) models.

3.4.4 Eulerian methods

In the circumstances where the empirical approaches fail to conveniently predict the blast response of a material, the advanced numerical methods which benefit from continuum mechanics algorithms which describe the fluid advection and FSI seems vitally essential. These algorithms are embedded in the ALE methods, which account for obtaining solutions for the arbitrary motion of mesh points with respect to the reference Eulerian points that are fixed in space. In other words, the ALE equations are defined with regards to the material time derivative and reference configuration time derivative [142], [143]. The Eulerian methods developed here use ALE formulation and fluid structure interaction contact interface, and consist of Coupled and Uncoupled Eulerian Lagrangian analyses.

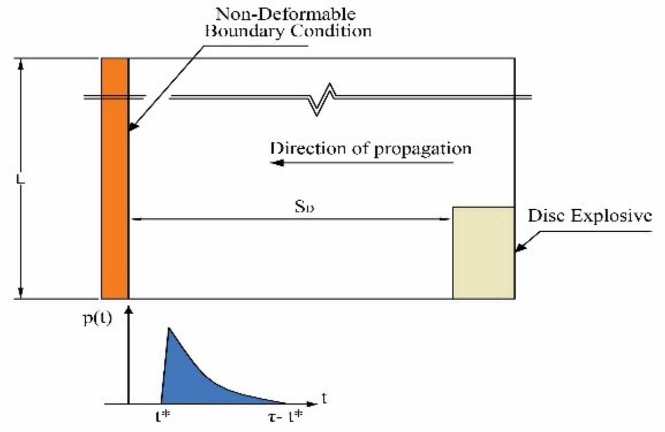

Figure 3-15- Eulerian arrangement to gauge the pressure-time history

In Uncoupled Eulerian Lagrangian (UEL) models, the multi-materials in the Eulerian medium consist only of the explosive and the air. Rigid boundary condition is assigned to the Eulerian boundary to monitor the inflow of pressure load (Figure 3-15), while non-reflecting flow-out boundary conditions are assigned to the side faces along the open fluid boundaries. The register of the pressure time history can be extrapolated and averaged to obtain the mean impulse , as per Eqn. (3-7), and applied in a separate Lagrangian analysis.

$$I = 2\pi \int_{0}^{\tau} \int_{0}^{R} r.P(r,t)drdt \tag{3-7}$$

Where 'I' is, the impulse imparted to the plate and $P(r,t) = p(r)p(t)$ is the product of load shape and pulse shape parameters. Using the numerical method, an estimate to Eqn. (3-7) is given by compiling the summation of the product of the average impulse density (impulse per unit area) by the area of targeted elements (referred to as the mean impulse) as follows. The target surface was subdivided into mesh grid zones of 9 elements with the corresponding average pressure. The integral of the pressure load in each zone satisfies the impulse density value. To obtain the impulse from impulse density, it was assumed that the pressure load is symmetric over the Cartesian directions. Thus, the integral of the impulse density along the diagonals evaluates the mean impulse.

Observations on UEL model with load parameters $D_e = 50mm$ and $S_D = 38mm$ gauged three distinct phases corresponding to the FSI:

i. Phase "i" the expansion of explosive, from time of detonation to its interaction with the structure, denoted t^*, found as $\approx 15\mu s$
ii. Phase "ii" explosive plate interaction, which lasted for $36\mu s$.
iii. Phase "iii" expansion of the explosion from time of separation from plate to expansion of the plate equilibrium.

The physics of the problem in the Coupled Eulerian Lagrangian is similar in the above phases, but on the deformable target surface. Detonation was assumed to occur instantanuously. Upon contact with the detonation front, the material point within the unreacted explosive instantanuously transfers to gaseous material which is accompanied with sudden release of energy from the chemical reaction [67], resulting in advection of the gaseous fluid through the Eulerian mesh points. The fluid mesh points can be transferred using first or second order advection. By default, ABAQUS programme burn incorporates second order advection to transfer the state variables (pressure, velocity, explosive product density). This advection method incorporates a process referred to as the flux limiting to ensure the advection is monotonic and to reduce the oscillations occuring after the shock wave [19], [144]. At the fluid target interface, the FSI algorithms are enforced by the contact pairs between the fluid mesh points and the structure, allowing the plate to slide through the Eulerian mesh. The contact at the fluid structure interface was assumed frictionless.

Since the load is axsysimmetric, only a quarter symmetry of the Eulerian cube medium is modelled with square plan of 300mm with height of 200mm, to encompass the steel plate with clamps, air medium and the explosive materials, presented in Figure 3-16. The air is modelled with the 'ideal gas' Equation of State given as

$$P = (C_p - C_v)\rho_a T \tag{3-8}$$

where C_p and C_v are the specific heat at constant pressure and volume, respectively, ρ_a is the air density, T is the temperature and P is the pressure. The data of air and explosive is given in Table 3-7. The specific internal energy of air is computed by integrating the specific heat constant over the temperature, or $E_0 = C_v T$. The flow pressure, volume and temperature of adiabatic condition, using expression the ideal gas law (Eqn. (3-8)) and the associated conservation of energy [70] are given by:

$$\frac{p}{P_{so}} = \left(\frac{V_{so}}{V}\right)^{\bar{\gamma}} \tag{3-9}$$

$$\frac{T}{T_{so}} = \left(\frac{V_{so}}{V}\right)^{\bar{\gamma}-1} \tag{3-10}$$

$$\frac{V}{V_{s0}} = \left(\frac{P_{so}}{p}\right)^{\frac{1}{\bar{\gamma}}} \tag{3-11}$$

Where $\bar{\gamma} = C_p/C_v$, V and V_{so} are the flow volume and the initial volume of quiescent medium (air), respectively. p and P_0 denote the flow pressure and initial pressure, respectively and T and T_{so} denote the temperatures accordingly.

Table 3-7- Explosive and air parameters for Eulerian models

Material	ρ $(kg.m^{-3})$	Det. Wave speed v (m/s)	A	B	R_1	R_2	ω	E_m	Pre-det. bulk modulus
PE-4	1601	8123	6.0977 $\times 10^{11}$	1.295 $\times 10^{10}$	4.5	1.4	0.25	6.057×10^{6}	0
Air	ρ $(kg.m^{-3})$	C_p (kJ/kgK)	C_v (kJ/kgK)	**P (Pa)**	**E$_0$ (kJ/kg)**		**μ_0 (Dynamic viscosity, $(\mu Pa.s)$)**		
	1.293	1.005	0.7176	101325	2.05×10^{5}		18.27		

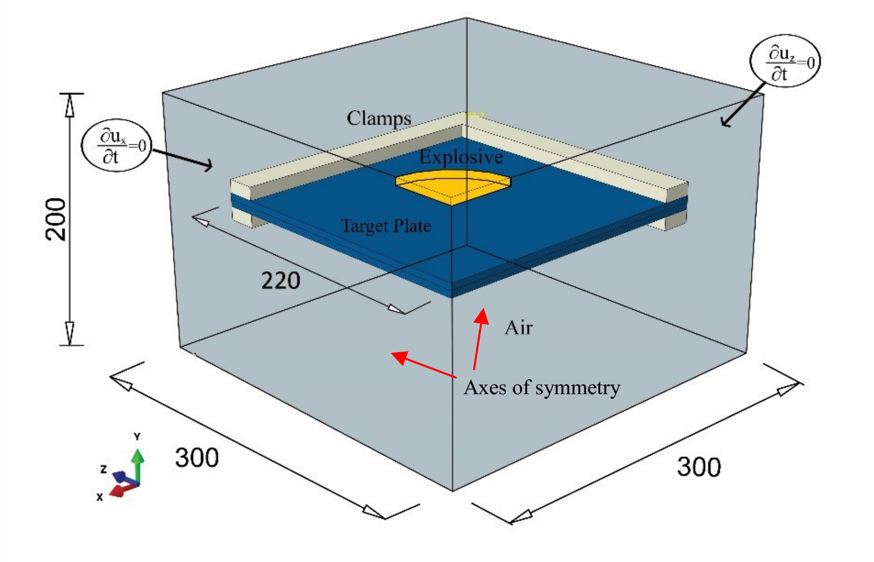

Figure 3-16 CEL model configuration

For the air blast explosions, the disc explosive is modelled using the Jones-Wilkins Lee Equation of State

$$P = A\left(1-\frac{\omega\rho}{R_1\rho_0}\right)e^{-R_1\frac{\rho_0}{\rho}} + B\left(1-\frac{\omega\rho}{R_2\rho_0}\right)e^{-R_2\frac{\rho_0}{\rho}} + \frac{\omega\rho^2}{\rho_0}E_{m0} \qquad \textbf{(3-12)}$$

where ρ is the explosive product density, ρ_0 density at the beginning of process, A, B, R_1, R_2, and ω are the material constants [67]. The expansion of the explosive is dependent on its geometry. A disc explosive expands primarily in vertical direction rather the horizontal direction. The shape of explosive is a significant factor in the type of wave propagation and deformation response. Nurick et al [145] showed that the Inverted Truncated Cone explosive resulted in higher impulse, but lower deformation than, the cylindrical explosive as the impulse was spread over a larger portion of the plate area. The increase in the charge mass of ITC explosive brought about the saturation impulse where no significant increase in deformation was observed at the increase of impulse.

CHAPTER 4

Experimental and Numerical Results

4.1 BACKGROUND

Following the methodology of studies, the numerical and experimental results are investigated and compared in this chapter. Following this introduction, a mesh sensitivity analysis is carried out and the transient deformation of the converged numerical models were validated against the experimental DIC techniques in Section 4.3. The pressure distribution and impulse, plate profile and strain localisations were investigated in Section 0. The results were cast in dimensionless form to investigate the correlations between the results and the current empirical and theoretical models from the literature. In Section 4.5, empirical models of Nurick and Martin [60] were extended which pass through the large scatter of data for armour steel panels. The major part of the work in this chapter was published in International Journal of Impact Engineering [119].

4.2 RESULTS

4.2.1 Mesh sensitivity and strain localisation

Initial treatment of the numerical methods entails a mesh convergence parametric study. The convergence deems necessary for both pure Lagrangian and Arbitrary Lagrangian Eulerian methods. The models were set up with three levels of mesh discretisation, from coarse (10×10) to fine (40×40) element meshes of S4(R) shell elements, giving the element thickness ratio in decreasing order of 5mm-1.25mm, respectively. The most suitable mesh was then validated against the experimental models.

Accordingly, in view of the Coupled Eulerian Lagrangian models, the convergence of the state variables, such as velocity field and pressure (incident and reflected) as well as the force fields depends upon both the element size of the Eulerian medium as well as the Lagrangian plate whereupon the blast was imparted. The Eulerian medium was discretized with EC3D8R Eulerian brick elements, varying from 1.25mm to 10mm as depicted in Table 4-1. Thus, the fraction of the medium which accounts for the explosive material encompasses approximately 40 elements, in accordance with minimum explosive element numbers discussed by [67], [146]. Although such refinement would lead to expensive computations, it is found as the reasonable discretisation without inducing computational errors in analysis as the coarser mesh would not satisfy the convergence. Hexahedral elements of the cubic type Eulerian medium are advantageous over the spherical type medium to overcome the material leakage problems insomuch as FSI was concerned [146], [147], a problem also most commonly associated with C3D8R brick elements for the plate. It occurs when the wave pressure associated with in the material mesh point of Eulerian elements pass through the Lagrangian mesh points (without rupture).

Table 4-1 Element configuration model B4 and AX24

Model config. (AX24 and B4)	no. of elements	Element length (mm)
Steel plates	100	20
	400	10
	1600	5
Eulerian Domain	49392	5-10
	111925	2.5-10
	369820	1.25-10

Table 4-2 Mesh refinement & $\bar{\varepsilon}_{pl}$of Model B4-AX24

Model config.	Element length/ thickness	W (mm)	$\bar{\varepsilon}_{pl}$
B4	4.33	18.23	1.71
	2.16	25.7	5.42
	1.08	28.2	7.90
AX24	4.33	22.36	2.70
	2.16	24.22	5.40
	1.08	24.4	6.50

The general response of structure is characterised with initial elastic stiffening, followed by appearance of the plastic flow stress once the yield limit is reached. The plastic flow response occurs sporadically in certain regions while the rest of the structure responds elastically. After a certain time interval the structure behaves as elastic rebound following the residual stresses [148].

Table 4-2 presents the influence of element refinement on mid-point transverse deflection and the equivalent plastic strains $\bar{\varepsilon}_{pl}$ captured at time 0.3ms (occurring when principal stresses were maximum). At the onset of loading phase, the elastic strains occurring throughout the structure are instantaneously ensued by plastic strains localisation at the boundaries as well as the plate mid-point. As predicted, the highest plastic strains associated with the CEL models was attributed to the localised elements at the midspan of peripheral clamped boundaries, which propagated along the support edges while the central plastic zone spread outward. The central node plastic strain and strain rate tensors underwent an abrupt rise to the highest principal plastic strain (ε_{11}) occurring at 0.08ms, at which the strain rate vanished. Boundary elements, however, underwent a more gradual increase in principal strain (ε_{11}) as the equivalent plastic strain ($\bar{\varepsilon}_{pl}$) approached the plastic strain in the centre, as shown in Figure 4-2.

As shown in Figure 4-1, very coarse Lagrangian mesh (10×10 elements) resulted in simulation errors, which is postulated to be due to excessive relative distortion of the localised elements to their adjacent elements. The convergence was satisfied with the refinement of element length to thickness ratio of ~1. It is noted that the mesh refinement led to an increase in maximum central deflection, plastic strain and stresses, however, the local stresses at boundaries do not converge. In general, according to [149] the stresses and strains should be convergent if:

$$|\sigma_f - \sigma_m| < |\sigma_m - \sigma_c| \qquad \textbf{(4-1)}$$

with the subscripts denoting the mesh level, viz. σ_c the stress of the coarse mesh, σ_m and σ_f those of the medium and fines meshes, respectively. Yuan and Tan [75] reported that in the convergence study of fully clamped plates, the plastic strain as well as key stresses at the plate boundary ($\bar{\varepsilon}_{pl}$ and σ_{yy}) do not converge with mesh refinement. Unrealistic strain localisations at the boundaries cannot be deterministic for the ductile fracture modes of more uniform blasts, (Mode II*, in Table 2-1) but have no effect on Mode I (large inelastic deformation) response or higher modes with respect to the localised blast load (such as capping of the plate centre) studied here.

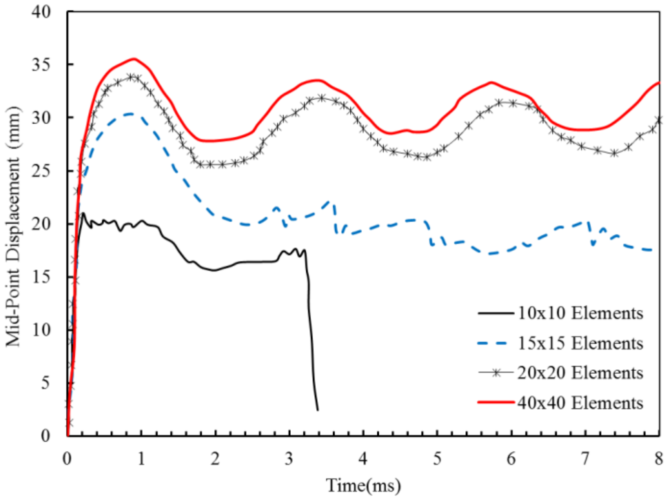

Figure 4-1- Mesh refinements of Mild steel with 25g PE4 (Model MSP1)

The resistance of the beam to dynamic loading was due to inertia, elastic bending stiffness and plastic hinge formation at the midspan.

Finding the plastic deformation can be difficult as they are interspread with elastic deformations. The regions where plastic flow occurs may appear intermittently.

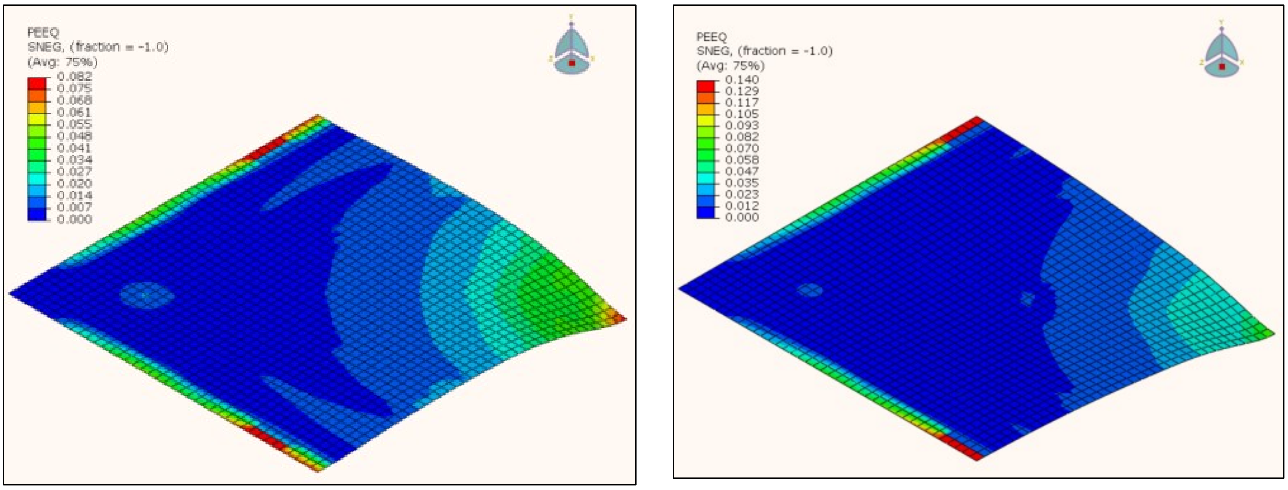

(a) (b)

Figure 4-2- (a) Equivalent plastic strain @1.167ms (b) Final deformation @3ms. The plastic strain develops inward from the localised boundaries along the plastic hinge lines.

4.3 VALIDATION OF NUMERICAL RESULTS

4.3.1 Validation of numerical models

In this section, the transient deformations of the numerical models are validated against the practical values obtained through state of the art DIC tests presented in Figure 4-3 - Figure 4-4. The candidate panels were AR-440T grade steel (designated B4 and AX24) CEL models. The transient response of two further AR-500T panels as well as a mild steel panel (denoted MS24 hereinafter) was also investigated, as illustrated in Figure 4-5 and Figure 4-6. The load parameters for MS24 comprised of 24g charge mass, 50mm diameter and $S_D = 38mm$. The AR-500T panels were subject to 24g and 33g charge masses and identical configurations to other AR-440T panels with the exception of lower thickness and higher yield stress, as discussed in Section 3.2.1. Of all the panels investigated here, only the AR370T and Mild steel with 25mm stand-off, 40g charge and 50mm charge diameter exhibited partial tearing. A further study on the rupture of the armour panels is presented in Chapter 8.

During the DIC tests, the frame rate of the camera was restricted to 30,000fps. This limitation induced motion blur as the plate velocity was high in the initial frames, between 3.2ms-4.0ms shown in Figure 4-3. The motion blur resulted in the detail of the central portion of the plate being lost as the speckle pattern could not be resolved.

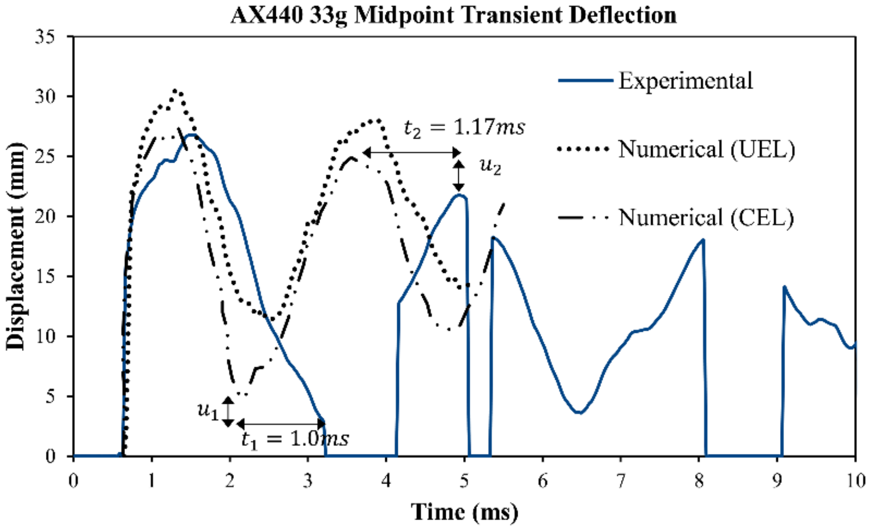

Figure 4-3- Time History plot of midpoint displacement, Experiment (from DIC) vs CEL and UEL models, for ARMOX B4.

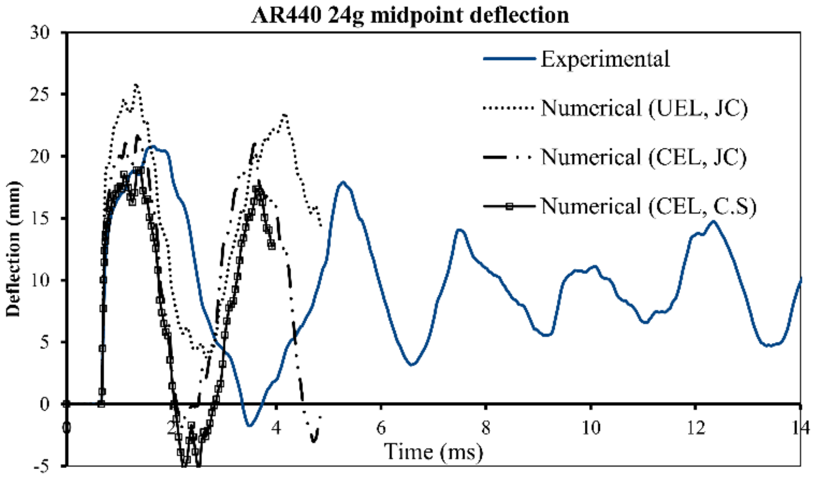

Figure 4-4 Time history plots of midpoint displacement, Experiments (from DIC) compared with the CEL and UEL simulations for AX24, based on Cowper Symonds and JC models.

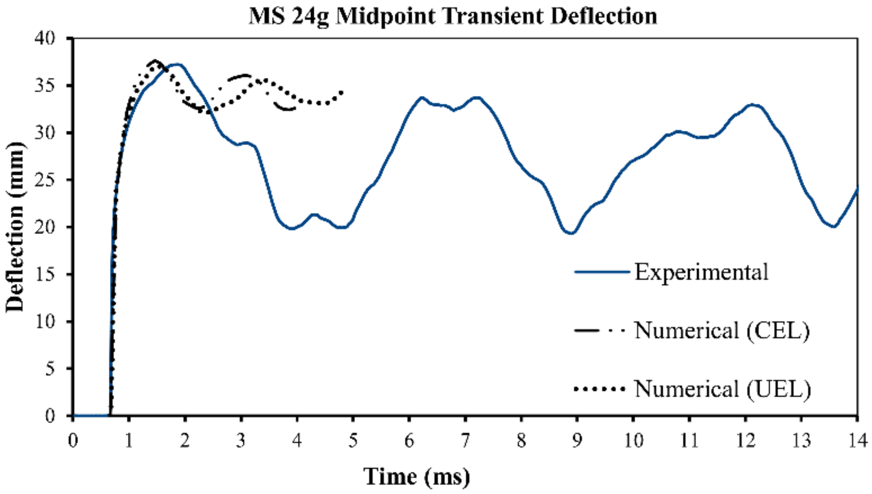

Figure 4-5 Time history plots of midpoint displacement, Experiments (from DIC) compared with the CEL.

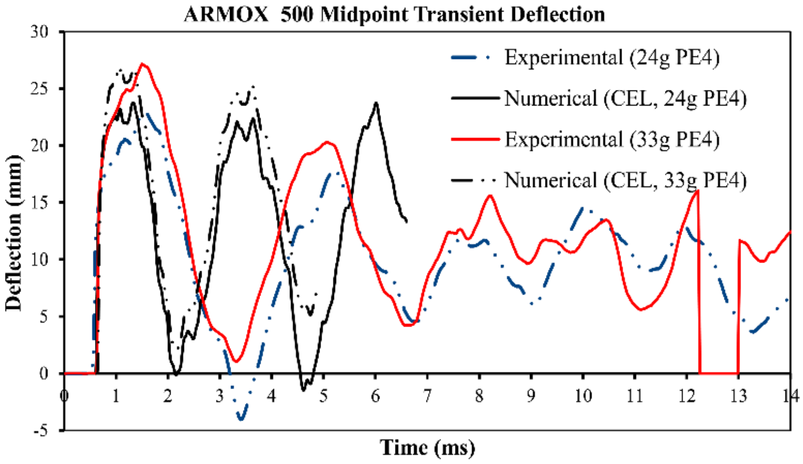

Figure 4-6 Time history plots of midpoint displacement, DIC compared with the ARMOX 500T CEL simulations on 33g and 24g PE4 @ 38mm stand-off

4.4 COMPARISON OF NUMERICAL AND EXPERIMENTAL RESULTS

4.4.1 Pressure and impulse

Table 3-4 summarises the displacement and impulse of Numerical vs experimental models. The total impulses calculated experimentally from the pendulum swing is concurrent with the mean impulse from UEL simulations, with error of less than 10%. In Figure 4-7 a comparison of the effect of stand-off on total impulsive density (impulse per unit area) imparted on AR370T models is given. It should be recognised that, measurement of pressure time history from CEL model is fought with difficulty due to the motion of the target plate.

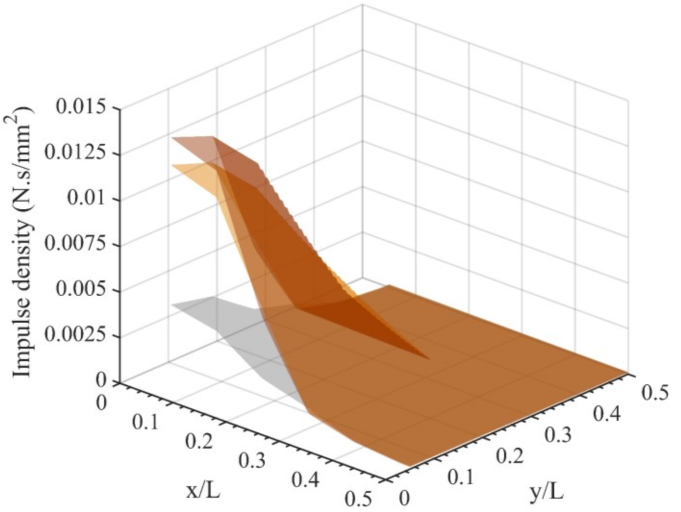

Figure 4-7- Impulse density of AR-370T steel, ASP1 (brown), ASP3(yellow) and ASP5(grey)

Following Bonorchis & Nurick [67], a comparison of the pressure time histories from a UEL model with no clamps and one clamp boundary conditions (as is the case of the experimental test) is sought to investigate the influence of boundary conditions on the total impulse transmitted to the plate. The loading arrangements in this comparative study consisted of 40g PE4 explosive, had 50mm diameter and positioned at 50mm stand-off from the target. The schematic of the model is drawn in Figure 4-8. The UEL model with one clamped was identical to no-clamp case except with specifying rigid chamfers at the edge of the plate. The schematic of pressure distribution across the target plate is illustrated in Figure 4-9.

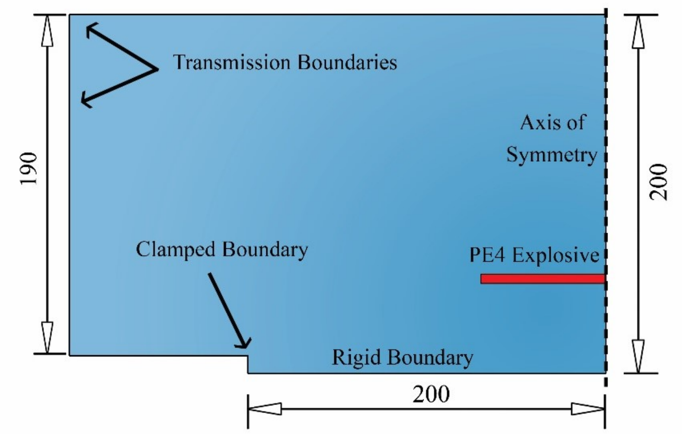

Figure 4-8- Schematic of the UEL model with clamped boundaries

Clearly, as observed in Figure 4-10, the pressures recorded at gauge points of the two models are coincident, suggesting the boundaries have infinitesimal contribution in absorbing the impulse. This is because in the current work, geometric characterisation gave the quotient of the 200mm plate half-length to the charge radius (20-37.5mm) was large (5.3-10). Even accounting for the larger stand offs (50 mm) used herein, this is considered conservative in preventing the pressure recirculation along the clamp edge observed by Bonorchis and Nurick [67] at closer boundary distances. Such a design quotient was 3:1 in the authors work.

Table 4-3- Steel panels' configurations and load parameters- I_{sim} is the mean impulse from Uncoupled Eulerian analysis, compared against the experimental impulse on Mild steel and AR-370T by [61].

Configurations					Configurations				
Mat.	**S_D (mm)**	**Model**	**$I_{expt.}$ (N.s)**	**$I_{sim.}$ (N.s)**	**Mat.**	**S_D (mm)**	**Model**	**$I_{expt.}$ (N.s)**	**$I_{sim.}$ (N.s)**
Mild Steel	25	MS-P1	56.4	51.0	**AR- 370T**	38	AS-P5	80.5	78.1
		MS-P6	82.9	82.4			AS-P6	100.1	98.3
		MS-P8	68.2	65.0			AS-P7	82.2	67.1
		MS-P10	80.7	81			AS-P8	91	85.5
AR- 370T	25	AS-P1	80.0	80.1	**AR- 440T**	25	B3	57.3	57.4
		AS-P2	66.1	62.2			B6	94.8	86.0
	50	AS-P3	82.2	77.3		38	AX24	43.75	43.4
		AS-P4	143.2	135.6			B4	57.8	55.0
							B7	129.1	108.2

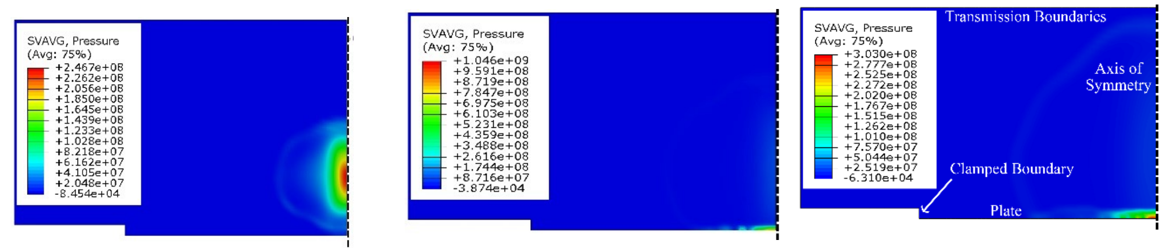

(a) 10μs (b) 20μs (c) 30μs

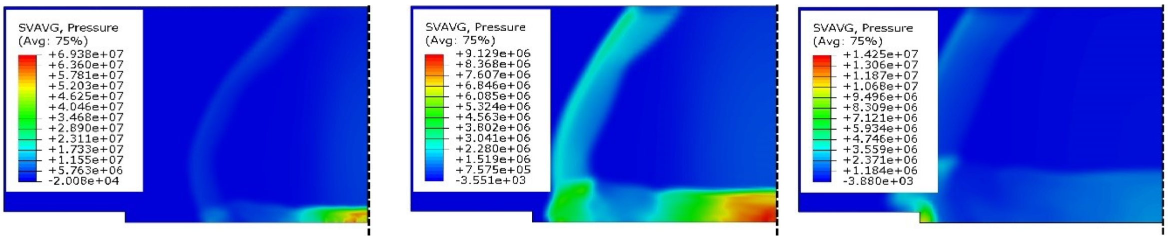

(d) 40μs (e) 60μs (f) 80μs

Figure 4-9- Distribution of the pressure load at various time points, in the front face of the UEL model with one clamp

Furthermore, the pressure recirculation in the clamps lasts only for a brief time, the majority of the load would be dissipated in the plate before the pressure has built up in the clamps. Accordingly, the total calculated impulse from the one clamp model was a mere average of 1.6% higher than the no clamp model. Thus, the UEL models herein predict the transmitted impulse with reasonable degree of accuracy and compare favourably with the total impulse measured by the ballistic pendulum. As the charge radius to plate length increases to one third, (as in the case of the model in Ref. [67]) the pressure recirculation duration at the boundaries increase, leading to an increase in the impulse.

When the pressure time history is implemented on the structure in a separate simulation (evaluated based on FSI on rigid target), the results overpredict the actual response compared to the coupled method. In fully coupled model, *ceteris paribus*, the structural flexibility alone takes part to diminsih the impulse, resulting in the magnitude of the deflection to decrease [70] (Eqn. (2-9)). The ability to acquire instantaneous velocity relieves the thin plate from the pressure acting at the fluid structure contact interface, leading to a reduction in the transmitted impulse. However, as the plate thickness increases, the structure stiffness increases and the impulse on heavy plate limit would be asymptotic to that of the rigid target, as discussed by Taylor [31] and Kambouchev and Radovitzky [32]. The latter authors extended the work of Taylor [31] on uniform incident waves and expressed the reduction in the transmitted impulse in terms of single dimensionless FSI parameter on compressible fluids and various plate thicknesses. The authors showed that the transmitted impulse ratio depended on the plate mass but is unaffected by the shock intensity.

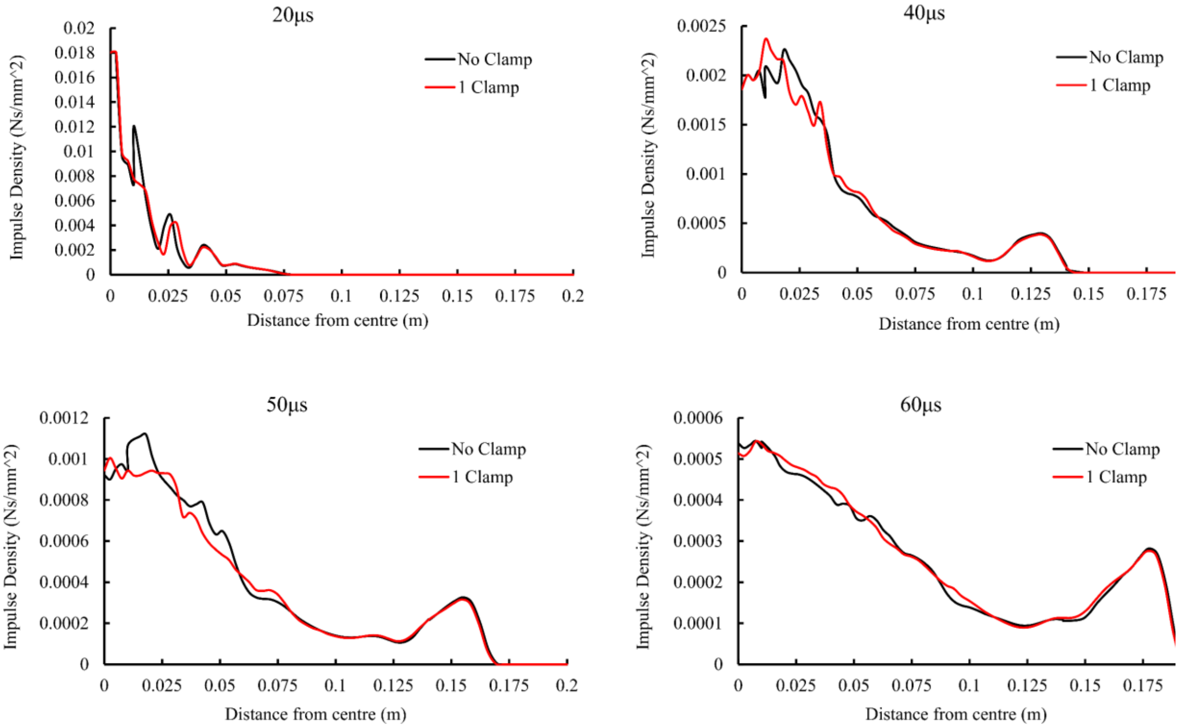

Figure 4-10-pressure time histories of 1 clamp compared with no clamp boundary conditions

4.4.2 Deflections and correlation of parameters

Table 4-4 shows the results of the maximum and residual transverse deflections from the numerical and experimental models. It should be mentioned that, while the accuracy of the fully coupled Eulerian analysis is computationally expensive, the CEL analyses registers the outcome with reasonable degree of accuracy, with the similar time history plot of the transverse deflections.

Table 4-4- Maximum and final deflection of the Steel plates -values in mm.

Material.	Model	W_f CEL	W_f Expt.	Difference from Expt. (%)	Material.	Model	W_f CEL	W_f Expt.	Difference from Expt. (%)
AR-370T	ASP1	30.37	29.50	2.95	**Mild Steel**	MS-P1	32.25	30.20	6.79
	ASP2	28.53	21.90	30.27		MS-P6	51.03	53.70	4.97
	ASP3	18.23	14.40	26.60		MS-P8	47.20	42.00	12.38
	ASP4	30.00	25.60	17.19		MS-P10	55.50	41.60	33.41
	ASP5	22.79	21.30	7.00	**AR-440T**	B3	21.78	17.20	26.63
	ASP6	23.42	27.10	13.58		B4	16.10	14.57	10.50
	ASP7	13.60	17.60	22.73		B6	16.35	22.10	26.02
	ASP8	20.00	18.60	7.53		B7	24.50	22.80	7.46

As observed in the Figure 4-3- Figure 4-6, the predicted vibration by the numerical models lags the actual vibration observed from the experiments. The difference of the occurrence of the first minima in Figure 4-3, $u_1 = 1.96mm$ close to the next peak difference $u_2 = 2.3mm$, and lagging time is maintained throughout, i.e. $t_1 \cong t_2$. It should be recognised that, the actual prediction of the response is intrinsically difficult [150] as the plethora of parameters, including the material rate sensitivity or adiabatic shear, could affect the transient deformation of the plate as follows. Due to the proximity of the charge, the deformations are localised in narrow shear zones, the response in the central region is governed by the plastic flow in the central region of the plate. The adiabatic heat generated due to the high strain rates gives rise to elevated temperature in the localised region, while the surrounding region strain hardens. This leads adiabatic shear localisation when the thermal softening overcomes the strain hardening effects. [62]

For the design purposes, estimating the maximum transverse displacement is usually deemed more important than captured the exact nature of the elastic vibrations which follow. The maximum transient displacement may even be preferred over the permanent deformations, since it may transition the structure to higher failure modes (such as partial tensile tearing in the centre). Finally, while the relative motion of the frames could give rise to the difference in post peak behaviour, it is not hypothesised as the reason of the counterintuitive post peak behaviour. As many parameters influence the localised response of the panel - the prediction of transient permanent deformation is rendered intrinsically complex, and to date most experimental and numerical studies on the transient deformations such as that of Ref. [79] were performed on structures subject to uniform blasts.

It is also of interest to study the influence of structural flexibility on the magnitude of the pressure load in the UEL and the fully coupled analysis (CEL). A model with rigid target surfaces was implemented and the pressure data at the gauge points on the target interface was captured. The predicted pressure-time histories were averaged and implemented in a second stage model with Lagrangian elements. This was an uncoupled model (UEL). The trajectory of transient deformation for the AX24 and MS24 test plates modelled this way are shown in Figure 4-3 and Figure 4-4. The magnitude of the deformation showed that, using the UEL simulations, averaging the pressure registered on the rigid target surface leads to an increase in the magnitude of maximum deformation. For the various models investigated, the plate maximum deflection obtained from fully coupled analysis was found to be lower than the uncoupled method (Table 4-5), and closer to the experimental results, with maximum percentage error of 19.7% (UEL) compared to 8.8% (CEL) for the AX24 test. The lower displacement predictions of the CEL occurs as the impulse is diminished by the structural flexibility of the fully coupled model. In other words, for the flexible structure the pressure load obtained from UEL method is an overestimate of the actual pressure load applied to the plate.

Table 4-5- Maximum mid-point deflection (mm) for Armour and Mild steel

Configuration	AX24	B4	MS24
CEL	19.11	27.20	37.04
UEL	25.91	30.56	33.88
Experiment	20.80	26.78	37.19

The maximum deflection profile of the AR440 and Mild Steel panels were also compared with those obtained from the DIC tests. The profile shapes were predicted from CEL models and shown in Figure 4-11 and Figure 4-12. In Figure 4-12a, the transient deformation at maximum peaks 1.08ms and 1.33ms is also compared. It is interesting to note that the profile shape is similar to the experiment, with more bulging near the boundaries. Further, assuming the same detonation time, the deflection time histories in Eulerian Lagrangian studies are relatively coincident with the DIC data in terms of the peaks and permanent deflection. Despite the affinity, some disparities in the post peak behaviour was observed, with higher spring-back of DIC models (Figure 4-5).

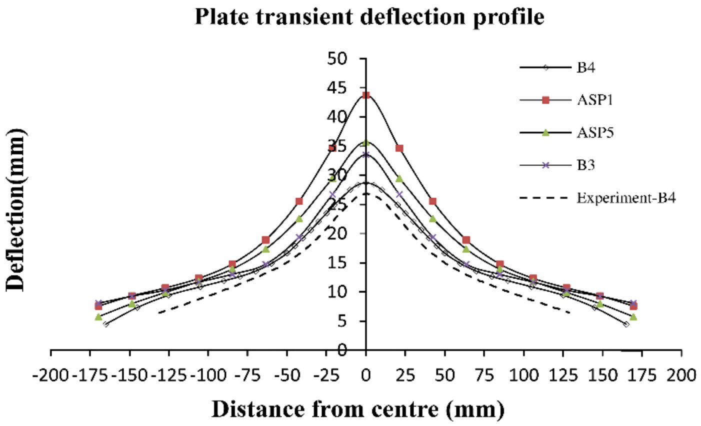

Figure 4-11 –Maximum transient deflection profiles –CEL (B4, ASP1, ASP5 and B3) vs experiment(B4)

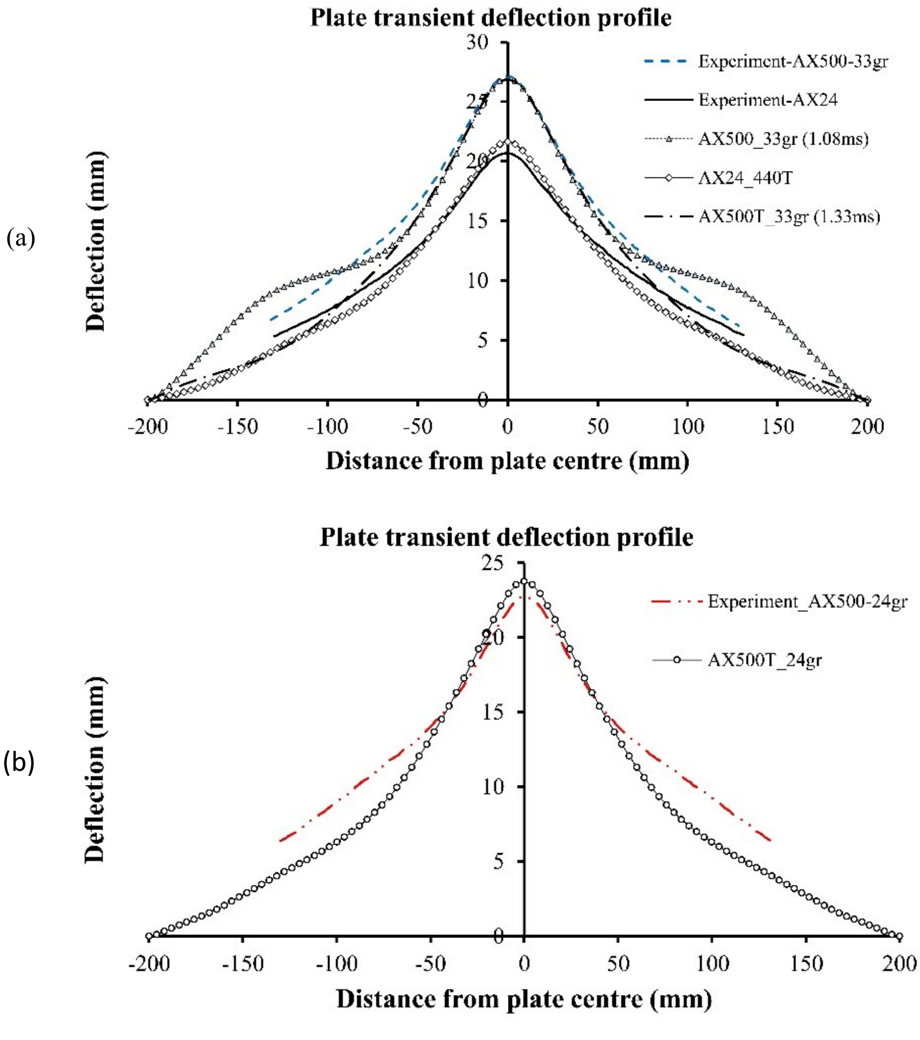

Figure 4-12- maximum transient deflection profile of (a) AX500T,33g and AX24 (b) AX500T,24g-CEL vs Experiments

4.5 CORRELATION BETWEEN PARAMETERS VIA EMPIRICAL STUDIES

Non-dimensional analysis was performed to investigate the difference between the theoretical models, the available empirical models in the literature, and three simulations which ascribe the rigid plastic model subject to the locally uniform pulse.

Experimental and numerical investigations on the effect of load parameters have been calibrated through non-dimensional analysis in the literature. Fundamental theoretical work by Jones [35] has evaluated the plate response to uniform or impulsive loading. The dimensionless kinetic energy, defined by Jones, predicts the large inelastic deformation of the plate loaded impulsively by uniform velocity V_0 as in Eqn. (2-12). The normalised deflection is described by a function of dimensionless kinetic energy λ for quadrangular plates (Eqn.(4-2)).

$$\frac{w_f}{H} = \frac{\left(1 + \frac{2\lambda}{3}\right)^{0.5} - 1}{2} \tag{4-2}$$

The results from various models were cast in dimensionless form and presented in Figure 4-13. For the sake of comparison, the results of (ASP3, MSP8 and B3) pure Lagrangian analysis were also drawn in this figure (denoted as Localised rectangular pulse). The models had identical load configurations and geometry, but different steel grades. The blast pressure was estimated using Figure 2-2 (a) having a rectangular pulse $20\mu s$ duration.

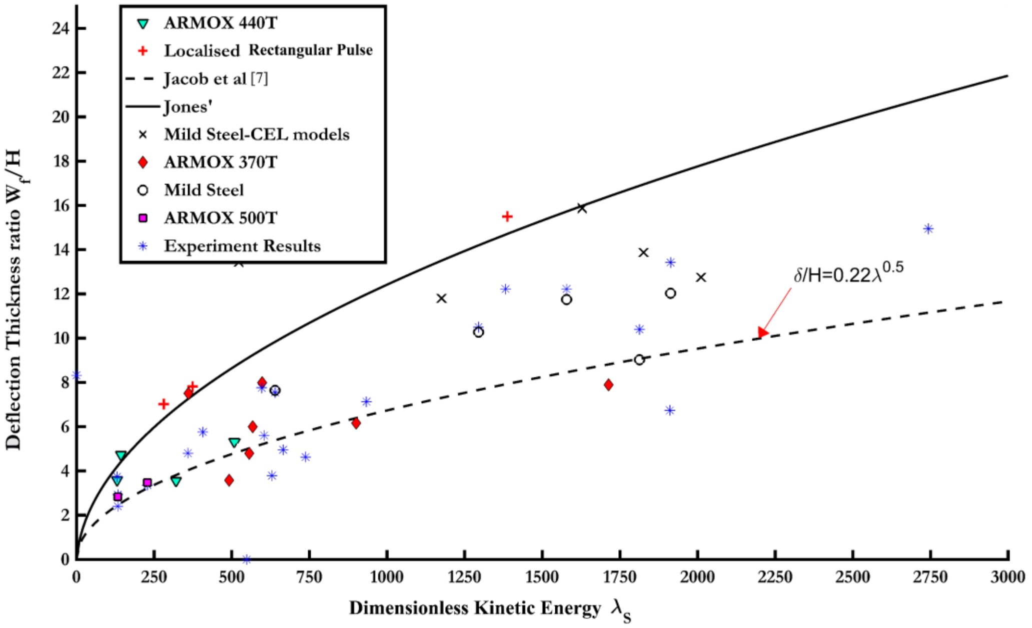

Figure 4-13- Comparison of numerical, experimental and empirical results proposed in the literature in dimensionless form.

The numerical models are compared against Jones' [35] theoretical prediction, which yields a similar prediction to the pure Lagrangian models. However, Jones' theoretical predictions overestimate the plate response in the localised blast load for the other models as well as the experiments. Hence, in the idealisation of the blast load, the spatial and temporal variation of the load play a significant role and Jones' idealisation of rigid, perfectly plastic plate of uniform load shape which acts impulsively on the plate is similar to the Lagrangian models. The actual distribution of the load is influenced by the load regime (impulsive/dynamic), may be treated as dynamic rather than purely impulsive [70] in some cases, the load distribution due to the proximity of the charge and its time variation . For example, consider the load parameters $m_e = 33gr$, $S_D = 38mm$ and $D_e = 50mm$, which has the exponential positive pulse duration $\tau = 30\mu s$, yields the region affected by the blast-taken as the position of the plate inflexion point in the plate profile- 60mm away from the midpoint. Evaluating the natural frequency $(\omega)$of the plate by a modal analysis, the abscissa of pressure impulse diagrams by Baker [151], was calculated as $\omega\tau = 0.5$, sufficiently high so as to treat the load with the similar or higher stand-offs as dynamic. Similar results would ensue with decreasing the charge mass. However, when the stand-off distance decreased to 25mm, the pressure load magnitude increases, causing larger transverse deformation. Consequently, the position of the inflexion point would increase to 80mm, suggesting rather impulsive load type with $\omega\tau = 0.26$. A transition from the idealised, partially impulsively loaded panels to the actual load shape, which is exponentially varying across the panel, leads to a significant difference between the simple models and the CEL approach.

It should also be recognised that; the material mesh elements can be idealised as rigid when the ratio of kinetic energy to the maximum strain energy stored elastically is sufficiently high to virtually ignore the influence of material elasticity. This condition may be applied to mild steel material model, for which the idealisation of pulse shape as per Eqn. (4-2) will not render much disparity in terms of accuracy. However, the armour steel grades underwent considerable elastic rebounds during the experiments, thus the material elasticity of such steel panels shall be retained in the theoretical analyses.

It transpires that the results are bounded between the Jones' model and the empirical trends found from experiments of Ref. [21], [59]. Eqn. (2-19) was employed by Langdon et al [61] to investigate the relationship between the impulse and the permanent deflection for armour steel. However, the effect of stand-off distance was ignored. The relationship of the normalised impulse was later altered by Jacob et al [21], to make the comparison of blast-loaded panels of different geometries and characteristic stresses, while taking the proximity of the charge into account. The authors introduced a scaling coefficient to parameterise the stand-off distance, which is accounted for in the cases where $S_D \geq R_e$ as per Eqn. (4-3), (4-4).

$$\gamma'_s = \frac{\left(1 + \ln\left(\frac{4LB}{\pi {R_e}^2}\right)\right)}{\left(1 + \ln\left(\frac{S_D}{R_e}\right)\right)} \tag{4-3}$$

$$\emptyset_{sq'} = \frac{I\gamma'_s}{2H^2\sqrt{(4LB\rho\sigma_0)}} \tag{4-4}$$

Through the curve fitting analysis, the final-normalised-displacement of the plate can be circumscribed to the curve of the Eqn. (4-6) with the ±1 leader. As illustrated in Figure 4-14, the impulse correction parameter decreases monotonically smoothly at higher stand-off and charge radius parameters (i.e. when load characteristics approaches those of distal charges), while the variation of impulse correction parameter with charge diameter is abrupt given the $\frac{S_D}{R_e}$~1 and $R_e \ll L$. The empirical expression in (4-6) is graphed in Figure 4-15.

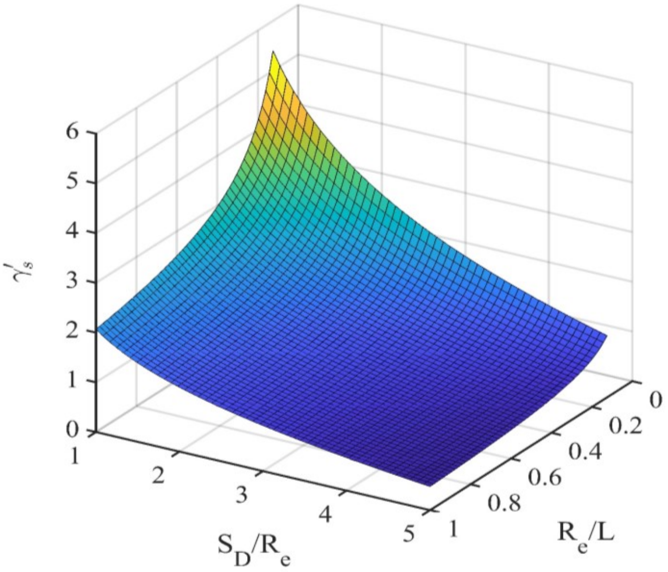

Figure 4-14- influence of charge radius (R_e) and stand-off on impulse correction parameter

Fallah et al [36] reported that a fit to the experiments was achieved by using the slenderness ratio, defined in Eqn. (4-5), into empirical Eqn. (4-4) to yield Eqn. (4-7), while the influence of slenderness ratio is graphed in :

$$\gamma_{sl} = \left(\frac{H}{2B}\right)^m \tag{4-5}$$

$$\frac{W_f}{H} = 0.52\emptyset_{sq'} + 1.1 \tag{4-6}$$

$$\emptyset_{sl} = \emptyset_{sq'}\gamma_{sl} = \frac{I\gamma'_s\gamma_{sl}}{2H^2\sqrt{(4LB\rho\sigma_0)}} \tag{4-7}$$

$$\emptyset_{sl'} = \frac{I\gamma'_s}{8B^2\sqrt{(2L\mu\sigma_0)}} \tag{4-8}$$

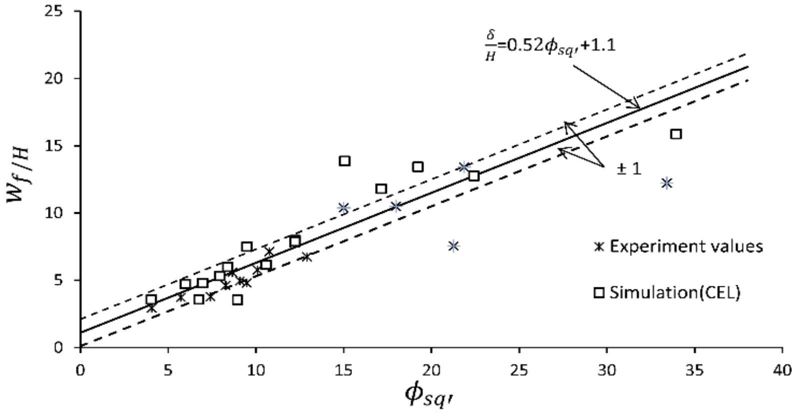

Figure 4-15- Damage number $\emptyset_{sq'}$ vs the normalised displacement

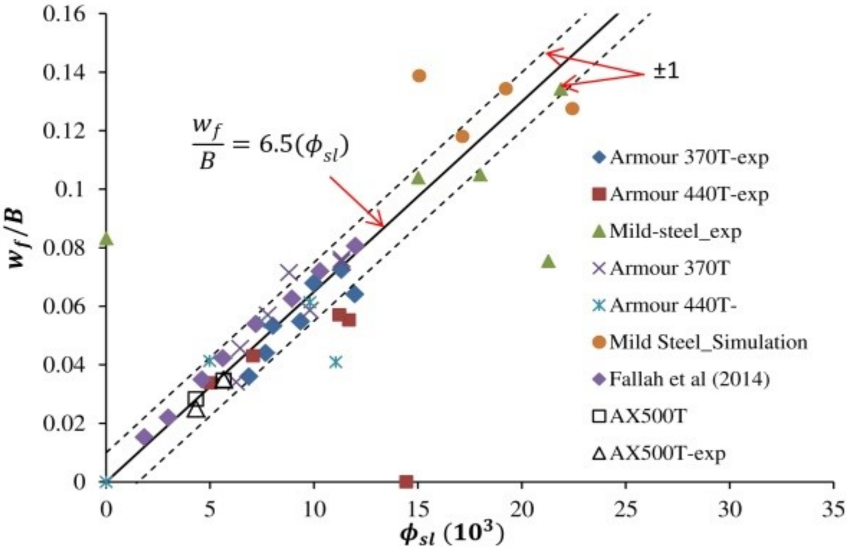

Figure 4-16- Correlations of permanent deflection/width ratio with the damage parameter $\emptyset_{sl}$

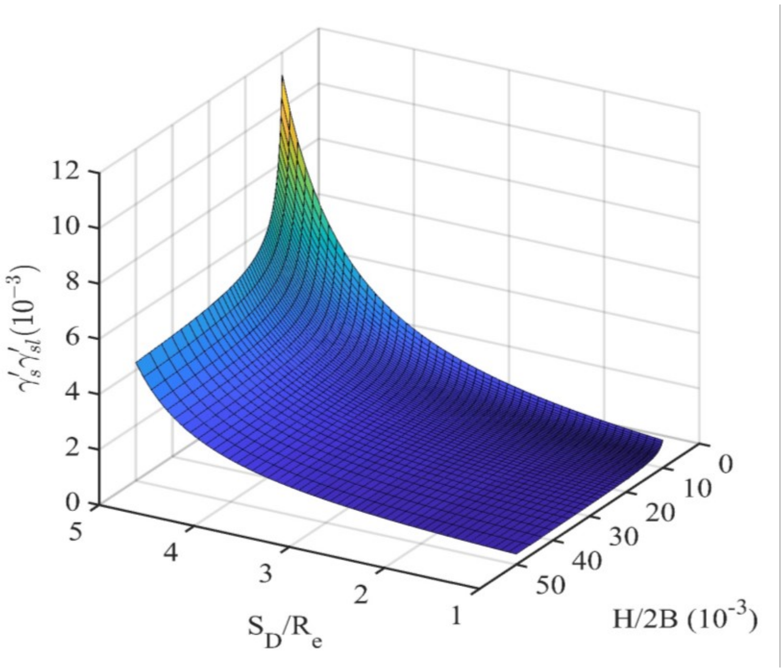

Figure 4-17- Influence of slenderness ratio and stand-off on impulse correction parameter $\gamma'_s\gamma_{sl}$, with $D_e/L = 1/8$.

The normalised displacement is related to the equation of best fit, the parameter 'm' from Eqn. (4-5) accounts for the material type, which was found to be 1.6 for Dyneema® HB26 panels and armour steel panels [36]. Assuming $m = 1.5$, Eqn. (4-7) can further be simplified to Eqn. (4-8) without loss of accuracy in the regression line, as illustrated in the Figure 4-16, while the influence of the slenderness ratio of the impulse correction parameter is plotted in Figure 4-17.

It is also noted that, the experimental models by [61] (outlined in Table 3-4) exhibited the mode I failure and did not rupture. Previous experimental research, according to [61], showed that the blast generated by laod parameters $S_D = 25mm$, $M_e = 40g$ and $D_e = 50$ perforated through both mild steel and AR 370T steel plates. Thus, contrary to the conventional design, the material strength and hardness are not conducive to predict the material resilience to localised blasts. This leads to the feasibility of establishing the rupture impulse that was not solely based on the strength of the steel. The non-dimensional analysis performed herein shows that these models attain the highest dimensionless impulses, $\emptyset_{sq'} = 12.22$ and 22.42, for armour steel 370T and mild steel, respectively. Clearly, even though the model ASP4 undergoes highest impulse (143N.s), it does not rupture as the higher stand-off/charge diameter ratio contributes toward reduction of the normalised impulse [22]. Therefore, These NDIP $\emptyset_{sq'}$ can be used for the preliminary design applications, to obtain the panel geometry (such as the desired thickness), based on simple algebraic manupulations from the Eqn. (4-8). Such a design procedure is conditional to ignoring the strain rate sensitivity of the material. Further details of the use of NDIP for preliminary design applications is presented by reference [36].

However, while the rupture impulse is partially influenced by the material ductility, other failure mechanisms such as specific energy to tensile failure (SETF)-which is a measure of both strength and ductility of the material-contribute to the rupture behaviour [61]. Since the SETF is known *a priori* (it is obtained from the quasi static tensile test), it is a useful indicator of rupture behaviour of different material types.

The design procedure can be carried out in the following manner: given the load parameters (charge type and mass, stand off, charge geometry), and the target geometry, the average impulse that a blast threat can generate is calculated using Eqn. (3-6) and/or measured empirically (by ConWep method or Dimensional analysis). Then, the non-dimensional analysis would be performed to predict whether the steel panel (Armox steel or Mild steel) response exceed the value of rupture impulse and to pinpoint the final deformation of the panel. Clearly, the complex nature of the loading and the materials strain rate sensitivity make it difficult to generalise the empirical values for all Armour steel and mild steel panels, but these values can be used as 'safe' design parameters together with consideration of SETF. Further information on the predicting the rupture of the ductile metallic panels is presented in Chapter 8.

4.5.1 Distribution of blast Load

The localised blast load has a spatial (load shape) and temporal (pulse shape) variation. In most works of the literature [46], [67], [152] the load shape is assumed to be constant over the central region and decay exponentially in a radial direction outside this zone, as illustrated in Eqn. (4-9).

In Figure 4-18 the spatial variation of registered pressure from the Eulerian analysis across the plate breadth was validated using the linear regression analysis. In most cases the percentage error of 5% was noticed, which indicates a good fit of the data points with exponential pressure equation with coefficient of confidence $R^2 > 90\%$, as presented in Table 4-6. The temporal variation is influenced by the pulse shape. According to [37], [152], the final deformation of a non-impulsive loaded plate is strongly dependent on the pulse shape; however, using the correlation parameters of Reference [37]-effective pressure, mean time and effective impulse- the pulse shape efects can be eliminated. A comparison of pressure time history for mild steel and armour steel Eulerian models is made in Figure 4-19 at 23mm away from the plate centre. In Figure 4-19-a the effect of charge mass is evident, however by comparison of deflections in Table 4-5 and pressure in Figure 4-19-b it can be deduced that the model B4 has dissipated more energy than MS24 in spite of the same pressure (impulse).

$$\begin{cases} p(r) = p_0 & 0 \le r \le r_e \\ p(r) = ap_0e^{-br} & r_e \le r \le R \end{cases} \tag{4-9}$$

Table 4-6- load parameters of explosive

Config.	Explosive parameters ap_0e^{-br}		R^2
	ap_0 (GPa)	Decay constant, b	
ASP1	3.11	104.13	97.30%
ASP7	2.14	101.25	90.04%
B4	2.85	96	91.95%
ASP4	3.054	69.04	95.69%

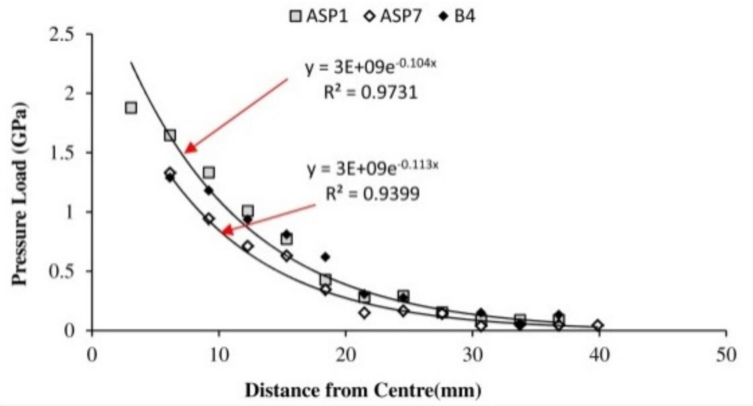

Figure 4-18– Curve fitting of the pressure load based on regression

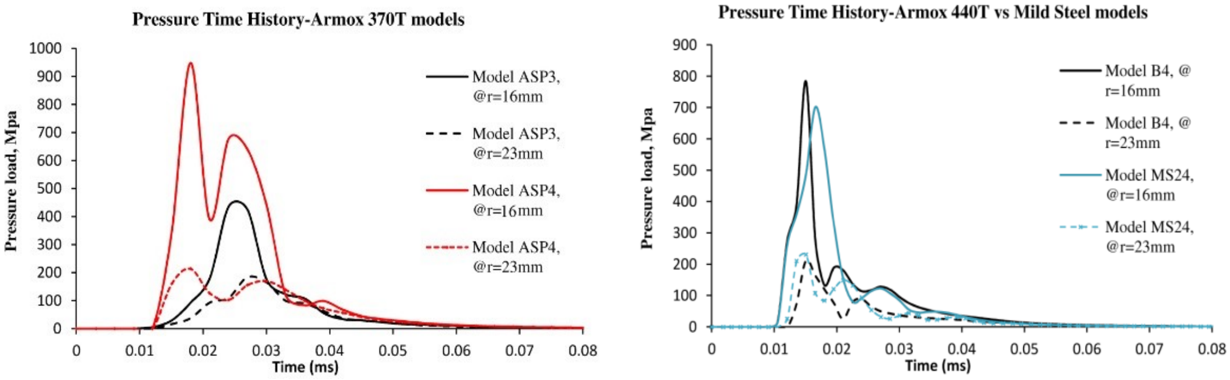

(a) (b)

Figure 4-19- Pressure time history of steel plates (a) ARMOX 370T- (b) B4 vs MS24

4.6 CONCLUDING REMARKS

This chapter investigated the experimental and numerical results on the response of steel panels to localised air-blast loading. The experimental data consisted of supplementary data set presented in reference [1] as well as additional blast test data on armour AR440T and AR500T used to validate the various numerical techniques. The numerical methods consisted of the coupled and uncoupled Eulerian Lagrangian techniques. A dimensionless analysis and the theoretical models by [35] were used to evaluate the results.

As expected, the ARMOX steel panels exhibited lower maximum and residual plastic deformations due to the higher ability of energy dissipation from the blast, which subsequently increase as the material yield strength increases (AR 500T compared to AR370T or mild steel).

The calculated impulse based on FSI models had close correlations with the experimental values. A regression analysis was performed to estimate the parameters of Eqn. (4-9) from the recorded pressure at the gauge points. Both Arbitrary Lagrangian Eulerian methods, viz., UEL and CEL, predicted more accurate response of the steel plates, although the coupled method exhibited a closer correlation with the actual behaviour of the plates. For the coupled model, the FSI governs the performance of the plate, The FSI phenomenon is influenced by the plate mass and stiffness. Increase in the thickness would affect both the mass and the stiffness of the plates, although the latter increases more rapidly. For example, an increase of the plate thickness from 3.81mm to 4.61mm increases the ratio of the transmitted impulse to total impulse on rigid target by average of 3%. Since the plates considered here are relatively thin ($0.95\% < H/2L < 1.1\%$), the transmitted impulse would be reduced due to the FSI effects, which justifies the lower deformation in CEL analysis compared to the UEL analysis. In the UEL analysis, the plate stiffness approaches infinity, all the incident pressure is reflected off the surface and full impulse is imparted to the plate

Contrary to the results of Bonorchis and Nurick (2009), the influence of clamped boundaries on the impulse was found insignificant due to the proximity of the charge. The majority of the load dissipates before the overpressure reaches the clamps. Similar to the results of Jacob et al [21], the effect of stand-off was significant as the specimen AR370T and B4 with (more) distal charges did not rupture despite the higher impulse. Thus, the NDIP was modified to incorporate the effect of stand-off, plate geometry and slenderness ratio, however, this parameter was dependent on the material. The speculation of rupture impulse threshold should be treated with the caveat that parameters such as hardness, ductility and strength alone would not ascertain the 'safe' design method, while SETF and NDIP should also be taken into account. Further details on prediction of rupture threshold is presented in Chapter 8.

The CEL models results closely correlated with those of the experiments regarding both maximum and final plate deflection. The theoretical model by Jones [35] considerably overestimates the armour steel plate midpoint deflection. The pulse shape, load shape and distribution, material elasticity and visco-plasticity (strain rate sensitivity) are the inherently deterministic factors that affect the response of the armour steel panels to localised blasts, however to date these parameters have not been examined by their own merits. Hence, using simplified models (such as based on idealisation of uniform distributed load) to predict of the localised deformation of ductile metallic plates would yield inaccurate results.

As a final remark, it has already been established that for blast loads of ${}^{R_e}/_{L} \geq 0.3$, the total measured impulse cannot be applied as a centrally localised impulsive pressure load, due to the contribution of clamps in reducing the impulse. A similar argument applies due to the influence of FSI for the range of the localised blast loads investigated here. However, total impulse measurement from the CEL model is not straightforward while the impulse reduction factor in Eqn. (2-9) is valid for uniform blasts.

CHAPTER 5

Theoretical Results of Simply-Supported Rigid-Plastic Square Plates

5.1 BACKGROUND

Most structural systems are fabricated with plate or beam elements which are made of steel alloys or other ductile metals with enhanced energy absorption as well as high post-yield load carrying capacity. Since these elements generally undergo large plastic deformations due to intense shock loads, prediction of their plastic response is essential for the engineer to incorporate in the design. In such cases, the theoretical predictions are conducive to cost-effective, the rapid assessment of the protective systems without the necessity of conducting expensive experiments. The work of this chapter is in press for the Journal of Engineering Mechanics [153].

5.2 BLAST LOADING ON STRUCTURES

In the sequel, there is a summary on different blast loads using associated characteristics for blast loading functions. The equations proposed by researchers [35],[36]–[38] have been used to lift the restrictions on temporal and spatial distributions of pulse loads as well as providing a realistic yet accurate approximation of localised blast load which proves feasible for such types of loading.

Methods of calculating response to shock loads have been proposed by Ref. [49]–[51]. Cox and Morland [92] obtained theoretical solutions for dynamic plastic response of simply supported square plates as well as the response of n-sided polygonal plates subjected to uniform dynamic load. Jones with co-authors presented an extensive series of theoretical and experimental research on various structural elements subject to spatially uniform pressure loads of rectangular temporal pulse shape [93], [74], [94]–[97]. In most cases, Jones' analytical models for impulsive loading provided solutions in good agreement with experimental works, when the ratio of kinetic energy to maximum strain energy stored elastically was more than ten [98]. Komarov and Nemirovskii [99] extended further the analyses of Jones [35] to the dynamic case with travelling plastic hinges to obtain the incipient plastic deformation in each of the two stages of motion.

5.3 AIM OF THE CURRENT WORK

In fact, as discussed previously, many theoretical analyses have been carried out that addressed the plastic response of the quadrangular or circular plates to impact or pulse pressure loads. In the theoretical calculations, the structure is often idealised to behave either as an elastic-perfectly plastic or a rigid-perfectly plastic medium. The latter model- in which the elastic effects are ignored for simplicity (and without great loss of accuracy) - is appropriate for the assessment of dynamic response of blast-loaded structures, provided the loading is treated as a short duration pulse and the ratio of kinetic energy to elastic strain energy is considerably high [98].

However, in the previous analytical investigations [35], [93], [118], [154], [155], certain limitations have been implemented, i.e., the loading has been characterised as a uniformly distributed pressure with rectangular temporal pulse shape, which renders the results suitable for response to global blast loads. Nevertheless, the proximal charges of short stand-off distance will induce blasts with localised responses, leading to much higher local deformation and strains as well as the possibility of triggering potential tearing mechanisms, a fact which necessitates the investigation of alternative loading functions.

In the following chapters, the analytical solutions of the response of quadrangular plates undergoing plastic deformations due to a generic localised blast is presented. The purpose of the current study is to extend, within the framework of limit analysis, the theoretical studies mentioned in section 1 to cases including localised blast loads through implementation of a modified loading function[36], [38], [152]. While the theoretical studies from the literature have focused on the general solutions for dynamic plastic deformation of plates subject to uniform impulsive loads, it can be shown that the general solutions can be obtained for square plates subject to any form of blast loading, i.e. localised or global.

Since the localised blasts affect only a small area of the structure severely, it is expected that boundary conditions are not significant and full plate action may not be required [152]. Thus, while the herein approach assumes the plates to be simply-supported along its periphery, as discussed later, the procedure is extensible to the clamped plates. Certain other assumptions and the fundamental equilibrium equations are discussed hereunder.

5.4 ASSUMPTIONS

For the simplicity of the analyses to be conducted, the following assumptions are made throughout the study:

In view of the Kirchhoff-Love plate theory, the quadrangular plate studied herein is assumed to be sufficiently ‘thin’ such that the effects of transverse shear and rotatory inertia can be neglected but not thin to the extent that in-plane actions can have a considerable effect on the plate response. Consequently, it is assumed that bending action is predominant and its effect transcends those of the membrane, transverse shear or rotatory inertia. The influence of transverse shear, rotatory inertia and in-plane actions shall be discussed in the following chapters.

Furthermore, the blast pressure load is assumed to be exerted on the structural elements laterally, such that the plate material particles follow straight trajectories normal to the un-deformed plate mid-surface. Consequently, it is assumed that in-plane displacement components vanish from equilibrium equations [51]. Moreover, the plate maintains its uniform thickness throughout the motion and through-thickness dilatational waves are not considered.

Finally, the effects of visco-plasticity are not considered here as in the case of high strength armour steel the response is independent of the strain rate.

5.5 MATERIAL PROPERTIES AND LOADING

Unless otherwise stated, in the sequel of theoretical analyses, the plate is assumed to be initially flat, monolithic metallic square plate with side length of 2L and thickness of H, with simply supported boundary conditions along its contours. The plate is subjected to a representative axi-symmetric localised blast load [152], [156]. Due to geometrical symmetry, only one quarter of the plate is considered in the analyses.

In most works of literature [22], [38], [46], [67], characterises a generic blast load, which is multiplicative of spatial (load shape) and temporal variations (pulse shape), i.e. $P(x, y, t) = p_1(x, y)p_2(t)$. The spatial variation of the load, as shown by [38] and Figure 5-2, maintains a uniform pressure within the radius r_e before decaying exponentially in radial characteristic dimension r, given in Eqn. (5-1). Thus, the load is axisymmetric and reduces the domain of study to only one quarter of the plate. The pulse shape of the blast varies due to the type of explosion. For example, gas deflagration or high explosive detonation would give rise to viz. sinusoidal, triangular, exponential, linear or rectangular pulse functions. While the pulse shape can have significant effect on the overall response of the non-impulsive structure, its effect can be eliminated by utilising the Youngdahl's correlation parameters[37], [91], [152], [157], which efficacy is confirmed for monotonically decaying pulses by [100]. For impulsive blasts, the pulse shape has no intrinsic effect on the system. For the study of non-impulsive blasts, a rectangular pulse shape is assumed here, as presented in Figure 5-1. The influence of alternative pulse shapes will be discussed in chapter 5.

$$p_1(r) = \begin{cases} p_0 & 0 \le r \le r_e \\ p_0 a e^{-br} & r_e \le r \le R \end{cases} \tag{5-1}$$

$$p_2(t) = \begin{cases} 1 & 0 \leq t \leq \tau \\ 0 & t \geq \tau \end{cases} \tag{5-2}$$

In Eqn. (5-1), $r = \sqrt{x^2 + y^2}$, the loading constant 'a' depends on the loading central diameter, viz. $a = e^{br_e}$ while the loading exponent 'b' can be found through monitoring the pressure time history numerically or experimentally. Thus, the load is axisymmetric and reduces the domain of study to only one quarter of the plate.

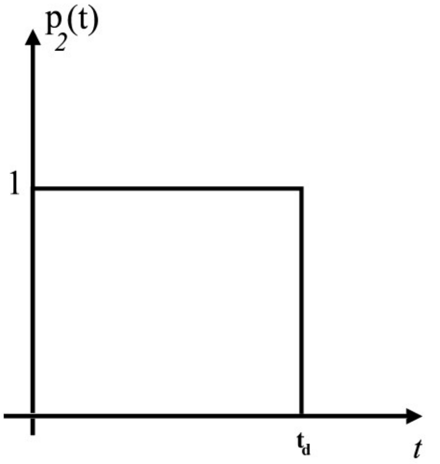

Figure 5-1. Temporally rectangular pulse shape

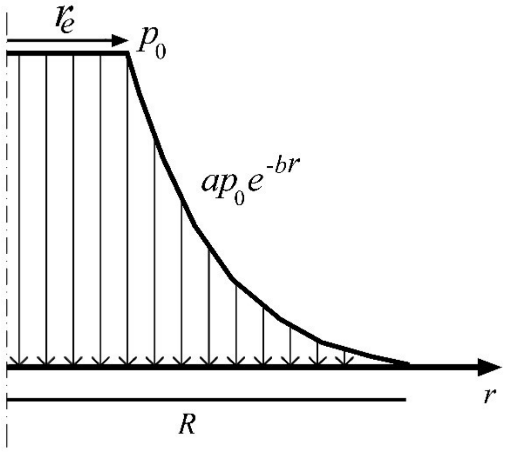

Figure 5-2. Spatially exponential distribution of load

5.6 GOVERNING EQUATIONS

When impacted by a centrally localised blast, the mechanism of deformation of a quadrangular plate (or beam as special case) is the creation of one central or two symmetric plastic hinges. Provided the elastic energy stored in the plated structure (and beam as a special case) is small compared to the kinetic energy imparted to the structure, and ratio of the duration of the blast to the natural period of the structure maintains small values, the elastic wave propagation and the elastic-plastic distribution of the stresses through thickness of the cross section may be neglected. In such cases, the rigid-perfectly plastic behaviour may be assumed and the plastic hinges may be considered as plastic joints. [35], [89], [158], [159].

The above assumption is the cornerstone of the constitutive framework of limit analysis. The number of plastic hinges and the permanent deformation depend on the distribution and magnitude of the pulse load. Clearly, for a uniform distribution of pressure, only the amplitude of the pulse can influence the nature of the response, while for a localised blast the deformation of the beam also depends on the load shape.

For a rectangular plate with infinitesimal displacements, i.e. when the influence of membrane action is ignored, the rate of plastic energy dissipation is found from Eqn. (5-3).

$$\dot{D} = \iint M_x\dot{k}_x + M_y\dot{k}_y + 2M_{xy}\dot{k}_{xy}dxdy \tag{5-3}$$

$$\dot{k}_x = -\frac{\partial^2 \dot{w}}{\partial x^2}\ , \dot{k}_y = -\frac{\partial^2 \dot{w}}{\partial y^2}, \dot{k}_{xy} = -\frac{\partial^2 \dot{w}}{\partial y \partial x} \tag{5-4}$$

where $\dot{k}_x$, and $\dot{k}_y$, are the rates of change of curvature in the associated generalised coordinates, while $\dot{k}_{xy}$ represents rate of warping of the plate which are perpendicular to the corresponding portion of the yield surface, according to the normality requirements of plasticity [35]. M_x, and M_y are bending moments per unit length in the respective generalised coordinates, denoted also as generalised stresses as they are obtained from stress tensors. and M_{xy} is the twisting moment per unit length. The shear forces per unit length in x and $y$of the Cartesian coordinate system are denoted as Q_x and Q_y. In what follows we shall, as is customary, differentiation with respect to time is denoted by placing a dot above a letter. The rate of external work on a finite plate area A is:

$$\dot{E} = \int (p(x,y,t) - \mu\ddot{w})\dot{w}d\bar{A} \tag{5-5}$$

For a rectangular plate element undergoing infinitesimal displacement normal to the plane mid-surface, when subject to lateral loads, the governing equations of motion are given by Eqns. (5-6)-(5-4):

$$\frac{\partial Q_x}{\partial x} + \frac{\partial Q_y}{\partial y} = \mu\ddot{w} - p(x,y,t) \tag{5-6}$$

$$\frac{\partial M_x}{\partial x} + \frac{\partial M_{xy}}{\partial y} - Q_x = 0 \tag{5-7}$$

$$\frac{\partial M_y}{\partial y} + \frac{\partial M_{xy}}{\partial x} - Q_y = 0 \tag{5-8}$$

5.7 YIELD SURFACEA AND FLOW RULE

The principle bending moments according to [160] are given by Eqns. (5-9)-(5-10). Provided the principle moments are arranged in this fashion, it can be assumed that the Johansen yield criterion in two-dimensional moment space governs the plastic flow. According to the normality requirement of the Drucker's stability postulate, the convexity of the yield surface applied and the state of the strains and the normal to (each) yield surface at each point along the yield path are co-directional. The associated yield surface is shown in the Figure 5-3, together with Tresca criterion. The requirement satisfying the yield condition is given as Max $\{|M_1|, |M_2|\} \leq M_0$, where M_0 i.e. the maximum plastic moment per unit length is found by Eqn. (5-11).

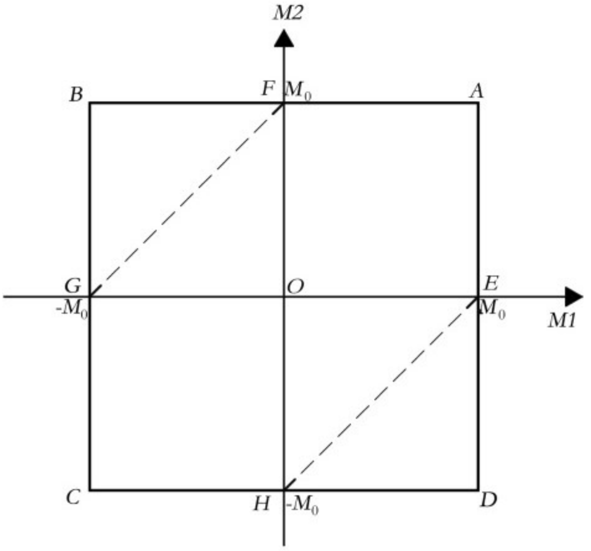

Figure 5-3. the Johansen yield surface (ABCD) vs Tresca (EAFGCH)

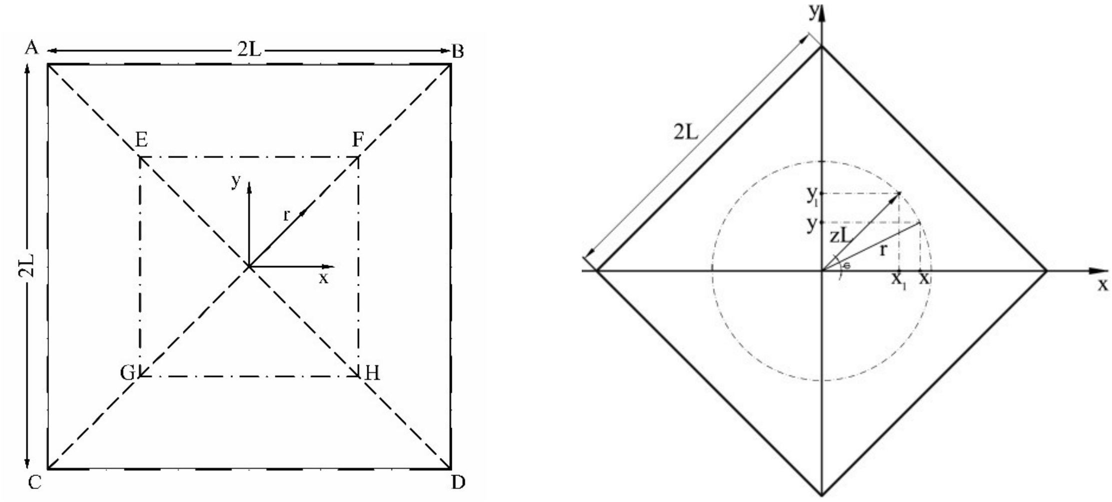

(a) (b)

Figure 5-4. - (a) The top view of a simply-supported square plate (coordinates x, y, r and dimensionless parameter z are shown), (b) the plate with side lengths 2L whose diagonals are in the Cartesian Coordinate axes

$$M_1 = (M_x + M_y)/2 - \frac{1}{2}\left[(M_x - M_y)^2 + 4M_{xy}^2\right]^{\frac{1}{2}} \tag{5-9}$$

$$M_2 = (M_x + M_y)/2 + \frac{1}{2}\left[(M_x - M_y)^2 + 4M_{xy}^2\right]^{\frac{1}{2}} \tag{5-10}$$

$$M_0 = \frac{\sigma_0 H^2}{4} \tag{5-11}$$

Considering the isotropic hardening for the yield function above, the position and shape of the yield surface remains fixed, while its size may vary to include the hardening effects. To address the hardening, yield stress σ_0 in (5-11) is replaced with the average of stress $\sigma_{av} = (\sigma_0 + \sigma_{UT})/2$.

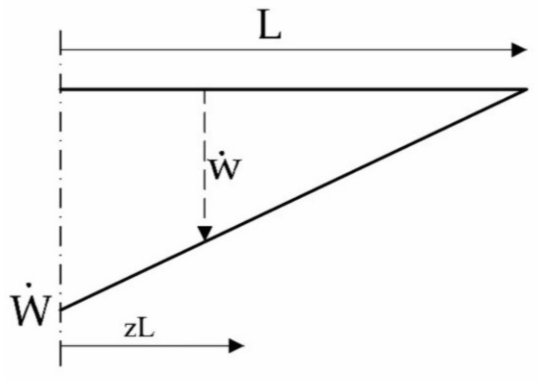

Figure 5-5. The assumed velocity profile

Cox & Morland [92] investigated a particular theoretical solution to dynamic plastic deformation of square plates subject to uniformly distributed rectangular pressure pulse. It was found convenient to introduce an auxiliary dimensionless coordinate z, given by $z = (x_1 + y_1)/\sqrt{2}L$ along the central axis.

However, it is pragmatic to introduce an auxiliary dimensionless coordinate z as illustrated in Figure 5-4 (b), for the plate whose plastic hinge lines lie on the diagonals of the square and construct the collapse mechanism. The Cartesian coordinates to the polar coordinate r (or z herein) whereby the blast load is defined (Eqn. (5-2)), the coordinates of r and z lie on the equipotential surface for the range $0 < z < 1$, as it may be assumed that the maximum loading range is on the inscribing circle to the plate, giving $p(x, y, t) = p(z, t)$.

Thus, it is straightforward to show that the theoretical solutions emerging from the dynamic equilibrium analysis along the plastic hinge line in Figure 5-4 (a)- given in Eqn. (5-12)-conform to the theoretical solutions characterised with the generalised auxiliary coordinate z in Figure 5-4 (b).

$$r = zL = \sqrt{x^2 + y^2},\ 0 < r < L \tag{5-12}$$

From the isotropy of stress-moment at the plate centre, the boundary conditions yield $M_x = M_y = M_0$ and $M_{xy} = 0$,while $M_y = M_0$ when ($y = 0$ and $0 \leq x \leq \sqrt{2}L$) and $M_x = M_0$ when ($x =$

0 and $0 \le y \ \le \sqrt{2}L$). Rearranging the Eqns. (5-6)-(5-8) and eliminating the shear force reactions leads to:

$$\frac{\partial^2 M_x}{\partial x^2} + 2\frac{\partial^2 M_{xy}}{\partial x \partial y} + \frac{\partial^2 M_y}{\partial y^2} = \ \mu\ddot{w} - p(x,y,t) \tag{5-13}$$

For brevity in analyses in the sequel, the solution to this Ordinary Differential Equation (O.D.E) is obtained by defining the generalised stresses (bending moments) and loads in terms of parameter z, as follows.

5.8 STATIC COLLAPSE PRESSURE

5.9 LOWER BOUND CALCULATIONS

For the problem discussed earlier, the lower bound calculations can be conducted by noting that the distribution of bending moment must satisfy the static equilibrium ($\mu\ddot{w} = 0$) of the generalised stresses and must nowhere violate the yield criterion. Using the boundary conditions, equation of motion (Eqn. (5-13)), and considering the principle moments in Eqns. (5-9) and (5-10), in a similar procedure to the work of Cox and Morland [92], it is assumed that the generalised stresses are attributed to a moment distribution function $f(z)$ as represented in Eqns. (5-14)-(5-16):

$$M_x = M_0 + x^2 f(z) \tag{5-14}$$

$$M_y = M_0 + y^2 f(z) \tag{5-15}$$

$$M_{xy} = xyf(z) \tag{5-16}$$

These equations must satisfy the yield condition of Figure 5-3, Eqns. (5-9)-(5-10); viz., for any coordinates $0 \le x \ \le \sqrt{2}L$ and $0 \le y \ \le \sqrt{2}L$:

$$\mathrm{M}_1 = M_0 \tag{5-17a}$$

$$-M_0 \le \mathrm{M}_2 \le M_0 \tag{5-17b}$$

which determines the plastic flow in the regime AD of the yield criterion. While Eqn. (5-17a) may be obtained by elementary calculations of Eqn. (5-9), the admissibility of Eqn. (5-17b) will be verified in section 5.12.3. Combining Eqns. (5-14) - (5-16) with Eqn. (5-13) and incorporating Eqn. (5-12) yields:

$$6f + 6z\frac{\partial f}{\partial z} + z^2\frac{\partial^2 f}{\partial z^2} = -p_0, \qquad 0 \le z \le r_e/L \tag{5-18}$$

$$6f + 6z\frac{\partial f}{\partial z} + z^2\frac{\partial^2 f}{\partial z^2} = -ap_0e^{-bLz} \qquad r_e/\mathrm{L} \le z \le 1 \tag{5-19}$$

which are valid for all coordinates across the plate provided the moments are arranged as per Eqns. (5-14)-(5-16). Therefore, on integration, the piecewise general solution to differential Eqn. (5-18) is:

$$f(z) = \begin{cases} -\frac{p_0}{6} + \frac{A_1}{z^2} + \frac{B_1}{z^3} & 0 \le z \le r_e/L \quad \text{(5-20a)} \\ \frac{-ap_0e^{-bLz}(bLz+2)}{(bLz)^3} + \frac{C_1}{z^2} + \frac{C_2}{z^3} & r_e/\mathrm{L} \le zL \le \mathrm{L} \quad \text{(5-20b)} \end{cases}$$

The boundary conditions satisfying the bending moment distributions are given by $M_x = M_y = M_0$, $M_{xy} = Q_x = Q_y = 0$ at $x = y = 0$, suggesting that the plastic flow in the centre of the plate is governed by corner A of Johansen yield criteria. The arbitrary constants $A_1 - C_2$ are obtained by imposing the boundary conditions, as well as the kinematic continuity of moment and shear at $z = r_e/L$, as follows.

$$\begin{cases} A_1 = B_1 = 0 & \text{(5-21a)} \\ C1 = \frac{-p_0((br_e)^2 + 2br_e + 2)}{2(Lb)^2} & \text{(5-21b)} \\ C2 = \frac{p_0((br_e)^3 + 3(br_e)^2 + 6br_e + 6)}{3(Lb)^3} & \text{(5-21c)} \end{cases}$$

The bending moment in an arbitrary section defined by normal n to the circle passing through the section is given by the projection of the bending moments along this normal, given as transformation Eqn.(5-22), according to [160], [161].

$$M_n = M_x\sin^2\phi + M_y\cos^2\phi + 2M_{xy}\sin\phi\cos\phi \tag{5-22}$$

It transpires that, at simply supported plate boundary ($z = 1$), $M_n = 0$ and $\phi = 45^o$. Substituting Eqns. (5-21a)-(5-21c) into Eqns. (5-20a)-(5-20b), together with substituting Eqns. (5-14) – (5-16) into Eqn. (5-22), yields the lower bound for static collapse pressure as

$$p_0 = p_c = \frac{\mathrm{M}_0}{\propto L^2} \tag{5-23}$$

where

$$\propto = \left(\frac{3Lr_e{}^2 - 2r_e{}^3}{6L^3}\right) + \frac{\left(ae^{-Lb}(Lb+2) + b^2 r_e(L-r_e) + bL - 2br_e - 2\right)}{L^3 b^3} \qquad \textbf{(5-24)}$$

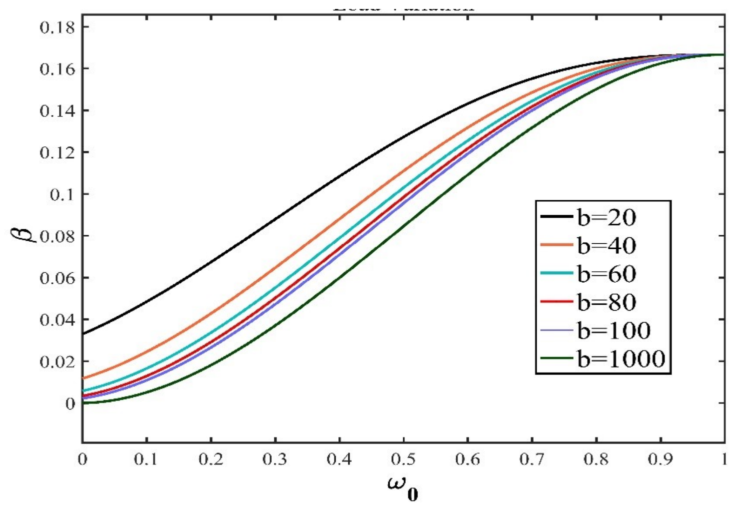

Figure 5-6. Load coefficient β across the panel-

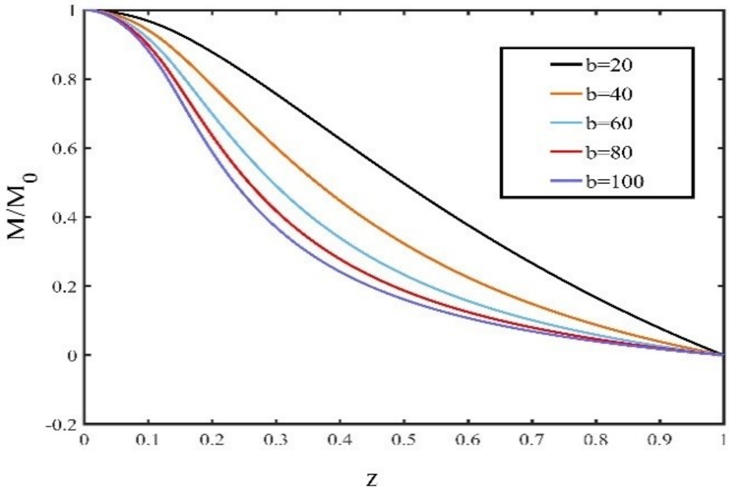

Figure 5-7. Distribution of static plastic bending moment across the panel for r_e=25mm, L=200mm

5.10 UPPER BOUND CALCULATIONS

The upper bound to the static collapse load of the square plate can be calculated by employing the principle of virtual velocities. In this manner, equating the rate of external work to the rate of internal energy dissipation through plastic work, i.e. $\dot{D} = \dot{E}$, Eqns. (5-3)-(5-5) require a kinematically admissible velocity field. It is assumed that the velocity profile is of a conical shape, shown in Figure 5-5 which is the same as the transverse deflection profile throughout the entire static phase.

$$\dot{w} = \dot{W}(1 - z) \tag{5-25}$$

While it is physically reasonable to assume the conical shape in Figure 5-5 for the velocity profile, it is also mathematically evident that for the case of $b \to 0$ (the case of uniform load) and $b \to \infty$ (i.e., the case of point load) the velocity shape function is of the form described in (5-25) and thus there is no reason as to why an alternative profile exists in the range of $0 < b < \infty$, i.e., the case studied hereunder. Thus, it is reasonable, as a first attempt, to assume the velocity field as this profile. With this assumption, the external work rate will furnish to the expression in (5-26).

$$\dot{E} = 2L^2\dot{W}_0\left(\int_0^{r_e/_L} p_u(1 - z)zdz + \int_{r_e/_L}^{1} p_u(1 - z)zae^{-bLz}dz\right) \tag{5-26}$$

Evaluating the integrals and using the principle of virtual velocities gives the upper bound plastic collapse load in Eqn. (5-26) as:

$$p_u = \frac{M_0}{\beta L^2} \tag{5-27}$$

where

$$\beta = \frac{ae^{-bL}(Lb + 2) + b^2r_e(L - r_e) + bL - 2br_e - 2}{(Lb)^3} + \frac{3Lr_e{}^2 - 2r_e{}^3}{6L^3} \tag{5-28}$$

It is evident from Eqns. (5-28) and (5-24) that, $\beta = \alpha$, hence the upper bound and lower bound are identical, i.e. $p_c = p_u = M_0/\beta L^2$ gives the exact plastic collapse pressure. For the value of $b = 0, r_e = L$ the Eqn. (5-23) simplifies to $p_c = 6\mathrm{M}_0/L^2$ which corresponds to collapse load in the case of uniform pressure load. The variation of load parameter β as a function of centre region radius and parameter b is shown in Figure 5-6. It is also evident from Figure 5-7 that principle moment distribution (ratio of M_2/M_0) is heavily dependent on the loading parameter b.

5.11 **DYNAMIC ANALYSES**

The dynamic analyses in this section are conducted by including the inertia term in equilibrium Eqns. (5-4)-(5-6). The kinematic relations in dynamic analyses are distinguished by two distinctive cases, as follows:

- Case I: where $1 \leq \eta \leq \eta_{crit}$

- Case II: where $\eta \geq \eta_{crit}$, in which η is the dynamic load amplification factor defined as $\eta = \frac{p_0}{p_c}$ and η_{crit} is defined in equation (5-40).

It is pragmatic to introduce the following parameters

$$\ddot{\bar{w}} = M_0/\mu L^2 \ , \ \bar{\tau} = \eta\tau, \quad \bar{m} = M_2/M_0 \tag{5-29}$$

5.12 CASE I- $1 \leq \eta \leq \eta_{crit}$

During this case, it is assumed that the velocity profile is the same as the static case discussed in the previous section0. However, the loading involves the temporal part of pulse shape as per Eqn. (5-2). It is pragmatic to investigate the structural response in two distinctive phases, i.e., $0 \leq \mathrm{t} \leq \tau$ and $\tau \leq t \ \leq T_f$, where τ is the duration of pulse load.

5.12.1 First phase of motion $0 \leq t \leq \tau$

During the first phase of motion, we maintain the temporal part to be of rectangular form (Eqn. (5-2)) while the spatial part follows Eqn. (5-1). The plastic flow of hinge lines lies on the regime AB of the Johansen yield criterion. The O.D.E 's in this phase are:

$$6g_1 + 6z\frac{\partial g_1}{\partial z} + z^2\frac{\partial^2 g_1}{\partial z^2} = \mu\ddot{w} - p_0 \qquad 0 \ \leq z \leq r_e/L \tag{5-30a}$$

$$6g_2 + 6z\frac{\partial g_2}{\partial u} + z^2\frac{\partial^2 g_2}{\partial u^2} = \mu\ddot{w} - ap_0e^{-bLz} \qquad r_e/L \ \leq z \leq 1 \tag{5-30b}$$

which have the same form as before except the function $f(z)$ from Eqns. (5-18) -(5-19) is substituted by $g(z)$. The general solutions to differential Eqns. (5-30a) and (5-30b) are:

$$g_1(z) = \begin{cases} \dfrac{\mu\ddot{W} - \ p_0}{6} - \dfrac{\mu\ddot{W}z}{12} + \dfrac{A_1}{z^2} + \dfrac{B_1}{z^3} & 0 \ \leq z \leq r_e/L \quad \text{(5-31a)} \\ \dfrac{-ap_0e^{-bLz}(bLz+2)}{(bLz)^3} + \dfrac{\mu\ddot{W}}{6} - \dfrac{\mu\ddot{W}z}{12} + \dfrac{D_1}{z^2} + \dfrac{E_1}{z^3} & r_e/\mathrm{L} \ \leq z \leq 1 \quad \text{(5-31b)} \end{cases}$$

By employing the continuity of generalised stresses and shear forces at $z = 0$ and $z = r_e/L$, the integration constants are determined as follows:

$$\begin{cases} A_1 = B_1 = 0 & \text{(5-32a)} \\ D_1 = \dfrac{\mu\ddot{W}r_e^3\left(2L - \sqrt{2}\right)}{24L^4} + \dfrac{-p_0((br_e)^2 + 2br_e + 2)}{2(Lb)^2} & \text{(5-32b)} \\ E_1 = \dfrac{p_0((br_e)^3 + 3(br_e)^2 + 6br_e + 6)}{3L^3b^3} - \dfrac{\mu\ddot{W}r_e^4\left(2L - \sqrt{2}\right)}{24L^5} & \text{(5-32c)} \end{cases}$$

By substituting Eqns. (5-32a)-(5-32a) in Eqns. (5-31a-b)and, considering Eqns. (5-22), (5-23), (5-28) and invoking the boundary condition at the plate contours, i.e. $\bar{m} = 0$, an expression for maximum transverse inertia is found as:

$$\ddot{W}_1 = 12\ddot{\bar{w}}(\eta - 1) \tag{5-33}$$

Two-time integration of Eqn. (5-33) then yields the displacement field as in Eqn. (5-34), when appreciating zero integration constants due to initial boundary conditions, i.e. $\dot{W}_1(0) = W_1(0) = 0$

$$W_1(t) = (6\ddot{\bar{w}}(\eta - 1)t^2) \tag{5-34}$$

5.12.2 Second phase of motion $\tau \le t \le T$

In the second phase of motion, the loading is complete and all motion is due to intrinsic inertia effects, the Eqns. (5-33)- (5-34) remain valid, except that the loading is lifted. Hence, Eqn. (5-33) is applicable although it becomes:

$$\ddot{W}_2 = -12\ddot{\bar{w}} \tag{5-35}$$

Time integration of Eqn. (5-35), together with employing the continuity of the velocity and displacement fields at $t = \tau$, gives the velocity and displacement in this phase, as in Eqns. (5-36) and (5-37).

$$\mu\dot{W}_2 = -12\,\ddot{\bar{w}}(t - \bar{\tau}) \tag{5-36}$$

$$W_2 = -6\ddot{\bar{w}}\,(t^2 - 2\bar{\tau}t + \eta\tau^2) \tag{5-37}$$

The second phase ceases at $t = T_f = \bar{\tau}$, which is when the transverse velocity $\dot{W}_2$ vanishes. Hence, Eqn. (5-37) gives

$$w_f = \frac{6\ddot{\bar{w}}\bar{\tau}^2(\eta - 1)(1 - z)}{\eta} \tag{5-38}$$

which is the displacement function at any point of the plate. It can be seen that, with $r_e = L$, this equation reduces to $w_f = 6\,M_0\tau^2\eta(\eta - 1)(1 - z)/\mu L^2$, which is the case of uniform pressure load.

5.12.3 Static and kinematic admissibility

It is essential to verify whether the mathematical treatment in 5.12 are statistically admissible, i.e. the Eqn. (5-17a) and inequality (5-17b) are not violated. Whilst Eqns. (5-14)-(5-16) satisfy $\mathrm{M}_1 = \mathrm{M}_0$, it is necessary to demonstrate that the shear forces at the centre vanish (i.e. $Q_x|_{z=0} = 0$ and $(\partial^2 M_x)/(\partial x^2) > 0$ (or $(\partial^2 M_y)/(\partial x^2) > 0$). While the former condition is clearly satisfied from Eqn. (5-31a), the latter condition, requires:

$$\frac{\partial^2 M_x}{\partial x^2} = \frac{\left(\left(6\left(2L^4z^3 - L^4z^4 - \frac{5}{2}z^2L^2x^2 + 1/2x^4\right)\right)(\eta - 1)M_0 - p_0L^6z^3\right)}{3L^6z^3} > 0 \tag{5-39}$$

which is obtained with the aid of variational parameters. Elementary calculation gives:

$$\eta \leq \left|\frac{12\beta}{12\beta - 1}\right| = \eta_{crit} \tag{5-40}$$

A similar procedure to establish the static admissibility of the velocity profile is achieved by satisfying Eqn. (5-17b), i.e. it is required to show that $-\mathrm{M}_0 \leq \mathrm{M}_2 = (\mathrm{M}_x + \mathrm{M}_y)/2 + 1/2[(\mathrm{M}_x - \mathrm{M}_y)^2 + 4{\mathrm{M}_{xy}}^2]^{1/2} \leq \mathrm{M}_0$. This inequality simplifies to the following:

$$-2\mathrm{M}_0 \leq (\mathrm{x}^2 + \mathrm{y}^2)\mathrm{g(z)} \leq 0 \tag{5-41}$$

The right-hand side of the inequality-at the plate centre- requires that $(\mu\ddot{W} - p_1)/6 - \mu\ddot{W}z/12 \leq 0$, which, when using Eqns. (5-33), (5-23), will lead to an identical expression to Eqn. (5-40).

In the case of $r_e = L$ and $\beta = \frac{1}{6}$; the right-hand side of the inequality simplifies to the condition for the case of uniformly distributed load, i.e. $\eta \leq 2$.

In the second phase of motion, the Eqn. (5-17b) (or (5-39)) must still be satisfied, but with setting $\eta = 0$, which yields:

$$-2M_0 \leq \frac{-2\,M_0(x^2 + y^2)}{L^2} \leq 0 \tag{5-42}$$

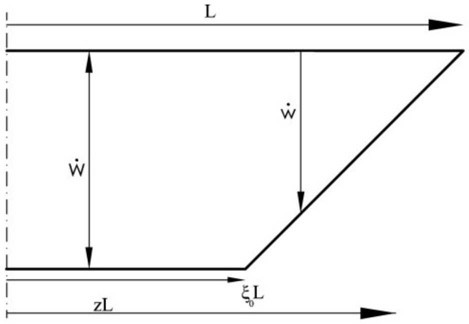

Figure 5-8. The velocity profile for the initial phase $t = \tau$

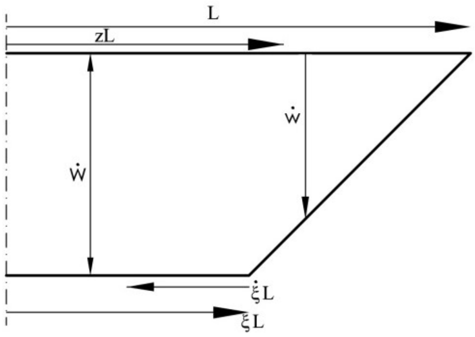

Figure 5-9. The velocity profile at $\tau \le t \le T_1$

By considering the fact that $(x^2 + y^2)/L^2$ is universally positive (Eqn. (5-12)), Eqn. (5-42) is valid for all values of $\omega_0 = r_e/L$ and L at plate centre. A plot of bending moment distribution for various values of η is shown in Figure 5-10. In this case, the loading parameter $b = 50$ and $\omega_0 = 0.125$, which are found by regression analyses on numerical results of registered pressure time history for an Armour steel model B4 found in Ref. [61].

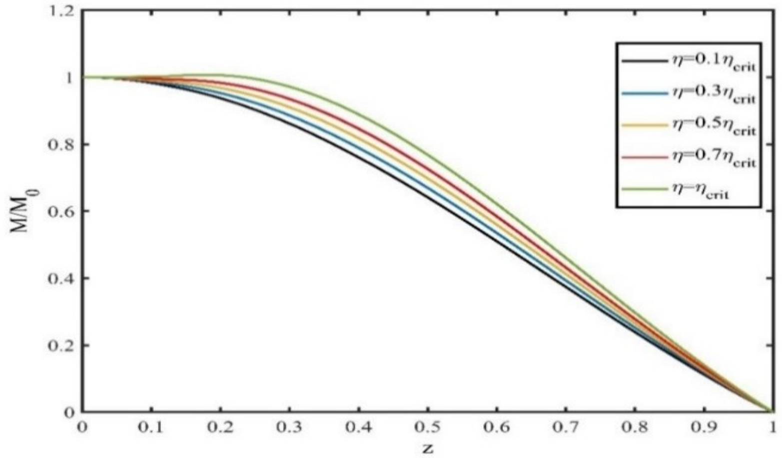

Figure 5-10. Principle bending Moment distribution with re=25mm and L=200mm for $0 \le t \le \tau$

5.13 CASE II: $\eta \ge \eta_{crit}$

5.13.1 First phase of motion

For the blast loads with high magnitudes, $\eta > \eta_{crit}$ then $p_1 >> p_c$ so the right-hand side of Eqn. (5-41) is no longer valid, since a yield violation occurs near the plate centre. This requires the velocity field profile to be modified. It is therefore assumed that the velocity profile is governed by three distinguishable phases, as the incipient plastic hinge forms in the central part of the plate (Figure 5-8). It is also assumed that in this phase, the plastic flow in the plate centre is characterised by corner A of the yield condition in Figure 5-3, which governs the central part of the plate for $0 \le z \le \xi_0$, whereas the remaining part of the plate $\xi_0 \le z \le 1$ is governed by the regime AB. Thus, the velocity profile will be of the form:

$$\dot{w} = \dot{W}_2 \qquad \text{for } 0 \le z \le \xi_0 \qquad \textbf{(5-43)}$$

$$\dot{w} = \dot{W}_2 \frac{(1-z)}{(1-\xi_0)} \qquad \text{for } \xi_0 \le z \le 1 \qquad \textbf{(5-44)}$$

where ξ_0 is time independent. It is also assumed that $r_e/L \le \xi_0$. Thus, the moment function $g_1(z)$ is replaced by $g_2(z)$ in the following form:

$$g_2(z) = \begin{cases} \dfrac{\mu\ddot{W} - p_0}{6} + \dfrac{A_3}{z^2} + \dfrac{B_3}{z^3} & 0 \le zL \le r_e \qquad \textbf{(5-45a)} \\ \dfrac{-ap_0 e^{-bLz}(bLz+2)}{(bLz)^3} + \dfrac{\mu\ddot{W}}{6} + \dfrac{D_3}{z^2} + \dfrac{E_3}{z^3} & r_e \le zL \le \xi_0 L \qquad \textbf{(5-46b)} \\ \dfrac{-ap_0 e^{-bLz}(bLz+2)}{(bLz)^3} + \dfrac{\mu\ddot{W}}{6(1-\xi_0)} - \dfrac{\mu\ddot{W}z}{12(1-\xi_0)} + \dfrac{F_3}{z^2} + \dfrac{G_3}{z^3} & \xi_0\mathrm{L} \le zL \le L \qquad \textbf{(5-47c)} \end{cases}$$

$$\begin{cases} A_3 = B_3 = 0 \\ D_3 = \dfrac{-p_0((br_e)^2 + 2br_e + 2)}{2(Lb)^2} \\ E_3 = \dfrac{p_0((br_e)^3 + 3(br_e)^2 + 6br_e + 6)}{3L^3b^3} \end{cases} \qquad \textbf{(5-48)}$$

The integration constants in Eqn. (5-45a)-(5-47c) are obtained by applying continuity conditions of $Q_x = 0$, $M_x = M_y = M_0$ at $z = 0$ and at $z = r_e/L$. It follows that at $0 \le z \le r_e/L$, $\mu\ddot{W}_2 = p_1$. Using the Kinematic conditions of $W_2 = \dot{W}_2 = 0$ at $t = 0$, the maximum displacement will become:

$$w_2 = \frac{p_0 t^2}{2\mu} \qquad \textbf{(5-49)}$$

The arbitrary function of the outer region, i.e. $\xi \le z \le 1$ is similar to Eqn. (5-31b), but with replacing the inertia term with $\ddot{W}/(1-\xi_0)$, while the constant of integration, in (5-32b-c) have now changed to F_3 and G_3, respectively and given in (5-50). As the bending moment in the central zone $0 \le z \le \xi_0$ is assumes its maximum value, it is appreciated that $Q_x = Q_0$ throughout this zone. This yields the integration constants as in Eqn. It is noteworthy that the continuity conditions of $g_2(z)$ and Q_x at $z = \xi_0$ also applies.

$$\begin{cases} F_3 = \dfrac{p_0\left(3a(-1+\xi_0)(Lb\xi_0+1)e^{-Lb\xi_0} + L^2b^2\xi_0^2\left(\xi_0 - \frac{3}{2}\right)\right)}{3L^2b^2(1-\xi_0)} \\ G_3 = \dfrac{p_0\left(4a(-1+\xi_0)[\,(Lb\xi_0)^2 + 2Lb\xi_0 + 2]e^{-Lb\xi_0} + (Lb\xi_0)^3\left(\xi_0 - \frac{4}{3}\right)\right)}{4L^3b^3(-1+\xi_0)} \end{cases} \tag{5-50}$$

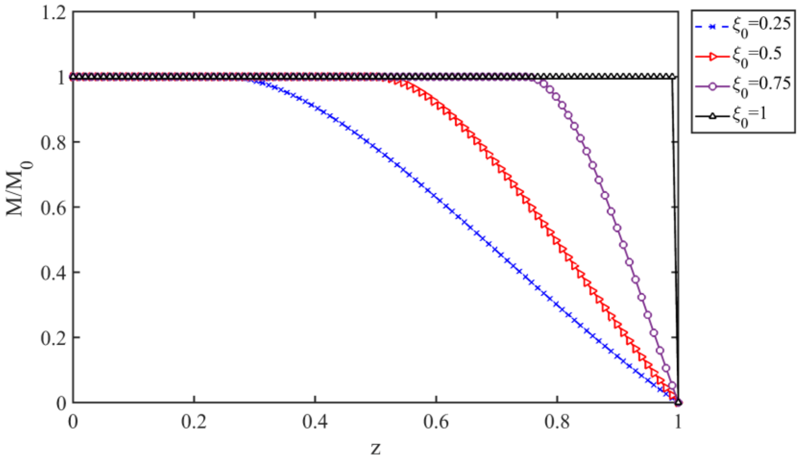

Figure 5-11. Distribution bending moment with various values of ξ_0. The loading conditions are $\omega_0 = 0.7$ and $b = 50.5m^{-1}$, on a plate with side-length of $L = 0.2m$

The expression of arbitrary function $g_2(z)$ should satisfy the boundary conditions at the plate contours, i.e. $\overline{m} = 0$ t $z = 1$, which yields an expression of the incipient plastic hinge and the loading amplification factor as

$$\eta = \frac{12L^3b^3\beta}{\gamma'} \tag{5-51}$$

where $\eta = p_0/p_c$, while the parameter γ' is:

$$\gamma' = 12a[b^2L^2(1-\xi_0)\xi_0 + (1-2\xi_0)bL - 2]e^{-Lb\xi_0} + 12a(Lb+2)e^{-Lb} \\ - 3(1-\xi_0)^2(\xi_0 + 1/3)L^3b^3 \tag{5-52}$$

The distribution of bending moment with various values of ξ_0 is presented in Figure 5-11. The expression of ξ_0 in Eqn. (5-52) is highly nonlinear which can be solved with the aid of numerical methods. However, for impulsive loading, or $\eta \to \infty$. thus $\gamma \to 0$ which occurs when the plastic hinges form at the supports, i.e. $\xi_0 \to 1$.

5.13.2 Second phase of motion $\tau \leq t \leq T_1$

In this phase, the loading is absent while the motion continues due to reserved velocity from the first phase. Concerning this, ξ_0 from Eqn. (5-44) is substituted by an active plastic hinge ξ, which moves inwards as demonstrated in Figure 5-9. The equilibrium of $p_1 = 0$ at the central zone predicts $\mu\ddot{W}_2 = 0$. Therefore, by implementing the continuity of the velocity field at $t = \tau$, the response as given in Eqn. (5-53), (5-54).

$$\dot{W}_2 = p_0\tau/\mu \tag{5-53}$$

$$W_2 = \frac{p_0\tau t}{\mu} - \frac{p_0\tau^2}{2\mu} \tag{5-54}$$

Thus, the motion is characterised by constant velocity throughout this phase, while the size of the central plastic zone diminishes monotonically. For the second region, the differential Eqns. (5-30a) and (5-30b) would furnish to

$$z^2\frac{\partial^2 g_2}{\partial z^2} + 6z\frac{\partial g_2}{\partial z} + 6g_2 = \mu\ddot{w}_2 = \mu\ddot{W}_2\left(\frac{1-z}{1-\xi}\right) + \mu\dot{W}_2\dot{\xi}\left(\frac{1-z}{(1-\xi)^2}\right) \tag{5-55}$$

with the succeeding general solution as:

$$g_2 = \frac{\mu\ddot{W}_2(2-z)}{12(1-\xi)} + \frac{\mu\dot{W}_2\dot{\xi}(2-z)}{12(1-\xi)^2} + \frac{D_4}{z^2} + \frac{E_4}{z^3} \tag{5-56}$$

The integration constants are obtained by conditions of $Q_x = 0$ and $M_x = M_y = M_0$ at $0 \leq z \leq \xi$, the continuity of Q_x and M_x at $z = \xi$ gives:

$$\begin{cases} D_4 = \dfrac{p_0\tau\dot{\xi}\xi^2(2\xi-3)}{6(\xi-1)^2} \\ E_4 = \dfrac{-p_0\tau\dot{\xi}\xi^3(3\xi-4)}{12(\xi-1)^2} \end{cases} \tag{5-57}$$

An expression in terms of the travelling hinge ξ is found by employing the simply supported boundary condition (Eqn. (5-22)) at corners of the plate:

$$(3\xi^2 - 2\xi - 1)\dot{\xi} = \frac{12\beta}{\tau} \tag{5-58}$$

An expression for the travelling hinge displacement is attained through time integration of $\dot{\xi}$, eliminating ξ_0, and appreciating that the that the plastic hinge remains stationery within $0 \leq t \leq \tau$. Thus, the kinematic continuity of ξ at $t = \tau$ gives

$$\xi^3 - \xi^2 - \xi - 1 = \frac{12\beta t}{\bar{\tau}} + \bar{\xi} \tag{5-59}$$

where

$$\bar{\xi} = \xi_0^3 - \xi_0^2 - \xi_0 - 1 - \frac{12\beta}{\eta} \tag{5-60}$$

Subsequently, the second phase terminates when $\xi = 0$, occurring at time T_1:

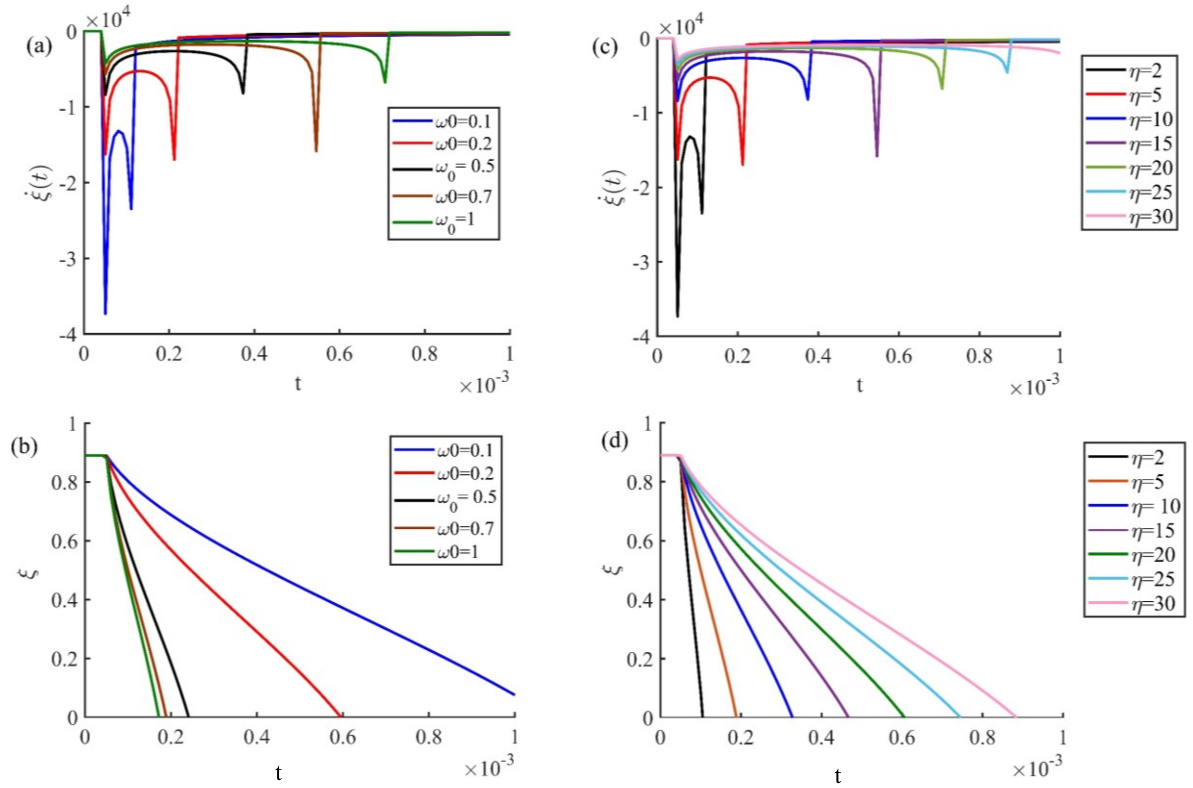

Figure 5-12- Time variation of the plastic bending hinge and its velocity in various load ratio(a) and (b), vs various overloading factor (c), (d)

$$T_1 = \frac{(12\beta - 1)\bar{\tau}}{12\beta} \tag{5-61}$$

Substituting Eqn. (5-61) into Eqn. (5-54) gives:

$$W_2 = -\frac{\ddot{w}\eta\tau^2\left(\eta\bar{\xi} + 6\beta + \eta\right)}{12\beta^2} \tag{5-62}$$

The variation of the plastic hinge and its time derivative is plotted in Figure 5-12.

5.13.3 Final phase of motion $T_1 \leq t \leq T_f$

The final phase of the plate motion will essentially develop since the kinetic energy from the previous phase has to be somehow dissipated. The transverse velocity profile is the same as Figure 5-5 as the plastic hinge closes ($\xi = 0$). The incipient deformation is identical to the circumstance of infinitesimal blast loads, viz., the condition of inequality (5-40). The solution to velocity and displacement fields at this phase is achieved by time integration of (5-35) and equating it with Eqns. (5-36), (5-53), (5-54), (5-61) at $t = T_1$. Thus, the transverse displacement at this phase furnishes to

$$W_3 = -\frac{p_0\left[\bar{\tau}^2\left(\bar{\xi}+1\right)^2 + 24\beta\bar{\tau}\left(t\bar{\xi}+\frac{1}{2}\tau\right) + 144\beta^2 t^2\right]}{24\eta\beta\mu} \qquad \textbf{(5-63)}$$

Recalling the parameter $\bar{\xi} = \xi_0^3 - \xi_0^2 - \xi_0 - 1 - 12\beta/\eta$. Motion ceases when $\dot{W}_3 = 0$, which occurs at time T_f (Eqn. (5-64)).

$$T_f = -\frac{\bar{\xi}\bar{\tau}}{12\beta} \qquad \textbf{(5-64)}$$

Substituting (5-64)in (5-63)gives:

$$W_f = -\frac{\ddot{\bar{w}}\,\eta\tau^2\left[\left(\bar{\xi}+\frac{1}{2}\right)\eta + 6\beta\ \right]}{12\beta^2} \qquad \textbf{(5-65)}$$

5.13.4 Static and Kinematic Admissibility

It is evident that the continuity requirements of generalised stresses i.e. $Q_x = Q_y = 0\,, M_x = M_y = M_0$ are satisfied at $z = 0$, $z = \xi_0$ and $z = \xi$ throughout all three phases of motion. Furthermore, the Eqn. (5-17a) are satisfied throughout the entire motion, irrespective of the phase of motion. It can also be observed that the inequality (5-17b) is satisfied for $0 \leq z \leq \xi$ for first and second phases of motion.

5.14 IMPULSIVE LOADING

A blast load of rectangular pulse shape with very short duration ($\tau \to 0$) and very high amplitude ($\eta \to \infty$ or $p_1 \gg p_c$) is known as impulsive loading. In the case of impulsive loading, the total change in momentum equals the total impulse imparted upon the system, hence the conservation of momentum implies that:

$$\int_0^{\frac{re}{L}} 8L^2\tau p_0 zdz + \int_{\frac{re}{L}}^1 8L^2\tau p_0 a e^{-bLz} zdz = \int_0^1 8L^2\mu V_0 zdz \tag{5-66}$$

The solution to the Eqn. (5-66) yields:

$$V_0 = \frac{\epsilon_1 \tau p_0}{L^2 \mu} \tag{5-67}$$

where $\epsilon_1 = \frac{-r_e^2 b^2 + 2ae^{-Lb}(bL+1) - 2r_e b - 2}{b^2}$. Defining the dimensionless kinetic energy as $\lambda = \frac{\mu V_0^2 L^2}{M_0 H}\left(\frac{L^4}{\epsilon_1^2}\right)$ and rearrangement of variables, the Eqn. (5-65), can be recast in the dimensionless form as:

$$\frac{W_f}{H} = -\frac{\lambda}{12\eta}\left[\left(\bar{\xi} + \frac{1}{2}\right)\eta + 6\beta\right] \tag{5-68}$$

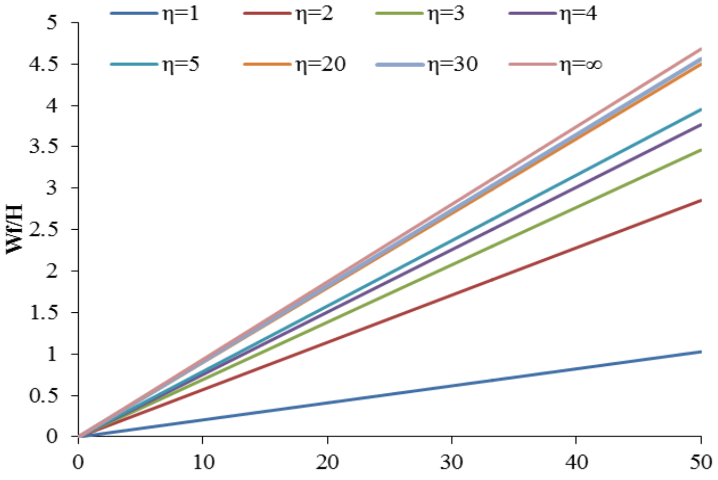

Figure 5-13. Plot of dimensionless kinetic energy for various values of η

For the case of $r_e = L$ and $\eta \to \infty, r_e \to L,\ \beta = \frac{1}{6}$ and $W_f/H \cong \lambda/8$, which conforms to results for the case of uniform pressure load. A plot of normalised deflection vs. the dimensionless kinetic energy is presented in Figure 5-13 for the case of $\omega_0 = 0.7, b = 50$ for various values of load ratio. It can be observed that with increase of η the plot is only marginally different from impulsive load, i.e. $\eta \to \infty$.

5.15 FULLY CLAMPED SQUARE PLATE

Whilst in practical applications, the protective plate elements are designated with fully-clamped conditions, the foregoing analysis for the simply supported plates can plainly be extended to the case of fully-clamped plate: the edge conditions of the moment, denoted by $\bar{m} = -1$, yields the static plastic collapse as $p_c = 2M_0/\beta L^2$; thus, the foregoing results may be furnished for the fully-clamped plates by merely changing M_0 to $2M_0$ in the parameter $\ddot{\bar{w}}$ and associated expressions accordingly.

However, it should be noted that, in contradiction to the global blasts, the boundary effects are not significant for the localised blast because such a blast impacts a small area of the plated structure [162]. Furthermore, in the case of global (uniform) loading, the difference between the clamped boundary and simply supported become only significant beyond mode I behaviour (large inelastic deformation) [163].

5.16 NUMERICAL ANALYSES

5.16.1 Limitations of the study

The analysis performed in section 5.11 was predicated on the assumptions of Kirchhoff –Love plate theory, which ignores the effects of transverse shear and rotatory inertia. Taking this limitation into account, it may be safely assumed that for the range of $1.2\% < \frac{H}{L} < 3.5\%$ and under infinitesimal loading conditions, the bending action dominates the structural behaviour, such that the build-up of membrane action associated with the plastic collapse can be disregarded. Furthermore, because the localised blast impacts a small area of the plated structure, the boundary effects are insignificant in contradiction to the global blast loading [162]. The numerical tests on some panels with aforementioned parameters but with clamped boundary conditions confirmed this statement. In the case of global (uniform) loading, the difference between the clamped boundary and simply supported become only significant beyond mode I behaviour (large inelastic deformation) [163].

5.16.2 Finite element modelling

Whilst considering the limitations of this study, the analytical solutions are validated against numerical simulations in this section. The simulations are performed in Finite Element (FE) hydrocode ABAQUS 6.13/Explicit®, a commercially available software capable of simulating the dynamic response for blast loading scenarios through analyses of various degrees of complexity.

A full 3D FE model was set up in ABAQUS 6.13 for rectangular plate of length $2L$, with simply supported boundary conditions and the geometric and material properties as in Table 5-1.Due to symmetry, only a quarter of the plate was designed.

Table 5-1- Plate geometric, material and loading parameters

Geometric and material properties		Loading	
$H\ (mm)$	2.6	$b(m^{-1})$	50
$L(mm)$	200	$\tau(\mu s)$	50
$\sigma_0(MPa)$	330	η	5
$\mu\ (\frac{kg}{m^2})$	20.4		

The plate was discretised with S4(R) shell elements of double curvature with hourglass control and pinned along the periphery. The fine mesh was chosen with a total of 2500 elements, giving the element length to thickness ratio of ~1.25, to ensure that the convergence is satisfied. Due to symmetry, only a quarter of the plate is modelled. For each case of $\omega_0 = r_e/L$, a pressure matrix corresponding to Cartesian coordinates was constructed by utilising Eqns. (5-2), and (5-12). This pressure matrix was mapped directly onto the panel.

The selected loading parameters were assumed constant as $b = 50$ and $\tau = 50\mu s$ Following a general static analysis, the values of dynamic collapse load p_1 was calculated to acquire constant dynamic load ratio $\eta = 5$ for a various range of loading radii, as illustrated in the Figure 5-14.

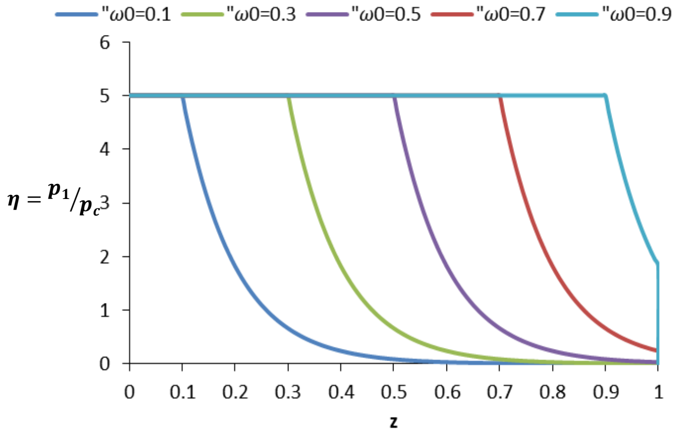

Figure 5-14. Pressure load with various values of ω_0

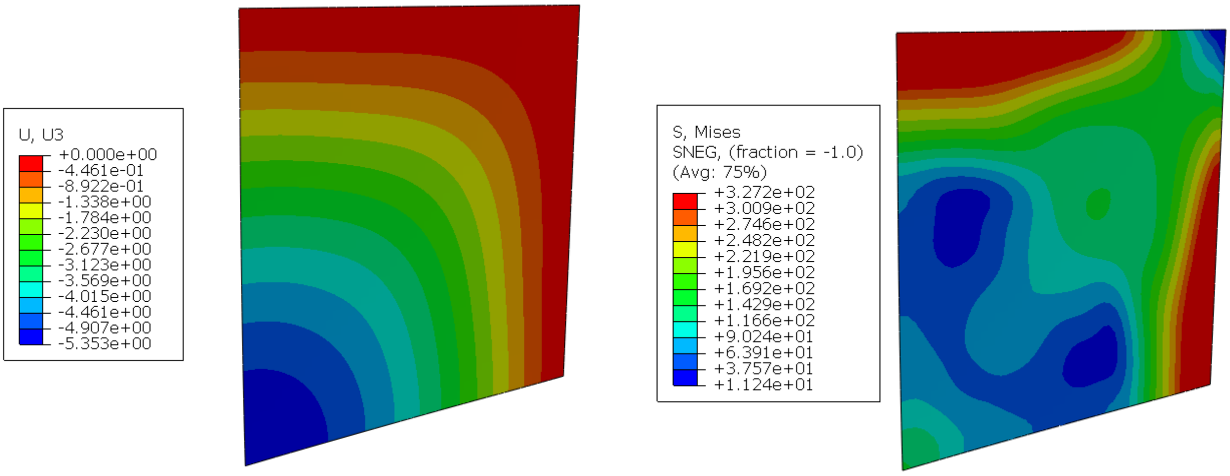

(a)

(b)

Figure 5-15. Schematic of displacement (a) and stress distribution (b) for load ratio $\eta = 5$ at $t = 5 \times 10^{-4}$

5.17 FINITE ELEMENT RESULTS AND VALIDATIONS

For the case of ω_0=0.7, a contour plot of transverse displacement and stress distributions is shown in Figure 5-15. To determine the permanent plastic deformation analytically, the position of the stationery plastic hinge is obtained numerically for various loading radii and plotted in Figure 5-16. It is interesting to note that for most loading radii, the length of ξ_0 (which should satisfy $\eta\gamma - 12\beta^3 L^3 b^3 = 0$ from Eqn. (5-51)) is predicted at 0.89th of the plate length. For close-in blasts with small loading radii/plate length ratio, the length of the stationery plastic hinge decreases accordingly. It turns out that in the case of $\omega_0 = 0.1$, for example, a solution of ξ_0 in Eqn. (5-51) exists at the plate centre, in addition to the hinges formed near the supports. Numerical observations on the position of first maximum equivalent plastic strain ($\bar{\varepsilon}_p$) corroborate with this statement.

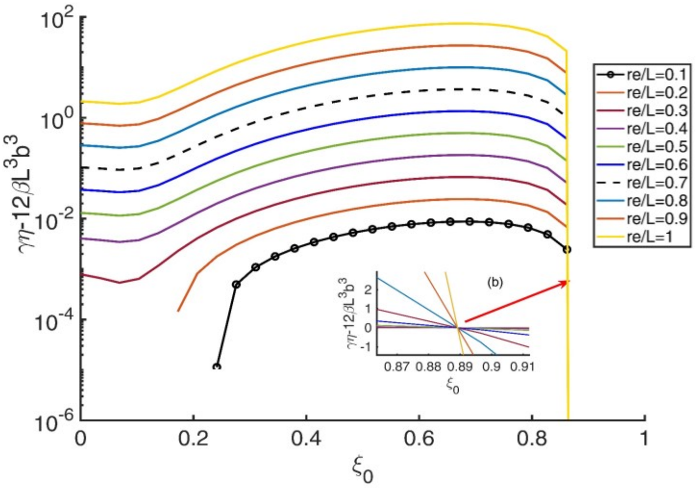

Figure 5-16. Numerical plot of Eqn. (5-51) with $p_1 = 20MPa$, $b = 100$ and various load radii.

Further, it is observed from Figure 5-17 that for the range of $H/L = 1.3\%$ and for low magnitude of dynamic loads, the numerical results for displacement compare favourably with the analytical results.

The theoretical solution for the impulsive loading from Eqn. (5-68) is also validated in Figure 5-18 against the experimental results on ARMOX steel and mild steel MS4 specimens obtained from [61], [76], [119] (square plates of test series I), accordingly. The empirical fit to the experimental data by [76] is also plotted for comparison. The duration time was chosen as $15\mu s$,to ensure that the ratio of loading time to natural period of structure is maintained low and in impulsive range. The chosen loading radius $r_e = 25mm$ was kept consistent with the charge radius, whilst 'b' was evaluated by curve fitting methods on the pressure loads of the gauge points from the numerical results. It is also important to note the deviation of data from the predicted curve when the dimensionless kinetic energy increases ($\lambda > 200$), the limit beyond which the membrane action significantly affects the transverse deflections. While the empirical fit of Ref. [76], which utilises the Eqn. (2-17), accounts for this action, the simplified theoretical model would provide a good estimate to the permanent deformations at low range of dimensionless impulse (i.e. $\lambda = \phi_{ql}^2 \leq 200$). This highlights the significance of developing a theoretical model whereby the membrane resistance is retained in the analysis.

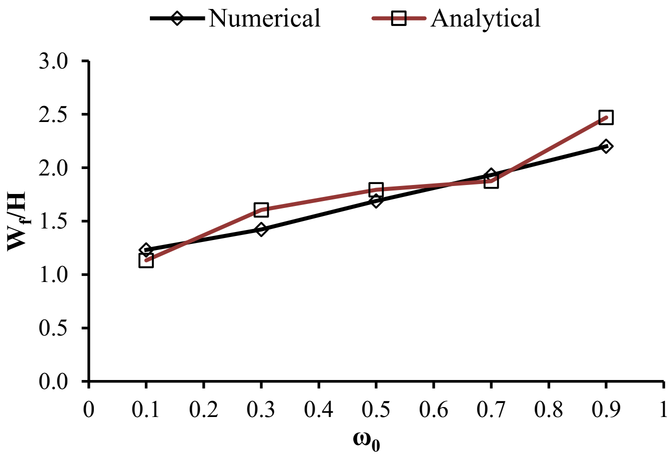

Figure 5-17. Prediction of displacement from analytical and numerical studies ($\eta = 5$)

It should be noted that, for the case of ARMOX steel, the material is capable of higher energy absorption, while the deformation is not significantly affected by strain rate sensitivity. However, the response can be affected by the material elasticity which can pose a difficulty when implementing limit analysis. Regardless of this limitation, the application of modified load function considerably enhances the prediction of plate response as opposed to the previous models introduced by researchers [35], and [99] valid for uniform pressure.

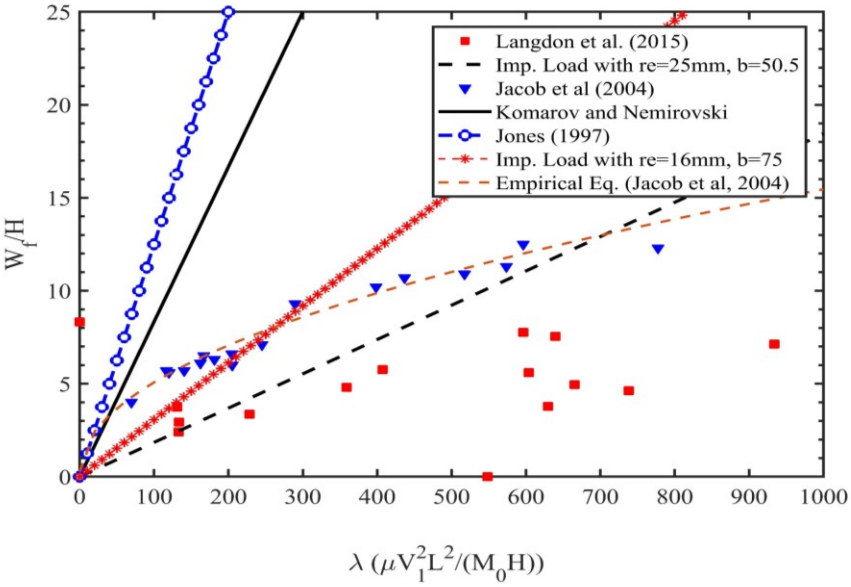

Figure 5-18. Comparison of experimental results and theoretical model of Eqn. (5-68) for an impulsively loaded plate.

5.18 SUMMARY AND CONCLUSIONS

This chapter dealt with a theoretical model to predict the transverse dynamic plastic displacement field of a generic simply supported, monolithic square plate subjected to localised blast loading. A piecewise continuous load function formerly studied by [38], [22], [152], was incorporated into the analyses, which is universal and adaptable for various loading scenarios from localised blasts to more distant loading.

The plate was assumed thin, to enable making use of Kirchhoff-Love theory as opposed to Mindlin-Reissner plate theory. As such, transverse shear and rotatory inertia effects can be ignored without loss of accuracy. The plate was, however, assumed thick enough not to be considered a membrane. The analyses were performed by means of limit analysis and the incipient velocity profile was governed by the travelling plastic hinge in the three stages of analysis for high amplitude loads (i.e. $p_0 \gg p_c$ or $\eta > \eta_{crit}$).

Close agreement was found when correlating the results of the theoretical model with the corresponding FE model for different load distributions. The transverse deflection-impulsive load relation was validated for different cases of load distributions. It was concluded that the analytical model yields satisfactory results for low impulse where bending effect is dominant, while for larger impulses on the thin plates, the membrane effects become significant. Thus, it is essential to investigate the influence of such blasts with consideration of the transverse shear and membrane forces.

Further, the theoretical solutions for impulsive load give better estimate than the previous rigid-plastic model by [35],[99] when validated against the experimental data for close-proximity and low impulse blast loads (i.e., $\lambda < 200$). The herein theoretical study is applicable to rapid assessment of the blast loaded plates where visco-plasticity of the material may be ignored (with little or no strain rate sensitivity), such as aluminium alloys and high strength armour steel. Structures made of armour steel undergo less deflection with higher energy absorption capacity when compared to their Mild steel counterparts.

As a final remark, while the aforementioned theoretical results are strongly sensitive to pulse shape, this effect can be virtually eliminated by using the Youngdahl's effective parameters, namely, the effective impulse and effective pressure. The interaction of these parameters with the load parameters β and η is illustrated in Figure 5-19. A detailed study on pulse dependence of the theoretical results is presented in Chapter 7.

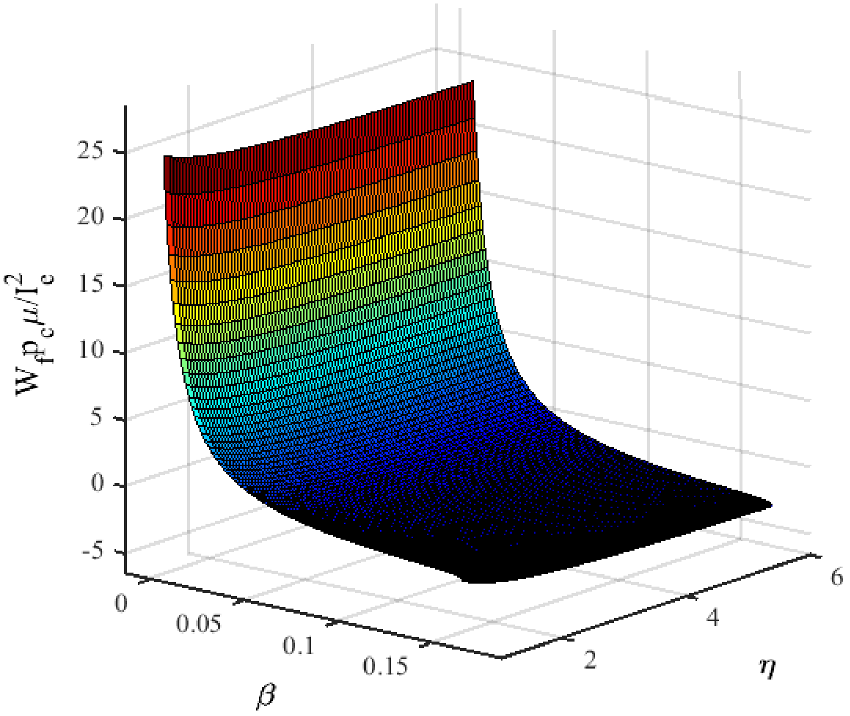

Figure 5-19. Interaction surface of load parameters on pulse independent displacement, I_e and p_e are the Youngdahl's effective impulse and pressure, respecively

CHAPTER 6

Dynamic response of square membranes

Major Portion of this work is published in International Journal of Mechanical Sciences.

6.1 BACKGROUND

Much of the earlier theoretical studies in the literature have been restricted to the classical theory of plates with infinitesimal deformations. Often, the pressure wave-either from deflagration or detonation process- on thin shells leads to large displacements brought about by finite displacements (geometry changes) which violates the assumptions of the small deflection theory. If a thin shell undergoes marked increase of transverse deformation beyond its thickness, it would exhibit finite displacements due to the evolution of membrane (catenary) forces. Such forces so emerged will resist out-of-plane deformation and decrease its maximum at the cost of accumulated in-plane tensile stresses. In fact, the experimental studies have revealed that the membrane forces dominate the overall performance of plated structures exhibiting large deformation [93], [101], [154], [164]

Zheng et al [98] investigated the elastic-plastic performance of stiffened square plates made of Q235 low carbon steel under confined blast. The confined blast was approximated with uniform distribution, leading to global deformation of the plate, while the deformation profile was unaffected by the stiffeners and no local buckling at the interface of stiffener and the plate was observed. Toolabi et al presented a mixed finite element formulation to enrich the shear strain and deformations of Mindlin Reissner plate [165].

While a small body of literature on theoretical works exists that has catered for this phenomenon [35], [103], [104], [166], these works considered only uniform pressure loads. It turns out from the results of Section 4.4.2-Section 4.5 (Figure 4-13-Figure 4-16), the predictive response of ductile metallic plates due to localised blasts cannot be delineated with available theoretical models, while the empirical models were also proposed on ad hoc basis and vary due to influence of the material type, load parameters and structural geometry. Thus, there is a paucity of information due to rarity of systematic theoretical analysis on the permanent response of plates emanating from localised blasts. Furthermore, in certain loading circumstances where the quotient of total dissipated energy to the energy absorbed elastically within the plate is insignificant, the actual elastic-plastic performance should not be disregarded.

However, finding the plastic deformations in elastic-plastic systems are fought with difficulty as they are inter-spread with the elastic ones, as the plastic region may disappear and re-appear. One vein to achieve this with mathematical brevity and without loss of accuracy is to assume the structural response as either wholly plastic or wholly elastic.

The objective of this chapter is to explore, within accurate and realistic bounds, the theoretical models predictive of the permanent response of the plate. Using this rationale, this chapter derives and investigates the primary features of a theoretical solution for blast loaded thin square plates. Membrane forces are introduced as a part of the solution and emerge as deformations become finite.

This work is thus set out in two parts. In the first part, using the principles thin shell theory on a rigid-perfectly plastic system, the previously examined solutions in Chapter 5 were extended to consider the influence large deflection plasticity theory of plates. This is achieved using the constitutive framework of limit analysis. The same problem is assessed, in the second part, but on wholly elastic plate, i.e. the influence of finite displacement was retained in the analysis of elastic membranes. This work has been published in International Journal of Mechanical Sciences [167].

The first part of this work is, as such, an extension of previous studies [35], [104], [168] which dealt with applying the bound theorems of plasticity to derive explicit closed form theoretical solutions which catered for the problem of dynamic response in locally blasted rectangular and circular plates.

I. PART I, DYNAMIC PLASTIC PERFORMANCE OF THIN SHELLS SUBJECT TO LOCALISED BLAST

The dissemination of this part is as follows. Following this introduction, the general assumptions made throughout the study have been presented. This is followed by a discussion of the governing equations Section 6.4 and possible deformation patterns in Section 6.5. In Section 6.6, the dynamic plastic performance of plates was rigorously analysed, encompassing the combined or mere influence of membrane and bending actions on each pattern in Sections 6.7-6.8. For high magnitude pressure loads, the results were cast in terms of impulsive velocity in Section 6.9, where the influence of boundary conditions and strain rate sensitivity were briefly studied. The theoretical results were validated against available experimental and numerical results in Section 6.12-6.14.

6.2 ASSUMPTIONS

The plates examined in hereunder are assumed to be ‘membranes’, implying that they are thin enough to render the contribution of transverse shear strains and rotatory inertia negligible. These effects are thus disregarded, although in-plane action plays a significant role in the overall response and has been included. In fact, it has been shown that the effect of transverse shear is not significant for locally blasted panels with slenderness ratio $\nu \geq 5$ [162]. The effect of rotatory inertia is even less significant [162].

The influence of finite displacements must be retained in the study to achieve reliable results for dynamic response of the membranes [100], [104], [105], [169]. Subsequently, the overall response of the structure is characterised by the deformed shape, rather than the base configuration. A direct consequence of this essential condition is that the membranal forces (N) to be included in the dynamic energy equilibrium equations. Hence, the overall response consists of the combined effects of bending and membrane phenomena.

The influence of visco-plasticity (strain rate sensitivity) has been investigated in the context of the problem; however, most armour graded materials, such as (RHA) and class 4 High Hardness armours (HHA) of interest are impervious to such phenomenological effect. The sensitivity of flow stress to strain rate would decrease the overall deformation, due to the increase of the material strength, but in some cases reduces the rupture strain [96]. For a detailed modal procedure to determine the dynamic response of visco-plastic plates subject to blasts and impacts, the reader is referred to Jones’ [105].

6.2.1 Geometry and load characteristics

The approach developed hereunder assumes the same geometry, prescribed loading and boundary conditions for the plates as those discussed in Section 5.5. Remark that for the uniform or point loads, only the load magnitude contributes to the length of the plastic hinge lines, while in generic blasts the length depends on both the magnitude and distribution.

The maximum plastic moment and the maximum membrane force per unit length are denoted by M_0 and N_0, respectively. It is assumed that the planar cross sections of the plate remain plane and normal to its neutral plane throughout deformation (Kirchhoff-Love plate’s kinematic assumption).

6.3 YIELD CONDITION AND FLOW RULE

By referring to the analysis of simply supported beams discussed in [35], using the Tresca yield condition, it may be assumed that for the simply supported plates, the plastic yield is governed by the constitutive equations as follows:

$$\frac{N}{N_0} = \frac{2w}{H}, |M/M_0| = \left(1 - \left(\frac{N}{N_0}\right)^2\right), \text{ if } \frac{w}{H} < \frac{1}{2} \tag{6-1}$$

$$\frac{N}{N_0} = 1, \quad \frac{M}{M_0} = 0, \text{ if } \frac{w}{H} \geq \frac{1}{2} \tag{6-2}$$

For prismatic sections:

$$N_0 = \sigma_0 H, \qquad M_0 = \frac{\sigma_0 H^2}{4} \tag{6-3}$$

Eqn. (6-1) represents two parabolas plotted in Figure 6-1. The state of stress and the normal to the yield surface are co-directional along the yield path of each parabola. From Eqns. (6-1)-(6-3), evidently, $M = M_0$ and $N = 0$ when $w = 0$ at the onset of motion. Thus, the plastic flow for a perfectly rectangular plate initiates at corner A of the yield curve, following the trajectory AB of the upper right quadrant as the transverse displacement increases.

For simplicity in the mathematical procedures, the yield curve is bound between the two square yield surfaces (broken lines in Figure 6-1) which circumscribe and inscribe the exact yield condition. The exact mathematical solution is bound between the two yield surfaces. Therefore, the normality requirement dictates that:

$$M = M_0 \text{ and } N = N_0 \tag{6-4}$$

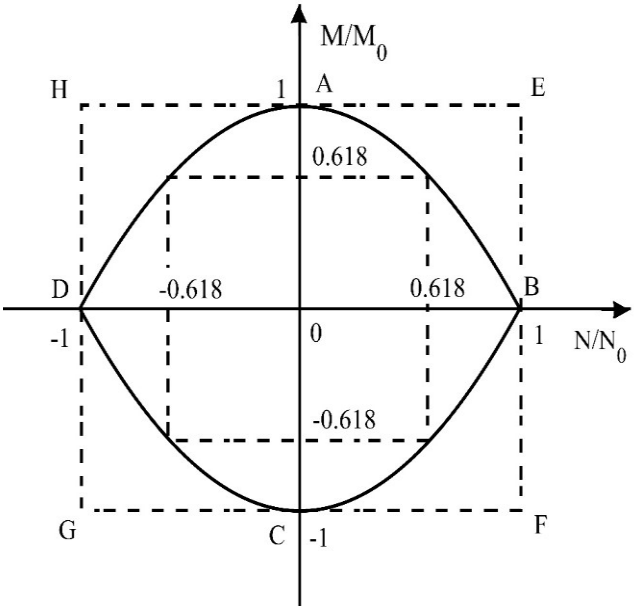

Figure 6-1. Exact yield curve of the plate, vs. the circumscribing and inscribing yield curves (broken lines)

The assumed isotropic hardening in the constitutive formulation is accounted for by replacing the yield stress with the average of the material initial yield and ultimate tensile stresses. It may be possible to have a kinematic hardening formulation or a combination of isotropic and kinematic hardening to incorporate the Bauschinger effects. However, in the context of rigid-perfectly plastic constitutive formulation there is no difference between the two and the simple idealisation adopted here serves the purpose.

6.4 GOVERNING EQUATIONS

6.4.1 Principle of virtual velocities

Consider an arbitrarily shaped surface element bound by an oriented closed path in Cartesian Coordinate system. Using Green's theorem, the equation of motion in its force vector field is converted into functional of energy conservation, wherein the total internal energy rate $\dot{\mathcal{D}}$ dissipated at the continuous velocity fields, at the plastic hinges and within the plastic zones, is equilibrated with the external work rate $\dot{E}$. For an arbitrarily shaped plate (and beams as special case) when the shear stain and rotatory inertia effects are ignored [35], [94], [168], it reads:

$$\int_A (p(x,y,t) - \mu\ddot{w})\,\dot{w}\,d\bar{A} = \int_A (M + Nw)\dot{\kappa}\,d\bar{A} + \sum_{m=1}^{n} \int_A (M + Nw)\dot{\theta}_m dC_m + \sum_{u=1}^{v} Q(\dot{w})_u dC_u \tag{6-5}$$

the over dot notation denotes differentiation with respect to time. In Eqn. (6-5), $\bar{A}$ denotes the elemental area, μ is the mass per unit surface area and $p(x, y, t)$ is the pressure field function. The expressions on the left-hand side represent the external work rate, the first term being work due to pressure field and the second term due to Lagrange-D'Alembert principle's inertia force, while the first term on the right-hand side is the strain energy dissipated in a continuous deformation field, the second term is the energy dissipated at m discrete plastic hinges of length C_m, each having an angular velocity of $\dot{\theta}_m = (\partial \dot{w}/\ dx_i)_m$, where x_i is the characteristic general coordinate in direction of the hinge line. The last term on the right-hand side is the energy dissipated in ν transverse shear hinges, each of length C_u and having a velocity discontinuity of $\dot{w}_u$. In this work, the final term may be ignored in the analyses since the transverse shears would not intrinsically affect the response of membranes [118], [162].

6.5 DEFORMATION PATTERNS

The dynamic response in terms of generalised deformations in a rigid, perfectly plastic structure is represented by evolution of plastic bending or shearing hinges. These hinges-either moving or stationery- are essentially discontinuity interfaces due to rotation (the bending hinge) or transverse shear strains (shearing hinge) leading to deformation localisations. At this weak discontinuity interfaces, the kinematic continuity of motion and the conservation of momentum must be fulfilled. In thin membranes, the thickness is of a small order of magnitude compared to the characteristic in-plane lengths, the transverse shear forces may be assumed inconsequential as opposed to significant membrane forces. Thus, the deformation localisation is characterised by bending hinges only.

The herein constitutive laws examine the plastic flow corresponding to circumstances as (i) an interactive yield surface due to combined bending and membrane action, and (ii) a yield curve where membrane forces are sufficiently large to solely govern the overall behaviour of the plate.

Considering first a rectangular plate of length $2L$ and width $2B$, the current approach entails two possible velocity profiles (A) and (B) as illustrated in Figure 6-2. Pattern (A) conforms to the stationery bending hinges while the length of bending hinge in pattern (B) is time dependent. Using the classical theory of plates, that a critical value of the load was found in Eqn. (5-40) beyond which the static admissibility associated with stationery hinges (pattern (A)) is violated.

Clearly, due to the severity of blast load, in the plates undergoing finite displacements, a transient phase in deformation profile would be induced [103], [104]. It may be assumed that the same static admissibility condition dictates the structures undergoing large deflections. Thus, it may be assumed that each pattern corresponds to a special velocity profile as follows:

i. Profile (1): Small deflection theory, giving rise to Pattern (A) with a stationery plastic hinge (Figure 6-3). The deformations are large enough to induce membrane forces. However, the response due to the build-up of membrane forces remains within the bounds of the critical overloading factor.

ii. Profile (2): the circumstances where the deformation is characterised by an incipient pattern (B) with the velocity profile illustrated in Figure 6-4, which progresses into that of Figure 6-5 and ultimately assumes the final form of pattern (A). Such a phenomenon that the hinge travels under a steady dynamic loading reflects the effect of large deflection theory [104].

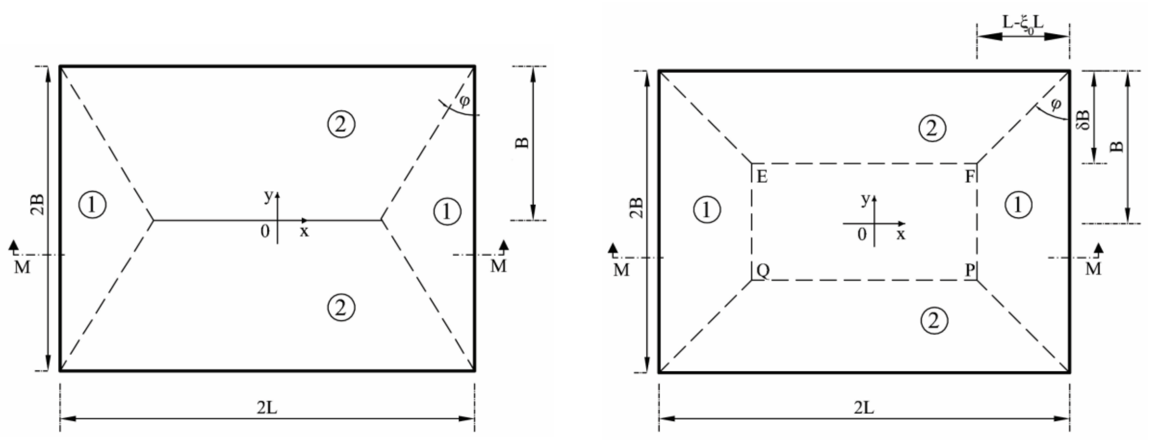

(A) (B)

Figure 6-2. Velocity profile patterns of the plate due to (A) infinitesimal transverse deflections, (B) large transverse deflections

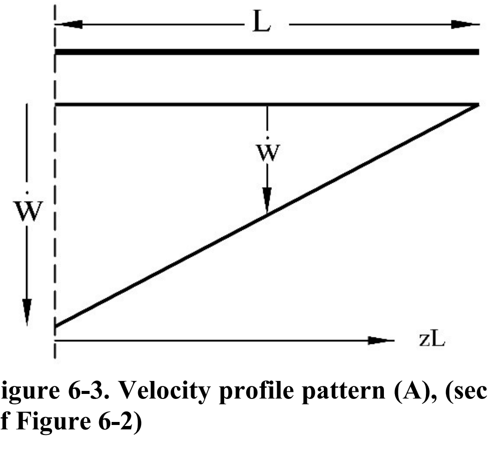

Figure 6-3. Velocity profile pattern (A), (section M-M of Figure 6-2)

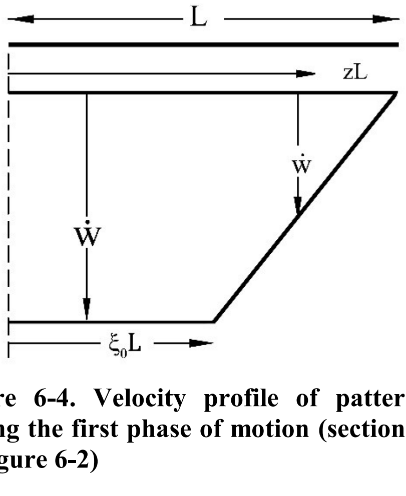

Figure 6-4. Velocity profile of pattern (B) during the first phase of motion (section M-M of Figure 6-2)

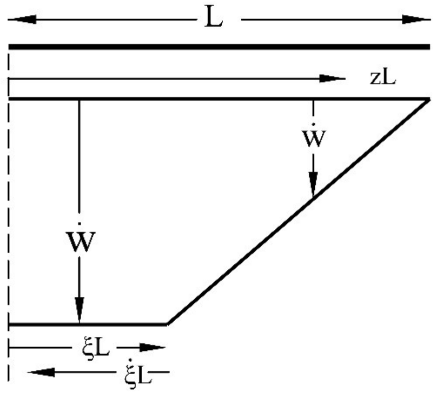

Figure 6-5. Pattern (B) velocity profile during the second phase of motion

Associated with Pattern (B) velocity profile, three distinct phases are sketched, namely phase (i) onset of loading, phase (ii) occurrence of a transient phase with travelling plastic hinge lines which move inward towards the plate centre with incipient deformation and phase (iii) the final phase of deformation. In the first phase, the transverse velocity profile may be written in the form:

$$\dot{w} = \frac{\dot{W}(L - x)}{L - \xi_0 L} \quad x > \xi_0 L \tag{6-6}$$

In zone 1 and

$$\dot{w} = \frac{\dot{W}(B - y)}{\delta B} \tag{6-7}$$

In zone 2. The velocity profiles in each zone are and kinematically admissible. The velocity profile of pattern (A) is recovered from Eqn.s' (6-6)-(6-7) by choosing $\delta B = B$ and eliminating ξ_0. The rotational velocities in each zone simplify to Eqn.s' (6-8a-c), when the shearing angle at the point along the centre line of the plate is ignored, i.e.:

$$\dot{\theta}_1 = -\frac{\partial \dot{w}}{\partial x}, \dot{\theta}_2 = -\frac{\partial \dot{w}}{\partial y} \text{ and } \dot{\theta}_3 = \dot{\theta}_1 \cos(\phi) + \dot{\theta}_2 \sin(\phi) \tag{6-8a-c}$$

where $\dot{\theta}_3$ is the rotational velocity along the plastic hinge at the intersection of zone 1 and zone 2, as plotted in Figure 6-6. If the plate is square, $\phi = \pi/4$ as in Figure 6-2, then both of its diagonals construct the plastic hinge lines. The dimensionless number defining the size of the rigid zone is given by ξ_0, while $\delta B = L(1 - \xi_0)$ and $B = L$ in such plates. Thus, the velocity profile of pattern (B) would take a conical shape and recast into

$$\dot{w} = \frac{\dot{W}(1-z)}{(1-\xi_0)} \tag{6-9}$$

which satisfies the Dirichlet boundary conditions. The parameter z in Eqn. (6-9) represents the auxiliary coordinate of the square plate whose diagonals lie on the Cartesian Coordinate axes as presented in Figure (5-4) (b). Given the deformation field in a rigid plated system along the equipotential surfaces has the same magnitude (e.g. the path EFGH in Figure (5-4) (a)), it may be assumed that the theoretical treatment with load defined by polar coordinate (*r*) is identical to the plate in , whose diagonals construct the plastic hinge lines.

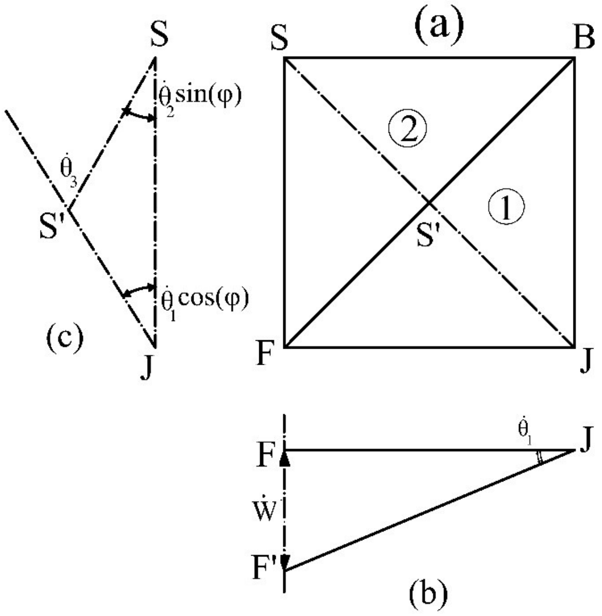

Figure 6-6. Profile of the plate at intersection of zone 1 and 2. (a) top view, (b) front section (c) profile at section SJ

Substituting Eqn.s' (6-4), and (6-6)-(6-9) into Eqn. (6-5), the internal energy rate of pattern (B) was derived as:

$$\dot{\mathcal{D}} = \frac{\left(2H + 4W(1-\xi_0)\right)\dot{W}M_0}{H(1-\xi_0)} \tag{6-10}$$

6.6 DYNAMIC PLASTIC BEHAVIOUR OF CASE 1 THIN PLATES: PATTERN (A)-

6.6.1 Phase 1 of motion ($t \leq \tau$)

The dynamic velocity field represented a roof shape profile identical to that due to the static velocity field which is illustrated in Figure 6-3. However, the velocity profile is now time dependent, which separates the motion into two distinct phases, i.e. phase (i) initial deformations at the onset of loading, and phase (ii) final phase associated with the residual deformations to dissipate the reserved kinetic energy.

With reference to the circumscribing yield curve, the plastic flow is assumed to initiate at corner E of the circumscribing yield surface of Figure 6-1. The internal energy dissipation rate is distinguished from Eqn. (6-10) given $\xi_0 = 0$, while the external energy rate reads as:

$$\dot{E} = L^2 \left[\int_0^{\frac{r_e}{L}} \left(p_0 - \mu \ddot{W}(1-z) \right) \dot{W}(1-z) z dz + \int_{\frac{r_e}{L}}^{1} \left(p_0 a e^{-bLz} - \mu \ddot{W}(1-z) \right) \dot{W}(1-z) z dz \right] \tag{6-11}$$

By evaluating Eqn. (6-11) and performing the integrations on the dynamic energy equilibrium equation, Eqn. (6-1) may be recast in terms of an ODE as:

$$A_1 \ddot{W} + B_1 W + d_1 = 0 \tag{6-12}$$

$$A_1 = \frac{-1}{6} \mu L^2 \tag{6-13}$$

$$B_1 = \frac{-4M_0}{H} \tag{6-14}$$

$$d_1 = 2M_0(\eta - 1) \tag{6-15}$$

where $\eta = p_0/p_c$ is the load amplification factor, provided the static plastic collapse is given by $p_c = M_0/\beta L^2$. The solution of the Eqn. (6-12) is expressed as:

$$W_1(t) = \frac{1}{2} H(\eta - 1)(1 - \cos(\omega_1 t)) \tag{6-16}$$

where the subscript denotes the phase of response and $\omega_1 = \left\{ \frac{24M_0}{\mu L^2 H} \right\}^{0.5}$ hereinafter referred to as the pulse factor. Clearly, $\omega_1^2 = B_1/A_1$. The form of Eqn. (6-16) may be obtained by ensuring the initial kinematic conditions, viz. $W_1(0) = 0$ and $\dot{W}_1(0) = 0$ are satisfied at the onset of loading to obtain the ODE constants.

6.6.2 Final phase of motion ($t \geq \tau$)

A transition from phase 1 to phase 2 occurs as the magnitude of the blast annihilates at the target interface. The motion is characterised merely by the inertia effects; however, the expressions (6-12) -(6-15) still govern the response during the second phase of motion. Thus, by evaluating the ODE parameters in Eqn. (6-12), the transverse displacement field and its time derivatives are derived as:

$$\frac{\ddot{W}_2}{H} = \frac{\omega_1^2}{2}\left\{(\eta - 1)\cos(\omega_1 t) - \eta\cos\big(\omega_1(t-\tau)\big)\right\} \tag{6-17}$$

$$\frac{\dot{W}_2}{H} = \frac{\omega_1}{2}\left\{sin(\omega_1 t)(\eta - 1) - \eta sin\big(\omega_1(t-\tau)\big)\right\} \tag{6-18}$$

$$\frac{W_2}{H} = \frac{-1}{2}\left\{(\eta - 1)\cos(\omega_1 t) \; - \eta\cos\big(\omega_1(t-\tau)\big) + 1\right\} \tag{6-19}$$

The ODE solution constants are obtained by imposing the continuity conditions i.e. by enforcing the same kinematic admissibility of the transverse deformation field and its time derivatives at $t = \tau$. This phase terminates when the plate has lost all its momentum at time T_2, as shown in (6-20), evaluated from $\dot{W}_2 = 0$. As the analyses are conducted within the framework of rigid-plasticity rather than elasto-plasticity, no residual vibration occurs, and maximum and permanent deflection fields are identical.

$$T_2 = \frac{1}{\omega_1}\arctan\left(\frac{\eta\sin\omega_1\tau}{1 + \eta(\cos(\omega_1\tau) - 1)}\right) \tag{6-20}$$

Substituting Eqn. (6-20) in Eqn. (6-19) yields the permanent transverse deformation as:

$$\frac{W_f}{H} = \frac{1}{2}\left(\sqrt{4(\eta^2 - \eta)\sin^2\frac{\omega_1\tau}{2} + 1} \; - 1\right) \tag{6-21}$$

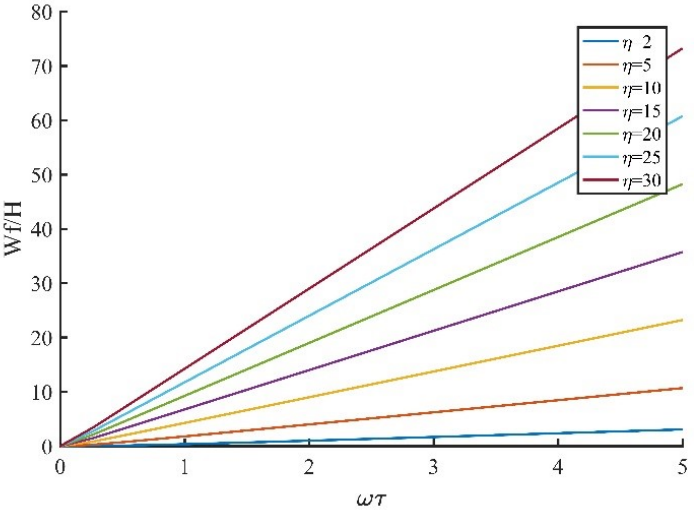

Figure 6-7. Variation of the normalised permanent (maximum) deflections with ω_1

Provided the plate has a prismatic section, it turns out that $\omega_1 = \sqrt{\frac{6\sigma_0}{\rho L^2}}$ depends only on the material properties σ_0 and ρ and side length L , thus its practical limits may be established. For example, given a monolithic ductile plate of $\rho = 7850\ Kg/m^3$, σ_0 varying between $300MPa$ for mild steel to $1210MPa$ for RHA steel, and the characteristic in-plane dimensions of prototype structures typically in the range of minimum $L = 0.2m$ to the maximum of $L = 2m$, the magnitude of ω_1 is typically restrained as $2185\ rad.s^{-1} \leq \omega_1 \leq 5000\ rad.s^{-1}$ for the structural elements of minimum characteristic lengths, while ω_1 assumes the range of $218\ rad.s^{-1} \leq \omega_1 \leq 480\ rad.s^{-1}$ associated with the large armour plate lengths. The pulse duration typically varies between $20\mu s$ for localised blasts to $200\mu s$ for distal blast loads. Hence, the range of $\omega\tau$ is restrained to values between 0.005 and 5. The influence of this parameter against the permanent deformation is plotted in Figure 6-7.

6.7 DYNAMIC PLASTIC BEHAVIOUR OF CASE 1 THIN PLATES: PATTERN (B)

6.7.1 First phase of motion ($t \leq \tau$)

A progressively severe blast in some cases would force the structural system to undergo a transition state in the deformation history to ensure the rate of strain energy dissipated in the plate at every instant of time equates the rate of external work done. The velocity profile in such circumstances needs to be modified into that assumed in pattern (B). This profile, during the first phase, is characterised by formation of a central incipient plastic hinge of length (ξ_0) because of large deflections. As the blast pressure is distributed throughout the structure, this plastic hinge travels toward the centre. It is further assumed that $\xi_0 > r_e/L$. With reference to the velocity profile in Eqn.s' (6-9) and (6-6), the total external energy rate is compiled as:

$$
\begin{aligned}
\dot{E} = 2L^2 \Bigg[& \int_0^{\omega_0} (p_0 - \mu \ddot{W}) \dot{W} z dz + \int_{\omega_0}^{\xi_0} (p_0 a e^{-bLz} - \mu \ddot{W}) \dot{W} z dz \\
& + \int_{\omega_0}^{1} \left(p_0 a e^{-bLz} - \frac{\mu \ddot{W}(1-z)}{1-\xi_0} \right) \frac{\dot{W}(1-z)z}{1-\xi_0} dz \Bigg]
\end{aligned}
\tag{6-22}
$$

where $\omega_0 = r_e/L$. Evaluating the integral and performing the analysis on the energy equilibrium, the expressions of the deformation fields boil down to an ODE as:

$$
A_2 \ddot{W} + B_2 W + d_2 = 0 \tag{6-23}
$$

where the parameters of this expression are obtained as:

$$
A_2 = \frac{-1}{6} \mu L^2 (3\xi_0^2 + 2\xi_0 + 1) \tag{6-24}
$$

$$
B_2 = \frac{4M_0(\xi_0 + 1)}{H(\xi_0 - 1)} \tag{6-25}
$$

$$
\begin{aligned}
d_2 = & \frac{2M_0 \eta \big((Lb\xi_0 + 2) e^{-b(L\xi_0 - r_e)} - (Lb + 2)\,\mathrm{e}^{-b(L - r_e)} + Lb[(b^2 r_e^2 + 2\,br_e + 2)(\xi_0 - 1)/2] \big)}{\beta(\xi_0 - 1)L^3 b^3} \\
& + \frac{2M_0}{\xi_0 - 1}
\end{aligned}
\tag{6-26}
$$

Eqn. (6-23) is a non-homogeneous, second order ODE with constant coefficients, which has a solution of the form:

$$
W_1 = \frac{d_2}{B_2} \{\cos(\omega t) - 1\} \tag{6-27}
$$

$$
\omega = \sqrt{\frac{B_2}{A_2}} \tag{6-28}
$$

And the form of Eqn. (6-27) is obtained by satisfying the initial conditions $W(0) = \dot{W}(0) = 0$.

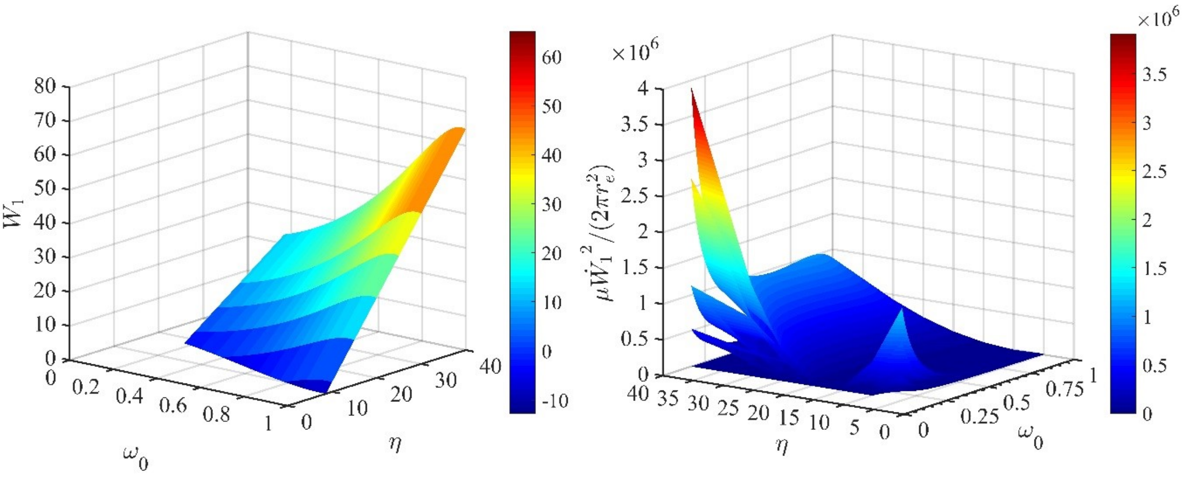

(a) (b)

Figure 6-8. The manifold of Velocity field during the first phase (a), Kinetic energy states at the end of phase 1 due to various load magnitude, where $L = 150mm, H = 4mm, \rho = 7850, \sigma_0 = 1100MPa, \xi_0 = 0.89$ (b)

The dependence of the initial velocity (and thus initial kinetic energy) on the load magnitude and radius is presented in Figure 6-8. The kinetic energy is mostly absorbed through the portion of the target that is affected by the blast load. The ordinate in Figure 6-8 (b) represents the kinetic energy density, or the kinetic energy per unit area of the central blast zone. For the central zone radii of the load beyond half the target length, the variation of this energy is smooth, while the blast emanating from the charge diameter to total target length of 0.25 is more plausible to cause tensile tearing, capping, and perforation through the plate. Furthermore, assuming a linear relationship between the central blast radius r_e and the geometry of the explosive as is done by researchers [22], [27], and with *a priori* knowledge of the blast pressure associated with certain mass of explosive disc, the more catastrophic threat scenarios are associated with explosives of lower radii and higher charge height than those of higher charge diameters and less height.

Clearly, as illustrated in the Figure 6-9 and Figure 6-10, pulse factor is also influenced by loading distribution. For proximal blasts, the pressure is concentrated at the localised region of the target centre ($\omega_0 \ll 1$) and decays instantly as it stretches over the target. The decay exponent of typical localised blasts varying between $50 \leq b \leq 120$ [22], [27]. The increase in the load decay exponent (b) would result in a reduction of the pulse factor, but increased central deformation. In contrast, uniform pressure loads assume larger values of the pulse factor as r_e increases while b decreases. Critical influence of the pulse factor on the load emerges when the length of the incipient plastic hinge appears at 0.9th of the characteristic plate length. Thus, it is necessary to accurately determine the position of the incipient plastic hinge in the plated systems undergoing the transition state.

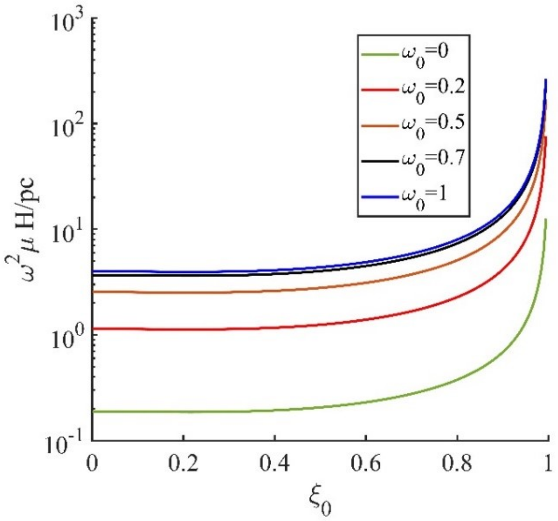

Figure 6-9.Variation of the normalized pulse factor with incipient plastic hinge due to load radius

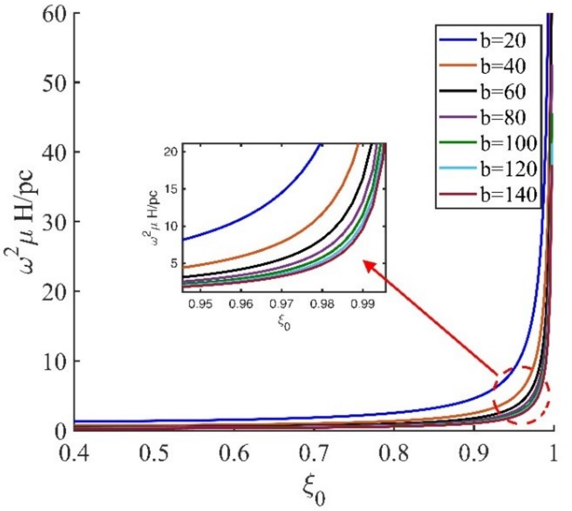

Figure 6-10- -Variation of the normalized pulse factor with incipient plastic hinge due to load decay exponent

However, the incipient plastic hinge emerges at the early phase response before the membrane state is reached [35]. By eliminating the membrane terms in Eqn. (6-5) and performing some straightforward calculations, the form of Eqn. (6-23) boils down to a function of the overload factor and incipient plastic hinge as:

$$f(\eta, \gamma') = \eta\gamma' - 12L^3 b^3 \beta = 0 \qquad \textbf{(6-29)}$$

Which is similar to and defined by Eqn. (5-51)-(5-52).

The exact solution of Eqn. (6-29) is complex due to the presence of the highly nonlinear terms and can be evaluated by numerical approaches. In the case of the static collapse, i.e. $\eta = 1$, no real root of this equation is found, confirming that the deformation to assume is as pattern (A). This is evident as in the case of static loads pattern (A) yields a lower upper bound for static plastic collapse, thus the central plastic zone will not form in the system.

The influence of overloading factor for a range of loading parameters is presented in Figure 6-11. Clearly, the length of the central zone increases with the radius of the load. In the uniform load scenario, $\xi_0 = 1$, the incipient plastic bending hinge occurs directly at the edges.

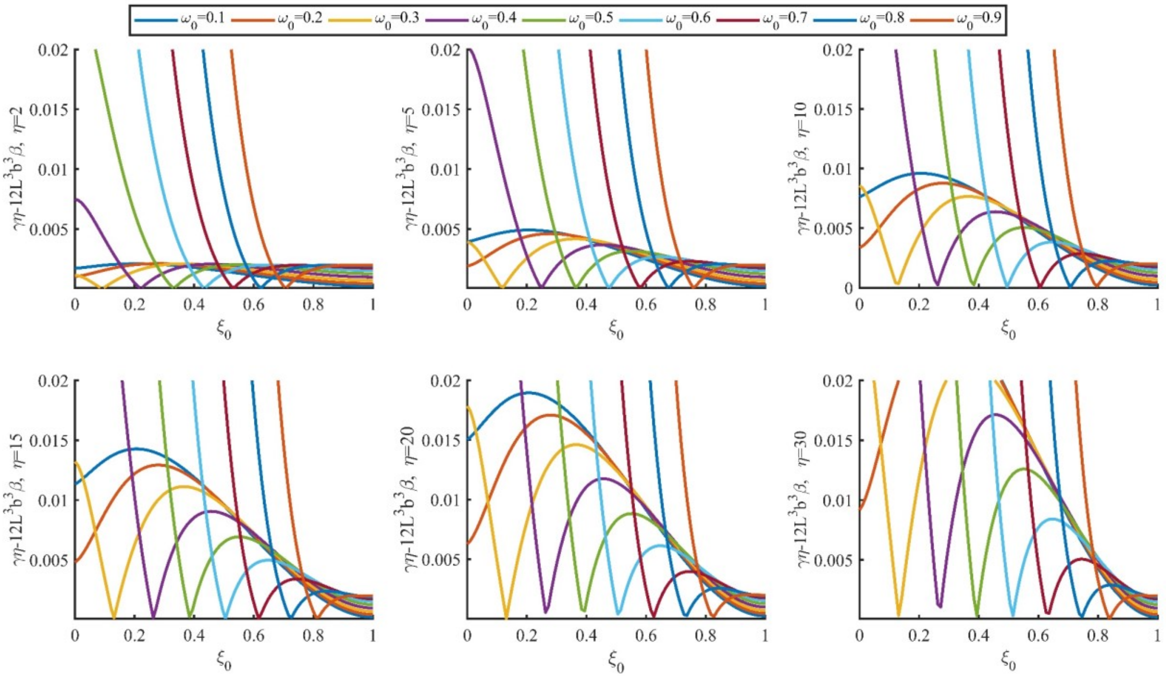

Figure 6-11. Evaluating the length of central plastic bending hinge length

6.7.2 Second phase of motion $\tau \le t \le T_1$

The mathematical procedure was carried out in an analogous manner to that of pattern (A). Since no shearing forces at hinge lines of the central zone occurs (i.e. $Q_i = \frac{\partial M_i}{\partial i} = 0$ because $M = M_0$, with i being the characteristic coordinate) and the membrane forces remain in plane parallel to the initial mid-plane of the plate [104], it follows that:

$$\mu\ddot{W}_2 = 0 \qquad \textbf{(6-30)}$$

Thus, the potential energy in the system eliminates, at the instant of sudden load removal, but some kinetic energy is reserved within the system, with an associated constant transverse velocity field that drives the motion to continue. The plastic hinge is, now, an active time dependent one traveling inward. The occurrence of this bending hinge is attributed with reduction in the dissipated energy. Provided $\xi \ge r_e/L$, the external energy rate consists of the convective derivative components of transverse velocity field, given by the expression

$$\dot{E} = 2L^2\left[\int_0^{\omega_0}(p_0 - \mu\ddot{W}_2)\dot{W}_2 z dz + \int_{\omega_0}^{\xi}(p_0 a e^{-bLz} - \mu\ddot{W}_2)\dot{W}_2 z dz + \int_{\xi}^{1}\left(p_0 a e^{-bLz} - \frac{\mu\ddot{W}_2(1-z)}{1-\xi} - \frac{\mu\dot{W}_2\dot{\xi}(1-z)}{(1-\xi)^2}\right)\dot{W}_2 z\left(\frac{1-z}{1-\xi}\right)dz\right] \qquad \textbf{(6-31)}$$

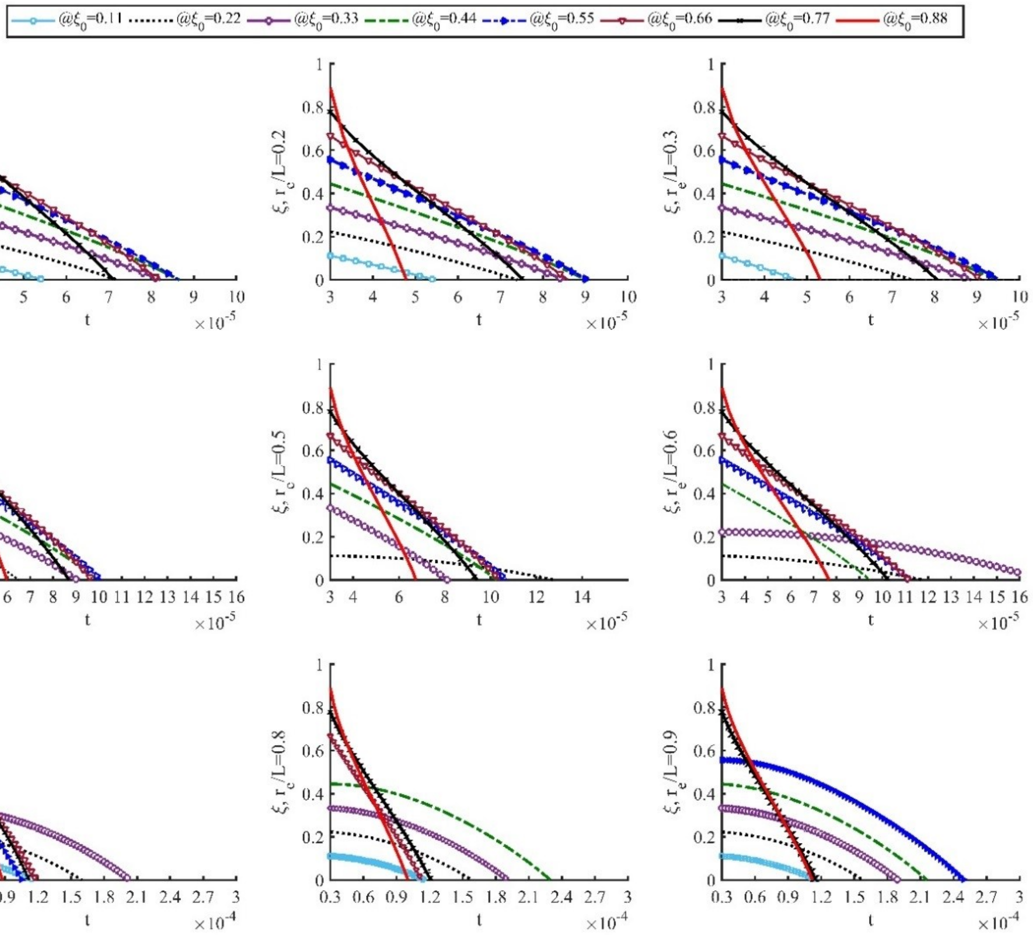

Figure 6-12. Determination of duration of the second phase of motion for various values of r_e , b=100 and $\eta = 10$, $\sigma_0 = 1210MPa$, $H = 4mm$ and $L = 0.2$

where $\omega_0 = r_e/L$ and the terms of transverse inertia may be eliminated to yield $\dot{E} = -\frac{1}{2}\dot{W}_2^2\left(\xi + \frac{1}{3}\right)\dot{\xi}L^2\mu$. The size of the central zone decreases monotonically while moving transversely and ultimately vanishes at time T_1. A time integration of the Eqn. (6-30) furnishes the maximum plastic transverse deformations into Eqns. (6-32), (6-33). The constants of integration are obtained by ensuring the kinematic conditions of displacement and velocity fields at the instant of load completion, while the constants A_2 and d_2 are defined previously in Eqns. (6-24)-(6-26).

$$\mu\dot{W}_2 = \frac{-d_2\sin(\omega\tau)}{\omega A_2} \quad \textbf{(6-32)}$$

$$\mu W_2 = \frac{d_2}{\omega^2 A_2}[\omega\sin(\omega\tau)(\tau - t) + \cos(\omega\tau) - 1] \quad \textbf{(6-33)}$$

Eqns. (6-30)-(6-33) should satisfy the constitutive equation of motion and the energy equilibrium outlined in Section 6.4.1. With reference to Eqn. s’ (6-31) and (6-10) and by using Eqns. (6-32), and (6-33), Eqn. (6-30) is recast an ODE as:

$$f\left(t,\xi,\dot{\xi}\right) = \frac{1}{6}\left(\frac{\mu L^2 d_2}{A_2\omega}\right)(3\xi+1)(\xi-1)\dot{\xi} + 2M_0 - \frac{4M_0 d_2(\xi+1)(\omega\sin(\omega\tau)\,(t-\tau)-\cos(\omega\tau)+1)}{A_2\omega^2 H} = 0 \qquad \textbf{(6-34)}$$

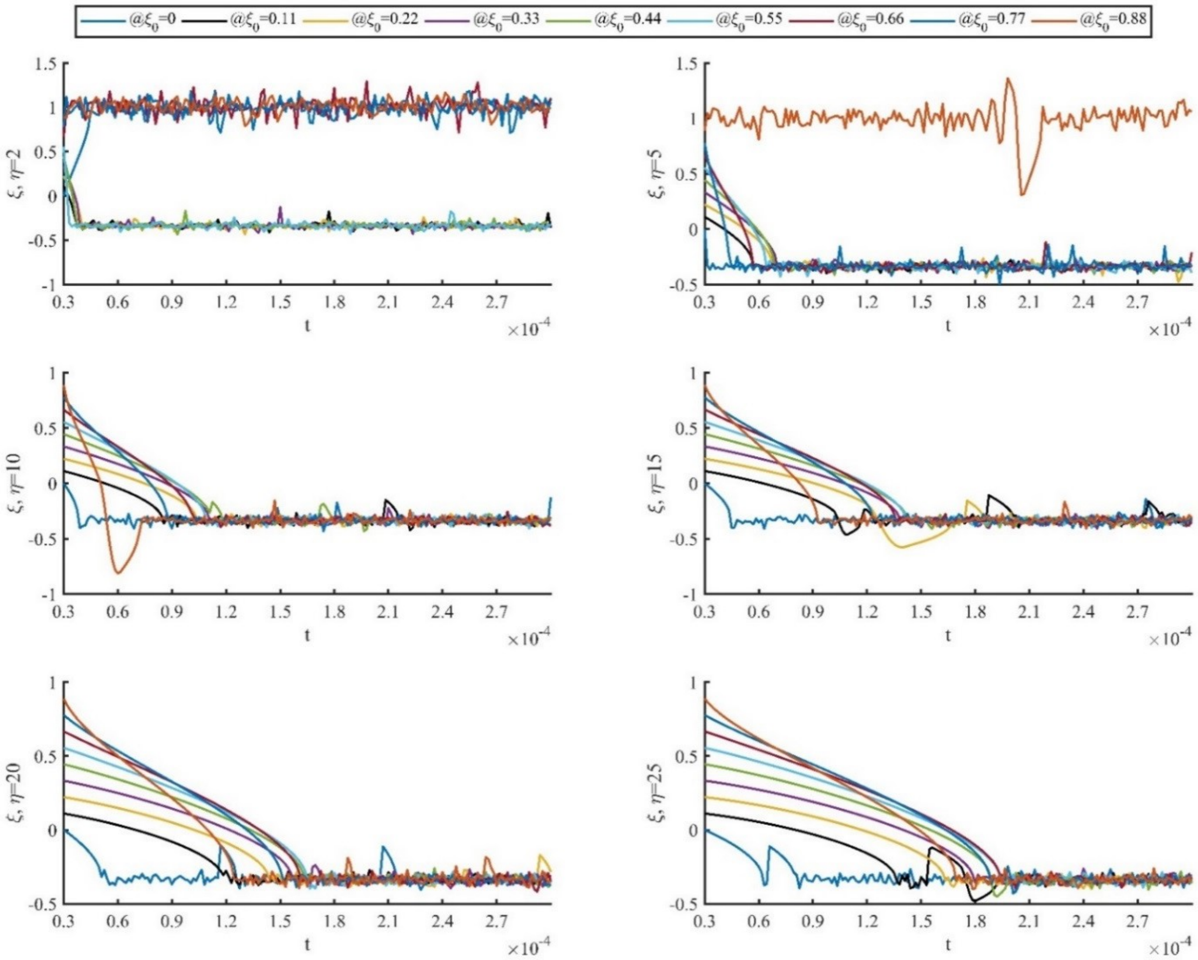

Figure 6-13. Determination of duration of the second phase T_2 of motion for various values of load dynamic amplification factor, $\sigma_0 = 1210$, H=4mm b=100 $\omega_0 = 0.12$

This equation is solved numerically by 5th order Runge-Kutta method embedded in MATLAB®, whereby the length of the active plastic hinge at any time is determined. The solutions to the ODE for various values of ξ_0 are compared in Figure 6-12-Figure 6-13, where a load duration of $\tau = 30\mu s$ for various load amplification factors was assumed. Indeed, the transient phase maintains for a time duration of T_2 until the plastic hinge length in ODE of Eqn. (6-34) vanishes. In the circumstances where no real solution of this ODE is found, commonly occurring when $\omega_0 \ll 1$ and $\xi_0 \ll 1$, the response may be governed by pattern (A) of motion.

While it may not be straightforward to investigate the static admissibility of pattern (B), it is evident that Eqn.s' (6-27), (6-30)-(6-33) are kinematically admissible. The theoretical solution is exact when the generalised stress field is statically admissible and the associated velocity field is kinematically admissible.

6.7.3 Third Phase of Motion $T_2 < t < T_3$

Phase 2 terminates as the in-plane motion of the plastic hinge line ceases at time T_2. Now, due to the reserved kinetic energy remaining from the previous deformation, the inertia is induced which marks a transition to phase 3, until all the residual kinetic energy is dissipated before the plate comes at rest. Thus, the plate profile develops from pattern (B) to that of the pattern (A) with inertia term characterised by Eqn. (6-17). The succeeding expressions of the transverse velocity and transverse deformation are recovered from successive time integrations of Eqn. (6-17). The integration constants in these expressions are found by ensuring the kinematic continuity conditions at $t = T_2$. The final form of the deformation fields may be written as of Eqns. (6-35) and (6-36).

$$\begin{aligned}\frac{\dot{W}_3}{H} = \frac{\omega_1}{2}\{\eta\left[\sin\left(\omega_1(T_2-\tau)\right)-\sin\left(\omega_1(t-\tau)\right)\right]+(\eta-1)(\sin(\omega_1 t)-\sin(\omega_1 T_2))\}\\ -\frac{d_2\sin(\omega\tau)}{A_2\omega H}\end{aligned} \tag{6-35}$$

$$\begin{aligned}\frac{W_3}{H} = \frac{1}{2}\omega_1(T_2-t)\{(\eta\ -\ 1)sin(T_2\omega_1)-\ \eta sin\left(\omega_1(T_2\ -\tau)\right)\}\\ +\frac{\eta}{2}\{cos\left(\omega_1(t\ -\tau\ )\right)-\ cos\left(\omega_1(T_2\ -\tau)\right)\}\\ +(\eta\ -\ 1)[cos(T_2\omega_1)-cos(\omega_1 t)]+\frac{d_1\sin(\omega\tau)}{A_1\omega H}(T_2-t)\\ -\frac{d_1\{\omega\sin(\omega\tau)\,(T_2-\tau)+\ 1-cos(\omega\tau)\}}{A_1\omega^2}\end{aligned} \tag{6-36}$$

When $\dot{W}_3 = 0$ the plate rests. Defining Γ in Eqn. (6-37), an expression of the final time of the deformation is delineated as per Eqn. (6-38).

$$\Gamma_2\ = \frac{1}{2}H\omega_1\sin(T_2\omega_1)\,(\eta-1)-\frac{1}{2}H\eta\omega_1\sin\left(\omega_1(T_2-\tau)\right)+\frac{d_2\sin(\omega\tau)}{A_2\omega} \tag{6-37}$$

$$T_f\ =\ -\frac{i}{\omega}\ln\left(\frac{2i\Gamma_2 e^{\frac{1}{2}i\omega\tau}\mp\ e^{\frac{1}{2}i\omega\tau}\sqrt{\left(-H^2\omega^2\eta(\eta-1)\left(e^{2i\omega\tau}+1\right)+\left((2\eta^2-2\eta+1)H^2\omega^2-\Gamma_2^2\right)e^{i\omega\tau}\right)}}{\omega H\left((\eta-1)e^{i\omega\tau}-\eta\right)}\right) \tag{6-38}$$

Under the impulsive loading conditions, the expression of the full form permanent deformation in Eqn. (6-36) may be further reduced by assuming the deformation time of phase 1 and 2 are infinitesimal such that $\sin\omega\tau \cong \omega\tau$, $1-\cos\omega\tau \cong \omega^2\tau^2/2$, $\sin\omega T_2 \cong \omega T_2$ and $1-\cos\omega T_2 \cong \omega^2 T_2^2/2$. These assumptions are pertinent to the most cases of localised blasts generated by high explosives, where the loading duration is infinitesimal ($\tau \leq 50\mu s$) compared to the natural period of the structure. Due to the low range of the stand-off, the reflected localised blast pressure induced by the wave front would be dissipated in a more diminutive timeframe than in distal blasts. The Full form of the Eqn. (6-36) may be used for higher accuracy or the longer loading duration is required, in which case the response of the plate can be idealised as quasi-static/dynamic load. In Figure 6-14 the dependence of the permanent deformation on the pulse factor ω is plotted.

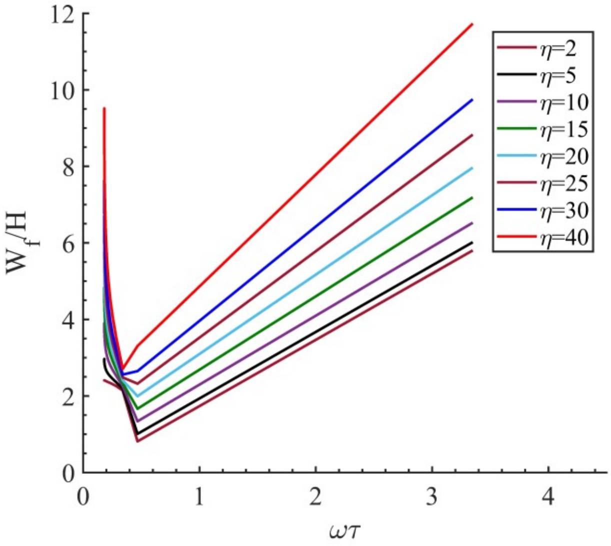

Figure 6-14. Variation of the normalised permanent deflections with $\boldsymbol{\omega}$, where $\boldsymbol{L = 150mm, H = 4mm, \rho = 7850, \sigma_0 = 1100MPa}$,

It is recognised that obtaining an explicit form of the permanent deformation is fraught with difficulty, due to the interdependence of the load parameters, duration of each phase and the plastic hinge lengths, while the increased number of variables brings about complications in the exact theoretical solution, particularly when the visco-plasticity and hardening effects are involved. However, a reduced closed form solution of the permanent deformation may be obtained by neglecting the bending moment contribution in the overall response of the plate as follows.

6.8 SIMPLIFICATION INTO A MEMBRANE

High intensity shock loads give rise to large plastic deformations, to the extent that the influence of finite displacements due to such loads governs the overall response of the structure. In such circumstances, the contribution of the membrane forces alone associated with the finite displacements transcends those of the bending moments and transverse shear effects especially for thick plates. This leads to further simplification of the energy equilibrium expressions as the plastic energy due to bending moment may be essentially neglected; the membrane forces solely govern the response throughout the motion. Thus, the Eqn. (6-5) boils down to

$$\int_A (p(x,y,t) - \mu\ddot{w})\,\dot{w}d\bar{A} = \int_A Nw\dot{\kappa}\; d\bar{A} + \sum_{m=1}^{n} \int_A (Nw)\dot{\theta}_m dC_m \qquad \textbf{(6-39)}$$

the mathematical approach introduced herein is identical to that outlined in Section 6.6, while the terms of M_0 from the internal energy rate vanish. With this simplification in mind, the mathematical treatment is carried out for both patterns of the velocity profile hereunder.

6.8.1 Pattern (A) of motion

In the first phase of motion, Eqn. (6-5) furnishes to

$$\ddot{W}_1 + \omega_1^2 W_1 + d_3/\mathrm{A}_1 \; = 0 \qquad \textbf{(6-40)}$$

where $d_3 = 2M_0\eta$; A_1, ω_1 defined in Section 6.6.1. The ODE of Eqn. (6-40) has a general solution as $W_1 = C_1 \sin(\omega_1 t) + C_2 \cos(\omega_1 t) - \frac{d_3}{\omega_1^2 A_1}$, the constants thereof are determined by ensuring the kinematic conditions at t=0, giving:

$$\frac{W_1}{H} = \frac{\eta}{2}(1 - \cos(\omega_1\, t)) \qquad \textbf{(6-41)}$$

Thus, the expression of the simplified membrane model is similar, but reduced form of, the solution pertaining to the combined bending and membrane, in terms of the ODE constant d_3. This phase continues for a duration of $t = \tau$ when the loading is complete.

In the same spirit to the previous analyses, the dynamic equilibrium equation of the phase 2 leads to:

$$\ddot{W} + \omega_1^2 W \; = 0 \qquad \textbf{(6-42)}$$

which has a closed-form solution as $W = C_3 \sin(\omega_1 t) + C_4 \cos(\omega_1 t)$. Comparing the solution in this phase with the previous phase, while ensuring the kinematic admissibility at $t = \tau$ yields:

$$\ddot{W}_2 = \frac{\eta H \omega_1^2}{2}\left[cos(\omega_1 t) - cos\big(\omega_1(t-\tau)\big)\right] \qquad \textbf{(6-43)}$$

$$\dot{W}_2 = \frac{\eta H \omega_1}{2}\Big(sin(\omega_1 t) - sin\big(\omega_1(t-\tau)\big)\Big) \qquad \textbf{(6-44)}$$

$$W_2 = \frac{\eta H}{2}\Big(cos\big(\omega_1(t-\tau)\big) - cos(\omega_1 t)\Big) \qquad \textbf{(6-45)}$$

This phase terminates at $T_f = \frac{\pi+\omega_1\tau}{2\omega_1}$, while the permanent deformation boils down to:

$$\frac{W_f}{H} = \eta \sin\frac{\omega_1\tau}{2} \tag{6-46}$$

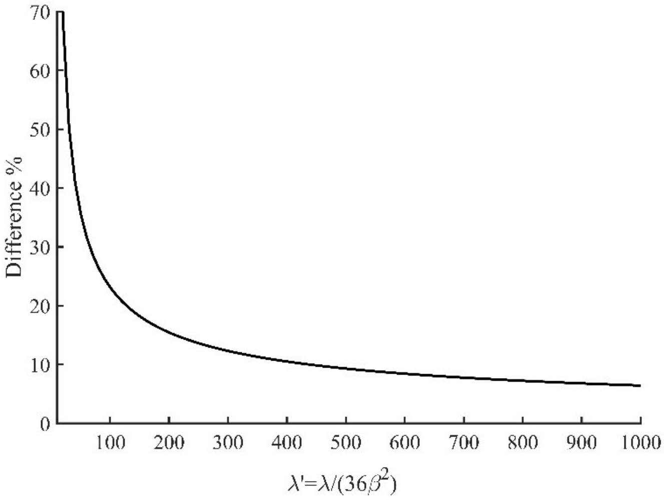

Figure 6-15. The difference between the results of membrane-only and combined bending and membrane analyses

The difference between the two analyses (combined bending and membrane and membrane only) decreases exponentially, giving a smooth variation for high impulse magnitudes. The expression (6-46) yields about only 8% higher overestimation than its counterpart (Figure 6-15).

6.8.2 Pattern (B) of deformation

By compiling the energy equilibrium equation for pattern (B), in the first phase of motion, the foregoing results in Section 6.6.1, i.e., the expressions (6-23)-(6-26) still hold, while the succeeding term $2M_0/(1-\xi_0)$ in Eqn. (6-26) vanishes, viz.:

$$d_4 = \frac{2M_0\eta\big(\,(Lb\xi_0+2)e^{-b(L\xi_0-r_e)} - (\,Lb+2)\,\mathrm{e}^{-b(L-r_e)} + Lb[(b^2r_e^2+2\,br_e+2)(\xi_0-1)/2]\big)}{\beta(\xi_0-1)L^3b^3} \tag{6-47}$$

The deformation at the first phase of motion is:

$$W_1 = \frac{d_4}{B_2}\{\cos(\omega t)-1\} \tag{6-48}$$

where B_2 is defined in Eqn. (6-25). Thus, it is straightforward to show that the foregoing analyses in Sections 6.7.1-6.7.2 persists throughout the first and second phases of motion, the expressions for the displacement field and its time derivative may be merely obtained by replacing d_2 with d_4.

However, the ODE function describing the length of central plastic hinge line now boils down to an explicitly integrable function:

$$f(t,\xi,\dot{\xi}): \frac{1}{6}\mu\omega HL^2(3\xi+1)(\xi-1)\dot{\xi} - 4M_0(\xi+1)(\omega\sin(\omega\tau)(t-1)+1-\cos(\omega\tau)) = 0 \tag{6-49}$$

Using the separation of variables, through a subsequent time integration of Eqn. (6-49) the exact solution for the position of the plastic hinge is found as

$$\begin{aligned} F(t,\xi): 48M_0\left(\omega sin(\omega\tau)\left(\left(\frac{1}{2}\right)t^2 - t\right) + t - cos(\omega\tau)t\right) \\ - [12\mu\omega L^2H\{8ln(\xi+1) - 10\xi + 3\xi^2\} + C_5] = 0 \end{aligned} \tag{6-50}$$

$$\begin{aligned} C_5 = (24\tau\omega(\tau-2)sin(\omega\tau) - 48\tau cos(\omega\tau) + 48\tau)M_0 \\ + \left(-8\mu\omega HL^2 ln(\xi_0+1) - \mu\omega HL^2\xi_0(3\xi_0-10)\right) \end{aligned} \tag{6-51}$$

where the ODE constant C_5 is obtained by ensuring the kinematic continuity of the function $F(t=\tau,\xi=\xi_0)$ at the transition time point $t=\tau$. Since Eqn. (6-49) is a closed-form expression, it is tractable analytically to obtain the end phase of motion. This phase terminates at $t=T_2$ as the length of the central plastic zone vanishes, i.e. $\xi=0$. Thus:

$$T_2 = (1-2\tau) \mp \frac{\sqrt{6}}{12}\sqrt{24(3\tau-1)^2 - (\omega\tau M_0)^{-1}HL^2\mu(3\xi_0^2 + 8ln(\xi_0+1) - 10\xi_0)} \tag{6-52}$$

Provided $\xi_0 \ll 1$, the terms of ξ_0 in the surd may be ignored, then $T_2 \to \tau$ is suggestive of the solution approaches that of pattern (A) as the phase 1 and 2 merge together. While an exact solution to the Eqn. (6-50) at $\xi(t)=0$ exists, for brevity in analysis, the evaluation of T_2 in Eqn. (6-52) is approximated by truncating trigonometric terms into their equivalent Taylor series, i.e. $\sin\omega\tau \cong \omega\tau$, $1-\cos\omega\tau \cong \omega^2\tau^2/2$. The velocity profile of the third phase is given by

$$\frac{\dot{W}_3}{H\omega_1} = \frac{1}{2}\eta\left(sin(T_2\omega_1) - sin\left(\omega_1(T_2-\tau)\right)\right) - \frac{1}{2}\eta\left(sin(\omega_1 t) - sin\left(\omega_1(t-\tau)\right)\right) - \frac{d_4 sin(\omega\tau)}{H\omega_1\omega A_2} \tag{6-53}$$

Which is integrated over time to yield the corresponding dispalcement field, the integration constant is unequivocally derived by imposing the kinematic continuity conditions, in the similar fashion to Section 6.7.3

$$\begin{aligned} \frac{W_3}{H} = \frac{1}{2}\omega_1\eta(T_2-t)\{sin(T_2\omega_1) - sin\left(\omega_1(T_2-\tau)\right)\} \\ + \frac{\eta}{2}\{cos\left(\omega_1(t-\tau)\right) - cos\left(\omega_1(T_2-\tau)\right)\} + \frac{1}{2}\eta[cos(T_2\omega_1) - cos(\omega_1 t)] \end{aligned} \tag{6-54}$$

$$+\frac{d_4\sin(\omega\tau)}{A_2\omega H}(T_2-t)-\frac{d_4\{\omega\sin(\omega\tau)\,(T_2-\tau)+\,1-cos(\omega\tau)\}}{A_2\omega^2}$$

It may be shown that the motion of the plate ceases at time T_f expressed as:

$$T_f=\frac{\left\{\omega_1\tau+2\arccos\left(\cos\left(T_2\omega_1-\frac{\omega_1\tau}{2}\right)-\frac{d_4\sin(\omega\tau)}{HA_2\eta\omega_1\omega\sin\left(\frac{\omega_1\tau}{2}\right)}\right)\right\}}{2\omega_1} \quad \textbf{(6-55)}$$

and the permanent deformation achieved through substitution of Eqn. (6-55) in (6-54).

6.9 IMPULSIVE LOADING

In the case of impulsive loading, the total change in linear momentum equals the total impulse imparted upon the system, hence the conservation of linear momentum yields the impulsive velocity, defined in Eqn. (5-67). The associated permanent deformation of each scenario is furnished in terms of the dimensionless initial kinetic energy λ as follows.

6.9.1 Pattern (A)

The impulsive velocity is evaluated in terms of duration as $\tau=\frac{\beta}{\eta\omega_1}\sqrt{24\lambda}$ as $\sin\frac{\omega_1\tau}{2}\cong\frac{\omega_1\tau}{2}$. Eqn. (6-25) then furnishes to:

$$\frac{W_f}{H}=\frac{1}{2}\left(\sqrt{\frac{24(\eta-1)}{\eta}\lambda\beta^2+1}\,-1\right) \quad \textbf{(6-56)}$$

Provided the response is solely governed by membrane action, and the duration of the load is infinitesimal to the natural period of structure, by using the approximation $\sin\frac{\omega_1\tau}{2}\cong\frac{\omega_1\tau}{2}$, the permanent deformation can be recast in terms of the dimensionless kinetic energy as:

$$\frac{W_f}{H}=\beta\sqrt{6\lambda} \quad \textbf{(6-57)}$$

when $r_e\rightarrow L$, and $\beta\rightarrow\frac{1}{6}$ the Eqn. (6-57) converges to the solution found in the literature [35].

6.9.2 Pattern (B)

The impulsive load case of the plated elements undergoing the travelling bending hinge may be treated in the same fashion as to the case of stationery plastic bending hinges. The dimensionless kinetic energy may now be expressed as:

$$\lambda = \left(\frac{\omega\tau\eta}{\beta}\right)^2 \left\{\frac{-3\xi_0^3 + \xi_0^2 + \xi_0 + 1}{1 + \xi_0}\right\} \tag{6-58}$$

Using the bounds theorems on the exact yield surface (Figure 6-1), the solutions investigated herein inscribe and circumscribe the exact dynamic plastic collapse of membrane as illustrated in Figure 6-16. The solution to the inscribed yield criterion can be obtained by replacing λ with $\lambda/0.618$ in the expressions of each pattern. Clearly, the difference between the two curves is inconsequential where the response is influenced by active bending hinge (Figure 6-16b), highlighting the reliability of the solutions sought hereabove. However, for design applications, given the prescribed charge mass and stand-off, both circumscribing and inscribing curves may be implemented to estimate the response of the metal plates to reduce the estimation errors even further.

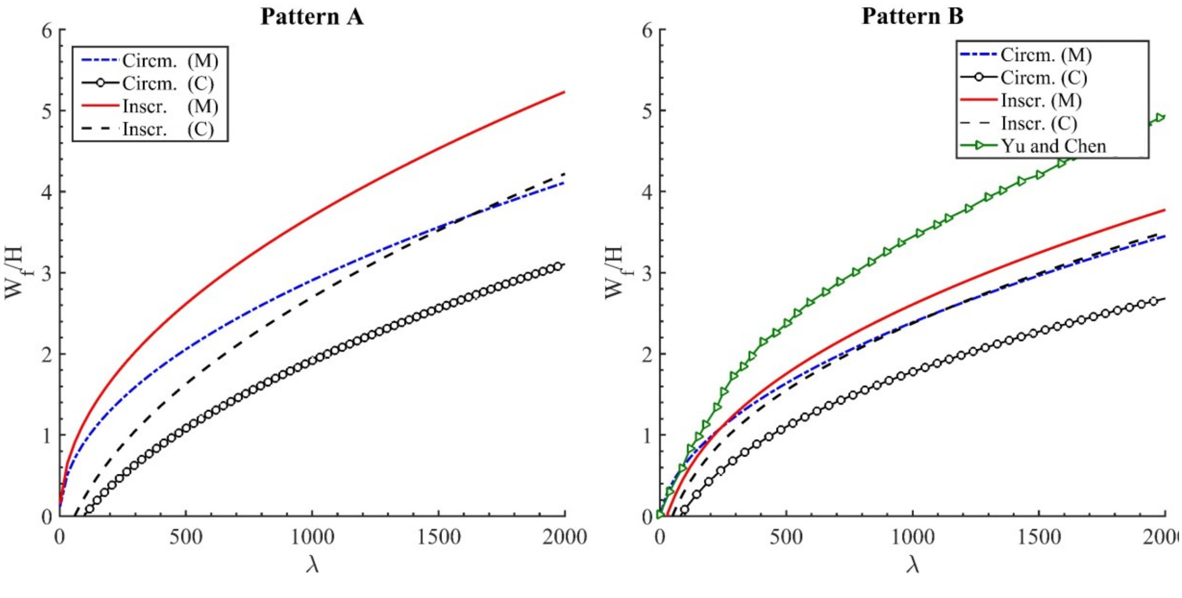

(a) (b)

Figure 6-16. Maximum permanent transverse displacements for various impulse values, with combined bending and membrane effects (C), without bending effects (M) comparison of (a) pattern (A) and (b) pattern (B)

6.10 PLATES OF VARIOUS BOUNDARY CONDITIONS

The dynamic plastic collapse of plates which are secured with various boundary conditions is treated analogously to that of the simply supported plates. In such circumstances, the energy dissipated in the plastic hinge at the plate peripheries corresponding to the fully clamped edges is essentially considered when formulating Eqn. (6-10). This is given by $\alpha_b M_0 \dot{\theta}_2 L$, where $\alpha_b = 1{,}2$ is the half the number of clamped faces. For example, for $\alpha_b = 2$ the panels are fully clamped, while for $\alpha_b = 1$ only the two faces (typically the opposite sides) are clamped. Thus, an additional term of αM_0 would be added to Eqn. (6-26). The deformation of first and second phase of panels for pattern (A) would become:

$$W_1 = \frac{1}{2} H(\eta - 1 - \frac{\alpha_b}{2})(1 - \cos(\omega_1 t)) \tag{6-59}$$

$$W_2 = -\frac{1}{2} H \left\{ \left(\eta - \frac{\alpha_b}{2} - 1\right) \cos(\omega_1 t) - \eta \cos\bigl(\omega_1 (t - \tau)\bigr) + \frac{\alpha_b}{2} + 1 \right\} \tag{6-60}$$

The permanent deformation of the impulsively loaded fully clamped plate with stationery bending hinges is furnished to

$$\frac{W_f}{H} = \left(\frac{2\bar{\lambda}}{3} + 1\right)^{1/2} - 1 \tag{6-61}$$

where $\bar{\lambda} = 9\beta^2 \lambda$. Eqn. (6-61) is analogous to the expressions of fully clamped, uniformly loaded plate found in the literature [35], except with the influence the load shape characteristics modified by the coefficient β.

Similarly, in the case of moving bending hinge, Eqn. (6-27) remains valid, but with d_2 replaced with $\bar{d}$ as:

$$\bar{d} = \frac{2M_0 \eta \Bigl((Lb\xi_0 + 2) e^{-b(L\xi_0 - r_e)} - (Lb + 2)\, \mathrm{e}^{-b(L - r_e)} + Lb[(b^2 r_e^2 + 2\, b r_e + 2)(\xi_0 - 1)/2] \Bigr)}{\beta(\xi_0 - 1) L^3 b^3} + \frac{(2 + \alpha_b) M_0}{(\xi_0 - 1)} \tag{6-62}$$

Eqn. (6-62) indicates the ODE function $f\left(t, \xi, \dot{\xi}\right)$ in (6-49) is increased by αM_0. The permanent deformation due to the increased strain energy dissipated in the supports is expressed as:

$$\begin{aligned} W_3 = &\frac{1}{2} H\eta\{\cos(\omega_1(t-\tau)) - \cos(\omega_1(\bar{T}_2-\tau))\} \\ &+ \frac{1}{4} H\omega_1(t-\bar{T}_2)\left[\sin(\omega_1\bar{T}_2)\,(\alpha_b + 2 - 2\,\eta) + 2\eta\sin(\omega_1(\bar{T}_2-\tau))\right. \\ &\left. - 4\bar{d}\frac{sin(\omega\tau)}{A_2 H\omega\omega_1}\right] + \frac{1}{4} H(\alpha_b + 2 - 2\eta)\{\cos(\omega_1 t) - \cos(\omega_1\bar{T}_2)\} \\ &- \frac{\bar{d}(\omega(\bar{T}_2-\tau)\sin(\omega\tau) - \cos(\omega\tau) + 1)}{B_2} \end{aligned} \tag{6-63}$$

where $\bar{T}_2$ is the duration of the second phase of motion to be determined by numerical methods, in the same spirit as in Section 6.7.2.

6.11 STRAIN RATE SENSITIVITY (VISCO-PLASTICITY)

The scope of analysis in Sections 6.9 may be extended to encompass the strain-rate sensitivity effects of materials. Plastic hinges cannot develop in a strain rate sensitive material because an infinitely large strain would occur at a plastic hinge which would give rise to infinitely large stresses [105]. Thus, similar to the that of Jones [105] on the response of uniformly loaded circular and rectangular ductile metallic plates, the results here represent a modal solution, but with the localised effects retained in the study.

Perrone and Bhadra [170] presented an approximation method to approximate the influence of strain rate sensitivity using a mass connected by strings on either side. The system was loaded with uniform impulsive velocity $V_1 = V_0/\epsilon_1$ to incur large inelastic deformation such that the influence of finite displacement was retained in the study. The authors observed that the maximum strain rate is reached when half of the kinetic energy is dissipated, i.e. at $V_1/\sqrt{2}$, at which point the transverse deformation reached two third of the permanent deformation. The strain rate was halved to estimate for the average strain rate.

Using this approximation and considering the strain as $\varepsilon_x \cong (\partial w/\partial x)^2/2$ or $\varepsilon_y \cong (\partial w/\partial y)^2/2$ (ignoring the in-plane displacements), the strain rate, e.g. in zone I of pattern (A), is $\dot{\varepsilon}_x \cong W\dot{W}/L^2$, or $\dot{\varepsilon}_x = (1/2)(2W_f/3)(V_1/\sqrt{2})/L^2$ and the average equivalent strain rate, assuming $\dot{\varepsilon}_e \cong (\varepsilon_x + \varepsilon_y)/\sqrt{3}$, would be reduced to:

$$\dot{\varepsilon}_e \cong \sqrt{2} W_f V_1/(3L^2). \tag{6-64}$$

The Cowper-Symonds constitutive equation expressed by Eqn. (3-1) is assumed to govern the visco-plasticity phenomenon. The parameters D and q are the could be obtained empirically using the Servo-Hydraulic machines or Hopkinson Bar strain rate gauges. The prescribed values of e.g. $q = 5$ and $D = 40.4s^{-1}$ for mild steel or $q = 5$ and $D = 300s^{-1}$ for RHA steel here are most prevalent in the literature, although higher values of D have also been reported on various low carbon steel and aluminium grades to accurately capture the deformations of the experimental/numerical models[26], [60], [76]. Since the parameter q is quite large, even relatively rough estimates of strain rates would lead to reasonable predictions of the dynamic yield stress. Thus, the expression of equivalent strain rate may be implemented in Eqn. (3-1). To avoid iterations, the expression of W_f in Eqn. (6-64) is replaced by its equivalent expression of dimensionless kinetic energy, i.e. either Eqn. (6-57) for pattern (A) or using Eqn. s' (6-58), and (6-54) for pattern (B). Thus, using the estimate $W_f/H = \sqrt{(2/3)\bar{\lambda}}$, the parameter σ_0 in the expressions of dimensionless kinetic energy may be replaced by $\sigma_y{}'$, although σ_0 is retained in Eqn. (6-64) to avoid iterations. For example, for a simply supported plate, governed by roof shape velocity profile of pattern (A), we have $\dot{\varepsilon}_{ea} = 4\beta V_1^2\sqrt{(\rho/\sigma_0)}/\sqrt{3}L$, thus:

$$\frac{W_f}{H} = \left[\frac{2\bar{\lambda}}{3\left(1+\left(\frac{4\beta V_1^2\sqrt{(\rho/3\sigma_0)}}{DL}\right)^{1/q}\right)}\right]^{1/2} \tag{6-65}$$

6.12 VALIDATIONS OF THE THEORETICAL MODELS

The proposed theoretical methods were compared against the numerical and experimental studies using two categories. In the first category, a Finite Element model was set-up to investigate the assumptions of each pattern (A) scenarios (viz. membrane or combine bending and membrane action), while in the second category, the accuracy of each pattern of motion was investigated using the available experimental data. The experimental data by Jacob et al [21] on the effect of stand-off on blast phenomenon, as well as those of Langdon et al. [61], [133] on blast protection armour steel plates was used. The numerical results of Ref. [119] were also compared for the second approach. The difference between the experiments, despite the material type, geometry and load conditions presented in Table 6-1, was the method whereby the blast load was imparted on the panels. Jacob et al. [21] used a circular rigid-mild steel tube to provide the varying stand-off distance, the blast pressure was confined to a radial central portion of the target plates, while Langdon et al. [61] utilised polystyrene bridge arrangement to provide the stand-off. Both studies employed PE4 disc explosive to generate the blast wave pressure. Details of these studies have been discussed elsewhere [61], [133], thus, only the results of interest are presented here for validations.

6.12.1 Materials and models

In the current theoretical models, the influence of transverse shear and rotatory inertia were discounted. This corresponds to a range of plate thicknesses as $H/L \leq 0.025$, a range pertinent to most practical design applications.

The candidate plates from the first category were 400×400mm panels of ARMOX370T, ARMOX440T and Mild Steel (MS4), with material properties presented in Table 3-1. The armour steel types exhibit high strength and hardness compared to mild steel but lower ductility, leading to less Specific Energy to Tensile Fracture (SETF). The candidate armour steel of [61], [119] were ARMOS370T, ARMOX 440T and ARMOX 500T. The panel configurations were as presented in

Figure 6-17 draws the stress-strain curve of the armour steel specimen under uniaxial strain test. To account for the hardening of the materials, the mean flow stress for the analytical was averaged as $\sigma_0 = (\sigma_y + \sigma_{UT})/2$. A loading decay parameter of $b = 50m^{-1}$, typical of most blast waves was taken for all blast scenarios studied here.

Table 6-1- Experimental tests load configurations by [61], [119], **where D_e represents charge diameter**

Designation	**Stand off (mm)**	**D_e (mm)**	ω_0
AR370T-AR440T	25-50	40-50	0.33
MS4		75	
MS	25-300	34	0.32

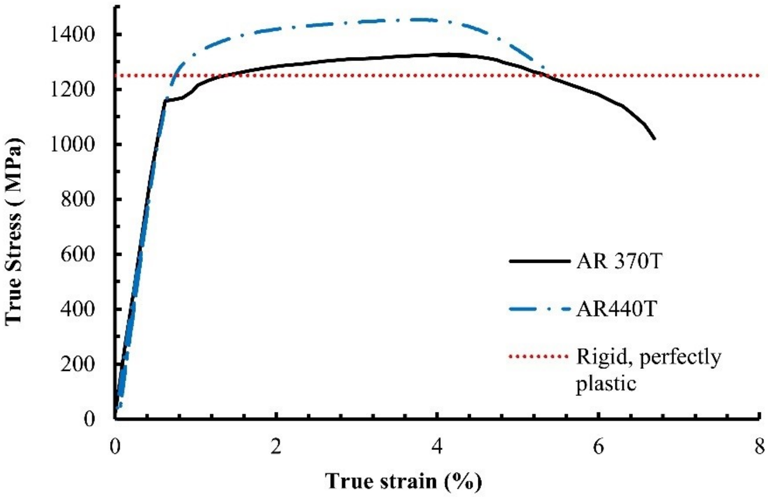

Figure 6-17. Stress strain curve of armour steel models.

The experimental specimens of Jacob et al. had characteristic dimensions of 244mm ×244mm, yield strength of 244MPa and slenderness ratio $H/L = 0.015$, while the loading was confined to the exposed area of 106mm diameter.

6.13 **FINITE ELEMENT (FE) MODEL AND VALIDATIONS**

A full 3D Finite Element model is set up in commercial software ABAQUS® Explicit 14.4 on ARMOX steel and mild steel candidate materials. The blast load is axi-symmetric and the plate has 2 axes of symmetry. This simplified the size of numerical model to only a quarter of the plate with associated symmetry boundary conditions as illustrated in Figure 6-18.

The Young modulus of the steel panels was assumed 200GPa and Poisson ratio as 0.3. The modified Ramberg-Osgood constitutive model-with perfect plasticity- was assumed for the steel materials. The strain rate sensitivity was investigated for mild steel plates only. The panels were discretized with a mesh of four noded S4R elements (doubly curved, generic shell elements with finite in-plane strain formulation) having 5 Simpson points of integration through the plate thickness. A total of 12550 elements were used (elemental length of 4mm) to satisfy mesh convergence. An additional 20mm along the plate periphery was considered for the two upper and lower clamps. The clamps were tied to the plate by penalty contact of coefficient 0.3 and modelled as rigid body. This model was similar to pure Lagrangian models discussed in Section 3.4

The loading was implemented by a FORTRAN coded user defined subroutine VDLOAD in each case. To maintain low ratio of loading duration to the natural period of the plate, a rectangular pulse shape profile with low duration ($\tau = 50\mu s$) was assumed for the pulse shape. With respect to the spatial distribution of the load, the radius of the centrally blast loaded plate was calculated as 100mm and 50mm for AR440T and AR370T, respectively. The magnitude of the load varied in the range of 20-70MPa, as shown in Figure 6-19, which corresponds of a range of blast loads with various stand-off distances for the same charge mass. Using the procedure to determine the impulsive asymptote (simplified model), the results of membrane/combined bending and membrane cases are compared in Table 6-2.

The mild steel panels, on the other hand, had various loading constant zone radii, while the magnitude of the load was adjusted to yield constant total impulse of 50N.s. Thus, using the expression $I = \int\int p(x, y, t)dxdydt$, a crude estimate for the calculated pressure was found as $p_0 = I/(\pi r_e^2 \tau)$. Subsequently, each considered load parameter $\omega_0 = [0.25, 0.5, 0.75, 1]$ corresponds to pressure of $p_0 = [127, 34.8, 14.1, 7.96]\ MPa$, respectively.

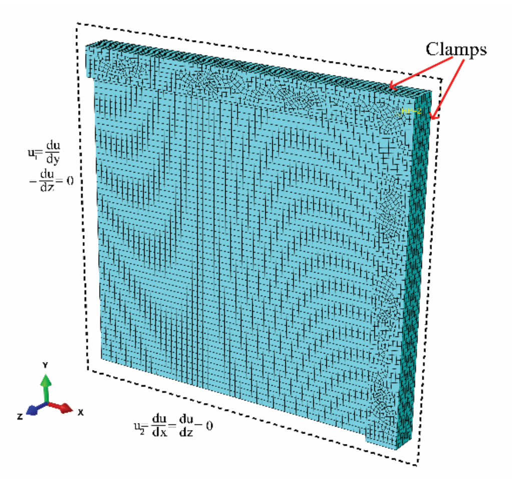

Figure 6-18. FE mesh of the quarter plate model

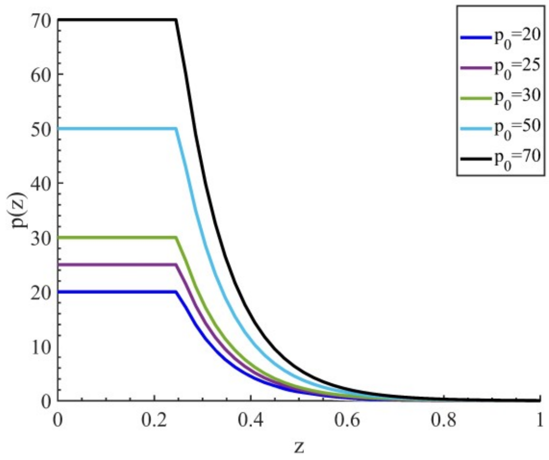

Figure 6-19. Spatial distribution of the blast loads (central intersection view)

It turns out that the theoretical results on armour panels agree with the numerical counterparts, the maximum average difference occurring at $p_0 = 20MPa$ as 22% and 19.5% for AR370T and AR440T, respectively. The membrane formulation would overpredict the results in the low range of magnitude of pressures. In such circumstances, the *ab initio* assumption is violated unless the bending moment contribution in energy formulation is retained in the study. By referring to the accuracy of the mild steel model which retained the visco-plasticity effects, Perrone and Bhadra's method [171] with $D = 40.4$ yields maximum of 23% larger displacement on $\omega_0 = 0.5$ (Figure 6-20).

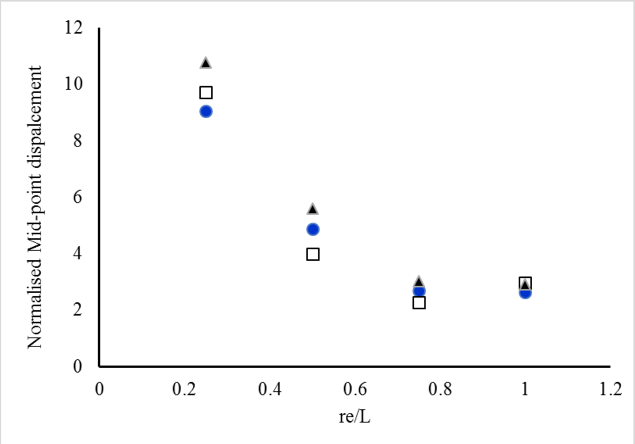

Figure 6-20. Comparison of numerical and theoretical results (Eqn. (6-65)) on MS4 panels, □ Numerical results, ● theoretical results with $D = 40.4s^{-1}$ and $q = 5$, ▲ theoretical results with $D = 1300s^{-1}$ and $q = 5$

Table 6-2- The predicted normalised Mid-point deformation combined (C) and membrane only (M) of circumscribing yield curve for Full Eqn. (using the expression of permanent displacement field) vs. simplified (using impulsive asymptote)

	AR440T						**AR370T**					
		W_f/H **(C)**		W_f/H **(M)**				W_f/H **(C)**		W_f/H **(M)**		
p_0	λ	**Full Eqn.**	**Simpl.**	**Full Eqn.**	**Simpl.**	**ABAQUS**	λ	**Full Eqn.**	**Simpl.**	**Full Eqn.**	**Simpl.**	**ABAQUS**
20	37.30	1.113	1.135	1.595	1.610	1.222	85.00	0.63	0.69	1.08	1.09	0.964
25	58.27	1.496	1.503	1.994	2.013	1.763	132.81	0.88	0.92	1.35	1.36	1.167
30	83.91	1.885	1.882	2.392	2.416	2.504	191.25	1.13	1.16	1.62	1.63	1.280
50	233.09	3.459	3.439	3.987	4.026	4.396	531.25	2.18	2.17	2.69	2.72	2.585
70	456.87	6.045	5.020	5.582	5.637	5.43	1041.25	3.24	3.23	3.77	3.80	4.176

6.14 DISCUSSION OF THE RESULTS AND OF EXPERIMENTAL VALIDATIONS

In Figure 6-21 correlates between the analytical models of pattern (A) and (B) and the results of Jacob et al. [21]. The radius of the blast r_e is estimated as the charge radius. Under the circumstances where the charge radius to plate length ratio is more than a third, pattern (B) gives a more conservative estimate in accordance with the experimental values. Clearly, the prediction of the permanent displacement necessitates the accurate prediction of the load radius and exponent from the experimentally/numerically captured pressure time histories, or using empirical estimates [27]. The pressure loads of shorter stand-off result in higher values of permanent deformation, evidently as most of the blast is concentrated on the localised region of the target. Due to the proximity of the blast the ratio of r_e/L decreases, while the decay exponent increases. However, the length of the target plate is restrained to the portion to which most of the blast load is absorbed. This can be estimated as the exposed area of the plate.

Upon circumstances of proximal blasts, provided the ratio of the charge diameter to the expensed length of the target is infinitesimal, such as those in [119] (Figure 6-22), the majority of the load is dissipated before reaching the target boundaries, thus, it is reasonable to consider the effective length of the panels in use of pattern (A). Such a model, when compared against the experimental data with exposed area of 300×300mm target where in the range of ${}^{r_e}/_{L} \ll 1$, would give an upper bound prediction while the results of pattern (B) are too conservative estimates to the prediction of the permanent deflection of the panels. This suggests that if ${}^{r_e}/_{L} \ll 1$ the incipient bending hinges remain stationary.

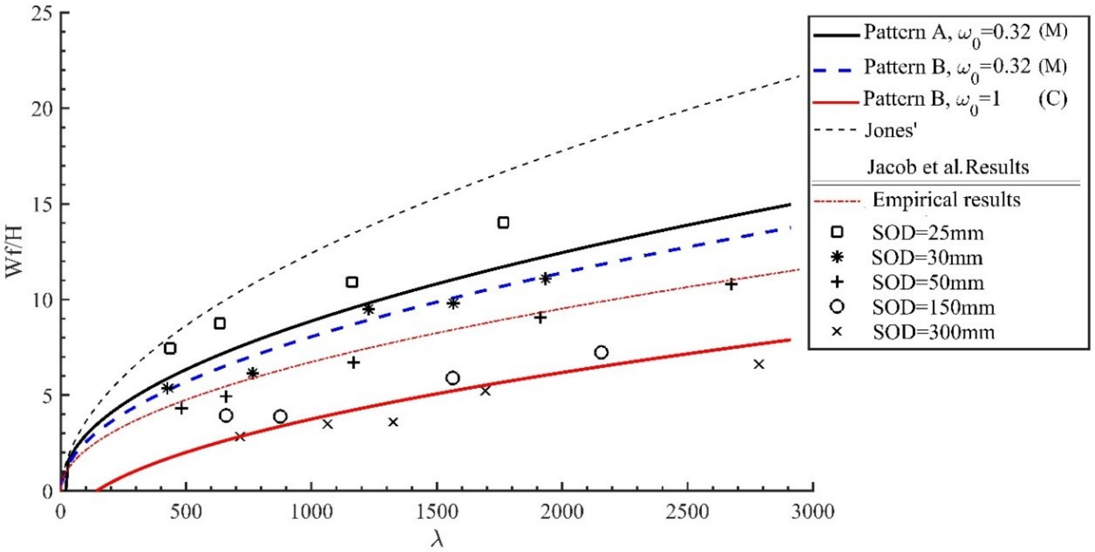

Figure 6-21. Predicted curves of the permanent deformation due to membrane effect (circumscribing yield criterion), compared against the experimental data by Jacob et al.

An odd result of [21] presented in Figure 6-21 was that, while the blast load scenarios with increased stand-off (i.e. SOD=300mm) may be assumed as uniform, the associated predicted deformations deviated from the theoretical predictions available in the literature. This is because of ignoring the strain rate sensitivity effects, assuming the stationery bending hinge while in fact the plastic hinge is moving one, and the adiabatic shear deformations.

Adiabatic shear deformations occur due to the elevated temperature induced by proximal blasts causing the large strain localisations [65], [66], [172]. The adiabatic heat generated due to the high strain rates leads to the elevated temperature in the localised region while the surrounding region of the plate strain hardens. In such cases the thermal softening may overcome the strain hardening effects. Thus, the mathematical treatment incorporating the adiabatic shear effects is fraught with difficulty, and to date the authors are unaware of an exact solution where this effect was retained in the analyses of this kind. However, the concurrence of the, herein, theoretical approach and the available experimental/ numerical results in the literature is promising.

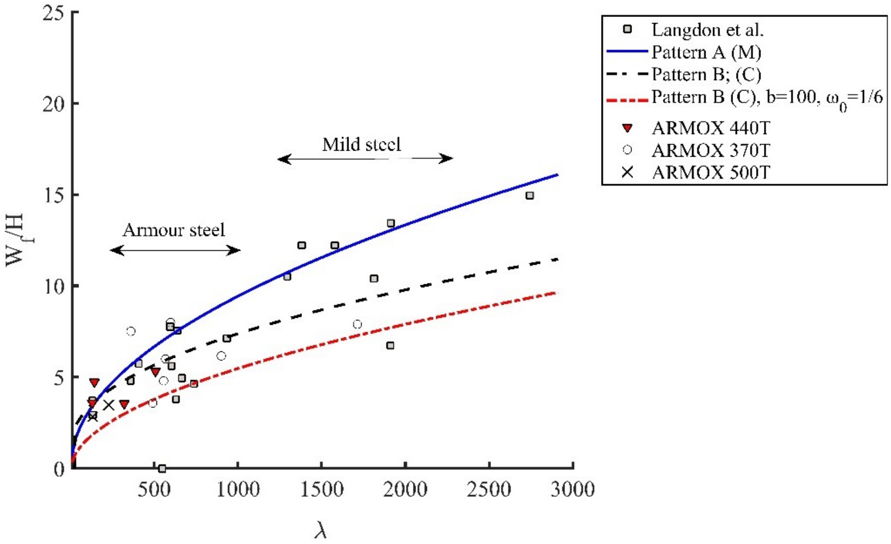

Figure 6-22. Prediction of the permanent deformation, theoretical models vs. the experimental data of Langdon et al. [61]

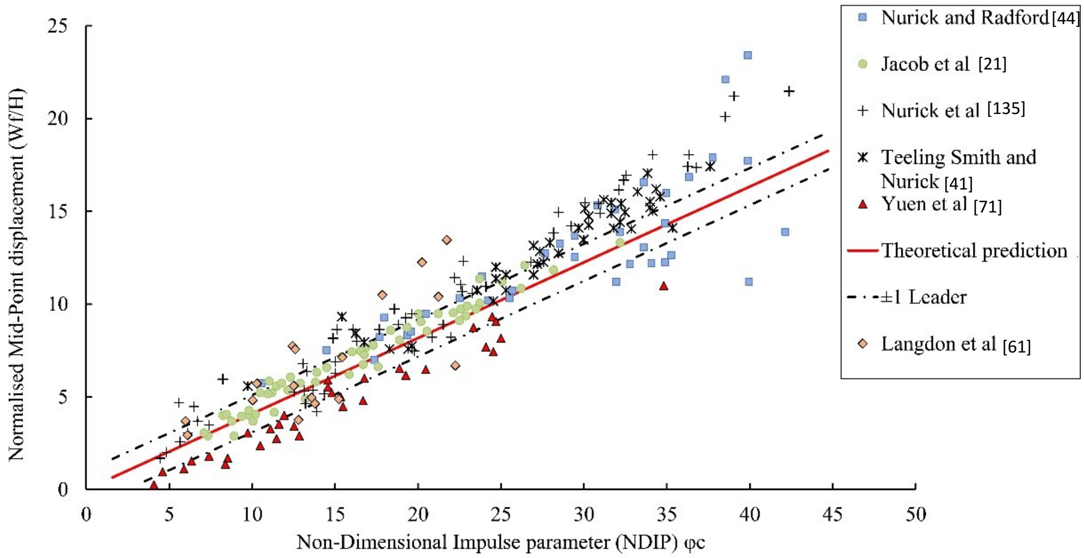

Figure 6-23. Theoretical predictions of deformation of the square plate (membrane only) with $\boldsymbol{\beta = 1/12}$ and $\boldsymbol{b = 50m^{-1}}$ (typical values of blast wave) compared against the experimental data by researchers post 1989.

In Figure 6-23, the solution of membrane case is compared against the experiments post 1989. The curve is casts into Non-Dimensional Impulse Parameter (NDIP) $\phi_c = \sqrt{\lambda}\,/2$ and a critical estimate of $\beta = 1/12$ was considered.

II. PART II: ELASTIC RESPONSE OF SQUARE MEMBRANES SUBJECT TO LOCALISED BLAST LOADING

Modern armour graded steel plates are widely used in protective systems against transient pulse pressure loads, such as localised blasts. The combined elastic-plastic response which contributes to dissipation of total impulse from such extensive loads accounts for energy stored elastically which limits the deformation, while the energy dissipated as plastic work (which is almost entirely converted to heat) limits the extent of transferref forces in the structure. Due to the tailored metallurgy, armour steel panels benefit from high elastic energy storage capacity which contributes to dissipation of total impulse from extensive blast loads within the bands of their elastic region. Higher elastic energy storage capability mitigates the catastrophic damage and the ensuing large deformations otherwise occurring in the case of the conventional graded metallic panels. While blast assessment of the armour plated structures is significant in design and application of protective systems, limited studies are available on their response to the localised blasts.

The organization of part II is as outlined. Following a brief literature review of the elastic response of plates to blasts in Section 6.15, the associated governing equations are presented I Section 6.16. In Section 6.17 a localised blast elastic energy parameter is determined. the theoretical solutions are sought in Section 0 and validated in Section 6.19 by numerical models. Section 6.20 discusses the elastic-perfectly plastic response of the plate while Section 6.21concludes the theoretical solutions of this chapter.

6.15 **BACKGROUND**

Derived based on the finite displacement theory, the Föppl Von-Kármán model is particularly pragmatic to capture the pronounced variation of shell transverse deformation field with its membranal strains using the minimal geometric nonlinearity [173]. In fact, the scientific literature devoted to applications of this model spans from buckling and post-buckling of plates in aerospace engineering [174], [175] to blast response of laminate glass [81], [176], [177], from instabilities of composites under thermal loads [178] to wrinkling of soft biological tissues [179]. Recently, in the fields of aerospace, structural ad mechanical engineering, the complex response of plates to blast loads of distinct types has highlighted the limitations of the classical theories and the need for consideration of geometric nonlinearities using the FVK method. This is particularly integral to determination of the response of structures whose contribution of the elastic energy through the plate to the total kinetic energy cannot be ignored.

In fact, for thestructural systems made of rate insensitive material and no hardening, the dynamic response is strain rate independent the constitutive equations may be treated as that of elastic-perfectly plastic or rigid-perfectly plastic isotropic material. It has been argued by Li and Meng [180] and Fallah et al [88], that when the dimensionless structural response $\alpha = \mathrm{R}_0/Ky_c$ (where R_0, K, y_c denote the resistance, stiffness matrix and critical deformation, respectively) is less than unity and the maximum pressure p_0 does not exceeds the structure resistant, the rigid-perfectly plastic simplification may not be applicable. In such circumstance, the quotient of the energy stored elastically in the system to the kinetic energy of the plate is noticeable [35], [98], [181].

Teng et al [182] examined the transient deflection of the simply supported and clamped square plates under uniform blast load with exponentially decaying time function. The FVK expressions were reduced to Duffing equations by using the variational techniques. The authors employed the Poincaré-Lindstedt perturbation method to analyse the plate response. While the transient deformation at the first approximation was concurrent with that of numerical models, prediction of the response was limited to the loading phase only.

Linz et al [176] presented an experimental and numerical study on the performance of laminated glass due to blast loads. The material properties (average stiffness, Poisson's ratio and average areal density) of the full composite action was estimated as an average of the properties of each lamina (consisting of glass and Polyvinyl Butyral (PVB)). The analytical model employed FVK expressions to capture the PVB membrane forces and maximum deformations. The authors assumed a trigonometric expansion of the displacement function truncated into order of seven cosine terms. The assumption of using a single term for the deformation and Airy stress function series was found appropriate for the lower intensity blasts to characterize the pre-crack behaviour of the composites. However, the Digital Image Correlation of the experimental specimens revealed that such a deflection shape would not be suitable for more intense loading. The curvature field measured from DIC technique was non-uniform, being concentrated on the plate edges. Their analytical model, however, was incomplete, i.e. the elastic post loading behaviour of the plate was not investigated analytically. Clearly, the transient pulse load induced dynamic response is a two-step process which comprises a forced and a free vibration, the latter occurring after the load is complete.

Yuan and Tan [100] examined the response of elastic-perfectly plastic beam to uniform pulse pressure loads by extending the minimum Δ_0 technique from Symonds [148] Three distinct phases of motion were assumed whereby the motion was classified into phase 1- elastic vibration, phase 2- perfectly plastic deformation and phase 3- residual elastic vibration at this phase. The influence of membranal stretching was only retained at phase III when the motion was characterised by travelling plastic hinge. Thus, the elastic and plastic responses were distinctly separated in each phase of motion while the influence of membrane forces in the elastic regime was ignored.

Thus, the objective of this work is to derive the theoretical equations for the non-linear elastic response of the square plates subjected to the localised blasts. The plates examined here are assumed simply supported, wholly elastic, encountering large deformations, the influence of geometry changes due to membrane forces has been retained in the analyses conducted. This is achieved by implementing the well-known Föppl-Von Karman (FVK) nonlinear theory. The combined effects of elastic-perfectly plastic plates is discussed further in the context of the problem.

6.16 **GOVERNING EQUATIONS**

The plated structure studied in this part comprises an initially flat, monolithic, ductile metallic square membrane with side length of $2L$, thickness of H and areal density of $\mu = \rho H$. The Young modulus is E, and ρ represents the density of the material of the plate. The plate is secured along its periphery with simply supported boundary conditions.

The general expression of the strain tensor with respect to the displacement field u is given as:

$$\varepsilon_{ij} = \frac{1}{2}(u_{i,j} + u_{j,i} + u_{k,i}u_{k,j}) \tag{6-66}$$

where the subscript comma denotes the differentiation with respect to the vector, i.e. $u_{i,j} = du_i/da_j$. The reference space general coordinates $C(i,j,k)$ may be replaced by their Cartesian counterparts $C(x,y,z)$ for convenience. Thus, given the Cartesian coordinates (x,y) on C centred in its centroid, and the characteristic in plane displacement $v = (v_x, v_y)$, w being the transverse displacements, the strain tensor components and those of the curvature tensor using the reciprocity conditions $(a_{ij} = a_{ji})$ in a 2-dimensional state of stress are simplified to:

$$\varepsilon_x = \frac{\partial v_x}{\partial x} + \frac{1}{2}\left(\frac{\partial w}{\partial x}\right)^2, \quad \varepsilon_y = \frac{\partial v_y}{\partial y} + \frac{1}{2}\left(\frac{\partial w}{\partial y}\right)^2,$$
$$\gamma_{xy} = \frac{\partial v_x}{\partial y} + \frac{\partial v_y}{\partial x} + \frac{\partial w}{\partial y}\frac{\partial w}{\partial x} \tag{6-67a-c}$$

$$\kappa_x = -\frac{\partial^2 w}{\partial x^2}, \quad \kappa_y = -\frac{\partial^2 w}{\partial y^2}, \quad \kappa_{xy} = -\frac{\partial^2 w}{\partial x \partial y} \tag{6-68}$$

The second term of the Eqns. (6-67a-c) represent the membranal strains whose associated deformation gradients are the sole contributors to the nonlinearity. The compatibility condition of the strains is given by

$$\frac{\partial^2 \varepsilon_x}{\partial y^2} + \frac{\partial^2 \varepsilon_y}{\partial x^2} - \frac{\partial^2 \gamma_{xy}}{\partial x \partial y} = \kappa_{xy}^2 - \kappa_x \kappa_y = -\det k \tag{6-69}$$

$$\nabla \times k = 0 \tag{6-70}$$

Eq. (6-69) represents the Gaussian invariant curvature $\bar{\kappa}$ (Gauss Theorema Eregium). The Föppl-Von Kármán Equations read:

$$D_r \nabla^4 w(x, y, t) - H\mathcal{L}(w, \Phi) = p(x, y, t) \tag{6-71}$$

$$\nabla^4 \Phi(x, y, t) = -\frac{E}{2}\mathcal{L}(w, w) \Leftrightarrow -\mathrm{E}(\kappa_x \kappa_y - \kappa_{xy}^2) \tag{6-72}$$

Eq. (6-72) is a compatibility equation, where $\phi(x, y, t)$ represents the Airy stress function, $D_r = \frac{EH^3}{12(1-v_e^2)}$ is the flexural rigidity of the plate, ∇^4 is the biharmonic operator, (also referred to as the square of the Laplacian operator). Thus, the Gaussian curvature is quadratic with respect to the transverse displacement field. The function $\mathcal{L}(w, \Phi)$ in (6-71) is the differential operator represents

$$\mathcal{L}(w, \Phi) = \frac{\partial^2 w}{\partial x^2}\frac{\partial^2 \Phi}{\partial y^2} + \frac{\partial^2 w}{\partial y^2}\frac{\partial^2 \Phi}{\partial x^2} - 2\frac{\partial^2 w}{\partial y \partial x}\frac{\partial^2 \Phi}{\partial x \partial y} \tag{6-73}$$

Eq. (6-72) is a compatibility equation as discussed earlier, as $\mathcal{L}(w, \mathrm{w})$can also be recovered by replacing Φ with w in (6-73). Eqns.' (6-71)- (6-73) are coupled, highly nonlinear, fourth order Partial Differential Equations (P.D.E) which represent the geometric nonlinearities of an elastic system induced by in-plane displacements and membranal forces. Indeed, even for simple engineering problems, the exact solution of von Karman Equations is extremely notorious. Minimization of the FVK energy functionals calls for numerical Finite Element techniques, boundary elements or variational methods. An iterative technique, combined with Galerkin's-Ritz method is sought hereunder to simplify the inherently cumbersome calculations.

The Galerkin-Ritz method was employed here as an efficient variational strategy to dynamically update the dependence of the membranal stresses on the transverse displacement field (Eqn. (6-74a)). The technique to minimize the total elastic energy can be sketched as.

$$FVK_1: \int\int_{(A)} \{D_r \nabla^4 w^{i+1} - H\mathcal{L}\left(\mathrm{w}^{\mathrm{i}}, \Phi^{\mathrm{i+1}}\right) + \mu\ddot{w}^{\mathrm{i+1}}\}\delta w dA = \int\int_{(A)} p(x,y,t)\delta w dA \tag{6-74a}$$

$$FVK_2: \int\int_{(A)} \left\{\nabla^4 \Phi^{\mathrm{i+1}} + \frac{E}{2}\mathcal{L}\left(\mathrm{w}^{\mathrm{i}}, \mathrm{w}^{\mathrm{i}}\right)\right\}\delta\Phi \, dA = 0 \tag{6-74b}$$

In Eqns. (6-74a)- δw and $\delta\Phi$ represent a virtual weight function attributed to the displacement and Airy stress function, respectively.

The mathematical procedure to solve the FVK expressions is as follows:

i. Assume an ansatz for the displacement field components and the associated stress tensors.

ii. Determine the membrane stress from the compatibility relation (6-74b).

iii. The final form of transverse displacement and velocity fields will be nonlinear, but in the reduced closed form in an elliptic manifold.

As the initial informed guess (ansatz) for the displacement and Airy stress functions it is assumed they take a form expandable as infinite trigonometric series as:

$$w(x,y,t) = \sum_m \sum_n \mathrm{W_{mn}}(t) \cos\frac{m\pi x}{2L} \cos\frac{n\pi y}{2L} \tag{6-75}$$

$$\Phi(x,y,t) = \sum_m \sum_n F_{mn}(t) \cos\frac{m\pi x}{2L} \cos\frac{n\pi y}{2L}$$
$$(m = 1,3,5, \dots \; and \; n = 1,3,5, \dots) \tag{6-76}$$

The characteristic displacements fields and the associated stress tensors in (6-75)-(6-76) are each expressed multiplicative of the relevant temporal and spatial distributions. Clearly, these expressions satisfy the displacement boundary conditions at the plate periphery as well as at its centre. The bending and membrane strain energy contributors would become:

$$\mathcal{L}(w,\phi) = \frac{1}{32}\frac{\pi^4}{L^4} m^2 n^2 \sum_m \sum_n W_{mn} F_{mn} \left(\cos\frac{m\pi x}{L} + \cos\frac{n\pi y}{L}\right) \tag{6-77}$$

$$\nabla^4 w = \frac{1}{16}\frac{\pi^4}{L^4}(m^2+n^2)^2 \sum_m \sum_n W_{mn} \cos\frac{m\pi x}{2L} \cos\frac{n\pi y}{2L} \tag{6-78}$$

6.17 LOCALISED BLAST

The temporal and spatial part of the localised blast load have been defined by Eqns. (5-1)-(5-2). The virtual work of the load (per unit displacement) is expressed in the right-hand side of Galerkin's expression (6-74a). The load is rotationally symmetric and thus independent of the polar angle θ. Thus, while the integral may be evaluated in two circumstances, i.e. (i) considering a circular plate of radius $R = L$ and (ii) with the radius being $R = \sqrt{2}L$. In fact, the difference of the evaluated integrals between the two cases is infinitesimal and may be ignored. By implementing the transformation of coordinates, such a functional may be simplified in terms of a single parameter α_1 to express the load distribution over the central zone as well as its decay type given as:

$$\begin{aligned}
&\int\int_A p_0 \cos\left(\frac{\pi x}{2L}\right)\cos\left(\frac{\pi y}{2L}\right) dxdy + \int\int_A p_0 a e^{-br}\cos\left(\frac{\pi x}{2L}\right)\cos\left(\frac{\pi y}{2L}\right) dxdy \\
&= \int_0^{\frac{\pi}{2}}\int_0^{r_e} p_0 \cos\left(\frac{\pi x}{2L}\right)\cos\left(\frac{\pi y}{2L}\right) r dr d\theta + \int_0^{\frac{\pi}{2}}\int_{r_e}^{L} p_0 e^{-(br-br_e)}\cos\left(\frac{\pi x}{2L}\right)\cos\left(\frac{\pi y}{2L}\right) r dr d\theta \\
&= \frac{\pi p_0}{2}\left\{\int_0^{r_e} r\cos^2\left(\frac{\pi r\sqrt{2}}{4L}\right) dr + \int_{r_e}^{L} r\cos^2\left(\frac{\pi r\sqrt{2}}{4L}\right) e^{-(br-br_e)} dr\right\} \\
&= \alpha_e p_0 L^2
\end{aligned} \tag{6-79}$$

In matrix form, the elastic external load parameter, α_e may be furnished as the product of matrix α_{ij} and $\boldsymbol{f}_{jk}$:

$$\alpha_\mathrm{e} = \frac{1}{L^2 b^2 (2L^2 b^2 + \pi^2)^2}\left[\alpha_0 + tr(\alpha_{ij} \,.\, \boldsymbol{f}_{jk}\delta'_{ik})\right] \tag{6-80}$$

Where δ'_{ik} represents the Kronecker delta, the components of α_{ij} and $\boldsymbol{f}_{jk}$ are defined in (A. 1)-(A. 7) and (A. 8), respectively. It can be seen from Figure 6-24 that the various parameters of α_1 converge to a unique value pertinent to the case of uniformly distributed load as $r_e \rightarrow L$ independent of the decay type.

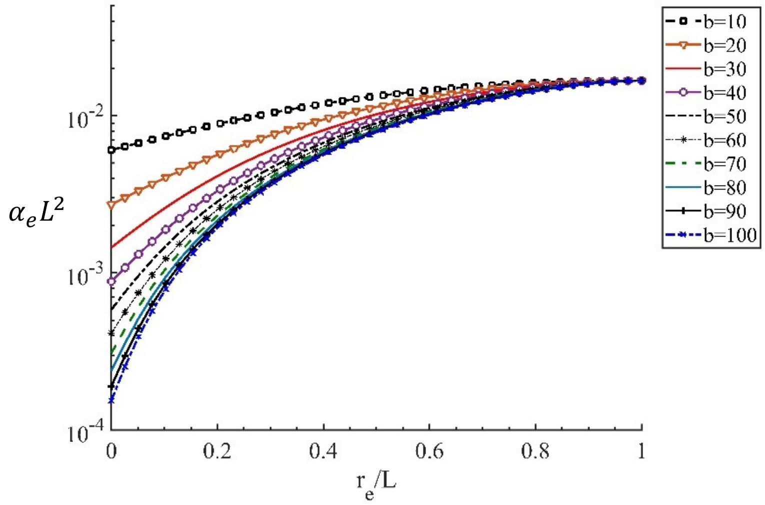

Figure 6-24. Influence of the load parameters on the value of α_1

An elastic moment per unit length is defined for convenience as

$$M_{el} = \alpha_e p_0 L^2 \tag{6-81}$$

In the sequel that follows, the mathematical treatment is carried out in two stages of motion, the first being characterised by the forced vibration due to the pressure pulse load, which transitions into a free vibration instantaneously after the load is complete at $t = \tau$.

6.18 DYNAMIC RESPONSE

6.18.1 First Phase of Motion

For the brevity in the mathematical analysis, only the first term of the truncated series ($m = n = 1$) was considered. Thus, the first iteration is expressed as:

$$\mathrm{w}^{(1)}(x, y, t) = \mathrm{W}^{(1)}(t) \cos\frac{\pi x}{2L} \cos\frac{\pi y}{2L} \tag{6-82}$$

$$\Phi^{(1)}(x, y, t) = F^{(1)}(t) \cos\frac{\pi x}{2L} \cos\frac{\pi y}{2L} \tag{6-83}$$

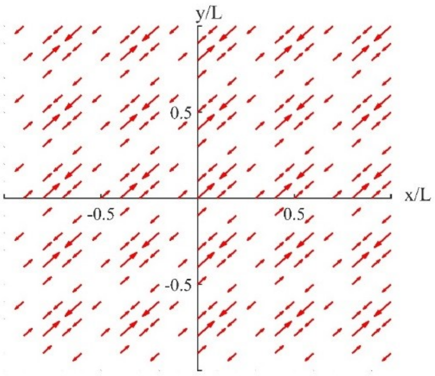

Figure 6-25. Gaussian curvature field

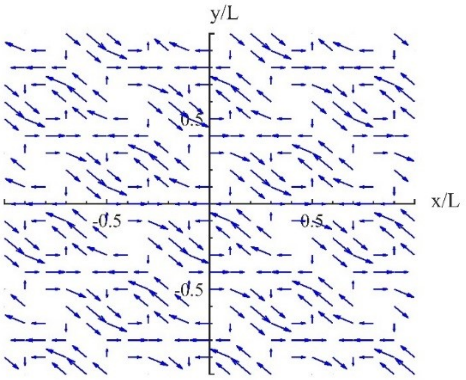

Figure 6-26. Mises stress field

The compatibility Eq. (6-74b) yields:

$$F^{(i+1)} = -\frac{4E}{3\pi^2}\left\{W^{(i)}\right\}^2 \tag{6-84}$$

By substituting Eqn.s' (6-84), (6-77)-(6-78) in (6-74a) and performing the calculations, the form of FVK is reduced to an O.D.E in terms of the transverse displacement field $W^{(i)}$. Defining the dimensionless parameters $\bar{w} = W/H$, $\epsilon = \frac{8H^2}{9L^2}$ as the small perturbation parameter, the infinite dimensional variational problem (Eq. (6-74a)) boils down to a sequence of finite O.D.E's as

$$\mathcal{D}_\delta\colon\ \omega_\mathrm{e}^2\bar{w}^{(i+1)} + \ddot{\bar{w}}^{(\mathrm{i}+1)} + \frac{\mathrm{E}}{\rho\mathrm{L}^2}\epsilon\left(\bar{w}^{(i)}\right)^3 = \frac{\alpha_e p_0 L^2}{A_1 H} \tag{6-85}$$

where the parameter $A_1 = \frac{1}{4}\mu L^2$, while ω_e represents the pulse frequency given in Eqn. (6-87a). Eqn. (6-85) is a inhomogeneous form of Duffing equation, which, in crude terms, represents the motion of a nonlinear spring. [183]. Using the separation of variables, the integral of Eqn. (6-85) represents the kinetic energy of the system ($\dot{\bar{w}}^2 + \bar{w}^2 + \frac{\mathrm{E}}{2\rho\mathrm{L}^2}\epsilon\bar{w}^4 = h + \frac{2\alpha_e p_0 L^2}{A_1}$ - where h is the integration constant) in the elliptic manifold as ϵ is positive. Figure 6-27 sketches the kinetic energy where its abscissa is the transverse displacement field.

The first iteration of the displacement field is achieved by linearization of this O.D.E, i.e. eliminating the Airy stress function by $\mathrm{F}^1 = 0$. The general solution satisfying the initial boundary problems $\bar{w}(0) = \dot{\bar{w}}(0) = 0$ is expressed as

$$\bar{w}_1^{(1)} = C_0(1 - \cos(\omega_e t)) \tag{6-86}$$

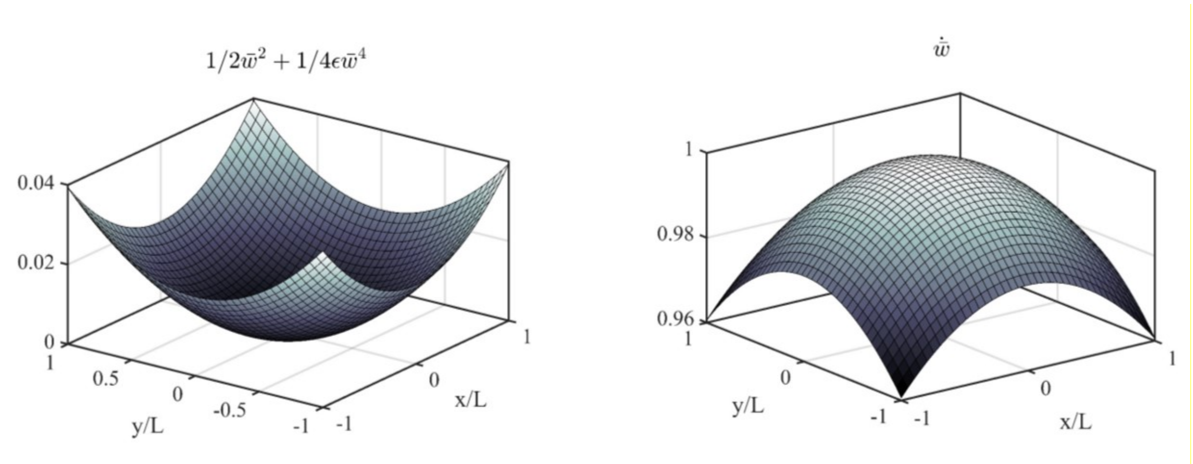

Figure 6-27. Manifold of the displacement function $F(w) = 1/2\bar{w}^2 + 1/4\epsilon E\bar{w}^4$ and kinetic energy of the system per unit mass.

where

$$\omega_e = \frac{1}{2}\sqrt{\frac{D_r}{\mu}\frac{\pi^2}{L^2}} \tag{6-87a}$$

$$C_0 = \frac{16M_{el}L^2}{\pi^4 D_r H} \tag{87b}$$

From Eqn. (6-86) the second iteration for the Airy Stress function at the plate centre is attained. Sequentially, the O.D.E Eqn. (6-85) is re-evaluated and solved to determine, unequivocally by imposing the initial boundary conditions, the transverse displacement as

$$\bar{w}_1^{(2)} = \frac{\Gamma\sin^2\left(\frac{1}{2}\omega_e t\right)}{8A_1\omega_e^2}\left(\frac{16\alpha_e p_0}{\Gamma} - 15 + 5\sin^2\left(\frac{1}{2}\omega_e t\right) + 2\sin^4\left(\frac{1}{2}\omega_e t\right)\right) + \frac{15\Gamma t\sin(\omega_e t)}{32A_1\omega_e} \tag{6-88}$$

where $\Gamma = \frac{8}{9}E\frac{H^3}{L^2}C_0^3$. The procedure may be continued to evaluate the expression displacement field in the third iteration, written in matrix form as:

$$W_1^{(3)} = tr(\boldsymbol{\mathcal{A}}_{ij}\boldsymbol{B}_{jk}\delta'_{ik}) + tr(\boldsymbol{T}_{ij}\boldsymbol{\mathcal{G}}_{jk}\delta'_{ik}) \tag{6-89}$$

where δ'_{ik} is the Kronecker delta, $\boldsymbol{B_{jk}}$ and $\boldsymbol{T_{ij}}$ are the matrices of trigonometric components given in Eqn.s' (6-90)-(6-91), respectively, $d_e = 6.77 \times \frac{10^7 H\pi^2}{6L^2} E\Gamma$ and $\boldsymbol{\mathcal{A}}_{ij}$ and $\boldsymbol{\mathcal{G}}_{jk}$ represent the polynomial matrices of displacement field, given in (A. 9)-(A. 17) and (A. 18)-(A. 22), respectively. In the case of impulsive loading where $\tau \rightarrow 0$, convergence of the displacement field is satisfied after 2 iterations, as a difference of less than 3% was observed between consecutive high order iterations Thus, for brevity in the analysis the mathematical procedure may be carried out with two iterations for the next phase of motion.

$$\boldsymbol{B}_{jk} = \begin{bmatrix} sin(\omega_e t)^2 & d_e sin(3\omega_e t)^2 & d_e sin(2.5\omega_e t)^2 \\ sin(\omega_e t) & d_e sin(3\omega_e t) & d_e sin(5\omega_e t) \\ sin\left(\frac{1}{2}\omega_e t\right)^2 & d_e sin(1.5\omega_e t)^2 & d_e sin(3.5\omega_e t)^2 \end{bmatrix} \quad \textbf{(6-90)}$$

$$\boldsymbol{T}_{jk} = d_e \begin{bmatrix} sin(7\omega_e t) & \sin(4.5\omega_e t)^2 & \sin(4\omega_e t)^2 \\ sin(4\omega_e t) & \sin(6\omega_e t)\, t & sin(2\omega_e t)^2 \\ sin(2\omega_e t) & 1 & 1 \end{bmatrix} \quad \textbf{(6-91)}$$

6.18.2 Second phase of motion

The loading is complete at time $t = \tau$, however, the motion continues due to the initial inertia. Thus, the actual transient dynamic of the system comprises of the forced vibration part contingent upon the load duration [184], ensued by free vibration beyond $t = \tau$.

The analysis in this phase may commence by enforcing the same procedure as the previous phase of motion- i.e. linearisation of the FVK functional in the iterative technique. However, it turns out the maximum amplitude of the transverse displacement grows unboundedly, after a each cyclic response, due to the presence of a mixed mode secular term, which grows unboundedly, rather than reflecting the periodic motion within the bounds of the phase plane [183]. The unbounded growth of the displacement in the phase plane is represented in Figure 6-28. As observed, the presence of secular term would have negligible effect at the first phase of motion, provided the loading phase has been curtailed to a short period (i.e. $\tau \sim 30\mu.s$). We may adjust/scale the amplitude of the oscillations to eliminate the secular term by exercising two methods hereunder. Remark that the expressions of the normalised frequency and transverse displacement in the case of forced vibrations, using the second method are expressed in (A. 23)-(A. 26)

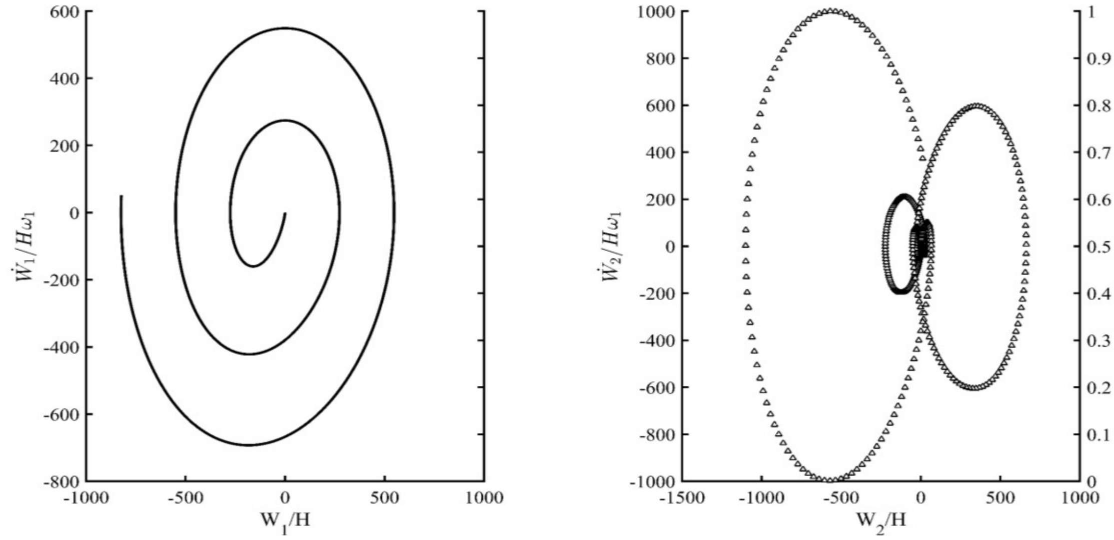

(a) (b)

Figure 6-28. Unbounded growth of displacement and its gradients with 10KPa load and $r_e = 25mm$ at (a) first phase of motion (Eq. (6-88) , (b) second phase of motion with $t_d = 30\mu s$ represented by Eqns.(A. 26)-(A. 27)

Linearization of the highly nonlinear FVK would otherwise not be concurrent with the periodic response that is predicted of the physics of the problem. Thus, in the first method the nonlinear term is maintained by increasing the incipient increment of stresses. The increase of stresses aims to normalize the oscillation amplitudes. To this end, an ansatz of the stress is assumed whereby the displacement field is achieved sequentially. The Airy stress function at time $t = \tau$ was heuristically presumed as $\mathrm{F}_2^{(1)} = F_1^{(2)}(\tau)$, which furnishes the Eqn. (6-85) as

$$\left(\omega_{\mathrm{e}}^2 - \frac{2\pi^2}{3\rho L^4} F_2^{(1)}\right) \overline{w}_2^{(1)} + \ddot{\overline{w}}_2^{(1)} = 0 \tag{6-92}$$

Eq. (6-92) has a solution of the form:

$$\overline{w}_2^{(1)} = \mathrm{C_0}\{\mathrm{C_{11}} \sin(\omega_3 \mathrm{t}) + \mathrm{C_{12}} \cos(\omega_3 \mathrm{t})\} \tag{6-93}$$

$$\omega_3 = \sqrt{\omega_e^2 + 4\epsilon \frac{E C_0^2}{\rho L^2} sin\left(\frac{1}{2}\omega_e \tau\right)^4} \tag{6-94}$$

where the constants $C_{11}, C_{12}$are defined in (A. 28)-(A. 29), while the oscillation frequency has been raised to reduce the amplitudes. Further iterations of the temporal part of Airy stress function are possible, the first of which is evaluated, in Eqn. (6-95), by either using Eqn. (6-93) in (6-84) or incorporating (6-93) back into the Eqn. (6-74b):

$$F_2^{(2)} = -\frac{4E}{3\pi^2}\mathrm{C}_0^2\{\mathrm{C}_{11}\sin(\omega_3 t) + \mathrm{C}_{12}\cos(\omega_3 t)\}^2 \tag{6-95}$$

Accordingly, Eqn. (6-95) is substituted in Eqn. (6-85) (with $p_0 = 0$) to evaluate the second iteration of the displacement field as

$$\begin{aligned}\overline{w}_2^{(2)} = {} & \mathrm{C}_{13}\sin(\omega_e t) + \mathrm{C}_{14}\cos(\omega_e t) \\ & -\frac{\Gamma}{4\mathrm{A}_1 C_5}\Big\{(\omega_e^2 - \omega_3^2)\mathrm{C}_{12}(3\mathrm{C}_{11}^2 - \mathrm{C}_{12}^3)\cos(\omega_e t)^3 \\ & + \mathrm{C}_{11}(\mathrm{C}_{11}^2 - 3\mathrm{C}_{12}^2)(\omega_e^2 - \omega_3^2)\sin(\omega_3 t) \\ & - 3\big((\omega_e^2 - 3\omega_3^2)\mathrm{C}_{11}^2 - 2\mathrm{C}_{12}^2\omega_3^2\big)\mathrm{C}_{12}\cos(\omega_3 t) \\ & - \mathrm{C}_{11}\big((\omega_e^2 - 7\omega_3^2)\mathrm{C}_{11}^2 - 6\mathrm{C}_{12}^2\omega_3^2\big)\sin(\omega_3 t)\Big\}\end{aligned} \tag{6-96}$$

where the kinematic constants,C_5, C_{13}, C_{14} and C_5, are expressed in Eqns.(A. 30), (A. 31)-(A. 32) and (A. 33), respectively.

The second method entails the Poincaré-Lindstedt perturbation method. To this end, the frequency response is adjusted as $\bar{\tau} = \overline{\omega}t$, where $\overline{\omega} = \omega_e + \epsilon\overline{\omega}_e$ and ϵ is a small number. The displacement field is assumed to be a truncation of iterative terms as

$$W(\bar{\tau}) = W^{(1)}(\bar{\tau}) + \epsilon W^{(2)}(\bar{\tau}) + O(\epsilon^2) \tag{6-97}$$

$$\omega_e^2(W(t) + \ddot{W}(t)) + \frac{E}{\mu H L^2}\epsilon W^3(t) = 0 \tag{6-98}$$

where the higher order terms may be ignored for simplicity as ϵ is small. The first iteration of the truncated series is obtained when $\epsilon = 0$, i.e. by disregarding the nonlinear term of the Eqn. (6-85) and satisfying the kinematic continuity conditions at $t = \tau$ as:

$$W_1/H = C_0(cos(\omega_e(t-\tau)) - cos(\omega_e t)) \tag{6-99}$$

Substituting (6-99) and in Eqns. (6-97) and (6-98) and ignoring the higher order terms gives

$$\begin{aligned}\frac{W_2}{H} = {} & C_{15}cos(\bar{\tau}) + C_{16}sin(\bar{\tau}) \\ & + \frac{EC_0^3}{32L^2\rho\omega_e^2}\{-3cos(3\bar{\tau} - 2\omega_e\tau) + 3cos(3\bar{\tau} - \omega_e\tau) + cos(3\bar{\tau} - 3\omega_e\tau) \\ & + 6cos(\bar{\tau} - 2\omega_e\tau) - 6cos(\bar{\tau} + \omega_e\tau) - cos(3\bar{\tau})\} \\ & + \frac{C_0\overline{\omega_e}}{2L^2\rho\omega_e}\left(cos(\bar{\tau} - \omega_e\tau) - cos(\bar{\tau})\right) \\ & + \frac{2}{3}C_0\omega_e t(sin\left(\omega_e(t-\tau) - sin(\omega_e t)\right)\left(\frac{2}{3}\overline{\omega_e}\omega_e L^2\rho + C_0^2 E cos(\omega_e\tau) - EC_0^2\right)\end{aligned} \tag{6-100}$$

With C_{15}, C_{16} expressed in (A. 34)-(A. 35). The value of $\overline{\omega_e}$ can be unequivocally determined to eliminate the secular term appearing in Eqn. (6-100), whereby the response can be made periodic:

$$\overline{\omega_e} = \frac{3}{2}\frac{EC_0^2}{\omega_e L^2\rho}\left(1 - cos(\omega_e\tau)\right) \tag{6-101}$$

and the corresponding Airy stress functions is obtained by using Eqn. (6-84).

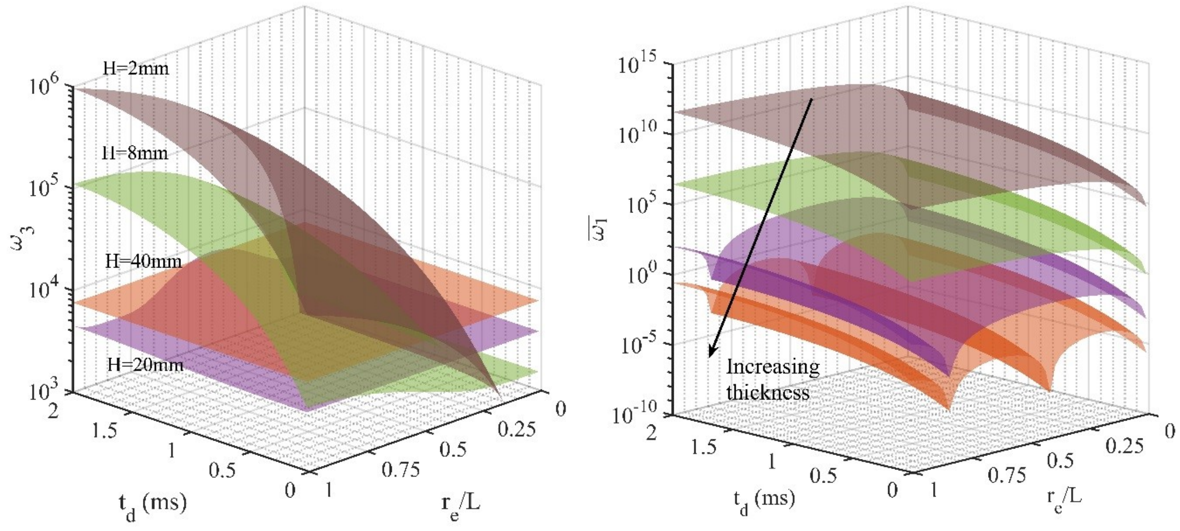

(a) (b)

Figure 6-29. Influence of the load duration and central blast zone radius on the normalised amplitude of oscillation on Increase stress method (a) and Poincaré-Lindstedt method (b) , with H=2,8,20 and 40mm and 200mm plate half length.

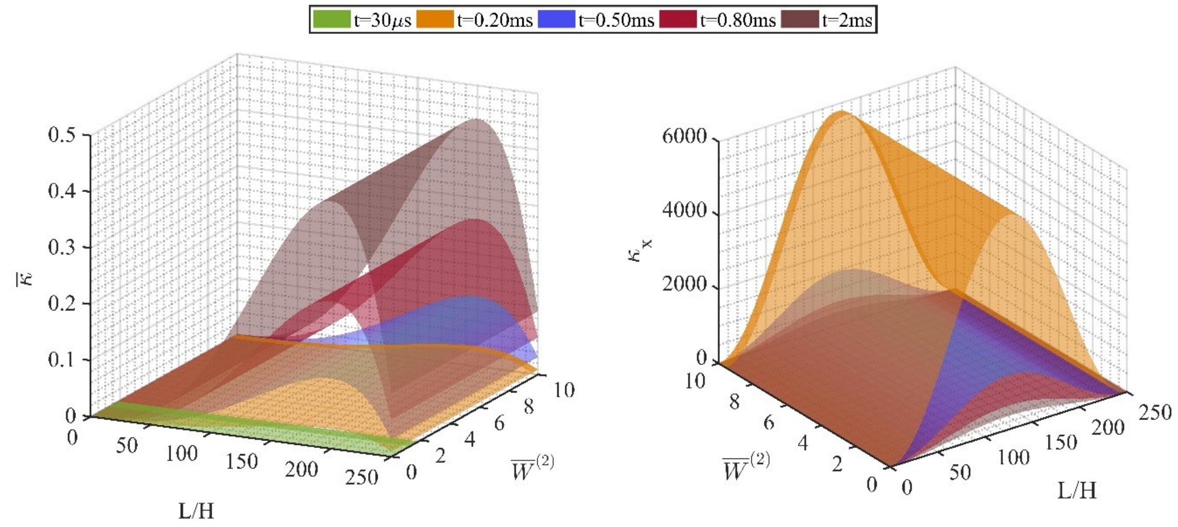

(a) (b)

Figure 6-30- Profile of curvature distribution at the plate centre due to variation of slenderness ratio, (a) Gaussian curvature, (b) curvature in x direction, $r_e = 0.25L$.

Figure 6-29 shows the dependence of the frequency in each approach on the load parameters. In the case of heavy plate limit (H/L>0.1) the oscillation frequency ω_3 is not affected by the loading conditions since ω_e in Eqn. (6-94) is large. Where the quotient of the frequencies (ω_3/ω_e) approaches unity corresponds to the circumstances of impulsive localised loads due to proximal charges, i.e. $\tau \to 0$ and $r_e/L \ll 1$. The central blast load radius effect is less significant on Poincaré Lindstedt virtual frequency. An increase in either oscillation frequencies ω_e or ω_3 clearly decreases the oscillation peaks of deformation.

The variations of curvature with plate thickness is illustrated in Figure 6-30 and a contour plot of stress and equivalent strain distribution are presented in Figure 6-31-Figure 6-32. The equivalent Mises stains is given in (6-102), while the components of strains are derived by substitution of Eqn. (6-96) or (6-100) in Eqn.s' (6-67a-c). In a similar spirit, the components of the stress tensor may be derived from the Airy Stress function, as $\sigma_{11} = {\partial^2\Phi}/{\partial y^2}$, $\sigma_{22} = {\partial^2\Phi}/{\partial x^2}$ and $\sigma_{12} = -{\partial^2\Phi}/{\partial x \partial y}$.

$$\boldsymbol{\varepsilon_{eq}} = \frac{1}{3}\sqrt{6\varepsilon_{11}^2 + 6\varepsilon_{22}^2 + 3\varepsilon_{12}^2} \qquad \textbf{(6-102)}$$

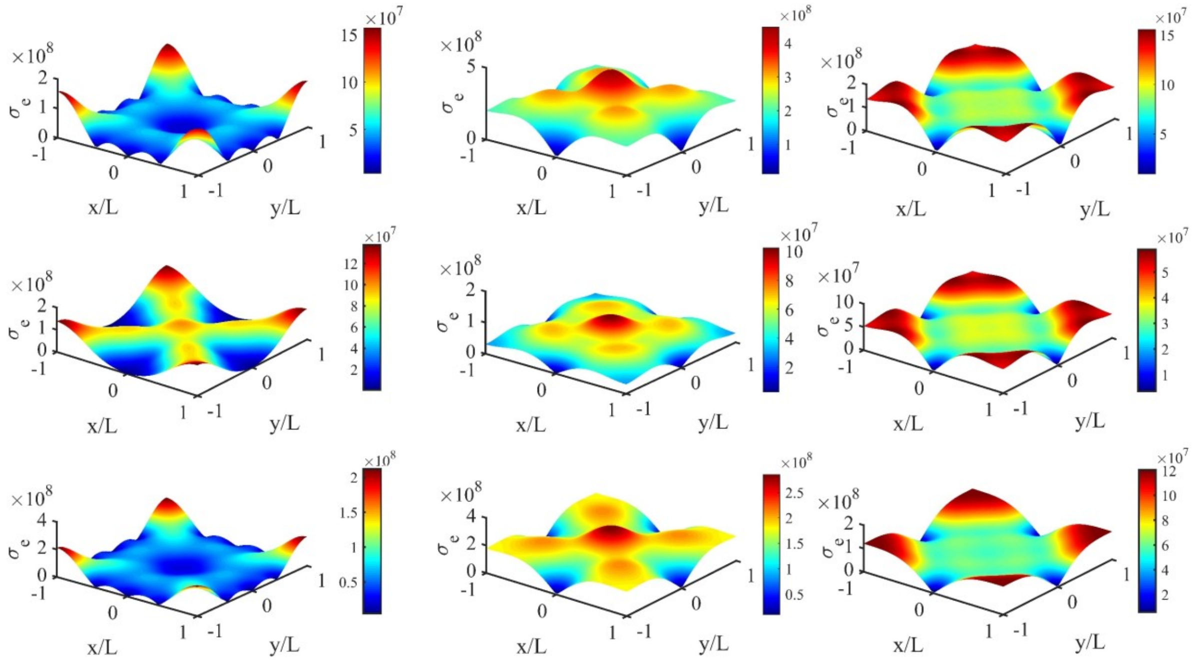

Figure 6-31. Variation of Mises stresses over time throughout the plate.

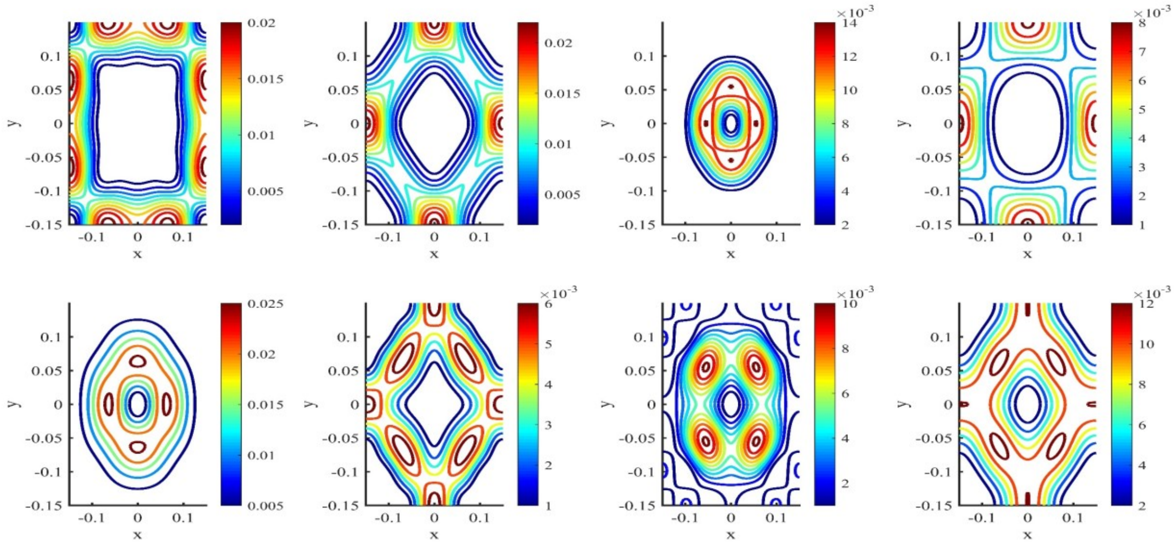

Figure 6-32- Contour plot of evolution of equivalent Mises strains over time throughout the plate.

6.19 NUMERICAL VALIDATIONS AND DISCUSSIONS

In this section, the analytical solutions are validated with the numerical models devised in Finite Element commercial software ABAQUS®14.4 Explicit. A full 3D quadrangular plate of 4.6mm thickness was set up with total geometric exposed area of $400 \times 400\text{mm}$. The material and geometric properties were those of AR440T, given in Table 3-1. The plate was fixed along its periphery with simply supported boundary conditions. The axisymmetric properties of the load reduce the numerical studies to consider only a quarter of the plate, while the influence of finite deflections (geometry changes) was retained in the numerical model.

The models were discretized with a mesh of four noded S4R isoperimetric shell elements with identical mesh discretization as those examined in Figure 6-18 and in Section 6.13. Two blast load scenarios of 40MPa and 200MPa magnitude but with same pulse duration of $30\mu s$ were assumed. The central uniform blast zone radius was assumed 25mm and 50mm for each case.

The transient deformation of the panels was captured and compared in each blast scenario in Figure 6-33-Figure 6-35. The comparison of the transient deformation from the analytical model with the numerical model serves two purposes, viz. (i) to ensure the accuracy of the harmonic vibration's displacement field at every instant of time, and (ii) to estimate the components of stress tensor in the state of general principle stresses and the associated membrane forces. The latter are so derived to predict the yield point of the plate beyond which the trajectory of the force displacement curve follows straight line (i.e. that of the rigid-perfeclty plastic plate). The increase of peaks in Figure 6-34 may be associated with the presence of the secular term ($tsint$) from first phase of motion which becomes significant when the central blast load radius and impulse increase. Both methods provide concurrent estimate for the transient deformations with the numerical models, however, the P.L method shows more accuracy when higher order terms are involved.

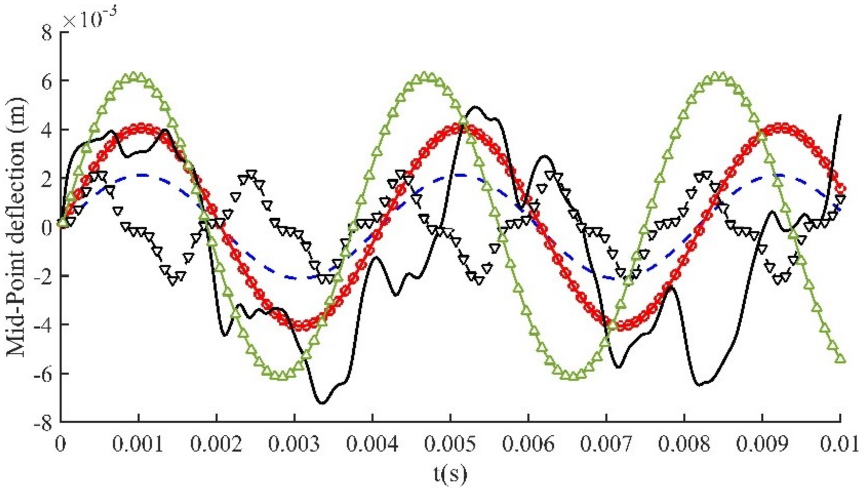

Figure 6-33. $p_0 = 40MPa$**,** $r_e = 25mm$**,** $b = 50$**,** - - **First iteration,** —⊖— **second iteration,** — **FE model,** -▽- **P.L method (second iteration),** —△— **P.L method (truncated series)**

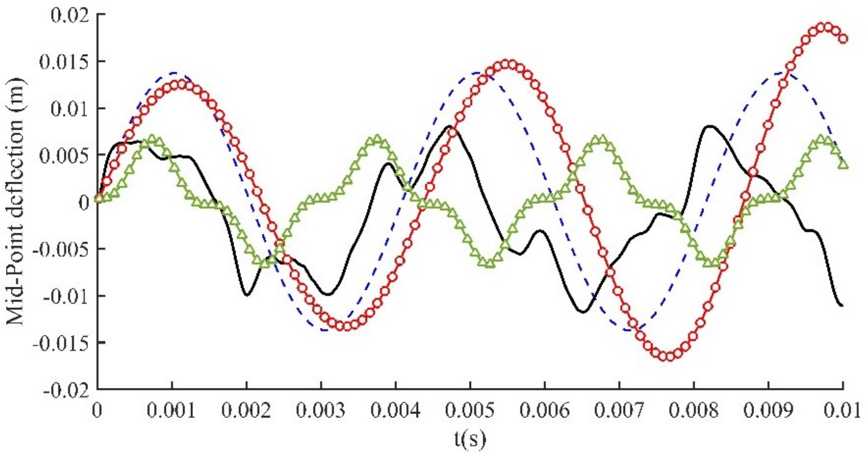

Figure 6-34. $p_0 = 40MPa$**,** $r_e = 50mm$**,** $b = 50$**,** - - **First iteration,** —⊖— **second iteration,** — **FE model,** —△— **P.L method (truncated series)**

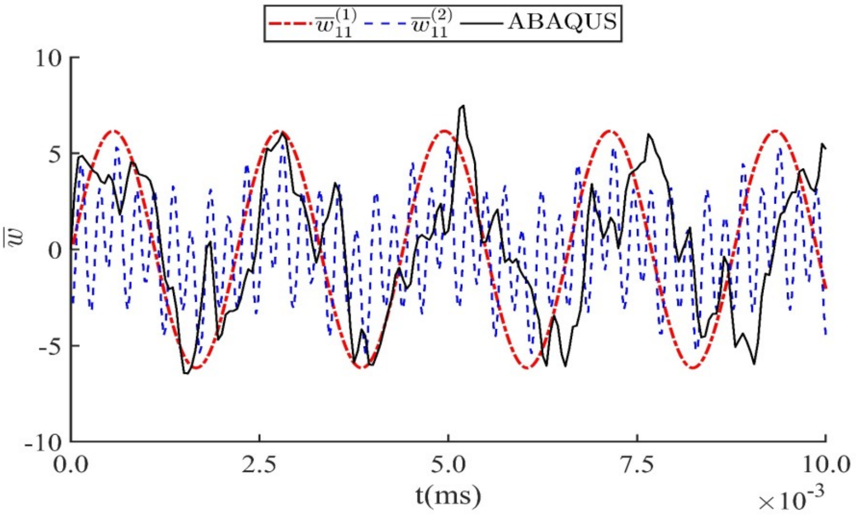

Figure 6-35. Transient deformation of AR440T with 200MPa load and $r_e = 25mm$ from P.L method.

6.20 ELASTIC-PLASTIC RESPONSE OF THE PLATES

As discussed earlier, the actual response of the structure may be simplified into a three stage of elastic-plastic response: the first stage may be presumed to wholly elastic, which is terminated when the yield criterion is invoked, followed by a rigid, perfectly plastic stage. Finally, the motion is concluded with a residual elastic vibration, corresponding to a 'latent' elastic strain energy of the rigid-plastic stage [148].

According to Symonds [148], the three stage analysis may be idealised, preferably, into a primarily dominating rigid-plastic form solution with infinite elastic stiffness, together with the 'latent' elastic deformations by permitting the flexural rigidity to revert to its actual value from infinity. The actual deformations would be summation of the rigid-plastic part as well as the elastic deformations.

The foregoing analysis assumed the material performance is either wholly elastic or wholly plastic. Indeed, the material points through plate section strain plastically when the trajectory of the stress state reaches the yield curve of the associated constitutive yield criterion. Since large nonlinear deformations are of concern, it may be presumed that the bending strain energy is insignificant to the membrane strain energy. To determine the elastic-plastic deformations, it is assumed that the response is predominantly governed by the membrane forces.

In the 3D state, the principle stresses are the roots of the Eqn. (6-103).

$$\boldsymbol{\sigma^3 - I_1\sigma^2 + I_2\sigma - I_3 = 0} \tag{6-103}$$

where

$$\boldsymbol{I_1} = \sigma_{ii} \tag{6-104}$$

$$\boldsymbol{I_2} = \sum_{\mathbf{ii}} = \begin{vmatrix} \sigma_{11} & \sigma_{12} \\ \sigma_{12} & \sigma_{22} \end{vmatrix} + \begin{vmatrix} \sigma_{22} & \sigma_{23} \\ \sigma_{23} & \sigma_{33} \end{vmatrix} + \begin{vmatrix} \sigma_{11} & \sigma_{13} \\ \sigma_{13} & \sigma_{33} \end{vmatrix} \tag{6-105}$$

$$\boldsymbol{I_3} = \begin{vmatrix} \sigma_{11} & \sigma_{12} & \sigma_{13} \\ \dots & \sigma_{22} & \sigma_{23} \\ \dots & \dots & \sigma_{33} \end{vmatrix} \tag{6-106}$$

In (6-104) the Einstein's summation convention holds. The principle stresses reduce to Eqn. (6-107) in 2-Dimensional state:

$$\boldsymbol{\sigma_k} = \frac{\sigma_{11} + \sigma_{22}}{2} \pm \sqrt{\left(\frac{\sigma_{11} - \sigma_{22}}{2}\right)^2 + \sigma_{12}^2} \tag{6-107}$$

With $k = 1{,}2$ giving the maximum and minima of the principle stresses, respectively. Eqn. (6-107) may be substituted in Eqn. (6-108) to determine the membrane forces as presented in (6-108)-(6-109).

$$N = \int \sigma_k dZ \tag{6-108}$$

$$N = -\frac{\pi^2 F_c(t) H cos\left(\frac{\pi(x+y)}{2L}\right)}{4L^2} \tag{6-109}$$

which states a quadratic relationship of the transverse displacement field with the membranal forces, which attains a peak at each peak of displacement field. When $N = N_0$ the plate yields. Yielding occurs almost instantaneously before the plate reaches its first peak. The normalised membrane force displacement of armour steel and mild steel are plotted in Figure 6-36-Figure 6-38 in various case of loading scenarios. The path of deformation, having reached the critical point of yielding, follows the straight line governed by Rigid-perfectly plastic theory.

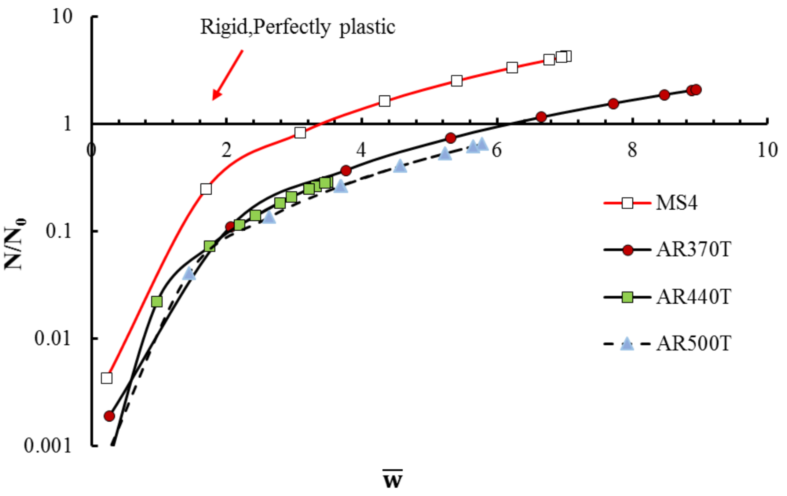

Figure 6-36- Force vs normalised mid-point displacement plot of steel plates, with $p_0 = 250MPa$, $r_e = 50mm$

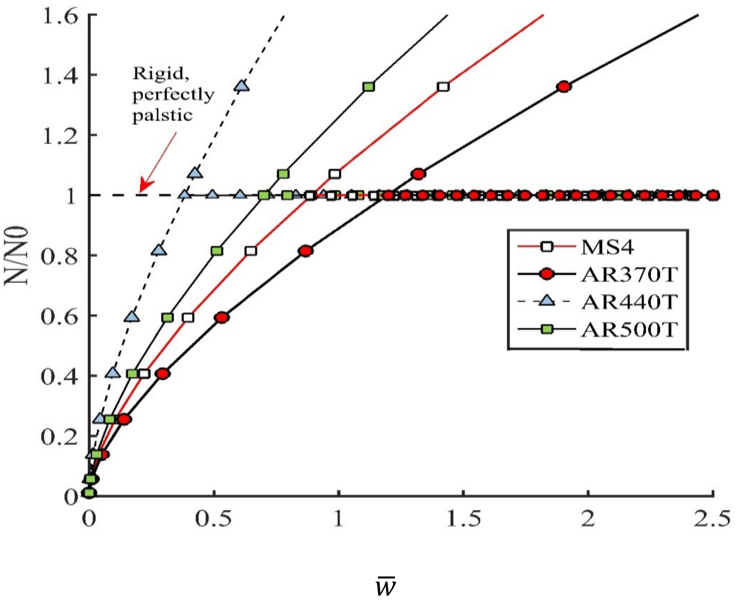

Figure 6-37 Force vs normalised mid-point displacement of the panels subject to localised blast load with parameters $p_0 = 600MPa$, $\tau = 20\mu s$ and $r_e/L = 0.33$ and $b = 50m^{-1}$

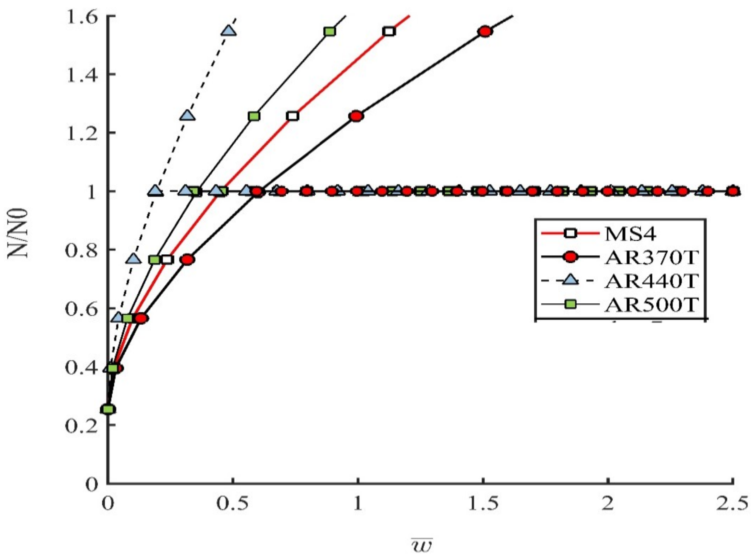

Figure 6-38 Force vs normalised mid-point displacement of the panels subject to load parameters $p_0 = 20MPa, \tau = 0.1ms$ and $r_e/L = 0.33, b = 50m^{-1}$

6.21 CONCLUDING REMARKS

This chapter extended the classical theory of the plate, discussed in chapter 5, to a rigorous analysis on the localised blast response of plates using (nonlinear) large deformation theories in two parts. The scope of part one encompassed the nonlinear dynamic performance of thin, strain rate insensitive, rigid-perfectly plastic square plates of various boundary conditions. In part two, a nonlinear elastic solution was sought using the Galerkin's variational technique combined with perturbation techniques. In both parts spatial distribution of the localised blast load was represented by a piecewise continuous function

Each of the blast parameters of the spatial distribution have been found as bijective functions of the stand-off distance and the explosive mass [22], [27]. The loading type is, therefore, universal which enables the theoretical solution capable of modelling close-in to uniform blast load responses.

The pulse shape effects have not been studied here. This is because the method of eliminating the pulse shape proposed by Youngdahl has well been examined in the literature [75], [91], [114], [152], [157]. The difference between the rectangular and linear pulse shape for circular plate was found 5% [169]. Thus, the permanent transverse deflection may be furnished using the impulsive simplification for the assumed rectangular pulse, irrespective of the pulse shape. For blast of high magnitude and low pulse duration, the transverse deformation was reduced into an expression of dimensionless initial kinetic energy and found to be consistent with the available experimental results in the literature.

The plates were assumed as ‘thin’ membranes, indicating the influence of transverse shear and rotatory inertia (corresponding to the Mindlin-Reissner plate theory) could be disregarded. With large deflection theory in mind, the influence of the geometry changes, or finite displacements were retained in the analyses. This reflects on the roof shaped deformation profile having stationery or travelling plastic hinges, which latter results yield more conservative estimates than the former.

A final remark seems in order. While the results are most suitable for rate insensitive materials, such as high strain ARMOX steel [185], the results prove to be conservative when implemented on the materials which exhibit visco-plasticity (strain rate sensitivity) effects. However, using the modal method proposed by researchers [105], Perrone and Bhadra’s approximation and Cowper-Symonds equation, the commentary on the response of rate sensitive materials has been discussed in the context of the problem. The current results in each case may further be analysed to retain the visco-plasticity phenomenon using Cowper-Symonds, or Johnson-Cook [128], constitutive models.

CHAPTER 7

Thick Plates: Effect of Transverse Shear

7.1 BACKGROUND

In most cases, the idealisation of the plated elements as thin plates or membranes with rigid-perfectly plastic material suffice for treatment of these elements with large inelastic deformation due to the proximal blast loads with reasonable estimation. The theoretical treatment of the thin plates utilises the Kirchhoff Love theory with/without the influence of finite displacements. There are, however, cases where the influence of the transverse shear effects cannot be ignored. These cases consist of sufficiently thick plate where the Mindlin-Reisner theory of plates that accounts for the shear deformation through thickness of the plate in the mathematical treatment [162].

Jones and Co-authors have examined the response of the thick beams and circular plates a to uniform [111]–[115]. With the increase in plate thickness, the plastic work rate due to bending transcends the membrane plastic work rate [117]. Further increase in the plate thickness renders a considerable contribution of the influence of rotatory inertia and shear deformation, as presented in Figure 7-1 and Figure 7-2. The retention of transverse shear, combined with the influence of rotatory inertia, could give rise to an increase in the shear sliding at the support and a decrease in the central deformation of the plate.

Rotatory inertia effects will contribute toward the moment equilibrium conditions for stocky circular plates or beams in which case, it has been shown the plastic hinges do not develop in the plate [111], [112]. However, Ref. [111] observed 11.5%-14% change in the quantities due to the rotator inertia, discussing further that the rotatory inertia may be included in the analysis where high accuracy is required in the stocky plates, having dimensionless plastic shear to moment ratio $\nu = 1.5 \leq \mathrm{Q_0\ R/2M_0}\ < 4$, where R is the radius of the circular plate. Li and Huang [118] showed that while the inner plastic region undergoes a small transverse shear force, it increases rapidly in the outer plastic region. On the other hand, the bending moment is large throughout most of the region and only decreases rapidly near the supports. It transpires that the transverse shear forces induce sliding at the support at which interface the deformation profile is discontinuous.

7.2 AIM OF THE CURRENT WORK

The work in this chapter has been submitted to the International Journal of Impact Engineering [186]. To the best of author's knowledge, to date, no work has been published on the performance of thick quadrangular plates due to localised blast loads. Thus, the major thrust of this work focuses on the impulsively loaded plates, while the influence of the dynamic loads is also presented for simply supported plates of moderate thickness ($\nu > 4$).

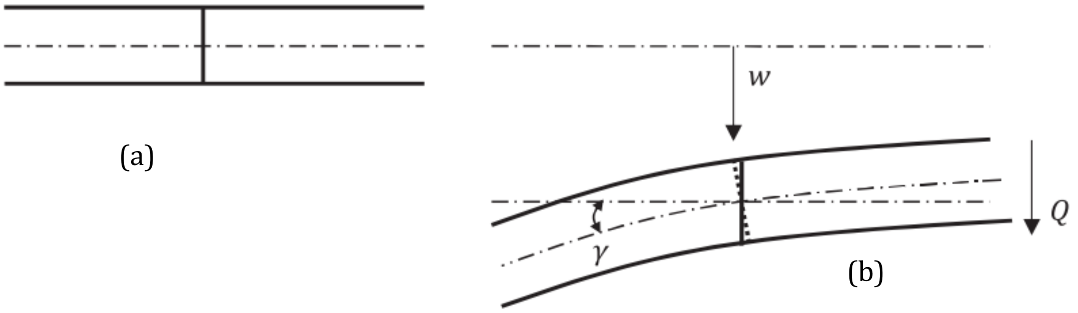

Figure 7-1-Pure plate shearing (a) undeformed shape (b) deformed shape

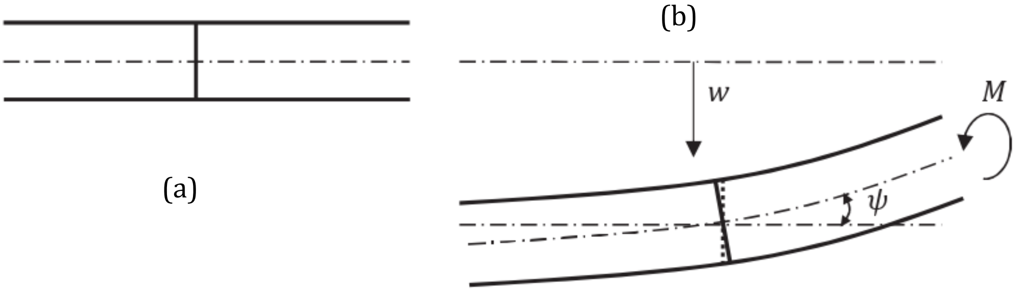

Figure 7-2- Pure plate bending (a) undeformed shape (b) deformed shape (after [35]**)**

7.3 DYNAMIC EQUILIBRIUM EQUATIONS

The governing equilibrium equations in Cartesian coordinates for the dynamic performance of a plate element that is loaded laterally are given as:

$$\frac{\partial Q_x}{\partial x}+\frac{\partial Q_y}{\partial y}= \mu\ddot{w}-p(x,y,t) \tag{7-1}$$

$$\frac{\partial M_x}{\partial x}+\frac{\partial M_{xy}}{\partial y}-Q_x= I_r\partial^2\psi/\partial t^2 \tag{7-2}$$

$$\frac{\partial M_y}{\partial y}+\frac{\partial M_{xy}}{\partial x}-Q_y= I_r\partial^2\psi/\partial t^2 \tag{7-3}$$

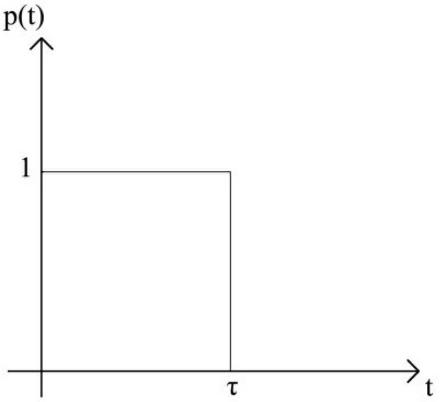

Figure 7-3- Temporally rectangular pulse shape

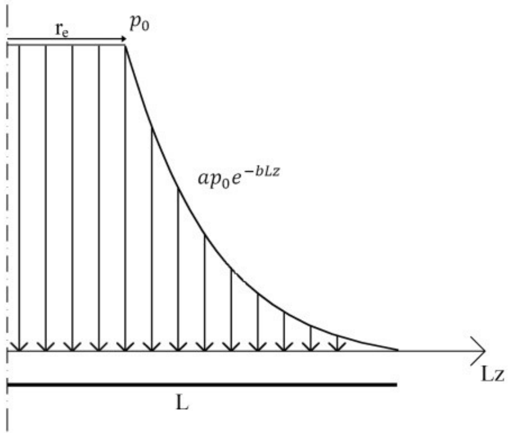

Figure 7-4- Spatially exponential distribution of load

where I_r is the rotatory inertia, the transverse shear strain is defined by $\gamma = \partial w/\partial x - \psi$; the $\partial w/\partial x = \psi + \gamma$ is the out of plane rotation of a line- in x direction- originally normal to the initial mid-plane due to bending, curvature rates in due to bending in x, y and twisting in xy directions are defined by $\dot{k}_x = \partial\dot{\psi}/\partial x$, $\dot{k}_y = \partial\dot{\psi}/\partial x$ and $\dot{k}_{xy} = -\partial^2\dot{\psi}/\partial y\partial x$, respectively. Clearly, both the transverse shear strains and rotational inertia contribute to the dynamic equilibrium equations in Eqns. (7-2)-(7-3), when the out-of-plane rotations emerge from transverse shear strains. In the absence of rotatory inertia, the right-hand side of these equations vanish, which is the scenario under study herein.

By referring to the dynamic continuity conditions across discontinuity front in beams and circular plates, it is noted that for quadrangular plates, $[M_i] = -\dot{Z}I_r[\dot{\psi}_i]$, $[Q_i] = -\mu\dot{Z}I_r[\dot{w}]$, where $[A] = A_2 - A_1$ is the difference of the quantity A across the discontinuity interface [114], [115]. For a simply supported plate, the boundary conditions are:

$$M_n|_{z=1} = 0\,,\quad Q_x|_{x=L,y=0} = Q_y\big|_{y=L,x=0} = -Q_0,\quad w|_{z=1} = 0,\ \dot{w}|_{z=0} = \dot{W} \qquad \textbf{(7-4a-d)}$$

In a similar procedure to the work of Cox and Morland [92] presented in Section 5.9, the bending moments across the interface may be expressed in terms of moment function $f(z)$, where z is the auxillary generalised coordinates of plate (as illustrated in Figure 7-5):

$$M_x = M_0 + x^2 f(z) \qquad \textbf{(7-5)}$$

$$M_y = M_0 + y^2 f(z) \qquad \textbf{(7-6)}$$

$$M_{xy} = xyf(z) \qquad \textbf{(7-7)}$$

Eqns. (7-5)- (7-7) satisfy the moment boundary conditions at the plate centre and at the supports. However, they must also satisfy the kinematic admissibility conditions and the conservation of linear and angular momentum, i.e. they should nowhere violate the yield conditions. It transpires that the principle moments across the plate, M_2 and M_1 are bound to $-M_0 \leq M_n \leq M_1$, where M_n is the bending moment normal to the generalised coordinate in direction n, given in [160]. Provided the rotator inertia effects are ignored, combining Eqns. (7-5)-(7-7) with (7-1)-(7-3), given that $zL = \sqrt{x^2 + y^2}$ yields Eqns. (5-18)-(5-19)

In a similar procedure to the theoretical treatment in Section 5.9, the non-homogenous, ordinary differential equation is solved for various loading conditions that give rise to the corresponding velocity profile which must satisfy the yield conditions. While the definitions in Eqns. (7-5)-(7-7) give rise to $M_1 = M_0$, the principle moment M_2 and transverse shear forces would reduce to:

$$\frac{\mathrm{M}_2}{M_0} = 1 + z^2 L^2 f(z)/M_0 \tag{7-8}$$

$$Q_x = x\left(3f + \frac{z\partial f}{\partial z}\right) \tag{7-9}$$

$$Q_y = y\left(3f + \frac{z\partial f}{\partial z}\right) \tag{7-10}$$

7.4 YIELD CRITERION

It is assumed that the transverse shear strains emerging from the infinitely large shear sliding are sufficiently large to contribute to rotation changes at the onset of the motion. Considering the Drucker's plasticity postulate on convexity of the yield surface and ignoring the visco-plasticity (strain rate sensitivity) effects, the plastic flow is controlled by interaction of transverse shear and bending moment, in the extended yield surface square which circumscribes the Tresca's yield surface and normality conditions, as shown in Figure 7-6, the direction if the strain rate remains orthogonal to the yield surface at any point.

$$M_0 = \sigma_0 \, H^2/4 \tag{7-11}$$

$$Q_0 \cong \frac{\sigma_0 H}{2} \tag{7-12}$$

In Eqns. (7-11)-(7-12), M_0 and Q_0 being the maximum plastic bending moment per unit length and the maximum lateral shear force per unit length, respectively. It is pragmatic to define the following dimensionless parameters:

$$\overline{q_d} = Q_d/Q_0, \quad \overline{m} = M_2/M_0, \quad \bar{\lambda} = \frac{V_0^2 L^2 \mu}{M_0 H}, \quad \overline{w}_f = W_f/H, \tag{7-13a-g}$$

$$\tau^* = \mu L^2 V_0/M_0, \quad \bar{\ddot{w}} = \frac{M_0}{L^2 \mu} \quad \nu = Q_0 L/2M_0$$

The dimensionless parameter ν in Eqn. (7-13-g) characterises the ratio of plastic bending to shear and reduces to slenderness ratio L/H for the prismatic sections, a measure of plate geometry.

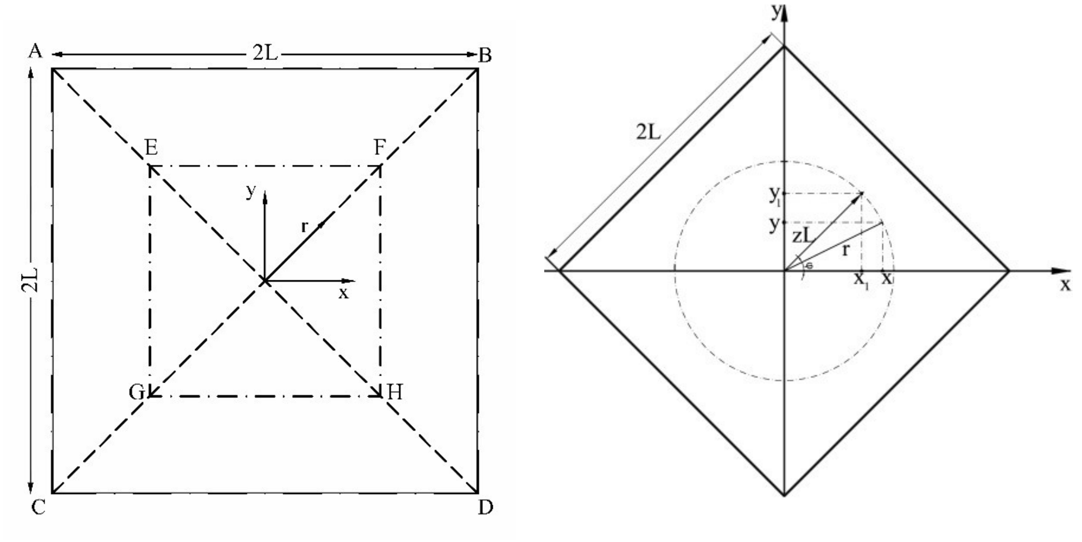

(a) (b)

Figure 7-5- (a) The top view of a simply-supported square plate (coordinates x, y, r and dimensionless parameter z are shown), (b) the plate with side lengths 2L whose diagonals are in the Cartesian Coordinates

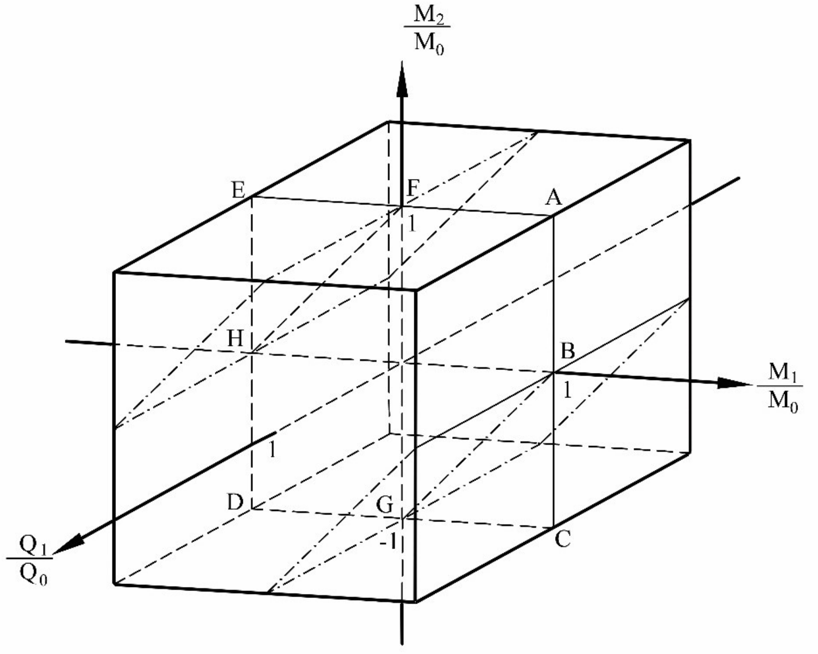

Figure 7-6 Tresca yield surface $(-.-)$ vs. the square yield surface (continuous bold line)

7.5 IMPULSIVE LOADING

The impulsive blast pressure is already defined in Section 4-14. It has been established that the impulsive velocity due to localised blast is given by:

$$V_0 = \frac{\tau p_0}{\mu}\left(\frac{\epsilon_1}{L^2}\right) \tag{7-14}$$

$$\epsilon_1 = \left[\frac{r_e^2 b^2 - 2ae^{-Lb}(bL+1) + 2r_e b + 2}{b^2}\right] \tag{7-15}$$

Most typical cases of localised blast the ratio of stand-off to charge diameter varies between 0.5 to 5, which correspond to the normalised loading radius $r_e/L \leq 0.2$ assuming small values and the loading exponent ranging from $50 \leq b \leq 100$. Thus, the impulse parameter ϵ_1 would have a range of $\epsilon_1 \leq 0.2L^2$, as observed in the Figure 7-7. It transpires that for the typical impulsive localised blasts, the impulsive velocity is irrespective of the loading distribution and is directly proportional to the peak pressure load and duration of the pulse pressure.

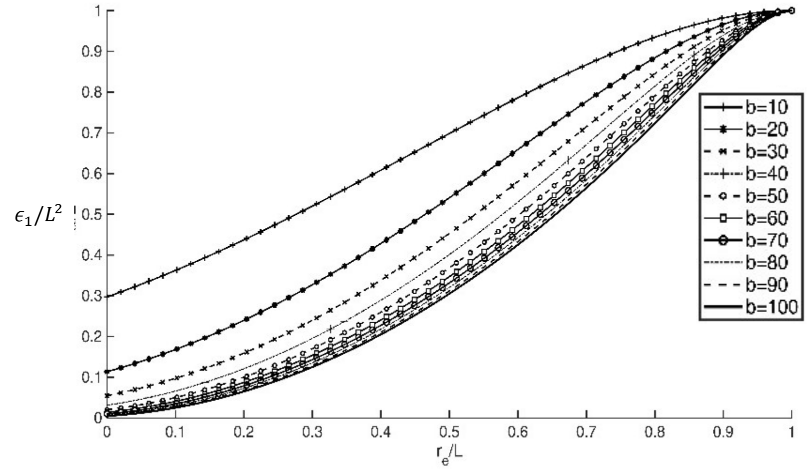

Figure 7-7- variation of α with the radius of the blast load

7.6 STATIC COLLAPSE PRESSURE

7.6.1 Transverse shear of plate in static pressure

Through the consideration of bound theorem, the exact static plastic collapse of the plate subject to a generic blast load was expressed in Eqn. (5-27). Substituting Eqns. (5-20a-b) in the

Eqn. (7-9) and using (5-21a-c) and (7-4-b) leads to the static transverse shear at the boundary in Eqn. (7-16). An identical expression would be reached if Eqn. (7-10) was employed.

$$\left|\frac{Q_s}{Q_0}\right| = -\frac{\left[(Lb+1)e^{-Lb+br_e} - \frac{1}{2}b^2r_e^2 - br_e - 1\right]}{2L^2b^2\beta\nu} \tag{7-16}$$

7.7 DYNAMIC COLLAPSE PRESSURE

Through consideration of static admissibility, it has been shown that a critical value of the dynamic amplification factor η exists such to avoid yield violation in the case of stationery plastic hinge. For square plates subject to uniform blasts, $\beta = 1/6$ thus, $\eta = 2$ [35], while for the localised blast, η has been evaluated as in Eqn. (5-40).

Now, using an identical procedure to the static case, by considering the shear sliding at the supports (i.e. Eqn. (7-4-b), the dynamic transverse shear is evaluated as:

$$\left|\frac{Q_d}{Q_0}\right| = \left(\frac{2L^2b^2\beta + ae^{-bL}(1+Lb) - bre - \frac{1}{2}b^2re^2 - 1}{4L^2b^2\beta}\right)\left(\frac{\eta}{\nu}\right) - \frac{1}{\nu} \tag{7-17}$$

The expressions (7-16) and (7-17) in various loading conditions are graphed in Figure 7-8-Figure 7-11.

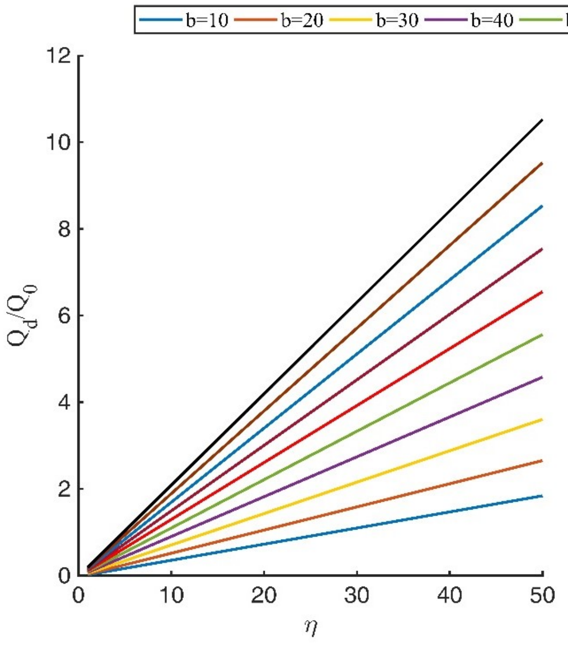

Figure 7-8-Influence of the Loading parameters on the Dynamic transverse shear at the plate contour. With $H/L = 0.02$ and $r_e/L = 0.125$

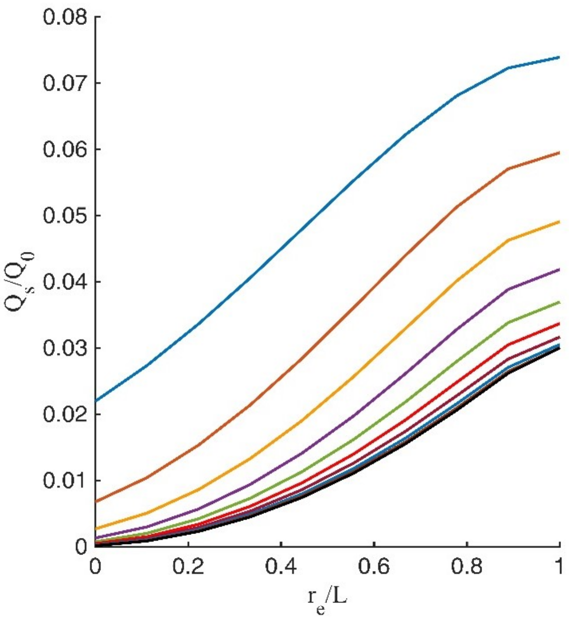

Figure 7-9-Static transverse shear effect with various loading type- With $H/L = 0.02$ and $r_e/L = 0.125$

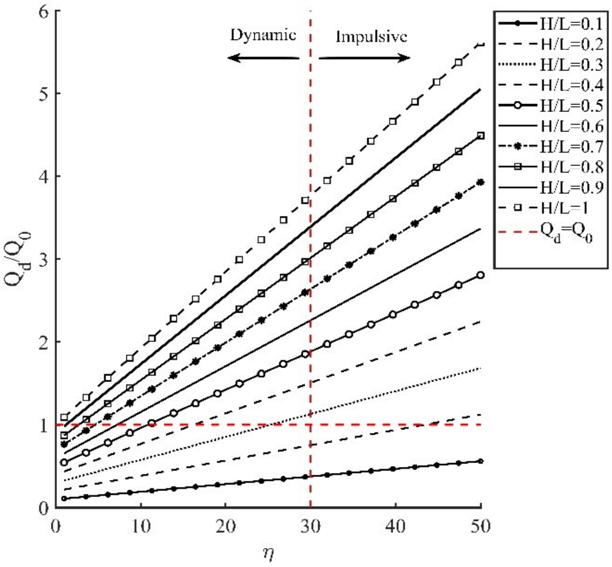

Figure 7-10-Influence of the overloading factor on the dynamic transverse shear ($r_e/L = 0.7$) b=50

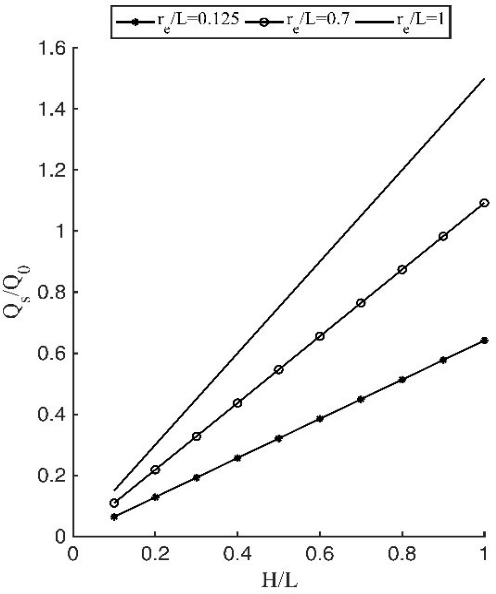

Figure 7-11-Influence of the thickness on the static transverse shear ($b = 50$)

From the observations in Figure 7-8-Figure 7-11, in the range of $H/L \ll 1$, evidently, the static transverse shears do not contribute to the overall response. As the loading is concentrated to the localised portion of the plate, i.e., r_e/L<<1-which is the typical case of the localised blasts, the transverse shears become vanishingly small. However, the dynamic shear sliding is highly influenced by the load amplification factor η. With the increases of η beyond 30, the region where the loading can be attributed as impulsive(as observed in Figure 5-13), considerable shear sliding may emerge even for plates of moderate-high thickness, i.e. H/L=0.3 or $\nu = 3.3$ (Figure 7-10). Transverse shear effects in low values of η is important only for very stocky plates which are not practical cases in the design of protective systems.

7.8 IMPULSIVE LOADING OF CLASS I (VERY STOCKY) PLATES ($\nu \leq 3/2$)

It may be assumed that the deformation profile of stocky plates of this class would take the form of Figure 7-12, as the plate is weak under the shear and the velocity profile is dominantly characterised by the shear sliding at both ends. Subsequently, from Eqn. (5-30), $f = \mu\ddot{W}/6$ (since $I_r = p_0 = 0$) which may be rewritten as:

$$\ddot{W} = \frac{-2Q_0}{\mu L} \tag{7-18}$$

since at $x = L$ and $z = 1$(or $y = L$ and $z = 1$), $Q = -Q_0$. Two-time integration of Eqn. (7-18), with $W(0) = \dot{W}(0) = 0,$ gives:

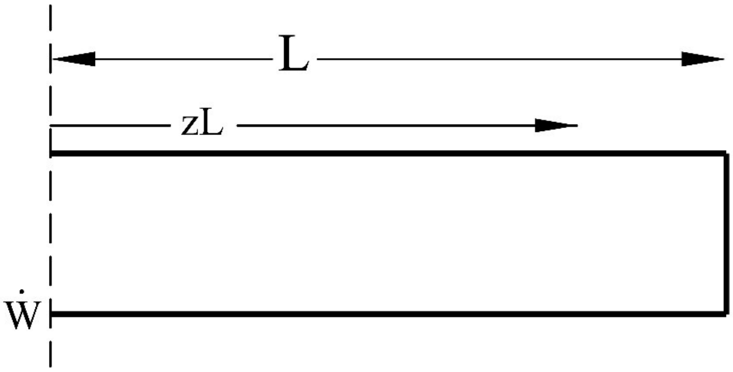

Figure 7-12-velocity profile of very stocky plates

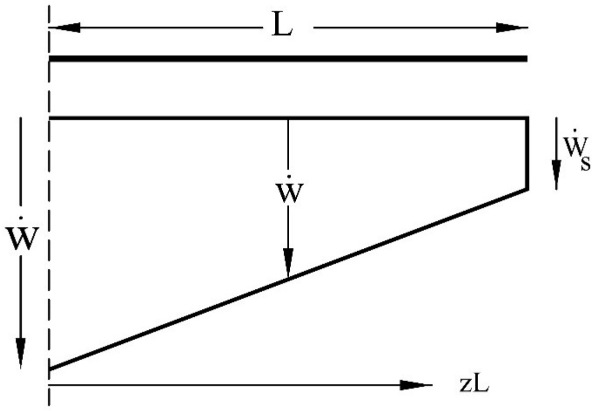

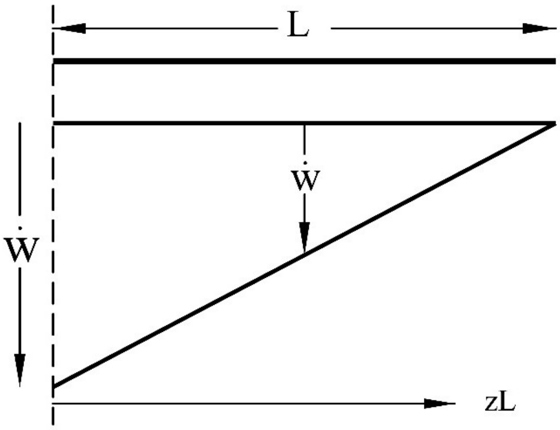

Figure 7-13- The assumed velocity profile-phase 1

Figure 7-14-The assumed velocity profile-phase 2

$$W(t) = \frac{-Q_0}{L\mu}t^2 + V_0 t \tag{7-19}$$

The plate rests at $T = V_0\, L\mu/2Q_0$ when the velocity of the plate vanishes. This gives the permanent deflection as:

$$\bar{w}_f = \frac{\bar{\lambda}}{8\nu} \tag{7-20}$$

Thus, the principle moment in Eqn. (7-8) may be expressed as :

$$\bar{m} = 1 - \frac{2\nu z^2}{3} \tag{7-21}$$

Provided $\nu \leq 1.5$, the static admissibilty is satisfied with the plate profile assumed in Figure 7-12. The bending moment penetrates the yield surface with $\nu > 1.5$ and the yield condition in the is violated. The yield violation implies an alternative velocity profile described as follows.

7.9 IMPULSIVE LOADING OF CLASS II (STOCKY) PLATES, $(1.5 < \nu \leq 2)$

The velocity profile of class II plates of $\nu > 1.5$, may be characterised in two phases of motion: an incipient velocity discontinuity at the support, occurring at the first phase due to the infinite shear sliding, as presented in Figure 7-13, which vanishes at the second phase as the shear sliding vanishes at the plate contours. The velocity profile in the first phase would take the form $\dot{w} = \dot{W}_s + (\dot{W} - \dot{W}_s)(1 - z)$, which develops into profile in Figure 7-14 in the second phase of motion. Thus, the moment function can be written as in Eqns. (7-22)- (7-23); with the constants $A_2 - D_2 = 0$ considering impulsive load case.

$$f = \begin{cases} \dfrac{\left(\mu\left((\ddot{W} - \ddot{W}_s)(2 - z) + 2\ddot{W}_s\right) - p_0\right)}{12} + \dfrac{A_1}{z^2} + \dfrac{B_1}{z^3} & 0 \leq z \leq r_e/L \quad \textbf{(7-22)} \\ \dfrac{-ap_0e^{-bLz}(bLz + 2)}{(bLz)^3} + \dfrac{\mu\left((\ddot{W} - \ddot{W}_s)(2 - z) + 2\ddot{W}_s\right)}{12} + \dfrac{D_1}{z^2} + \dfrac{E_1}{z^3} & r_e/\mathrm{L} \leq z \leq 1 \quad \textbf{(7-23)} \end{cases}$$

In the same fashion, the boundary conditions of transverse shear and bending moments at the plate contour, i.e. $Q_x(x = L, y = 0) = -Q_0$ and $M_2(z = 1) = 0$ results in two sets of simultaneous expressions, which solutions gives Eqns. (7-24)-(7-26):

$$\ddot{W} = -\frac{12M_0(2 - \nu)}{L^2\mu} \qquad \textbf{(7-24)}$$

$$W = V_0t - \frac{6M_0t^2(2 - \nu)}{L^2\mu} \qquad \textbf{(7-25)}$$

$$\ddot{W}_s = \frac{12M_0(1 - \nu)}{L^2\mu} \qquad \textbf{(7-26)}$$

This phase terminates $t = T_1$, denoted in Eqn. (7-27) as the time when the velocity discontinuity at the support disappears. Thus, the maximum deformation is furnished to Eqn. (7-28):

$$T_1 = \frac{L^2V_0\mu}{12M_0(\nu - 1)} \qquad \textbf{(7-27)}$$

$$\frac{W_1}{H} = \frac{\bar{\lambda}(3\nu - 4)}{24\,(\nu - 1)^2} \qquad \textbf{(7-28)}$$

with the inertia terms now known *priori*, the bending moment from Eqn. (7-21) at any point of the plate yields:

$$\bar{m} = -(z - 1)(z + 2\nu z^2 - 3z^2 + 1) \qquad \textbf{(7-29)}$$

At the plate centre; the range of $\nu > 2$, causes a yield violation $(\partial^2\bar{m}/\partial z^2 > 0)$. Consequently, the profile assumed in this phase is only valid for the range of $1.5 \leq \nu \leq 2$.

7.9.1 Second phase of motion

A time-derivative of Eqn. (7-25) suggests that the kinetic energy is maintained in the plate, which must be dissipated before the motion ceases. The velocity profile in this phase is now written as $\dot{w} = \dot{W}(1 - z)$; which furnishes the solution of the P.D.E (Eqns. (5-30 a-b)) to Eqn. (7-22), (7-23), but with $\ddot{W}_s = 0$. Thus, solving the condition of $\bar{m} = 0$ (at the plate contour) for transverse inertia gives $\ddot{W} = -12M_0/L^2\mu$, whereby the associated transverse velocity is:

$$\dot{W}_2 = 2V_0 - 12M_0t/L^2\mu \tag{7-30}$$

$$W_2 = V_0\left[2t + \frac{\tau^*}{24(1-\nu)} - \frac{6t^2}{\tau^*}\right] \tag{7-31}$$

The succeeding Eqns. (7-30)-(7-31) are obtained by ensuring the kinematic continuities of velocity and transverse displacement field with the previous phase at $t = T_1$. The plate rests at $t = \tau^*/6$, reducing the permanent transverse displacement to:

$$\bar{w}_f = \frac{\bar{\lambda}(4\nu - 5)}{24(\nu - 1)} \tag{7-32}$$

7.10 CLASS III PLATES ($\nu > 2$)

7.10.1 Phase 1- $0 < t < T_1$

As discussed before, when $\nu > 2$, a yield violation occurs at the centre of the class II plates, suggesting a modification to the velocity profile. To avoid the yield violation, it is assumed that the velocity profile of class III plates is characterised with three stages of motion, namely, (i) phase 1 with appearance of incipient stationary plastic hinge Figure 7-15, (ii) a transient phase 2, where the plastic hinge travels inward toward the centre of the plate (Figure 7-16) and (iii) phase 3 with the residual deformation as the length of the central plastic hinge line vanishes, wherein the velocity profile develops from Figure 7-16 to Figure 7-14. Thus, in the first phase of motion, the velocity profile may be assumed as:

$$\dot{w} = \dot{W} \qquad \mathbf{0 \leq z \leq \xi_0} \qquad \textbf{(7-33)}$$

$$\dot{w} = \frac{\left(\dot{W} - \dot{W_s}\right)(1-z)}{1-\xi_0} + \dot{W_s} \qquad \mathbf{0 \leq z \leq r_e/L} \qquad \textbf{(7-34)}$$

which are substituted in the succeeding moment function to:

$$f = \begin{cases} \left(\mu\ddot{W} - p_0\right)/6 + A_3/z^2 + B_3/z^3 & 0 \leq z \leq r_e/L \qquad \textbf{(7-35)} \\ \dfrac{\mu\ddot{W}}{6} - \dfrac{ap_0e^{-bLz}(bLz+2)}{(bLz)^3} + D_3/z^2 + E_3/z^3 & r_e/\mathrm{L} \leq z \leq \xi_0 \qquad \textbf{(7-36)} \\ \dfrac{-ap_0e^{-bLz}(bLz+2)}{(bLz)^3} + \dfrac{\mu\left(\dfrac{\left(\ddot{W}_1 - \ddot{W}_s\right)(2-z)}{1-\xi_0} + 2\ddot{W}_s\right)}{12} + \dfrac{F_3}{z^2} + \dfrac{G_3}{z^3} & \xi_0 \leq z \leq 1 \qquad \textbf{(7-37)} \end{cases}$$

It is also assumed that $\xi_0 \geq r_e$. The yield condition of the bending moment in the central zone yields $\bar{m} = 1$; hence, $Q = 0$ and $\mu\ddot{W} = p_0$ throughout the entire zone ($0 \leq z \leq \xi_0$). The succeeding time integrations of the latter expression gives $\dot{W}_1 = p_0t/\mu$ and $W_1 = p_0t^2/2\mu$, respectively. Accordingly, the constants of the moment function in the central zone are obtained by ensuring the kinematic continuity of the transverse shear and moment at $z = r_e/L$ and the plate centre; giving identical expressions to those of Eqns. (4-21a-b), whereas the constants in (7-37) are evaluated from the kinematic conditions of f at $z = \xi_0$, (i.e. $Q = 0$ and $\bar{m} = 1$) as:

$$F_3 = \frac{\left(-6a(\xi_0 - 1)(Lb\xi_0 + 1)e^{-Lb\xi_0} - (bL\xi_0)^2(2\xi_0 - 3)\right)p_0}{6L^2b^2(\xi_0 - 1)} - \frac{\ddot{W}_s\mu\xi_0^3}{6(\xi_0 - 1)} \qquad \textbf{(7-38)}$$

$$G_3 = \frac{\left[(3\xi_0 - 4)(bL\xi_0)^3 + 12a(\xi_0 - 1)((bL\xi_0)^2 + 2Lb\xi_0 + 2)e^{-Lb\xi_0}\right]p_0}{12L^3b^3(\xi_0 - 1)} + \frac{\ddot{W}_s\mu\xi_0^4}{12(\xi_0 - 1)} \qquad \textbf{(7-39)}$$

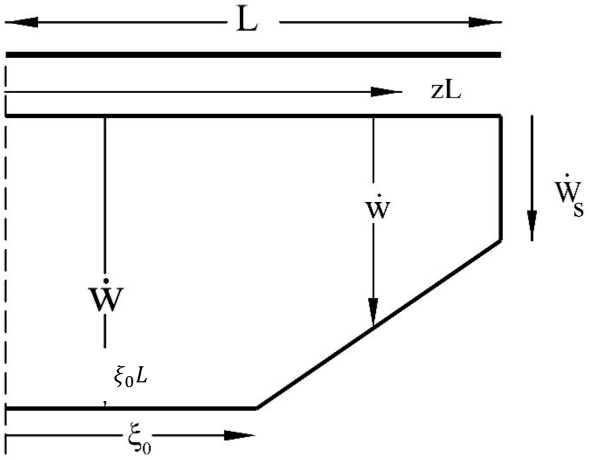

Figure 7-15 the assumed velocity profile for plates of $\nu > 2$ at first phase of motion

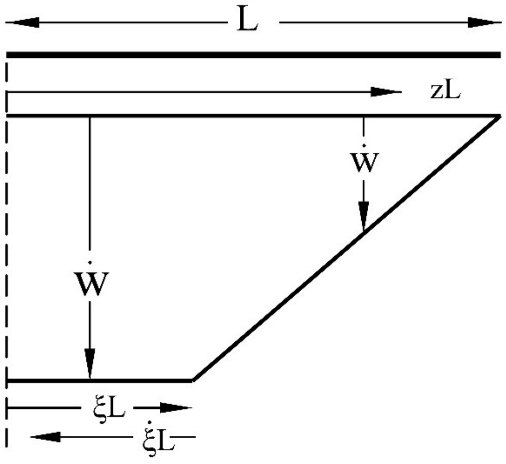

Figure 7-16- assumed velocity profile for plates of $\nu > 2$ at subsequent phase of motion

Thus, substituting Eqn. s (7-34)-(7-36) in (7-8)-(7-10), then enforcing the boundary conditions of $Q_x = -Q_0$ and $M_1 = 0$ at $x = L$ yields two sets of expressions, the former is used to evaluate the inertia at the support $\ddot{W}_s$ in Eqn. (7-40). Thus:

$$\ddot{W}_s = \left[\frac{\delta_1 p_0}{M_0 b^2(\xi_0^2 + \xi_0 - 2)} + \frac{12\nu}{(\xi_0^2 + \xi_0 - 2)}\right]\bar{\ddot{w}} \tag{7-40}$$

where $\bar{\ddot{w}} = V_0/\tau^*$ and δ_1 is given by:

$$\delta_1 = 6a(Lb\xi_0 + 1)e^{-Lb\xi_0} - 6a(Lb + 1)e^{-bL} + 2b^2L^2(\xi_0 + 1/2)(\xi_0 - 1) \tag{7-41}$$

The latter condition is used to evaluate an expression of the stationary plastic hinge ξ_0 in Eqn. (7-42).

$$\bar{m} = \frac{\Gamma_1 \eta}{12L^3b^3\beta} + \frac{\mu L^2(\xi_0 + 1)(\xi_0 - 1)^2\ddot{W}_s}{12M_0} + 1 = 0 \tag{7-42}$$

where

$$\begin{aligned}\Gamma_1 = {} & 12a\left(2 + b^2L^2\xi_0(\xi_0 - 1) + bL(2\xi_0 - 1)\right)e^{-Lb\xi_0} - 12a(Lb + 2)e^{-Lb} \\ & + L^3b^3(3\xi_0 + 1)(\xi_0 - 1)^2\end{aligned} \tag{7-43}$$

The expression of ξ_0 in (7-42) is highly nonlinear which can only be solved by numerical methods. It should be noted that, in the absence of the inertia term $\ddot{W}_s$, which occurs as ν approaches large values, Eqn. (7-42) converges to the plates under consideration of bending only. Eqn. (7-40) is similar to the analysis of [111], [114], except an additional term of load appearing in the first term of the bracket, emerging from the spatial distribution of the (dynamic) load type. A time integration[1] of (7-40) yields:

$$\dot{W}_s = \left[\frac{-\delta_1 p_0 \tau}{M_0 b^2(\xi_0^2 + \xi_0 - 2)} + \frac{12\nu t}{(\xi_0^2 + \xi_0 - 2)}\right] \bar{\ddot{w}}^{2} \tag{7-44}$$

This phase terminates when the shear velocity at the support vanishes, at time T_1given in (7-45):

$$T_1 = \frac{\delta_1 p_0 \tau}{12 b^2 M_0 \nu} \tag{7-45}$$

The permanent displacement corresponding to this time is given as:

$$\frac{W_1}{H} = \frac{\delta_1^2 p_0^3 \tau^2}{288 M_0^2 b^4 \nu^2 \mu H} \tag{7-46}$$

If the transverse shear effects are neglected, this phase lasts until the load disappears at $T_1 = \tau$. Considering the impulsive load scenario, $\ddot{W} = p_0 = 0$, only the last terms on the right-hand side of the expressions (7-38)-(7-39) would remain. In such a case, the transverse deformation at the discontinuity front reduces to $W_s = V_0 \mathrm{t} + (6 V_0 \nu t^2)/(\tau^* \, (\xi_0^2 + \xi_0 - 2))$. Thus, the end time of this phase may be evaluated as the velocity at the discontinuity front vanishes, occurring at $T_1 = -\tau^*/12(\xi_0^2 + \xi_0 - 2)$. The associated final deformation of this phase is given in Eqn. (7-47):

$$\frac{W_1}{H} = \frac{-\bar{\lambda}}{12[\xi_0^2 + \xi_0 - 2]} \tag{7-47}$$

---

[1] The first term contributes to the duration of the load and is integrated from the onset of motion until the load vanishes at $t = \tau$, while the second term is integrated arbitrarily. The discontinuity front at the support continues to decelerate beyond τ until it rests at $t = T_1$.

[2]

which is similar to the results obtained for impulsively loaded circular plates in Ref. [112], except the spatial distribution of the load contributes to the magnitude of the impulsive velocity V_1, and, by extension, the dimensionless kinetic energy. Hence, the moment and shear in the outer zone of the (impulsively loaded) plate simplify to:

$$\bar{m} = 1 + \frac{\ddot{W}_s(\xi_0 + z)(\xi_0 - z)^3}{12\ddot{\bar{w}}z(\xi_0 - 1)} \qquad \xi_0 \leq z \leq 1 \qquad \textbf{(7-48)}$$

$$Q_x = \frac{-\mu x\ddot{W}_s(\xi_0 - z)^2(\xi_0 + 2z)}{6z^2(\xi_0 - 1)} \qquad \xi_0 \leq z \leq 1 \qquad \textbf{(7-49)}$$

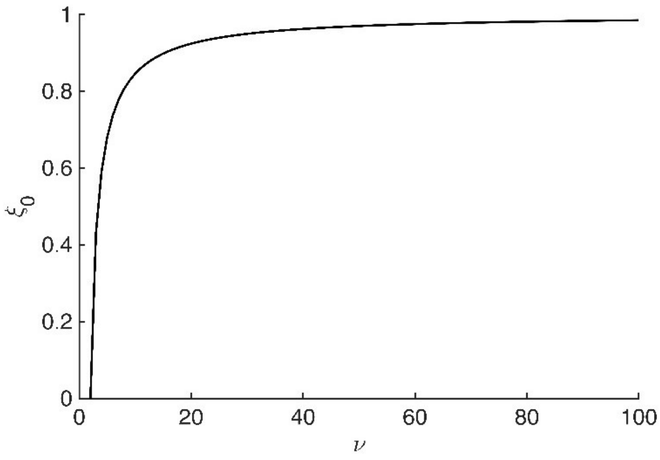

Figure 7-17-variation of ξ_0 with ν

Since M is continuous at the plastic bending hinge (i.e. $M_x = M_0$ at $x = \xi_0 L$ and $y = 0$ or $M_1 = M_0$ at $z = \xi_0$), an expression of the initial plastic hinge is achieved in Eqn. (7-50) and plotted Figure 7-17.

$$\xi_0 = \frac{\left(-1 + \sqrt{4\nu^2 - 8\nu + 1}\right)}{2\nu} \qquad \textbf{(7-50)}$$

7.10.2 Phase 2- $T_1 < t < T_2$

The second phase initiates as the transverse shear sliding is removed at the supports beyond $t = T_1$, the deformation profile takes that of Figure 7-16. Due to the absence of the loading, the central zone travels with constant velocity $\dot{W}_2$ while the size of the central zone diminishes monotonically as the time dependent plastic hinge $\xi(t)$ now moves inward. Thus, clearly $\ddot{W} = 0$, and the kinematic admissibility dictates that $\dot{W}_2 = \dot{W}_1$ at $t = T_1$, giving rise to $\dot{W}_2 = p_1 T_1/\mu$. The piecewise moment function in (7-35)- (7-37) remains valid, with $A_3 - D_3 = 0$ while constants Eqn. (7-37) become:

$$F_3 = \frac{\mu\xi^2\dot{W}\dot{\xi}(2\xi - 3\,)}{6(\xi\, -\, 1)^2} \qquad \textbf{(7-51)}$$

$$G_3 = -\frac{\mu\xi^3\dot{W}\dot{\xi}(\xi - 4/3)}{4(\xi - 1)^2} \qquad \textbf{(7-52)}$$

which were obtained by substitution of $\ddot{w}\ =\ (1 - z)d(\dot{W}/(1 - \xi(t)))/dt$ in Eqns. (5-30 a-b), using $p_1\, = 0$ and solving the Partial differential equation (P.D.E).

By appreciating the boundary condition of the principle moment at the edge, (i.e. $M_2|_{z=1}\, = 0$), an expression of the travelling plastic hinge is obtained:

$$\bar{m} = 1 - 1/4\tau^*\dot{\xi}(t)\left(\xi(t) + \frac{1}{3}\right)(\xi(t) - 1)\ = 0 \qquad \textbf{(7-53)}$$

A time integration of Eqn. (7-53) furnishes the succeeding expression of travelling plastic hinge in Eqn. (7-54):

$$t\ + \frac{\tau^*\xi(t)(\xi(t)^2 - \xi(t) - 1)}{12M_0} = \tau^* \qquad \textbf{(7-54)}$$

where the constant of integration is obtained from the kinematic conditions at $t = T_1$, $\xi(T_1) = \xi_0$. The size of the central platform zone decreases monotonically and ultimately vanishes as the plastic hinge $\xi(t)$ reaches the centre of the plate, i.e. $\xi(t)\, = 0$. This marks the end of phase 2 which occurs at time $t = T_2$, given as:

$$T_2 = \frac{\tau\delta p_0[p_0 L^2\xi_0(1 - \xi_0^2 + \xi_0) + 12M_0)}{144M_0^2 b^2 \nu} \qquad \textbf{(7-55)}$$

which is simplified to $T_2 = \tau^*/12$ for impulsive load cases.

7.10.3 Phase 3 $T_2 \leq t \leq T_f$

The central plastic hinge disappears at $t = T_2$. However, due to the reserved kinetic energy the motion continues with residual deformation until all kinetic energy is dissipated before the plate finally comes at rest. The velocity profile in this phase is expressed by a conical velocity which is identical to the previous case, i.e. the profile given in Figure 7-14; while the inertia term expressed by $\ddot{W}_3 = -12\ddot{\bar{w}}$. The solutions to the state variables (permanent deformation and velocity fields) at this phase are achieved by time integrations of this expression and ensuring the kinematic admissibility of the transverse velocity and deformation with the previous phase. The final displacement can be evaluated when the velocity vanishes, (i.e. $\dot{W}_3$=0):

$$W_f = \frac{p_c\left(\frac{\eta}{\beta}\left(-\xi_0^3 + \xi_0^2 + \xi_0 + \frac{1}{2}\right) + 6\right)}{1728\mu\eta}\left(\frac{\delta_1 \tau \eta p_0}{\nu M_0 b^2}\right)^2 \tag{7-56}$$

Regarding the impulsive load response, the inertia term is identical to Eqn. (7-24) and the deformation fields are furnished as per Eqns. (7-57)-(7-58).

$$\frac{W_3}{H} = \frac{2V_0 t}{H} - \frac{\bar{\lambda}}{24} - \frac{6V_0 t^2}{\tau^* H} \tag{7-57}$$

$$\dot{W}_3 = 2V_0 - \frac{12M_0 t}{L^2 \mu} \tag{7-58}$$

In such case of impulsive loads, Eqn. (7-56) simplifies to $\bar{w}_f = \bar{\lambda}/8$, similar to the results of [162] for circular plates, whereas the loading distribution affects the magnitude of $\bar{\lambda}$. The permanent deformation in the case of impulsive load would occur at $T_f = \tau^*/6$. The central and end-point permanent deformations of the plate in various values of ν are plotted in Figure 7-18, Figure 7-19.

Provided the transverse shear strains do not contribute to the element rotations, the transverse shear sliding along the plate periphery can be neglected. The end time of first phase of motion T_1 from Eqn. (7-45) occurs at $T_1 = \tau$ and reduces the terms of the Eqn. (7-56) to the solution of plates where the plastic flow is governed by the interactive yield curve of bending only. The combined influence of the load magnitude and the plate thickness (based on ν) are graphed in Figure 7-20-Figure 7-21.

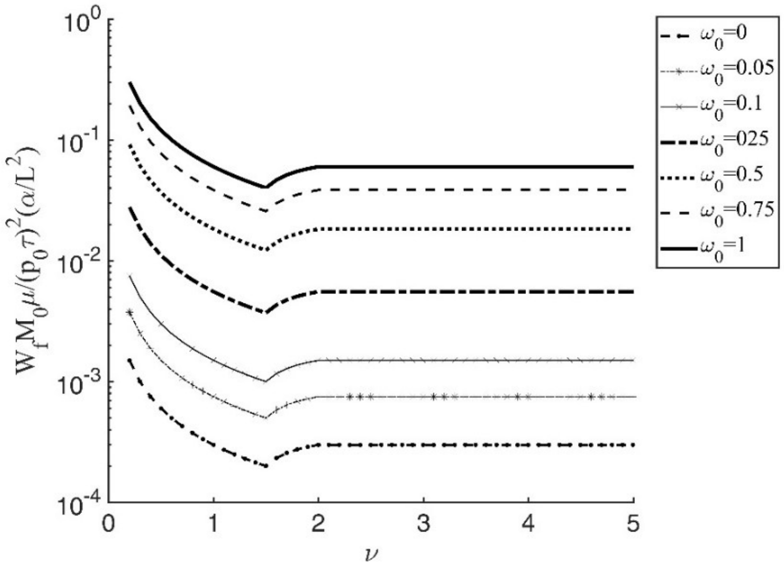

Figure 7-18- Variation of the permanent deformation (W_f) against ν for various loading conditions of impulsive load, where $\omega_0 = r_e/L$

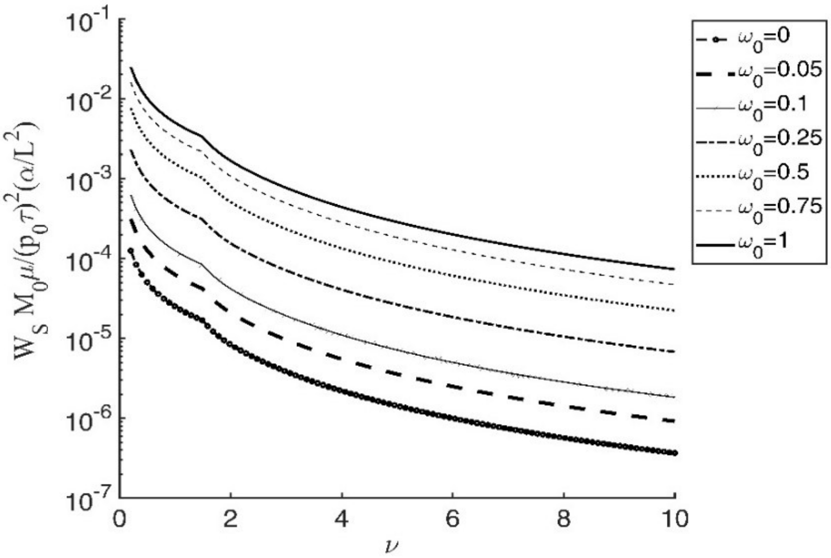

Figure 7-19- Variation of the deformation profile at discontinuous front (W_s) against ν for various loading conditions

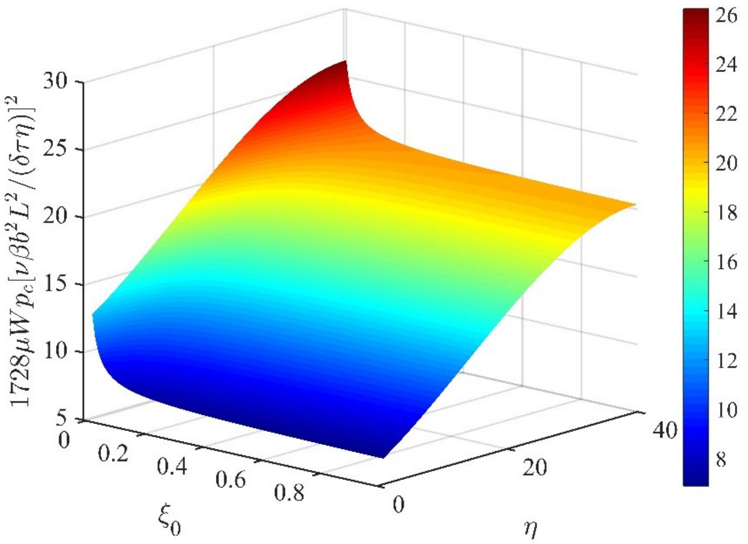

Figure 7-20- Intercative surface of dynamic load amplification factor, plastic hinge and central deformation

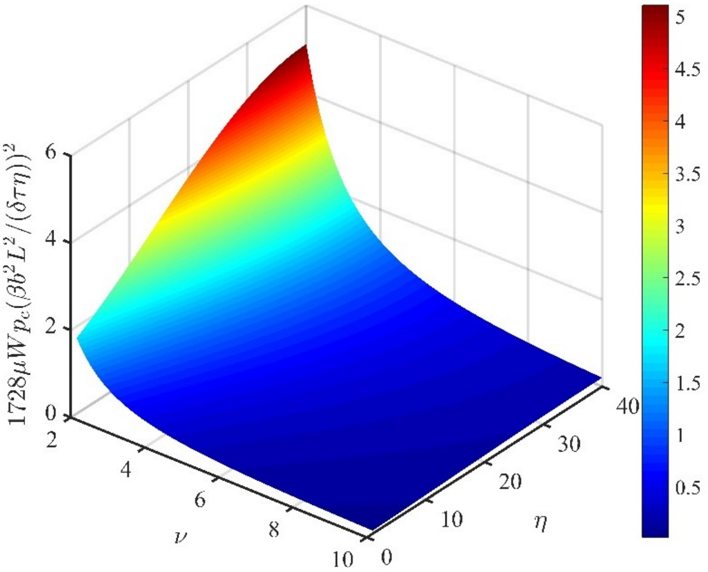

Figure 7-21- Influecne of the plate thickness and dynamic load amplification factor on the central deformation

7.11 FULLY CLAMPED PLATES

The foregoing analysis was limited to the simply supported plate systems, while in practical applications the plates are often designated with clamped boundary conditions. Notwithstanding this, the theoretical solutions in previous sections may be extended to the case of fully-clamped plate. Considering the boundary condition of principle moment at the plate contours, $\bar{m} = -1$, the static plastic collapse furnishes to $p_{cl} = 2M_0/(\beta L^2)$. Thus, all the expressions of fully clamped plate may be obtained by merely replacing M_0 with $2M_0$, η with $\bar{\eta} = 1/2\eta$ and ν with $\bar{\nu} = 1/2\,\nu$. The range of slenderness ratio in each class of the plate would be:

- Class I plates $\bar{\nu} < 3$
- Class II plates $3 < \bar{\nu} < 4$
- Class III plates $4 < \bar{\nu}$

7.12 **DYNAMIC PRESSURE PULSE LOADING**

In this section, a study on the influence of the pulse shape on the final response of the structure is presented, which includes exponential and linear pulse shapes. The type of explosion would give rise to the various pulse shape, i.e. exponential (high explosives), sinusoidal (gas deflagration/detonation) and linear. The diversity in the type of pulse pressure inhibits making correlation between various results.

However, hitherto, the foregoing analyses were limited to pulse pressure load having rectangular shape. A blast peak pressure with dynamic pressure more than 10 times the static collapse can be idealised as rectangular pulse [35], in which case the blast is idealised as impulsive and the pulse shape has no intrinsic effect on the response of the system. However, more often than not, the majority of the blast loads are non-impulsive and assume various pulse shapes (linear, exponential, sinusoidal). While the pulse shape can have significant effect on the overall response of the non-impulsive structure, its effect can be eliminated by utilising the Youngdahl's correlation parameters[37], [91], [152], [157], which efficacy is confirmed for monotonically decaying pulses by [100]. A general expression of the pulse shape introduced by Li and Meng [180] reads:

$$p_2(t) = \begin{cases} \left(1 - X\dfrac{t}{\tau}\right) e^{-Y\frac{t}{\tau}}, & 0 \le t \le \tau \\ 0 & \tau \le t \end{cases} \tag{7-59}$$

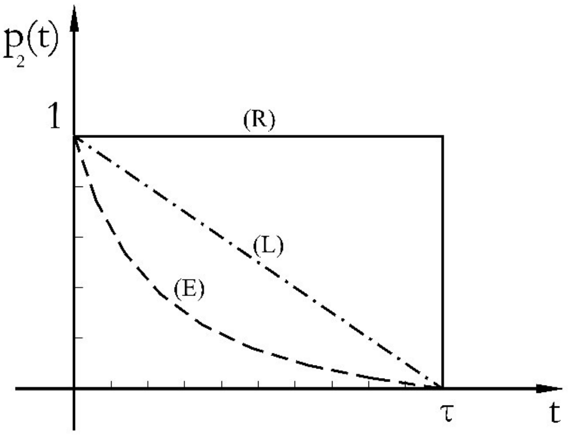

Figure 7-22- Typical temporal pulse loading shapes (R) rectngular (L) linear, (E) exponential

While the expression (7-59) represents a generic exponential function, in particular circumstances, it reduces to rectangular pulse (when $X = Y = 0$), or linear pulse (when $X = 1, Y = 0$), as plotted in Figure 7-22.

An exponential pulse shape is defined as illustrated in Eqn. (7-59). Using the same procedure as described in Section 7.10.1 for class III plates, the deformation field and its derivatives are:

$$\ddot{W}_1 = \frac{p_0\left(1-\frac{t}{\tau}\right)e^{-\frac{t}{\tau}}}{\mu} \tag{7-60}$$

$$\dot{W}_1 = \frac{p_0 t e^{-\frac{t}{\tau}}}{\mu} \tag{7-61}$$

$$W_1 = -\frac{p_0\tau(t+\tau)e^{-\frac{t}{\tau}}}{\mu} \tag{7-62}$$

The end time of motion at phase 1 occurs as the velocity across the discontinuity front at the support vanishes. Eqn. (7-40) remains valid but with loading taking account of the modification in the pulse shape. Thus, integrating Eqn. (7-40) yields:

$$\dot{W}_s = \left[\frac{\delta_1 p_0 \tau e^{-1}}{M_0 b^2(\xi_0^2+\xi_0-2)} + \frac{12\nu t}{(\xi_0^2+\xi_0-2)}\right]\bar{\ddot{w}} \tag{7-63}$$

The first and second term are integrated separately as in the same manner in Section 7.10.1. The duration of the first phase is evaluated as:

$$\mathrm{T}_1 = -\frac{\tau e^{-1} p_0 \delta_1}{12 M_0 b^2 \nu} \tag{7-64}$$

The velocity of the second phase remains constant which is evaluated by substituting the time T_1 in Eqn. (7-61). Phase 2 continues until time T_2 when the central hinge zone vanishes, given as:

$$\mathrm{T}_2 = T_1 + T_1 \frac{\eta e^{-\frac{T_1}{\tau}} (-\xi_0^3 + \xi_0^2 + \xi_0)}{\beta} \tag{7-65}$$

Thus, the mid-point deformation at this phase is:

$$\begin{gathered} W_2 = -\frac{e^{-\frac{T_1}{\tau}} p_0^2 \tau e^{-1} \delta_1 t}{12 M_0 b^2 \nu \mu} + A_4 \\ A_4 = -\frac{e^{-\frac{T_1}{\tau}} p_0 \tau^2 (144 M_0^2 b^4 \nu^2 - 12 M_0 e^{-1} b^2 \delta_1 \nu p_0 + p_0^2 e^{-2} \delta_1^2)}{144 M_0^2 b^4 \nu^2 \mu} \end{gathered} \tag{7-66}$$

Finally, the deformation, velocity and acceleration fields of the third phase are given by:

$$\ddot{W}_3 = -12\,\overline{\ddot{w}} \tag{7-67}$$

$$\dot{W}_3 = -12\,\overline{\ddot{w}} t + C_4 \tag{7-68}$$

$$W_3 = -6\overline{\ddot{w}} t^2 + C_4 t + C_5 \tag{7-69}$$

Where the constants of integrations are obtained by the kinematic admissibility conditions of the velocity and deformation fields at $t = T_2$ with those of the previous phase as:

$$C_4 = \frac{p_0 e^{-1} \delta_1 \tau \left(L^2 p_0 (\xi_0^3 - \xi_0^2 - \xi_0 - 1) e^{-\frac{T_1}{\tau}} - 12 M_0 \right)}{12 M_0 L^2 b^2 \nu \mu} \tag{7-70}$$

$$C_5 = -\frac{\left(p_0 L \xi_0 T_1 e^{-\frac{T_1}{\tau}} \right)^2 (\xi_0^2 - \xi_0 - 1)^2}{24 M_0 \mu} + \tag{7-71}$$

$$\frac{\left((\xi_0^3-\xi_0^2-\xi_0-1)T_1^2-\tau T_1-\tau^2\right)p_0L^2e^{-\frac{T_1}{\tau}}-6M_0T_1^2}{\mu L^2}$$

Thus, the permanent deformation would reduce to:

$$W_f=-\frac{\left(L^2p_0T_1^2\left(\bar{\xi}+\frac{1}{2}\right)e^{-\frac{T_1}{\tau}}+12M_0\tau(T_1+\tau)\right)e^{-\frac{T_1}{\tau}}p_0}{12M_0\mu} \qquad \textbf{(7-72)}$$

Occurring at:

$$T_f=\frac{\left(12M_0-L^2p_1\bar{\xi}e^{-\frac{T_1}{\tau}}\right)T_1}{12M_0} \qquad \textbf{(7-73)}$$

where $\bar{\xi}=\xi_0^3-\xi_0^2-\xi_0-1$.

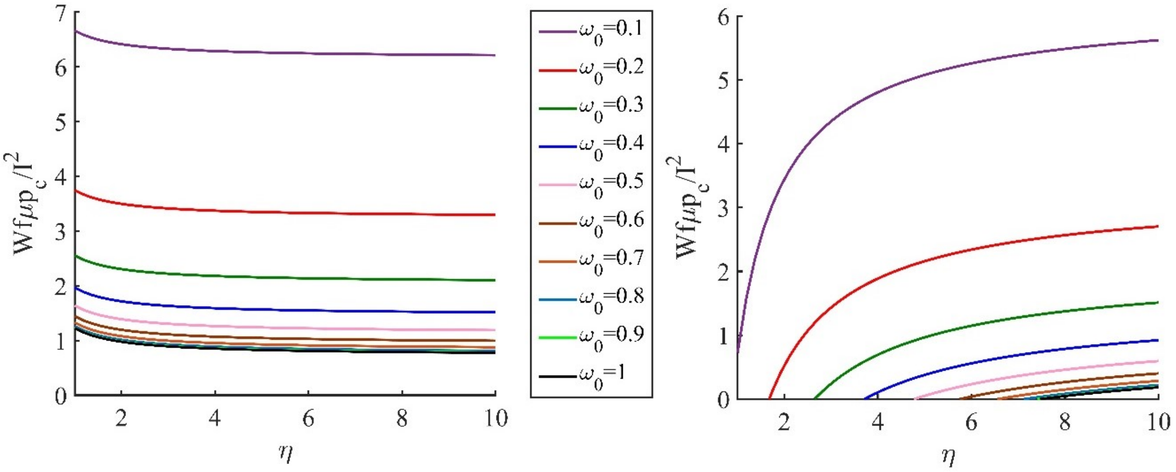

Figure 7-23- Pulse shape dependent response of the rectangular pulse (a) exponential pulse (b) ($\boldsymbol{b=50m^{-1}}$, $\boldsymbol{\nu=10}$) with various load radii.

The permanent deformation of the linearly decaying pulse, with $T_1=\delta p_1\tau/(24M_0b^2\nu)$ can be written as:

$$W_f=-\frac{\left((T_1-2\tau)\left((\bar{\xi}+1)\tau^2-(2\bar{\xi}+1)T_1\tau+\left(\bar{\xi}+\frac{1}{2}\right)T_1^2\right)\eta+8\beta T_1\tau(T_1-3\tau)\right)\eta T_1p_c}{48\tau^2\beta\mu} \qquad \textbf{(7-74)}$$

Occurring at:

$$T_f=\left(\frac{1}{24}\right)\left(L^2(\bar{\xi}+1)\tau^2-2T_1L^2\bar{\xi}\tau+L^2T_1^2\bar{\xi}\right)\eta/(\tau\beta L^2)+T_1 \qquad \textbf{(7-75)}$$

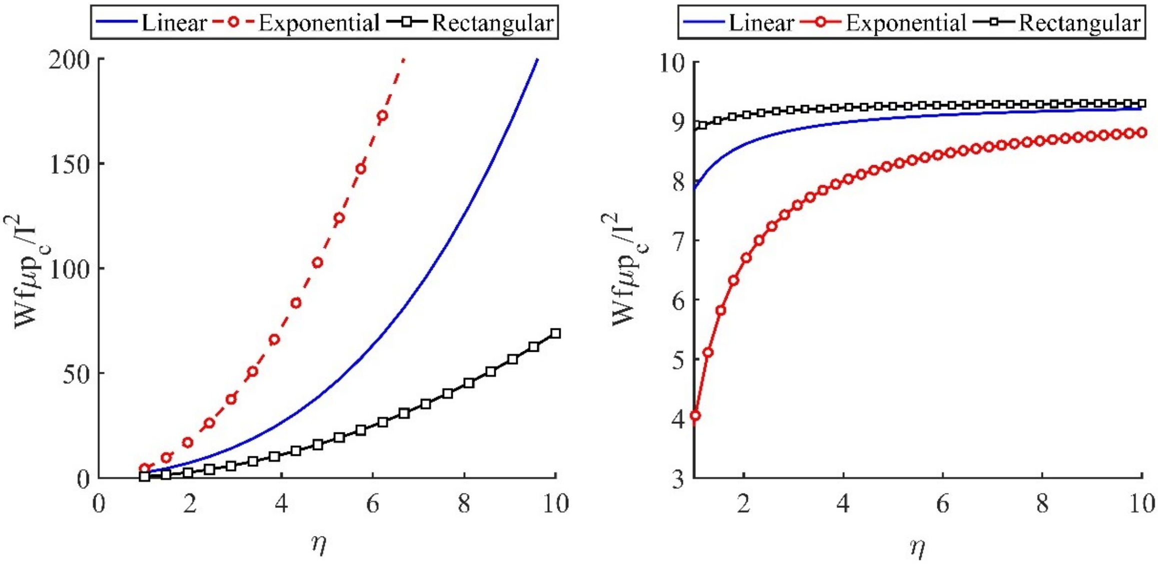

Figure 7-24- Pulse shape dependent response with transverse shear effects (a) without transverse shear effects (b) ($b = 50m^{-1}, r_e/L = 0.05,\ \nu = 10$)

A plot of exponential and rectangular pulse shape effects for various loading radii is graphed in Figure 7-23. Clearly, large variation in the response is observed as the loading radius decreases. The difference in the response also increases in the low range of the dynamic loading magnitude (i.e. $\eta > \sim 1$), as observed in Figure 7-24b. Clearly, there is a large variation in the normalised deformations due to the pulse shape, which increases with the increase of load magnitude as illustrated in Figure 7-24 (a). The reason for the difference in the curves of Figure 7-24 is when taking account of the transverse shear effects, the predicted duration of the first phase (T_1) is influenced by the magnitude of the loading, leading in turn to a divergence of the normalized permanent deformations. However, this is only valid for low magnitudes of the load. On the contrary, the deformation of the impulsively loaded plate, is pulse independent. This is also evident in Figure 7-24b on the plates where the intrinsic effect of the transverse shear is vanishingly small.

As discussed earlier, if the shear sliding during phase 1 of motion is neglected beyond loading duration, the term $T_1 = \tau$ yields $\delta_1 = -12b^2 M_0 \nu / p_1$. Clearly, the exercise on dynamic response of class III plates may be simplified to a particular case of the plates where bending effects transcend those of membrane and transverse shear.

The effect of pulse shapes can virtually be eliminated for monotonically decreasing pressure pulses by incorporating the Youngdahl's correlation parameters in the analysis:

$$I_{eff} = \int_{t_0}^{T} P(t)dt \tag{7-76}$$

$$t_m = \frac{1}{I}\int_{t_0}^{T} t.P(t)dt \tag{7-77}$$

$$p_e = \frac{I}{2t_m} \tag{7-78}$$

where I is the total impulse, $P(t) = p_1(x,y)p_2(t)$and p_e is the effective pressure, t_0 is the initial plastic deformation time, taken as zero, assuming the plasticity in rigid plate occurs instantaneously. T is the time where plastic deformation ceases and t_m is the centroid of the pulse. A rectangular pulse, for example, would give rise to $I_{eff} = p_0\tau$ and $p_e = p_0$ while centroid of the pulse occurs at $t_m = \tau/2$.

Evaluating the above for each pulse shape, a single plot, independent of the pulse shape is obtained in terms of the effective pressure and effective impulse, as given in Figure 7-25.

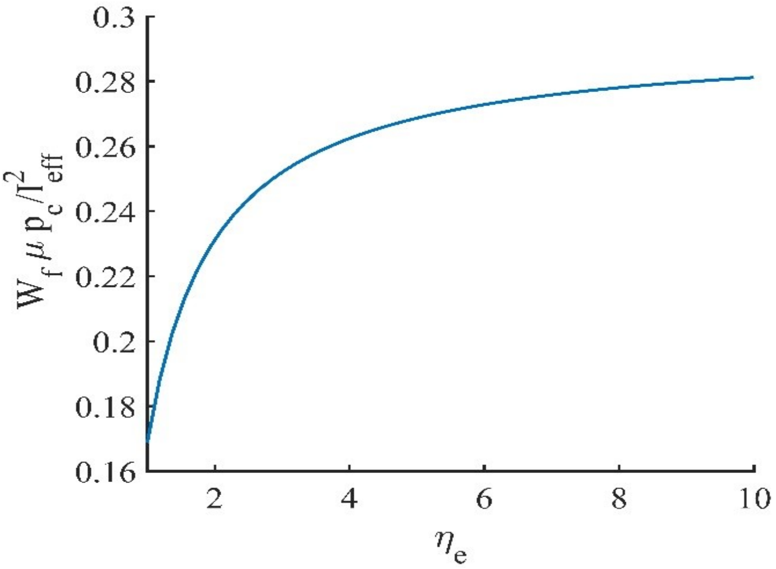

Figure 7-25 Pulse shape independent response of the rectangular pulse ($b = 50m^{-1}$, $\nu = 10, \omega_0 = 0.05$). $\eta_e = p_e/p_c$ is the effective overloading factor.

7.13 FINITE ELEMENT VALIDATIONS

7.13.1 Description of models

The analytical solutions of class III plates for simply supported and clamped plates are validated against full 3D numerical models in Finite Element commercial software ABAQUS® Explicit. Due to axisymmetric nature of the load, only a quarter of the plate was considered in each model with symmetry boundary conditions.

The parametric validations were carried out in two categories. The first category FE models were investigated in the pure Lagrangian reference frame, whereas the second category comprised of a full 3D CEL analysis. Full details of the CEL analysis and the material models has been discussed previously in Chapter 3 and in Refs. [57], [70], [119], [138].

The target plate was assumed monolithic flat panels made of either austenitic Mild steel and aluminium alloy AA5083 H116 (for the pure Lagrangian models) or ultra-hard armour steel alloy ARMOX440T from [131] (for the CEL models). The pure Lagrangian models were pinned along their periphery, while the CEL models were specified with two upper and lower clamps of 20mm width (details previously discussed in Chapter 3). The assumed material properties of the steel panels were density of 7850kgm^{-3}, Young modulus of 200GPa and characteristic in-plane lengths of 400×400mm, thicknesses of 60mm for Mild steels and 10mm for armour steels, with modified Ramberg-Osgood material model which was idealised as elastic-perfectly plastic with isotropy. The visco-plasticity phenomenon was disregarded in this study. However, the flow stress was taken as the average of yield stress (σ_0) and ultimate tensile stress σ_{ut} to approximate the influence of strain hardening, i.e. i.e. $\sigma_{\boldsymbol{av}} = 1/2(\sigma_0 + \sigma_{ut})$. The values of 330MPa and 1342MPa were chosen for Mild steel (M.S) and Armour steel (AR), respectively.

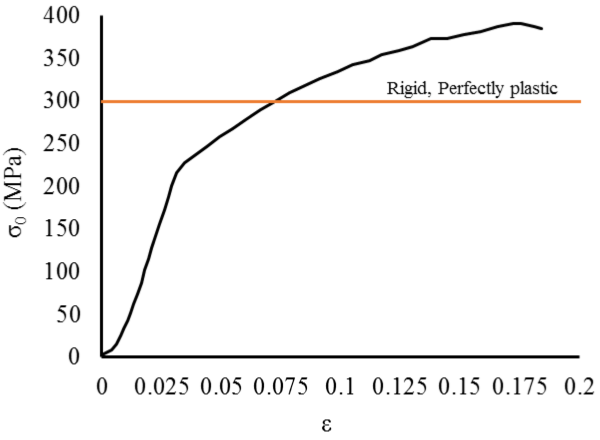

Figure 7-26- Quasi-Static Stress-strain plot of Aluminium alloy, after [61]

Table 7-1- The properties of the numerical model

Material	Material and geometric properties						Loading		
	σ_0 (MPa)	E (MPa)	ρ (kgm^{-3})	υ	L *(mm)*	p_0 (MPa)	τ μs	r_e *(mm)*	b (m^{-1})
Steel	330±5	200000	7850	3.33	200	2400	30	Various	100
Aluminium 5083 H116	300±5	79000	2190	15	150	Various	50	50	50

The aluminium alloy panels had characteristic lengths of 300×300 and 20mm thickness. The material and geometric properties of aluminium alloy were taken from [61] and are presented in Table 7-1. The loading was varied as $p_0 = [20,40,60,80,120]$MPa. The range of loading magnitude corresponds to detonation of 16gr TNT-or 12gr PE4 explosive, given the TNT equivalency of 1.34- which characterises blast scenarios at various stand-offs [20], [23], when using the Hopkinson Cranz law scaled distance presented in Table 7-2. Figure 7-26 presents the approximation of the plastic flow stress in aluminum alloy.

Table 7-2-various threat

Scaled model ($m_T = 16g$)		Prototype ($m_T = 2kg$)
Z	*SoD* *(mm)*	*SoD* *(cm)*
0.25	63	31.50
0.3	76	37.80
0.375	95	47.25
0.42	106	52.92
0.6	151	31.50

All panels were discretised with a mesh of four node S4R conventional shell elements, with finite membrane strains, hour glass control and reduced integration. Elemental length was 4mm in all cases to ensure mesh convergence. The S4R elements are compatible with thick plate's formulations. Due to the increased plate section thickness, the integration points per section of Mild steel panels was increased to 75 to accurately capture the through thickness state variables (stresses) and to accurately model the cross-sectional behaviour.

In each pure Lagrangian model, the loading was applied by FORTRAN-coded user-defined subroutine (VDLOAD) in ABAQUS/Explicit to describe the spatial and temporal shape of the blast. Regarding the CEL models, the loading magnitude and duration was determined by a preliminary Lagrangian-Eulerian analysis, set up with rigid target to delineate the load parameters for the analytical model. A total of four FE models were set up with Plastic Explosive 4 (PE4) cylindrical sheet explosive of designated charge diameter $D_e = [50,75,100,140]$ at constant 50mm stand-off from the target. The charge of design number 1 had depth of 22.26mm, while the depth of the rest was kept constant of 5.57mm. The clamps were also modelled as 10mm specified rigid chamfers at the edge of the target. Due to the increased charge radius to plate length ratio, the clamps would affect the wave propagation on the target, absorbing some portion of the total impulse generated by the charge [67]. The pressure registered with each target gauge point was recorded and plotted in Figure 7-27-Figure 7-28. A curve fitting tool in MATLAB® 2016 was utilised to predict the loading parameters b, r_e, as illustrated in Figure 7-29 and summarised in Table 7-3. This table also presents the charge properties and associated loading magnitudes of each designation.

Table 7-3- load parameters from the FSI model

Design number	1	2	3	4
$D_e(mm)$	50	70	100	140
$H(mm)$	10	10	10, 20	20
$M_e(g)$	70.0	39.4	70.0	137.3
$p_0\ (MPa)$	600	440	680	732
$r_e(mm)$	18.4	22.4	36.9	54.3
$b(\mathrm{m}^{-1})$	50.1	51.2	57.6	48.7

Two sets of parametric studies have been carried out to compare with the analytical solutions on impulsive and dynamic loaded panels. To ensure the plasticity occurring in the plate, the equivalent plastic strain ($\bar{\varepsilon}_p$) as monitored and it was ensured that the plate reaches 'residual' vibrations.

The design number 4 (with the 10mm target plate) experienced excessive distortion and was disregarded from the results, thus two further panels of 20mm thickness were investigated instead.

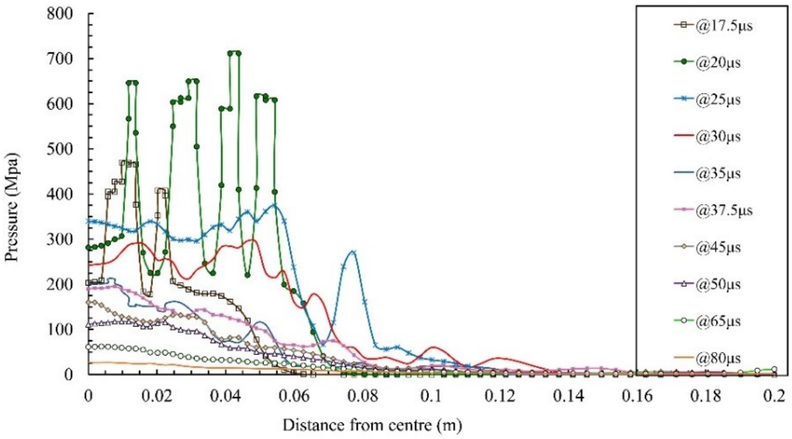

Figure 7-27- Recorded pressure at gauge points vs distance from the target -140mm PE4 explosive

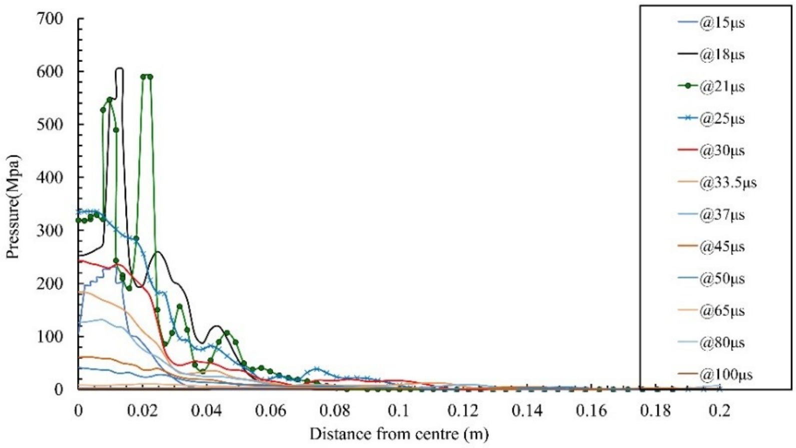

Figure 7-28- Recorded pressure at gauge points vs distance from the target -75 mm PE4 explosive

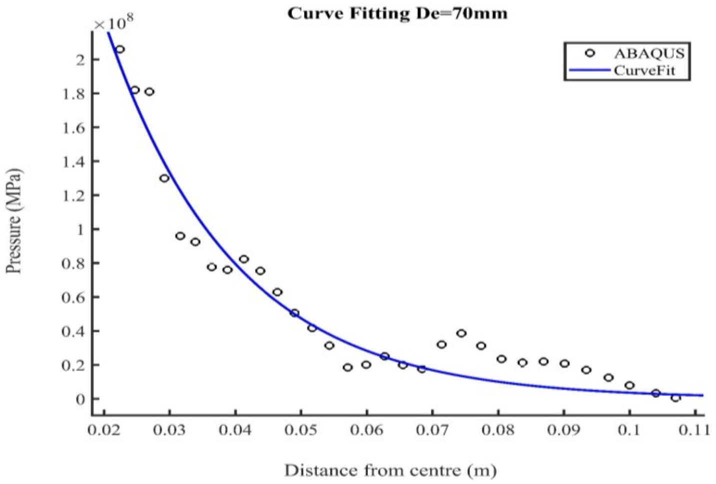

Figure 7-29- Curve fit of the loading parameters

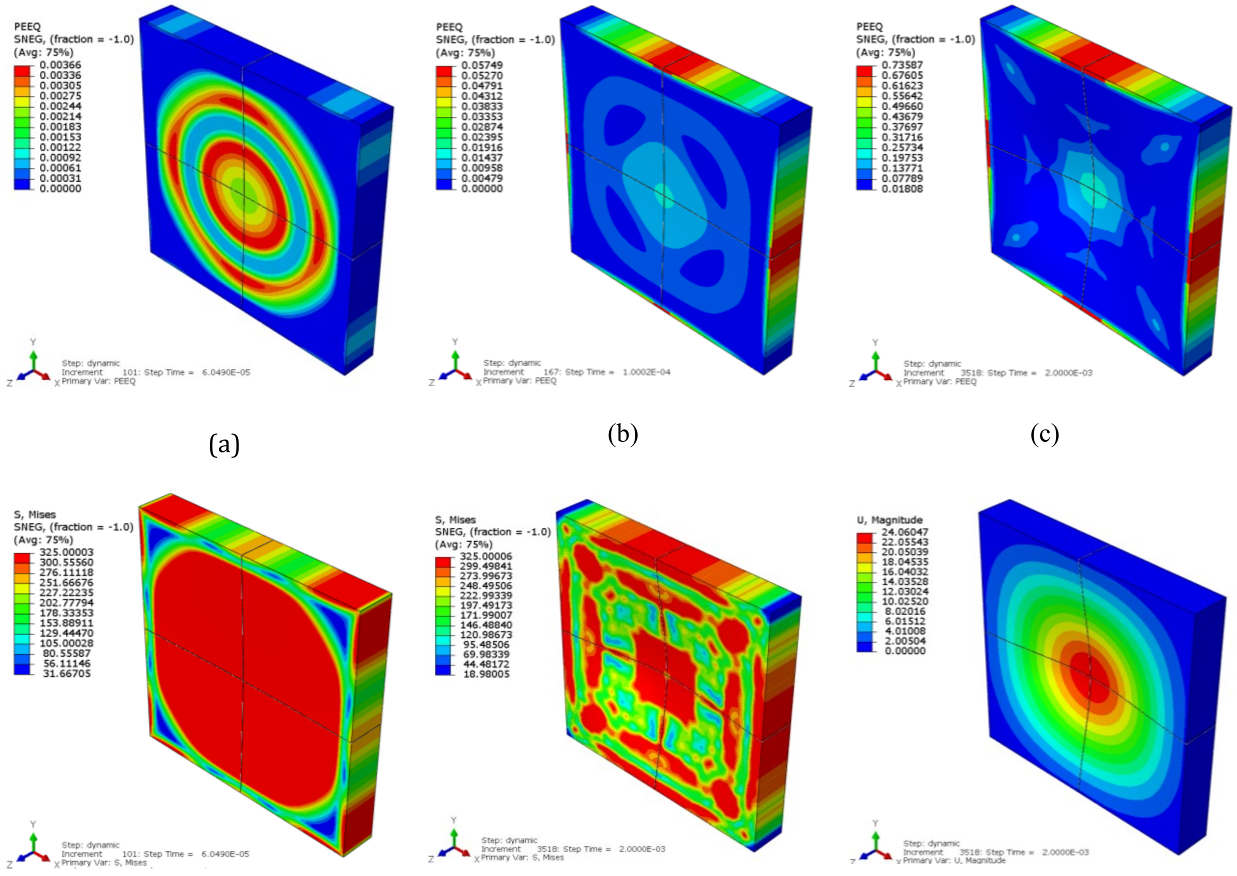

(a) (b) (c)

(d) (e) (f)

Figure 7-30- Distribution of the $\bar{\varepsilon}_p$, Mises stress and displacement fields in the plate with b=100 and $r_e/L = 0.5$. (a-c)- Distribution of $\bar{\varepsilon}_p$ at $t = 60\mu s, 0.1ms$ and $2ms$, respectively. (d-e) distribution of Mises stress at $t = 60\mu s$ and $2ms$, respectively. (f) permanent displacement at $t = 2ms$

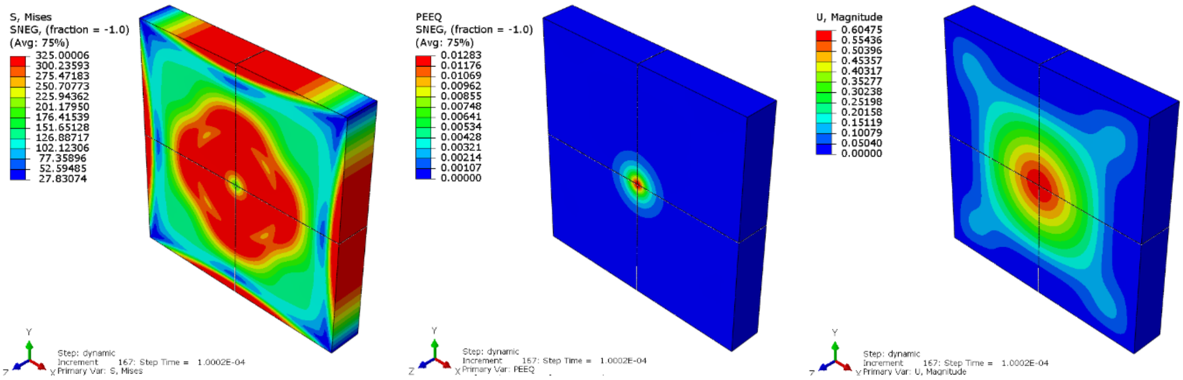

(a) (c) (e)

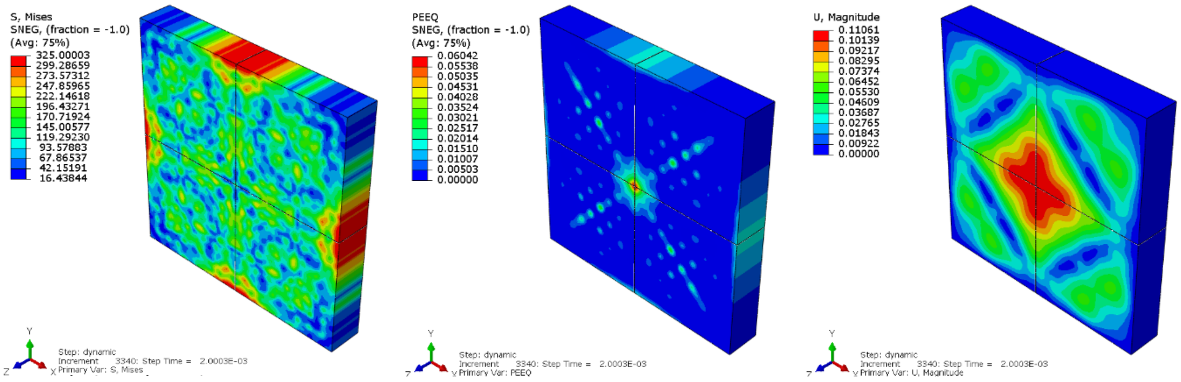

(b) (d) (f)

Figure 7-31 (a), (b) distribution of the Mises stress; (c), (d) Equivalent plastic strain ($\bar{\varepsilon}_p$); (e), (f) displacement field at $t = 0.1ms$ and $t = 2ms$ in the plate with $\nu = 3.\overline{3}$, b=100 and $r_e/L = 0.1$.

7.13.2 Pure Lagrangian models and results

Accurate prediction of the permanent displacement relies on verification of the position of the plastic hinge ξ_0. The position of the plastic hinge ξ_0 in beams and plates may be monitored numerically by tracing the maximum equivalent plastic strain ($\overline{\varepsilon_p}$) that appears instantaneously at the onset of loading. However, for the locally blasted plates, particularly those of loading radius $r_e/L < 0.4$, the trace of plastic strain becomes intrinsically cumbersome due to the complex nature of the load. Furthermore, there is always certain width observed with the maximum ($\overline{\varepsilon_p}$). Nevertheless, the size of central plastic zone broadens with the increase of load radius in the FE model, which corroborates with the analytical results. The distribution of the displacement, equivalent plastic strain and Mises stress fields at various times are illustrated in Figure 7-30 - Figure 7-31.

The numerical results in Figure 7-32 (a)-(b) compare favourably with those of the analytical model, with the error decreasing as the radius of the load increases. The results also indicate the assumed velocity profile predicts the permanent deformation with reasonable accuracy, with error less than 17% in for most loading radii (Figure 7-32 a). Some differences in prediction of the permanent deformation may be due to the influence of material elasticity. With the increase of the material strength, the strain energy stored elastically during the impact would be significant which influences the post-peak behaviour. However, as the plate thickness increases, the rigidity of the plate increases, thus the contribution of the elastic energy to dissipate the work done by the load decreases. Consequently, the system can be idealised as rigid body in which case the analytical formulations of rigid-perfectly plastic model suffice to predict the response, i.e. the case studied here.

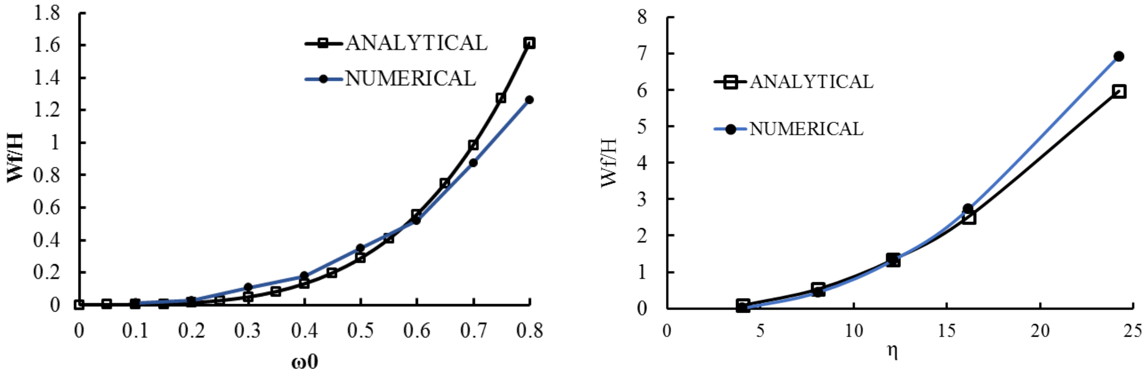

(a) (b)

Figure 7-32 (a) Variation of the permanent deformation with load radius, impulsive loading (b) Variation of the permanent deformation with load magnitude, dynamic load.

In Figure 7-33a comparison of the energy effectiveness ψ′, i.e. the ratio of the initial kinetic energy to Specific Energy to Tensile Fracture is also presented for 20mm panels. This parameter is conducive to compare the effectiveness of energy absorption of plates made of various materials for design purposes. The energy effectiveness obviates the need for experiments, since it may be calculated theoretically as the SETF, i.e. the area under the stress-strain curves measured experimentally in quasi-static tests, the load parameters and the impulsive velocity in most blast scenarios are known *priori*.

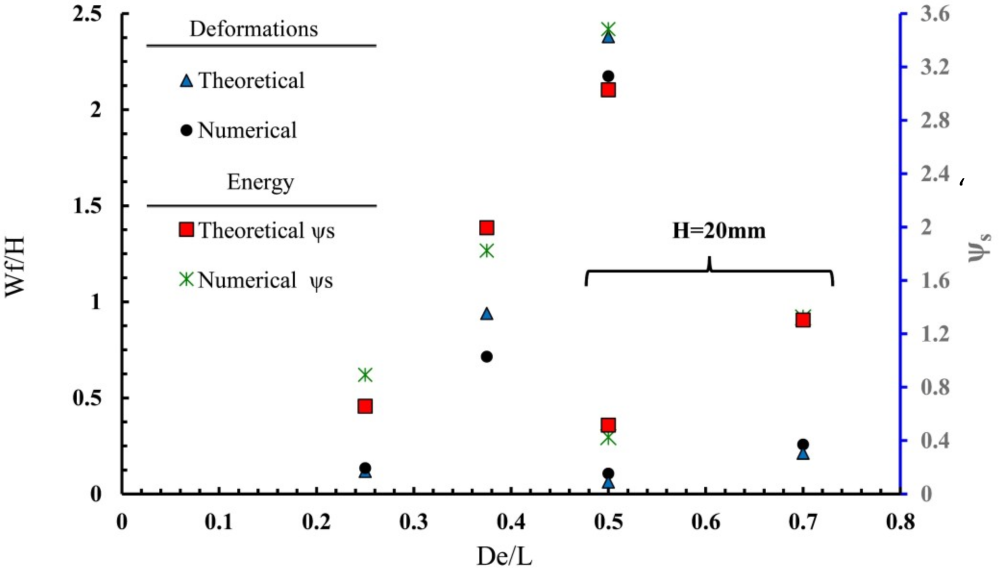

Figure 7-33 The dimensionless energy (ψ′) predicted theoretically ■ and numerically □ on 20mm plate, the dimensionless deformations predicted theoretically ▲ and numerically ● for 10 and 20mm target plate

7.14 **SUMMARY AND CONCLUSIONS**

In this chapter, an analytical model in chapter 4 was extended to predict the response of simply supported, monolithic thick square plates-which behaves as rate insensitive, ductile metal when impacted by dynamic and impulsive generic blasts.

While the Mindlin-Reissner plate theory was incorporated in the analysis, the plate was assumed to be sufficiently thick, with the focus on the transverse shear effects while ignoring the build-up of membrane resistance. Thus, the overall response is governed by the interaction of bending and transverse shear. With idealisation of rigid-perfectly plastic behaviour in mind, the analytical formulations for mid-point and support transverse deformations were obtained in terms of impulsive velocity that incorporates the localisation of the blast. The deformations were both affected by the transverse shear in the low range of plate slenderness ratio ($\nu < 2$). This range of ν is impractical in the design applications of protective systems. The midpoint and support transverse displacements have been found to be both affected by the transverse shear in the low range of ν. The influence of transverse shear was found even less significant for the localised blast. In such cases, the influence of bending would suffice to estimate the response of the plates.

On the contrary, the theoretical results showed that pulse shape effect plays a considerable role in the permanent deformation of the non-impulsively localised loaded plates. Thus, the assessment of the blast response is fraught with difficulty since it is impractical to experimentally monitor the pressure data of localised loads. However, the pulse shape effects virtually fall onto a single curve, when using $\eta_e = p_e/p_c$.

Parametric studies on impulsively loaded plate showed good correlations between the numerical and analytical models.

CHAPTER 8

Dimensional Analysis

8.1 BACKGROUND

It has already been established that the blast loads from proximal charges give rise to a localised mode of failure compared to the those emanated from far field charges. With the ever-increasing demand to identify the blast load parameters, the dimensional analysis provides a useful set of dimensionless numbers useful for scaling purposes and consequentially avoid unnecessary repetition of results in dimensionless space. Thus, the major thrust of this chapter is driven by the particular deliberation on the dimensionless form of the parameters influenced by localised blast. The dimensionless parameters aid the designers to predict the blast load conditions that will ensue rupture in the structural elements.

The context of the present chapter serves two purposes:

1- To conduct a dimensional analysis to derive a set of dimensionless parameters that can fully elucidate the parameters that characterise the phenomenon of the blast load, the generic blast load variations (both spatial and temporal) and plated structure response due to such phenomenon.

2- To ascertain the effectiveness of the structure to withstand various blasts scenarios. This is achieved by predicting the dimensionless impulse and energy absorbing effectiveness parameters.

A portion of the work in this chapter has been published in the International Journal of Multiphysics [27].

8.1.1 Dimensional analysis

Dimensional analysis is a useful tool of generalisation and is used here to ascertain the phenomenon of blast loading and the physics of response of full-scale prototype through the study of geometrically similar small-scale models, without the necessity of conducting experiments on the former. The principle of scaling enables the engineers to obtain a set of dimensionless parameters through multiplicative combination of defining variables used in numerical calculations or experimental measurements.

In the past, dimensionless parameters have been utilised by various researchers to study the elastic and/or plastic response of the structures to blast loads. The work by Neuberger et al. [24] on numerical analysis predicted a marginal 7% difference of dimensionless maximum deformation between the small-scale model and a full scale prototype four times as large. The authors stated the discrepancy was due primarily to the change in material properties during scaling. Their experimental results, however, showed a 10% difference in peak deflections.

In other works of literature, the small-scale model results have been generally furnished in terms of a non-dimensional impulse parameter (NDIP) against characteristic response deformations (viz., permanent normalised midpoint deflections), the empirical models alike have been proposed and discussed in Section 4-5. However, relying on impulse and deflections alone can be misleading, because in most practical cases, the loading regime may be characterised as dynamic rather than impulsive. Furthermore, much of the research in the literature was based on ad hoc basis, focused on providing expressions for the response of the structure. Such analyses are devoid of proposing expressions to actually describe the air blast load itself and the ensuing localised response. The present chapter derives a set of dimensionless parameters that can fully delineate both the blast loading effects and the structural response thereof. It is predicted that these parameters would aid the designer with some $priori$ knowledge of the blast phenomenon without the need to conduct complex experimental or numerical analysis.

8.2 NON-DIMENSIONAL PARAMETERS

8.2.1 Localised blast load

The presumed blast wave assumed throughout this thesis is generated from a cylindrical explosive of certain mass M_e, the heat energy per mass of Q_e, having the diameter D_e, which is placed at stand-off distance d from the target. This gives parameters defining the blast source uniquely as: M_e, d, D_e, and Q_e.

The blast wave pressure represents a multiplicative decomposition of functions of the spatial part (also called load shape) and temporal part (pulse shape) [152], given in Eqn. (8-1).

$$p(r,t) = p_0 p_1(r) p_2(t) \tag{8-1}$$

The spatial distribution of the blast is already discussed in (5-1). Thus, the parameters that fully define the loading profile are: p_0, t_d, α, b and R_e. It should be noted that the parameter $a = e^{bR_e}$ is not an independent parameter as it links the two functions proposed for the spatial distribution of loading. The temporal function of the blast is assumed as

$$p_2(t) = (1 - t/t_d)e^{-\alpha t} \tag{8-2}$$

It is assumed that the blast overpressure is imparted transversely on the target, i.e. the load is axisymmetric at the wave target interface, thus, a quadrangular plate of characteristic half-length L, characteristic thickness H, having the density ρ_p, made of ductile material of Young modulus E and quasi-static yield stress σ_0 gives rise to an axisymmetric displacement field of final maximum transverse deformation W_f. The dynamic flow stress is described with simplified form of Johnson-Cook constitutive model given in Eqn. (8-3).

$$\sigma'_y = [A_1' + B_1'\varepsilon^n][1 + Cln(\dot{\varepsilon}^*)] \tag{8-3}$$

where $A_1' = \sigma_0$ is the static yield stress, B_1' and n are the hardening constant and exponent, respectively. While this model ignores the Bauschinger effect, it conveniently predicts the visco-plasticity and strain hardening behaviour of isotropic material which undergo large deformations. Thus, the parameters attributed to the material and geometric properties of the plate are $W_f,\ H,\ \rho_p,\ \sigma_0\ , L, B_1', E, \dot{\varepsilon}$.

The rank nullity theorem was exercised, and the dimensional parameters identified in Table 8-1. By applying Buckingham's Pi-theorem, a system of 17 independent variables over the rank of 3-dimensional matrix of equations leaves a kernel of (17-3=) 14 dimensionless Π parameters. The coefficients of Table 8-1 satisfy the conditions of Eqn. (8-4).

Table 8-1 Dimensional parameters of load -structure system

Parameter	$[M]$	$[L]$	$[T]$	a_i	Parameter	$[M]$	$[L]$	$[T]$	a_i
W_f	0	1	0	a_1	b	0	-1	0	a_{10}
H	0	1	0	a_2	α	0	0	-1	a_{11}
ρ_p	1	-3	0	a_3	t_d	0	0	1	a_{12}
σ_0	1	-1	-2	a_4	p_0	1	-1	-2	a_{13}
L	0	1	0	a_5	Q_e	0	2	-2	a_{14}
B_1'	1	-1	-2	a_6	M_e	1	0	0	a_{15}
E	1	-1	-2	a_7	D_e	0	1	0	a_{16}
$\dot{\varepsilon}$	0	0	-1	a_8	d	0	1	0	a_{17}
r_e	0	1	0	a_9					

$$\begin{cases} a_1 - a_2 = 0 \\ a_{10} - a_{16} = 0 \\ 3a_{12} + a_{13} + 1/2\, a_{14} - a_{15} = 0 \\ a_{16} - a_{17} = 0 \\ 2a_{15} - 6a_{16} + a_{14} - a_3 - a_4 = 0 \\ 2a_{16} - a_{14} - 2a_{12} = 0 \\ a_{11} - a_{12} = 0 \\ a_2 - a_5 = 0 \\ a_9 - a_{16} = 0 \\ a_9 - a_5 = 0 \\ a_7 - a_6 = 0 \\ a_3 + a_{16} - a_{15} = 0 \\ a_6 - a_3 - a_{14} = 0 \\ a_8 + a_{12} = 0 \end{cases} \tag{8-4}$$

Solving the Eqn. (8-4), the 14 dimensionless parameters are extracted as defined by Eqn. ‘s (8-5)-(8-18):

$$\Pi_1 = \frac{W_f}{H} \tag{8-5}$$

$$\boldsymbol{\Pi_2 = bD_e} \tag{8-6}$$

$$\Pi_3 = \frac{p_0\sqrt{Q_e}t_d^3}{M_e} \tag{8-7}$$

$$\boldsymbol{\Pi_4 = \frac{d}{D_e}} \tag{8-8}$$

$$\Pi_5 = \frac{M_e}{D_e^3}\sqrt{\frac{Q_e}{\rho_p \sigma_0}} \tag{8-9}$$

$$\boldsymbol{\Pi_6 = \frac{D_e}{\sqrt{Q_e}t_d}} \tag{8-10}$$

$$\Pi_7 = \alpha t_d \tag{8-11}$$

$$\boldsymbol{\Pi_8 = L/H} \tag{8-12}$$

$$\Pi_9 = \frac{r_e}{D_e} \tag{8-13}$$

$$\boldsymbol{\Pi_{10} = r_e/L} \tag{8-14}$$

$$\Pi_{11} = \frac{E}{{B_1}'} \tag{8-15}$$

$$\boldsymbol{\Pi_{12} = \frac{\rho_p D_e^3}{M_e}} \tag{8-16}$$

$$\Pi_{13} = \frac{{B_1}'}{\rho_p Q_e} \tag{8-17}$$

$$\boldsymbol{\Pi_{14} = \dot{\varepsilon} t_d} \tag{8-18}$$

It should nevertheless be mentioned that various parametric relations may be recognised from the Eqns. (8-5)-(8-18), while through some algebraic manipulation, the unknown parameters of interest, $p_0, b, \; t_d, \alpha \,, r_e \,, W_f$ are all found to be related to the quotient $\left(\frac{d}{D_e}\right)$ as:

$$p_0 = \frac{EM_e}{\rho D_e^3} f_1\left(\frac{d}{D_e}\right) \tag{8-19}$$

$$b = \frac{1}{D_e} f_2\left(\frac{d}{D_e}\right) \tag{8-20}$$

$$t_d = \frac{D_e}{\sqrt{Q_e}} f_3\left(\frac{d}{D_e}\right) \tag{8-21}$$

$$\alpha = \frac{\sqrt{Q_e}}{D_e} f_4\left(\frac{d}{D_e}\right) \tag{8-22}$$

$$r_e = L f_5\left(\frac{d}{D_e}\right) \tag{8-23}$$

$$\frac{W_f}{H} = \frac{M_e}{\rho_p D_e^3} f_6\left(\frac{d}{D_e}\right) \tag{8-24}$$

The dimensionless functions are obtained by curve fitting approximations onto the results of a series of numerical studies. It should be stressed that, with armour steel in mind, the strain rate sensitivity parameters have not been investigated in this study, as the material exhibits little sensitivity to this phenomenological effect.

8.3 EXPERIMENTAL SETUP

8.3.1 Material characterisation

Some of the experimental tests on ARMOX steel panels have been carried out by Ref.'s [119], [133]. The details of the experimental setup have already been discussed earlier, however; the supplementary results of AR500T not in the scope of the earlier studies are set out in Table 8-2 and Figure 8-1. These panels had identical geometry to the earlier panels and tested on ballistic pendulum apparatus but subjected to a range of charge mass from 24g to 70g PE4.

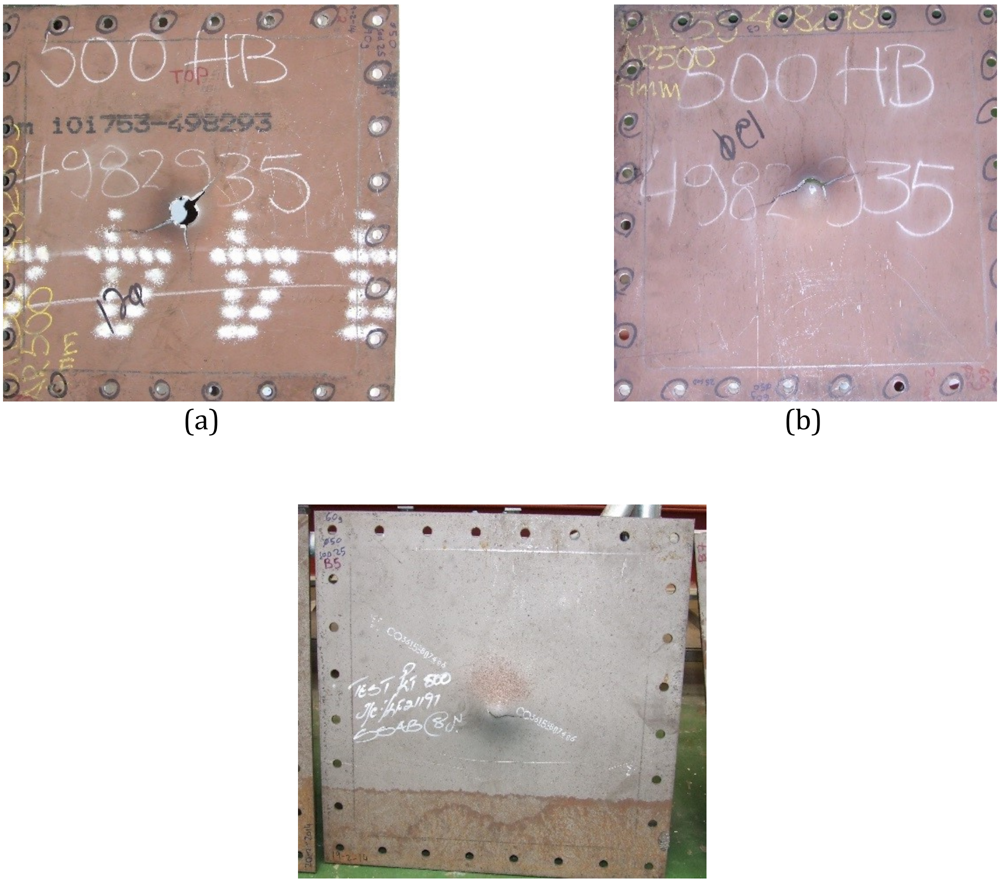
(a) (b) (c)

Figure 8-1- Rupture of ARMOX panels with 25mm stand-off, (a) 70g charge AR500T (specimen C2), (b) 60g charge AR500T (specimen C3), (c) 60g charge AR440T (specimen B5)

Table 8-2 Experimental results on armour panels with 50mm charge diameter

Test Configuration	Designation	d	M_e	W_f	Impulse (N.s)	Failure mode
AR370T	ASP1	25	40	29.5	80	II*c (partial tearing in central area)
AR440T	B5	25	60	Crack length 20.25mm	117.2	II*c
AR500T	C1	25	50	23.4	98.3	Itc
	C2		70	Capped 31mm dia., 4 cracks	114.7	IIc
	C3		60	Crack length 22.4mm	129.2	II*c
	C4	38	70	22.3	107.5	Itc
	C5		60	24.3	126	
	C7		33	13.98	57.34	
	C8		24	11.48	43.76	

8.3.2 Constitutive Damage models

Ductile damage and fracture of steel and RHA steel under ballistic conditions have been investigated numerically and experimentally. In addition, several constitutive damage models have been proposed in the literature. The multi-axial state of stress in a constitutive model has been commonly expressed as a function of accumulated plastic strain, plastic strain rate and absolute temperature [62], [187], [188].

Gàlvez et al [189] measured the stress intensity factor history-integral to calculating the fracture toughness, of armour AR500T using mixed numerical /experimental methods. The difference of the dynamic fracture toughness to the static counterpart was insignificant, clearly because the armour steel materials are insensitive to strain rates. Gupta and co-authors [190] investigated the constitutive behaviour of AR500T steel under varying stress state, strain rate and temperature and observed significant decrease in strength of beyond 200^{o}C, but significant increase in ductility.

In microscopic level, the terminology ductile damage denotes the fracture as a result of nucleation, growth and coalescence of the voids within the material [128], [191], [192], while in the macroscopic level, it is the connotation of the large deformation of the material at the onset of necking, which is followed by stress degradation. Fracture of the body results in discontinuity of the total displacement field, whereas dislocation reflects the discontinuity of the elastic/plastic displacement field. [193]

Ductile fracture is characterised by the accumulation of the plastic strain at the current stress state described by

$$\mathcal{D} = \int \frac{\dot{\varepsilon}_{pl}}{\varepsilon_f} dt \qquad \textbf{(8-25)}$$

where $\mathcal{D}$ is the damage parameter which equates to maximum 1 when the material element erodes, $\dot{\varepsilon}_{pl}$ denotes the plastic strain rate, while ε_f is the fracture strain, which is a function of the normalised third deviatoric invariant (ζ), temperature and strain rate at any proportional stress state, and the stress triaxiality (ς), given by Eqn. (8-26). Stress triaxiality is the quotient of mean flow stress (σ_m)- also referred to as the Hydrostatic pressure stress- to effective stress (σ_{eff}).

$$\varepsilon_f = \phi(\varsigma, \zeta) g(\dot{\varepsilon}_{pl}) h(T) \qquad \textbf{(8-26)}$$

At the onset of necking, the state of stress is represented by

$$\sigma = (1 - D)\bar{\sigma} \tag{8-27}$$

In Eqn. (8-27), σ and $\bar{\sigma}$ represent the state of stress tensor with and without damage, respectively. At the point of maximum damage parameter, the elemental stresses vanish, causing the material failure. In microscopic level, this is characterised by the coalescence and growth of voids in the material particles. Studies reveal that the triaxiality, the state of stress and material ductility are interrelated. Higher triaxiality increases the speed of void growth void growth [194] rapidly, resulting in the reduced ductility and hence fracture strain [190], [195], [196] .

The functions $\phi$and g can be identified from the JC ductile fracture criterion [128], [197] in (8-28).

$$\varepsilon_f = (D_1 + D_2 e^{-D_3 \varsigma})(1 + D_4 \ln \dot{\varepsilon}_{eq}{}^{*})(1 + D_5 T^*) \tag{8-28}$$

where $D_1 \ldots . D_5$ are the material constants determined from experimental tests. The ratio of strain rate to the reference strain rate is given as $\dot{\varepsilon}_{eq}{}^{*} = \dot{\varepsilon}/\varepsilon_0$, where the reference strain rate is usually set as $1s^{-1}$. T^* represents the homologous temperature, i.e. $T^* = {(T - T_r)}/{(T_m - T_r)}$ where T_r and T_m are the room temperature and melting temperature, respectively. Basaran [198] proposed an extended form of the ductility function $\phi(\varsigma, \zeta)$ defined by the JC model as a quadratic truncation of the stress triaxiality. The parameters $D_1 - D_5$ from JC model were averaged and compared against the parameters proposed by Bridgman [199] and Gupta et al [190] in Table 8-3, while Figure 8-2 illustrates the influence of the triaxiality on the fracture surface.

Table 8-3- JC parameters proposed in the literature

JC parameters	D_1	D_2	D_3	D_4	D_5
JC-Average	0.040	6.71	-2.63	-0.0035	1.4
JC-Bridgman	0.017	2.30	-3.10	-0.0035	1.4
JC-Gupta et al.	0.043	2.15	-2.76	-0.0066	0.86

Ignoring the temperature and strain rate effects, the JC parameters proposed by Bridgman and Gupta et al. yield conservative estimates of the fracture surface, as observed in Figure 8-2. In this work, the parameters from JC-Bridgman model were used to estimate the fracture strain at each triaxiality.

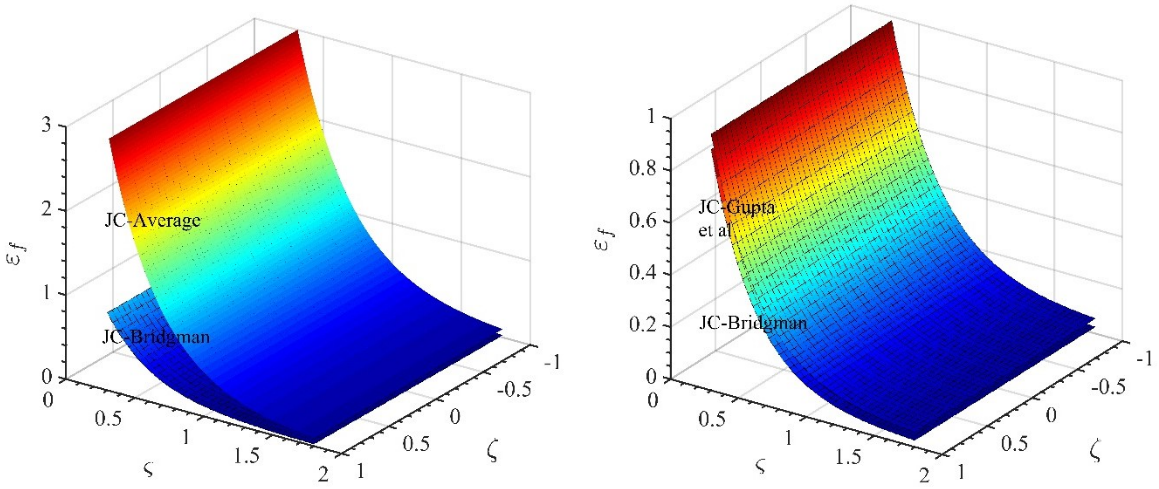

(a) (b)

Figure 8-2. Fracture surface of the JC models (a) JC- average parameters vs JC-Bridgman (b) JC Bridgman vs JC-Gupta et al

It is assumed that the material degradation occurs due to linear softening of the stress strain curve. In this work, Hillerborg's damage evolution [200], assuming the brittle fracture concept, is implemented in the FE models. To eliminate the mesh dependency, the energy per unit area of crack is defined as [144]

$$G_f = \int_0^{\bar{u}_{pl}} \sigma \, d\bar{u}_{pl} = \int_{\bar{\varepsilon}_0^{pl}}^{\bar{\varepsilon}_f^{pl}} \bar{L}\sigma d\bar{\varepsilon}_0^{pl} \tag{8-29}$$

where $\bar{L}$ is the characteristic lengths of the element formulation, $\bar{u}_{pl} = \bar{L}\bar{\varepsilon}_0^{pl}$ represents the traction separation displacement (crack tip displacement). The stress degradation beyond plastic strain at the onset of necking is assumed linear. Elements are removed when damage evolves in all section points.

8.4 NUMERICAL MODELS AND MATERIALS

A Multi Material Arbitrary Lagrangian Eulerian analysis representing free air blast load was performed in the same spirit as discussed earlier in Chapter 3. The details of the material models (air and explosive) are presented in (Table 4-3). The blast wave is assumed to be generated by detonation of a cylindrical composition-C4 (PE4) plastic explosive of prescribed mass $M_e = 40g$ at various stand-offs, having the characteristic diameter $D_e = 50mm$ and constant charge height determined as $h_e = \frac{4M_e}{\pi \rho_e D_e^2} = 12.73mm$. The detonation is assumed to initiate from the centre of the explosive mass. The value of specific heat energy Q_e for PE4 is taken from Ref [201].

A total of 9 UEL simulations were carried out over the range of $0.5 \le \frac{d}{D_e} \le 3$, which consisted of six simulations where stand-off increased incrementally by 25m, while the rest entailed $d = 27, 30, 38\text{mm}$. In crude terms, by utilising the Hopkinson- Cranz law, the assumed range corresponds to the full-scale spherical IED (Improvised Explosive Device) threats having diameter of 70-700mm at 300-500mm stand-off, assuming the spherical and cylindrical explosives to have the same mass to generate the same pressure load.

8.4.1 FE damage models

In this section, the panels which underwent rupture during the experiments were also investigated numerically, using the MMALE techniques, as comparison and supplementary to the experimental data.

The damage parameters of the panels were initially investigated using the pure Lagrangian simulations, with the revere FE technique. The prescribed loading consisted of a localised blast of 600MPa magnitude and 25mm central constant load radius, which lasted for $30\mu s$.

The relevant simulations were carried out using CEL technique, except the steel panels were further partitioned into three levels of mesh refinements across its characteristic in-plane directions. The central portion of the plate was a square of 60mm side length, discretised with a biased mesh of 1.5mm to 5mm element length, near the vicinity of the PE4 charge. Within this portion a smaller square of 30mm length was circumscribed, associated with an unbiased mesh of 1.5mm elemental length. The remaining of the plate had a coarser mesh of 5mm element length. Linear conventional shell and continuum shell elements with enhanced hourglass control and 7 Simpson's integration points through thickness were used. The plate prescribed with three elements stacking through section thickness as illustrated in Figure 8-3.

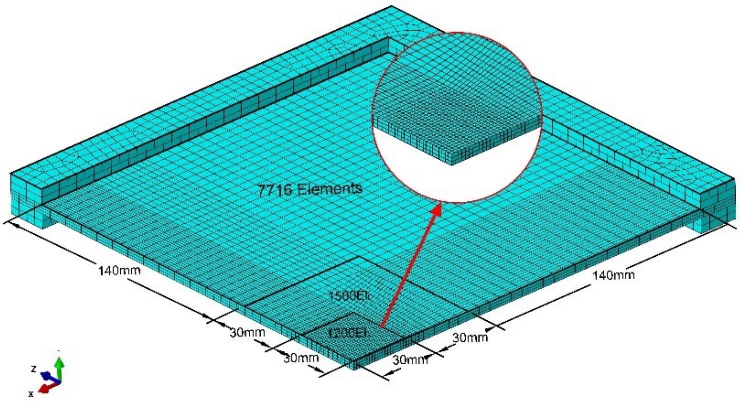

Figure 8-3. FE mesh of SC8R elements

8.5 DIMENSIONAL ANALYSIS RESULTS AND DISCUSSIONS

For each test, the inflow of pressure was quantified along the rigid target gauge points in radial direction. In Figure 8-4 and Figure 8-5 the pressure history at different gauge points is recorded, while Figure 8-6 illustrates the advection of the explosive and fluid surface interaction at different times, while

When the characteristic features of the loading parameters (spatial and temporal) are known a *priori*, an approximate to the transverse deflection of the plate in Eqn. (8-24) due to such a load can be measured by utilising UEL analysis. In each case, the loading in the separate pure Lagrangian analysis was implemented by generating a 3d matrix of the pressure load associated with the generalised coordinates of each element, applied directly onto the panels. Figure 8-7 shows the maximum displacement of the two panels at varying stand-off.

Using the curve fitting tool in MATLAB, a set of dimensionless functions are obtained as presented in Eqns. (8-30)-(8-37), and illustrated in Figure 8-8-Figure 8-14. To investigate the influence of charge mass on the decay exponent (b), the numerical results of 60g charge (19mm charge height) are also plotted in Figure 8-9.

$$f_1 = 0.11\left(\frac{d}{D_e}\right)^{-1.153} \tag{8-30}$$

$$f_2 = 4.591\left(\frac{d}{D_e}\right)^{-0.42} \tag{8-31}$$

$$f_3 = 21.56\left(\frac{d}{D_e}\right) + 54.3 \tag{8-32}$$

$$f_4 = \frac{0.359}{\left(\frac{d}{D_e}\right) + 2.138} \tag{8-33}$$

$$f_5 = 0.0363\ln\left(\frac{0.4d}{D_e}\right) + 0.0819 \tag{8-34}$$

$$f_6 = 344.8e^{-1.753\left(\frac{d}{D_e}\right)} \tag{8-35}$$

Eqn. (8-24) can be furnished in the form of Eqn. (8-36), where I^* is the impulse density (impulse per unit area). Thus, the dimensionless function relating the plate response to the impulse is given in Eqn. (8-37) and Figure 8-14. Table 8-4 summarises the impulse obtained in UEL method by using Eqn. (8-40) over the radial distance (R) of 200mm.

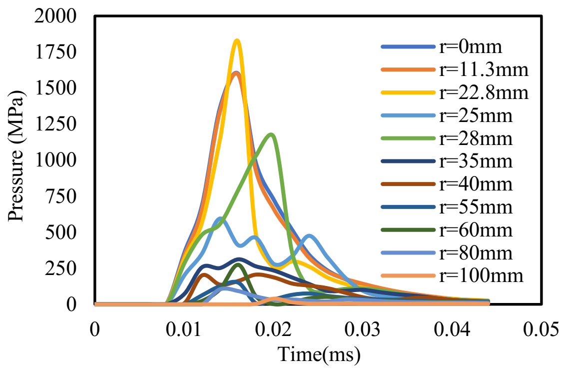

Figure 8-4. Pressure load at various radial local coordinates (($d/D_e = 0.25$)

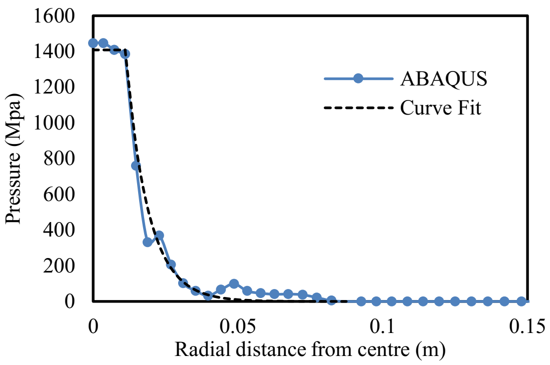

Figure 8-5. Curve fit of pressure load across the target ($d/D_e = 0.54$)

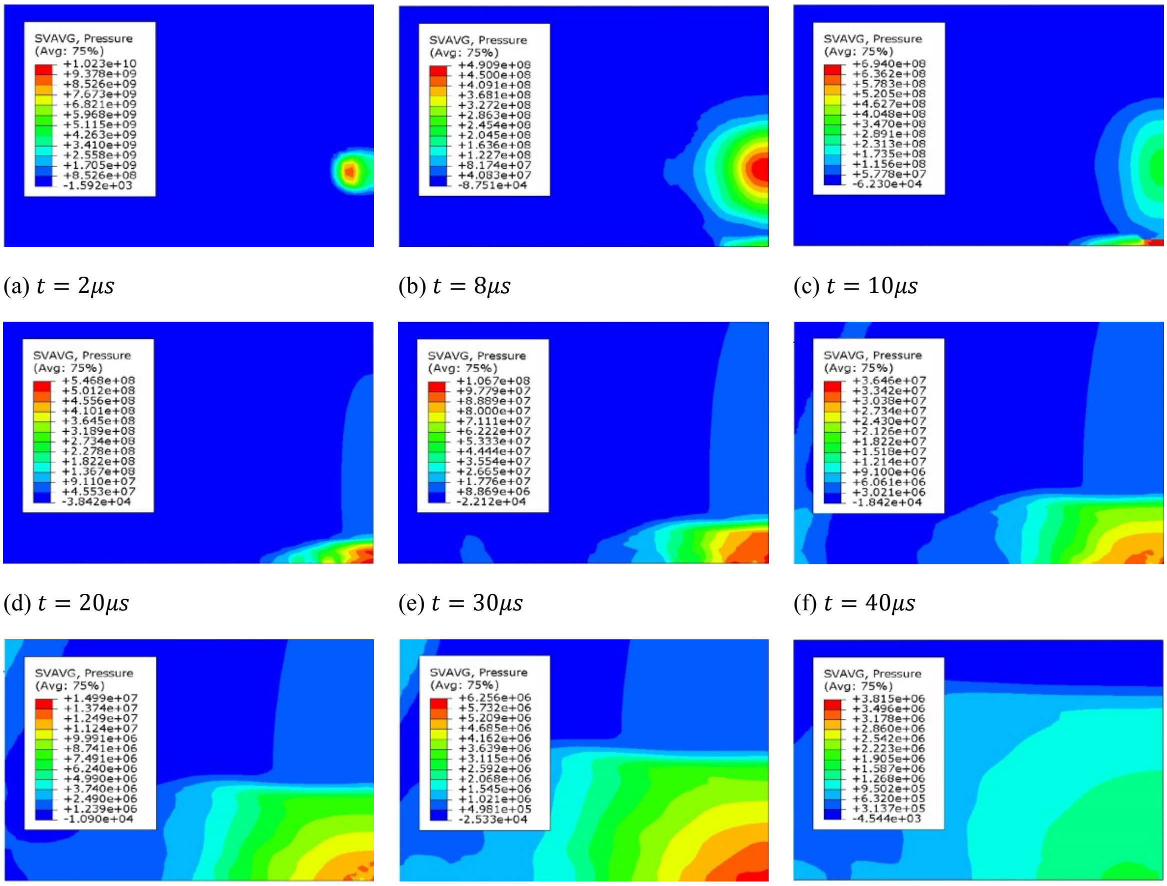

(a) $t = 2\mu s$ (b) $t = 8\mu s$ (c) $t = 10\mu s$

(d) $t = 20\mu s$ (e) $t = 30\mu s$ (f) $t = 40\mu s$

(g) $t = 50\mu s$ (h) $t = 60\mu s$ (i) $t = 80\mu s$

Figure 8-6. Advection of the blast wave from 40g explosive in air medium at 25mm stand-off

$$\frac{W_f}{H} = \frac{I^*}{H\sqrt{\rho_p \sigma_0}} f_7\left(\frac{d}{D_e}\right) \tag{8-36}$$

$$f_7 = -2.036\left(\frac{d}{D_e}\right) + 10.08 \qquad 0.5 \le \frac{d}{D_e} < 0.75$$

$$f_7 = 4.28\left(\frac{d}{D_e}\right)^{-2.5} + 0.1 \qquad 0.75 \le \frac{d}{D_e} \le 3 \tag{8-37}$$

Table 8-4- Mid-point deflection vs impulse of MMALE models for ARMOX 440T

Test Number	d/D_e	Impulse (I) (N.s)	Test Number	d/D_e	Impulse (I) (N.s)
1	0.5	65.11	5	1	51.78
2	0.54	59.87	6	1.5	44.41
3	0.6	56.68	7	2	33.99
4	0.76	54.52	8	2.5	24.82
			9	3	22.55

Clearly, regarding the proximal blasts with $\frac{d}{D_e} \le 1.5$, an incremental decrease in the abscissa leads to an abrupt increase in the ordinate of Figure 8-8-Figure 8-13. The value of $d = 1.5D_e$ can be considered as a transition point in the response type of the target plate, beyond which the variation of the deformation with pressure is smoot, the blast load is projected more uniformly onto the plate surface, therefore the deformation and the profile shape shift from a local to a more global mode.

As observed in Figure 8-9-Figure 8-12, while the load radius may be affected by the charge mass, the variation of load decay constant b with the charge mass is smooth linear. Thus, the spatial parameters b, r_e of most blasts are constrained to a specific range and cannot grow unrestrained. considering the mass of explosive and the fluid (air) in which the blast wave propagates, then Eqn. (8-20) may be modified as $b = \frac{M_e}{D_e^4 \rho_a} f'\left(\frac{d}{D_e}\right)$. Thus, combining this expression with Eqn. (8-31) yields:

$$f'_2\left(\frac{d}{D_e}\right) = \frac{D_e^3 \rho_a}{M_e} f_2\left(\frac{d}{D_e}\right) \tag{8-38}$$

giving:

$$bD_e = \frac{\rho_p}{\rho_a}\frac{W_f f_2}{H f_6} \tag{8-39}$$

The furnished expression (8-39), plotted in Figure 8-9, estimates the decay constant independent of the charge mass with reasonable degree of accuracy when combined with Eqn. (8-38), as presented in Figure 8-15.

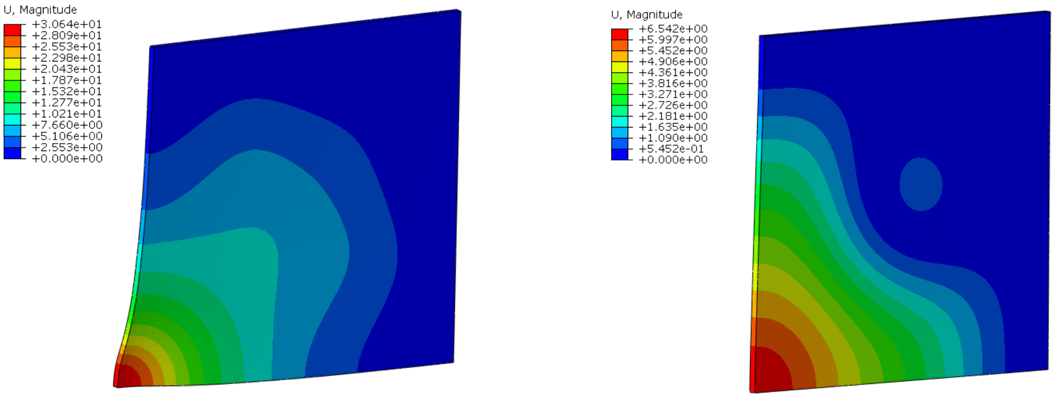

Figure 8-7. Maximum deformation of the panels with (a) $d/D_e = 0.5$ and (b) $d/D_e = 2$

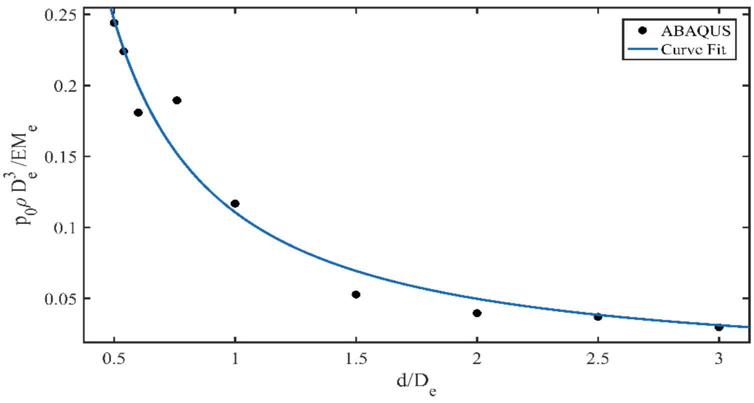

Figure 8-8. Dimensionless pressure load (Eqn. (8-30))

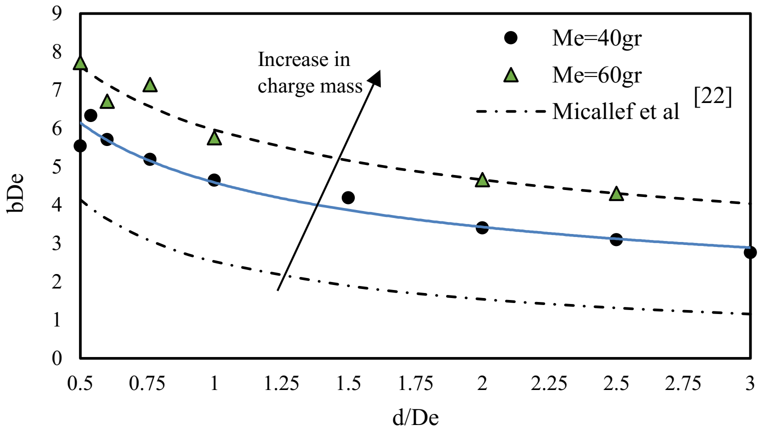

Figure 8-9. Dimensionless load shape decay constant (Eqn. (8-31))

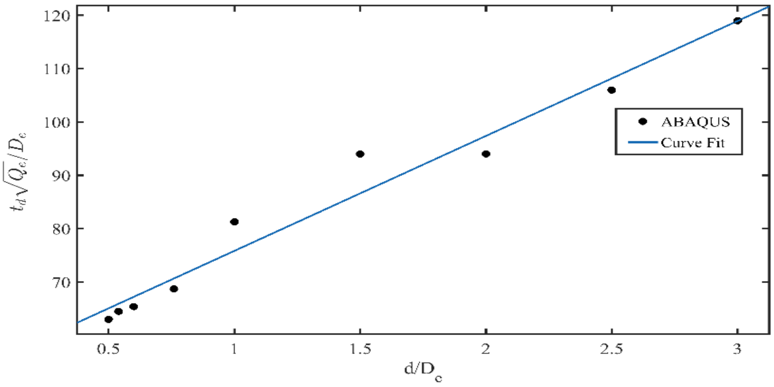

Figure 8-10. Dimensionless paraments relating the duration of the load (Eqn. (8-32))

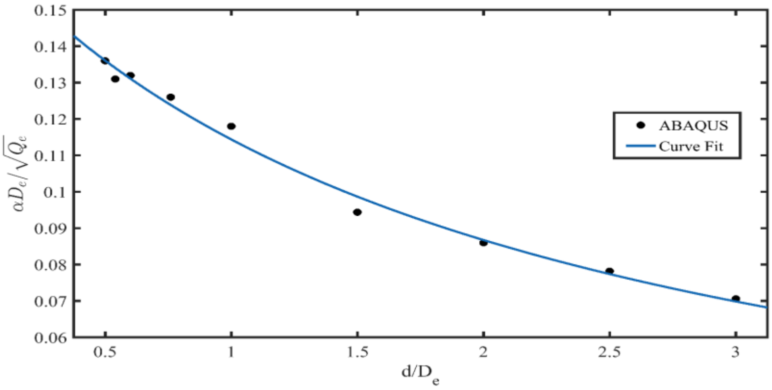

Figure 8-11. Dimensionless pulse shape decay constant α (Eqn. (8-33)

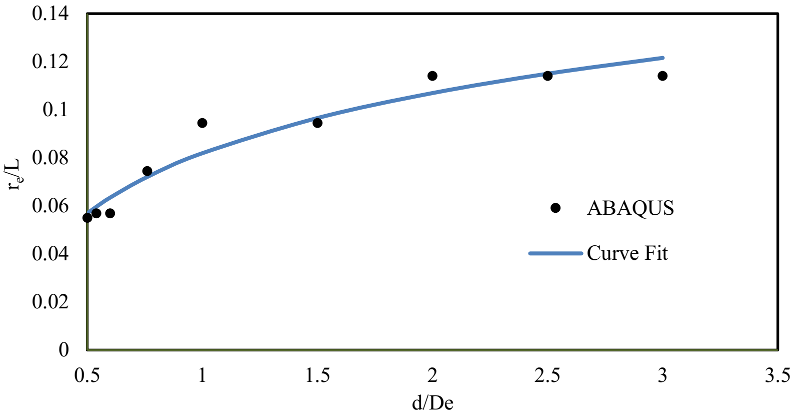

Figure 8-12. Dimensionless r_e (Eqn. (8-34))

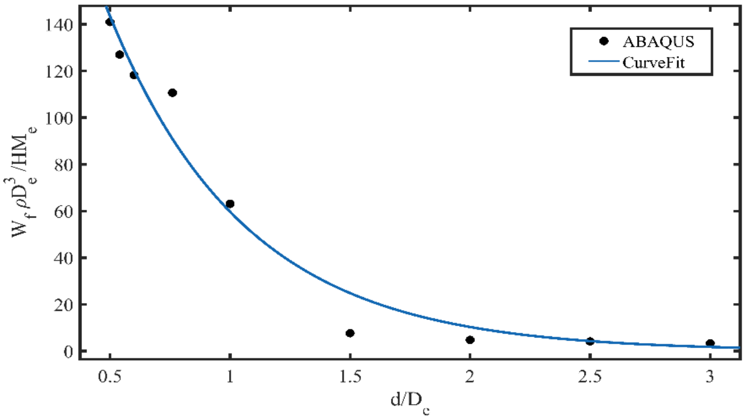

Figure 8-13. Dimensionless permanent deflections of the plate (Eqn. (8-35))

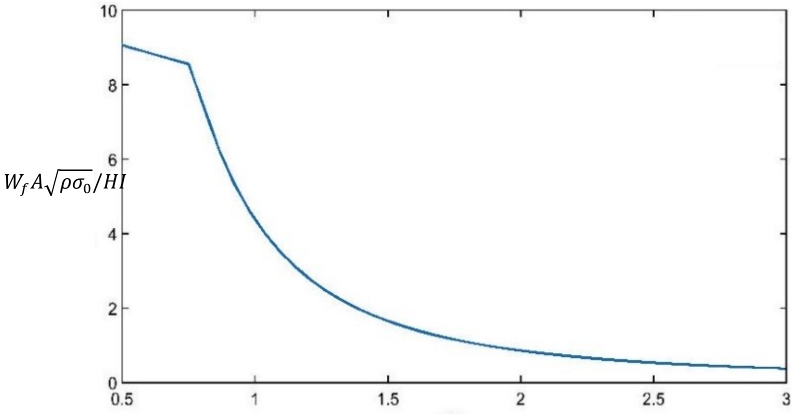

Figure 8-14. Curve fit of normalised displacement-impulse (Eqn. (8-37))

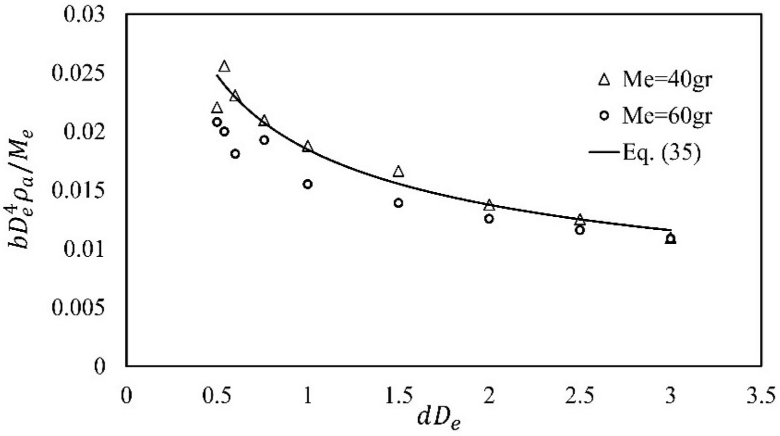

Figure 8-15. Normalised data of load decay parameter

8.6 PREDICTION OF RUPTURE IMPULSE

8.6.1 Damage models

A comparison of the crack lengths of panels is presented in Table 8-5. The cracks grow unidirectionally from the pinnacle of the deformed smaller dome at the plate centre Figure 8-16. Unfortunately, in light of the CEL model C2 failed during simulations, the relevant Lagrangian model was assessed (Figure 8-16 (a)). The Lagrangian model was subjected to a 780MPa load of 25mm central constant radius and 30 $\mu.s$ load duration. The JC-Bridgman fracture model overpredicted the damage surface, although the sketched trajectory of cracks is somewhat analogous to the experiment observations. The observed difference in the crack propagation of the numerical and experimental damage models is attributed to the estimation of the fracture strain, triaxiality and fracture energy.

Table 8-5- comparison of the panels crack length

Model		B5	ASP1	C3	C2
Crack length (mm)	Numerical	23.2	12.7	33.7	Capped 34mm dia, 4 cracks
	Experimental	20.25	-	22.4	Capped 31mm dia., 4 cracks

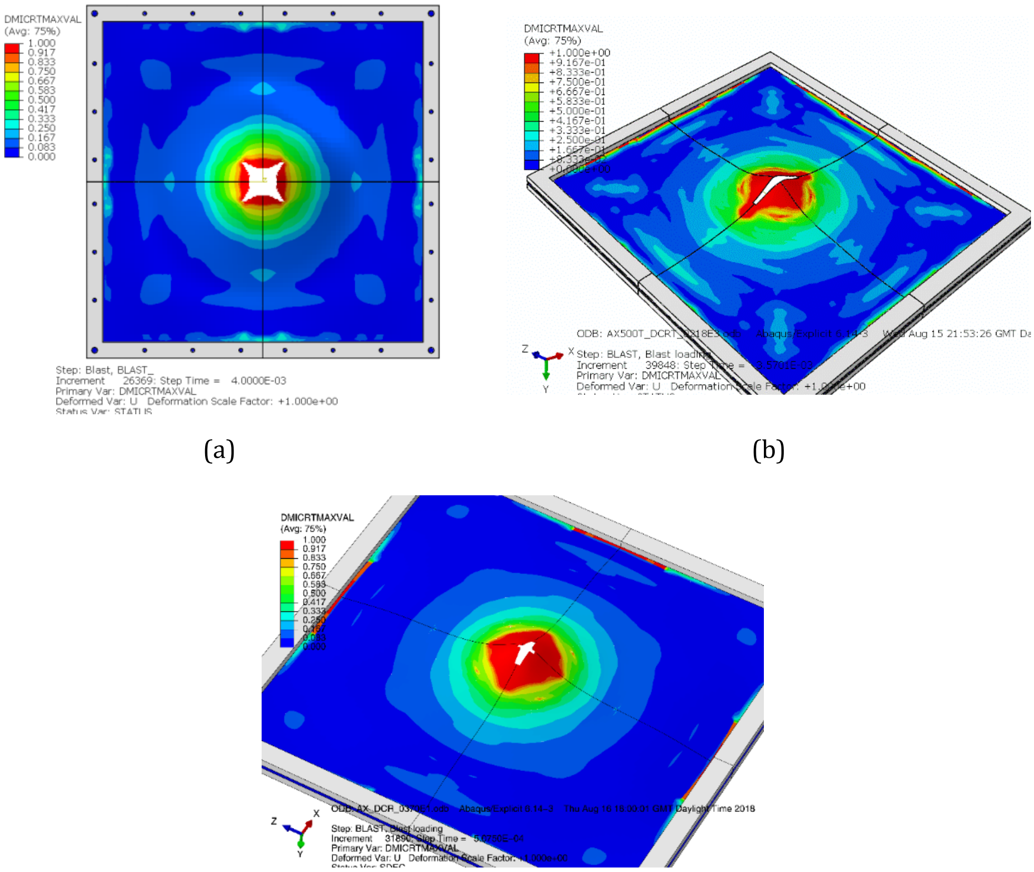

(a) (b)

(c)

Figure 8-16. Crack propagation along the panel axes (a) Lagrangian model C2, (b) model C3, (c) AR370T (ASP1)

8.6.2 Impulsive loading

Eqn. (8-40) represents the impulse imparted to the plate from the centre of projection to the characteristic radial distance $r^* = r$ from centre:

$$I(r) = 2\pi \int_0^{t_d} \int_0^{r} p(r^*, t) r^* dr^* dt^* \tag{8-40}$$

Assuming the impulse imparted over the square surface target of characteristic side length L is equivalent to a circular target of radius R, and defining $\omega_0 = r_e/L$ and $\varpi = r/L$, we integrate Eqn. (8-40) to give:

$$I(\varpi) = \begin{cases} \dfrac{\pi p_0 (\alpha t_d + e^{-\alpha t_d} - 1)(\omega_0 L)^2}{t_d \alpha^2} & \varpi < \omega_0 \\ \dfrac{\pi p_0 (\alpha t_d + e^{-\alpha t_d} - 1)}{t_d \alpha^2} \left((\omega_0 L)^2 + \dfrac{2}{b^2} \left((1 + \omega_0 L b) - e^{-bL(\varpi - \omega_0)} (1 + \varpi L b) \right) \right) & \varpi \geq \omega_0 \end{cases} \tag{8-41}$$

The total impulse that the charge could potentially impart to the target would thus be given by:

$$I(\infty) = \lim_{\varpi \to \infty} \{I(\varpi)\} = \frac{\pi p_0 (\alpha t_d + e^{-\alpha t_d} - 1)}{t_d \alpha^2} \left[(\omega_0 L)^2 + \frac{2(1 + \varpi L b)}{b^2} \right] \qquad \textbf{(8-42)}$$

Thus, a non-dimensional impulse, i, can be defined as the quotient of the impulse imparted to a target over the total impulse that the blast can generate:

$$i = \frac{I(\varpi)}{I(\infty)} = \begin{cases} \dfrac{(\omega_0 L)^2}{2 + 2\omega_0 L b + (\omega_0 L b)^2} & \varpi < \omega_0 \\ 1 - \dfrac{2e^{-Lb(\varpi - \omega_0)}[1 + \varpi L b]}{2 + 2\omega_0 L b + (\omega_0 L b)^2} & \varpi \geq \omega_0 \end{cases} \qquad \textbf{(8-43)}$$

Eqn. (8-43) indicates the efficacy of the plate to dissipate the transmitted impulse, measured against the total impulse required to penetrate the plate (rupture impulse or impulse threshold). Potentially, Eqn. (8-43) could be used in design purposes of protective armour plates. Most blast scenarios investigated here correspond to $50 \leq b \leq 120$, for the finite region of $0 < \varpi < 0.5$ the charge is 95% efficient (Figure 8-17). Turning the argument around, the reciprocal of Eqn. (8-43) determines the efficiency of the blast wave to perforate the target, with $I(\varpi)/I(\varpi) = 1$ indicating the full impulse imparted to the target, a measure used in military purposes.

For the blast loads generated by the same mass of explosive, Figure 8-18 suggests that most catastrophic scenarios would be the small charge diameter and larger charge height, rather than high charge diameter and lower charge height. This is due to the nature of the detonation waves in a cylindrical explosive, the shock front advances in the direction perpendicular to its orientation plane. The pressure wave generated by the explosive product of larger height/diameter ratio would therefore concentrate on the centre of its projection on the plate, imparting more energy locally, thus possessing a higher value of surface traction, giving rise to more localised penetrating effect. For example, within the finite region of $0 < \lambda < 0.5$, most localised blast load scenarios considered here correspond to the range of $60 < b < 120$, generating a potentially perforating impulse. To predict which panels would undergo rupture, a set of

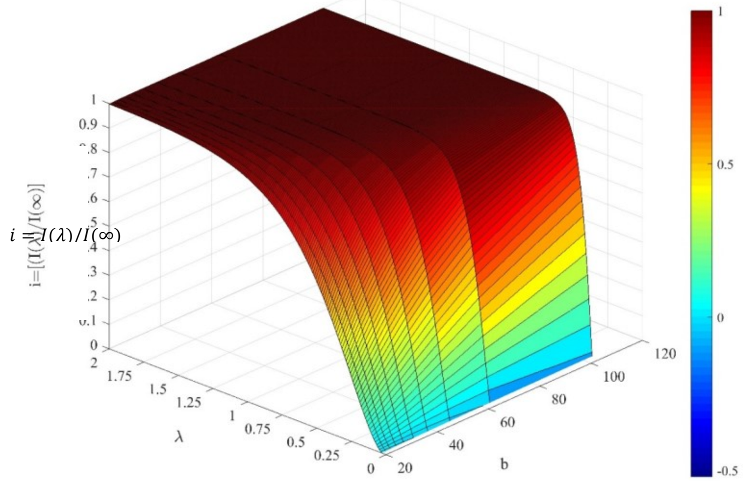

Figure 8-17. interaction surface of the dimensionless impulse i

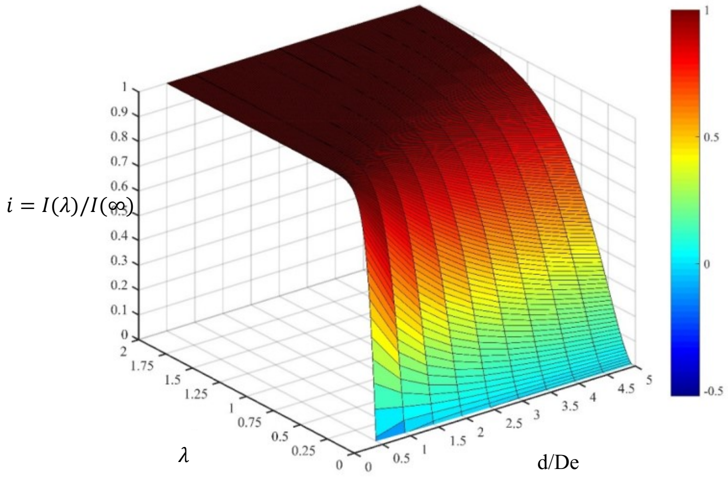

Figure 8-18. interaction surface of dimensionless impulse i against normalised stand off

8.6.3 Energy Absorbing Effectiveness Factor (EAEF)

8.6.3.1 Numerical investigations

Many parameters have been introduced by authors to assess the effectiveness of structural members subjected to static and dynamic loading [202]–[206]. A dimensionless energy absorbing effectiveness factor was introduced by Jones [207] as:

$$\psi = \frac{elastic\ and\ plastic\ strain\ energy\ absorbed\ by\ structural\ member}{enegy\ absorbed\ in\ the\ same\ volume\ of\ material\ up\ to\ failure\ in\ tension} \quad \textbf{(8-44)}$$

The denominator of Eqn. (8-44) is the energy absorbed in the same volume of material up to rupture in a uniaxial tensile test specimen. The dynamic energy absorbing effectiveness factor was also defined, similar to Eqn. (8-44) for the energy absorbing effectiveness factor subject to dynamic loads. Eqn. (8-44) can be modified and rewritten as:

$$\psi' = \frac{\int_0^{\varepsilon_f} \phi(\varepsilon, \sigma_0, \dot{\varepsilon}) \varepsilon d\varepsilon}{V_p SETF} \tag{8-45}$$

Where $\phi(\varepsilon, \sigma_0, \dot{\varepsilon})$ is the strain rate dependent stress tensor of the material subject to dynamic loads, V is the volume of the material and $SETF = 70MJ/m^3$ is the Specific Energy to Tensile Fracture of the material, which is the area under the stress strain curve of the material up to failure in the quasi-static test. Clearly, Eqn. (8-45) can be used to determine the effectiveness of structure under various blast loading scenarios, independent of the material type and geometry. This is particularly useful for the designer to determine the effectiveness of the structures of various geometry and material to dissipate the transmitted momentum of blast without rupture. For example, considering the blast generated by an explosive of $M_e = 60g$, $d = 25mm$ and $D_e = 50mm$, the ARMOX 440T panel of 4.6mm thickness ruptured during the experiment. Thus, the calculated energy absorbed effectiveness factor can be stipulated as the pivot threshold energy to predict rupture of various ARMOX440T panels, when subjected to various proximal or distal pressure waves at increased stand-off but generated with disc explosives of higher masses and (Figure 8-19).

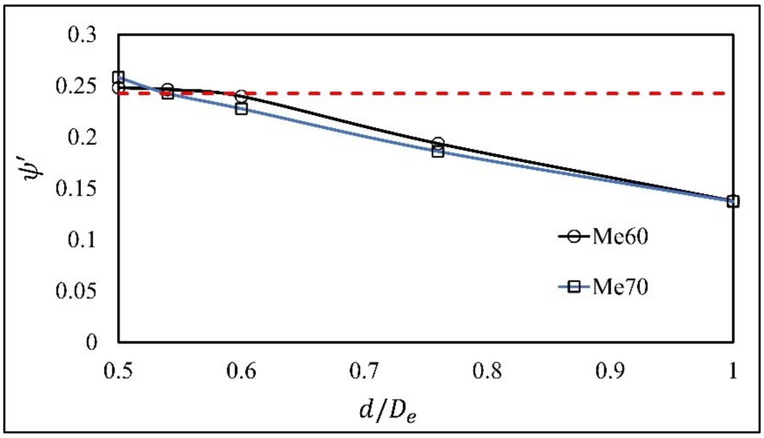

Figure 8-19. Dimensionless energy absorbing effectiveness factor ψ' for ARMOX 440T, the region of $\psi' > 0.248$ correspond to the blast load which is predicted to penetrate the plate.

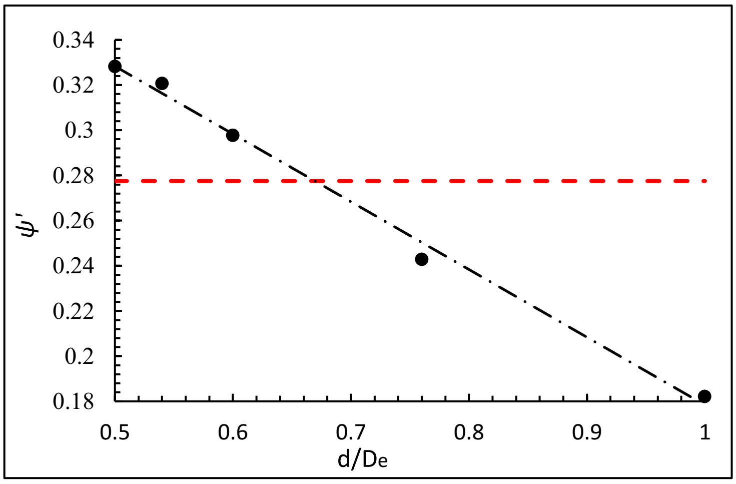

Figure 8-20. Prediction of the failure of ARMOX 370T panels with $M_e = 60g$ (____), using experimental result of ARMOX370T which exhibit Mode II failure (partial tearing at centre) with $M_e = 40g$, $d/D_e = 0.5$ (_ _ _ _).

The data from the AR370T plates are graphed in Figure 8-20. The plastic flow in the plate was characterised by Johnson-Cook visco-plastic model with strain hardening and rate sensitivity given as in (Table 3-2) with identical geometric properties to AR370T except with $H = 3.81mm$, $\sigma_0 = A_1 = 1157MPa$ and $\varepsilon_f = 8\%$. In this case, the threshold energy corresponds to loading parameters of $M_e = 40g$, $d = 25mm$ and $D_e = 50mm$ [61], which ensued partial crack in the centre of the plate. Table 8-6 summarises the deformation and the predicted failure modes of the plates. Whether the panels with higher value of ordinate in Figure 8-20 than those of the threshold energy will actually undergo mode II (tearing at the centre) or mode III (shear failure and capping) failure is not investigated here and requires further experiments.

Table 8-6- permanent and maximum transverse mid-point deflection of the plate from MMALE analysis

Test plate	d (mm)	Range of M_e (g)	W_f (mm)	W (mm)	Predicted Failure mode
AX370T	25	40	29.5	42.93	II (from expt.)
	25	60	-(*)	47.12	II
	27		33.73	45.20	II
	30		31.82	43.65	II
	38		26.21	38.58	I
	50		20.33	32.90	I
AX440T	25	60	28.91	40.21	II (from expt.)
	27		27.59	38.80	I
	30		27.78	37.84	I
	38		23.27	33.90	I
	50		17.46	28.79	I

8.6.3.2 Theoretical predictions of rupture impulse

McDonald et al. [52] carried out a series of experimental studies on class 1 RHA, HHA and improved rolled homogeneous armour (IHRA) steel. The authors proposed a minimum mass of PE4 explosive to induce rupture at stand-off 25mm and 13mm of 400mm side length and 4mm thick square plates. However, the relationship between the rupture impulse and the stand-off was not established. The impulse correction parameter was limited to the plates' assumed characteristic thickness. Thus, the results were valid to the range of stand off investigated while full relationship between the stand off, charge mass and rupture threshold may not be explicityly defined.

On the other hand, the concept of energy absorbing effectiveness enables a comparison of structural elements, varying in material properties and geometry, to be drawn on their effectiveness against the perforation impulse unequivocally. By implementing the principle of virtual velocities, the numerator of Eqn. (8-44) may be replaced by the total external energy imparted onto the target. The plate acquires its maximum momentum when the load is complete at $t = t_d$. By assuming an impulsive load regime and using the expressions of velocity and inertia from pattern (A) of motion, a substitution of time derivatives of Eqn. (6-16) in Eqn. (8-47) yields

$$\psi' = \frac{(cos(\omega_1\tau) - 1)(\rho\omega_1^2(\eta - 1)(cos(\omega_1\tau) + 1) - 48\beta p_0)(\eta - 1)}{48U} \tag{8-46}$$

The load parameters of each blast scenario may be evaluated empirically from the Figure 8-12-Figure 8-15 and Eqn. (8-45) whereby the EAEF of the panels is compared in Figure 8-21. The rupture threshold of the material may be estimated as the minimum value of the energy absorbing effectiveness factor ψ' where the cracks appeared through the surface of the material, which was calculated as 25. At this value, a transition from Mode I failure to higher modes was noticeable.

However, in accordance with the previous experimental findings, it turns out that the predictions of rupture impulse in Figure 8-21 are irrespective of the significant influence of stand-off effects, overestimating the rupture threshold of the panels with high impulse emanating from more distal charges (e.g. panel ASP6, ASP4 and C4). Higher impulse emanating from increase of charge mass would suggest higher energy absorbing factor, although the increase of impulse was offset by the stand-off. The disparity of the prescribed loading parameters (b, R_e, t_d, p_0) in each blast load scenario would further bring about complications in accurate estimation of the energy absorbing effectiveness factor. More often than not, the rapid assessment of localised blast response is not straightforward unless a *priori* knowledge of each load parameter is established accurately. To this end, Eqn. (8-45) may be modified into:

$$\psi'_s = \left|\psi' \ln\left(\frac{d}{D_e}\right)\right| \tag{8-47}$$

Which is the EAEF of impulsive loads. To eliminate the pulse dependence, however, the load magnitude p_0 and pulse duration τ may, be replaced with effective load p_e and centroid of the pulse t_m, respectively.

Using this approach, the pivot threshold of ψ'_s was identical for the investigated panels in the Table 8-7. Thus, the single non-dimensional parameter can estimate the disparity in the plethora of load configurations, as illustrated in Figure 8-22. The mere use of the Non-Dimensional Impulse parameter ϕ_{ql} should be couched in caveats as it does not account for the influence of the material type. For example, Armour ASP1, while the mild steel panel MSP6 and aluminium alloy AA5083H116 all ruptured due to similar loading configurations, each gave a different value of $\phi_{ql} = 12.21, 21.87$ and 6.08. In contrast, the difference in the values of ψ_s of these panels was inconsequaential. With the exception of models ASP1 and ASP4 which impulse measurement were higher than the ruptured panels, preliminary predictions of rupture impulse by mere utilisation of ψ'_s or ensemble with ϕ_{ql} is promising.

Table 8-7-tabulated data of the materials investigated in Figure 8-21-Figure 8-22

MODEL		ϕ_{ql}	ψ'_s			ϕ_{ql}	ψ'_s		ϕ_{ql}	ϕ_{ql}	ψ'_s
AR370T	ASP1*	12.21	4.95	A440T	AX24	4.51	0.39	Aluminium alloy	AL1	3.80	0.72
	ASP2	10.09	3.27		B1	5.84	0.66		AL2	3.72	1.74
	ASP3	12.55	5.88		B2	8.28	1.35		AL3	5.35	1.46
	ASP4	21.86	18.06		B3	5.91	1.70		AL4	5.40	3.78
	ASP5	12.29	1.93		B6	9.77	4.78		AL5*	6.08	4.81
	ASP6	15.28	3.01		B5*	12.08	7.36		AL7	3.04	1.14
	ASP7	13.58	0.38		B4	5.77	0.69		AL8	2.98	0.43
	ASP8	15.28	0.46		B7	12.90	3.55		AL9	2.12	0.53
MS4	MSP1	12.65	1.76	A500T	C1	11.29	3.02	GFPP	TW1	2.96	4.27
	MSP2	19.86	4.37		C2*	14.84	5.26		TW2	2.33	2.54
	MSP6*	21.87	6.54		C3	13.02	4.13		TW3	3.62	6.58
	MSP8	17.99	4.42		C4	12.34	1.98		TW4	2.88	10.18
	MSP10	21.29	3.82		C5	14.47	1.43		TW5	1.71	1.26
					C7	6.58	0.40		TW6	2.33	6.41
					C8	5.03	0.23		TW7	1.71	3.18

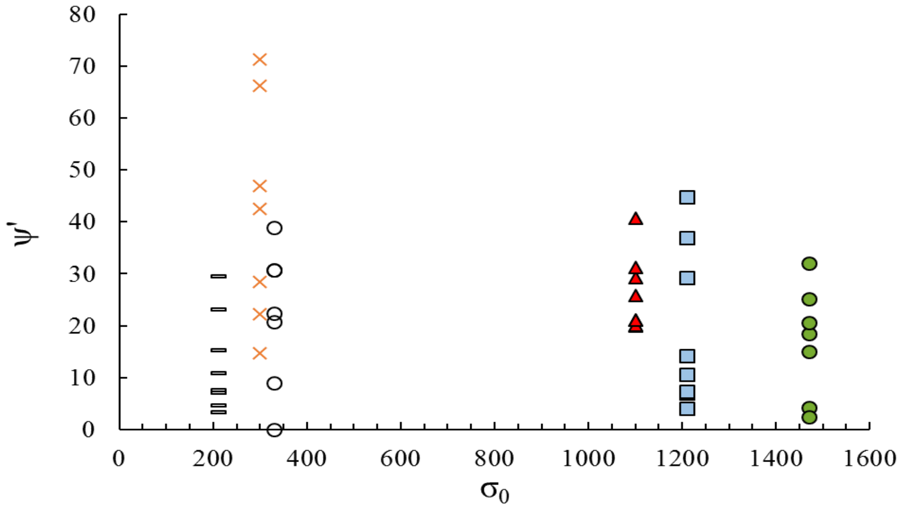

Figure 8-21. Graph of Energy Absorbing Effectiveness for various materials, (-) Aluminium alloy AA5083H116, × Twintex GFPP, ▲ AR370T, ■ AR440T, ● AR500T (data for Aluminium alloy and GFPP were taken from Ref. [61]

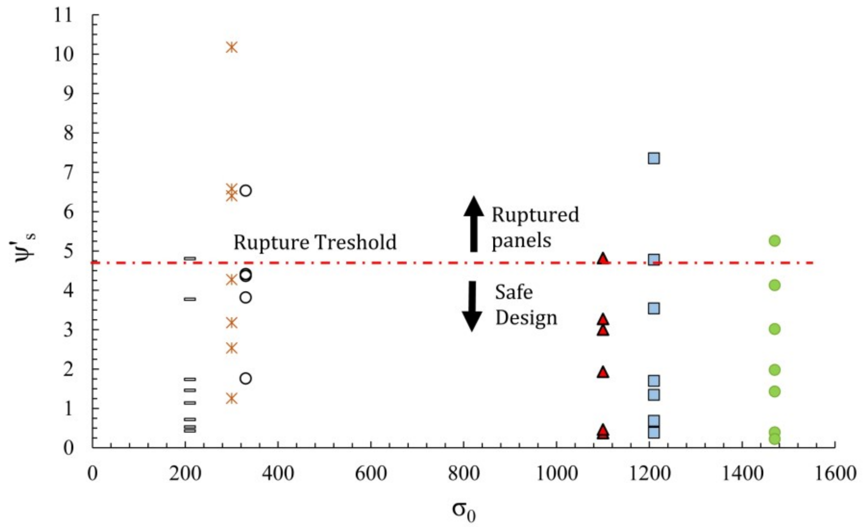

Figure 8-22. Prediction of rupture based on material type, accounting for the stand-off effects.

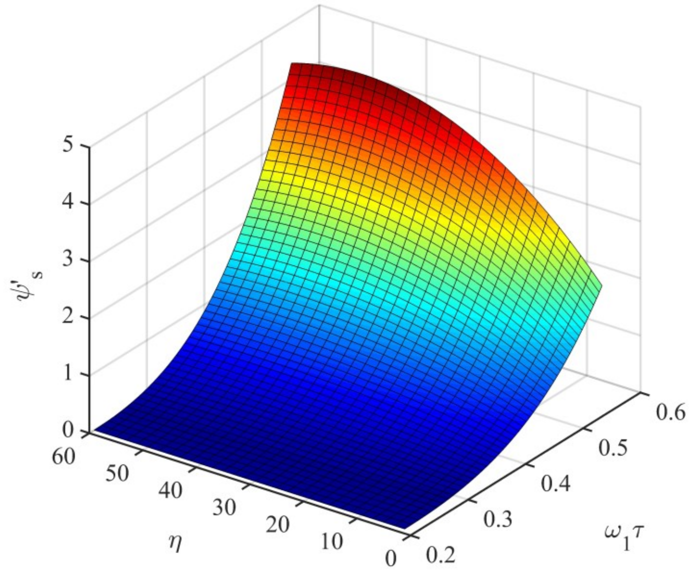

Figure 8-23-In teraction surface of the overloading factor $\boldsymbol{\eta}$, pulse factor $\boldsymbol{\omega_1}$ and $\boldsymbol{\psi'_s}$ (with $\boldsymbol{\tau = 50\mu s, r_e/L = 0.12, b = 100m^{-1}, H = 4mm, L = 150mm}$ for High hardness armour ($\boldsymbol{\sigma_0 = 1600MPa}$)

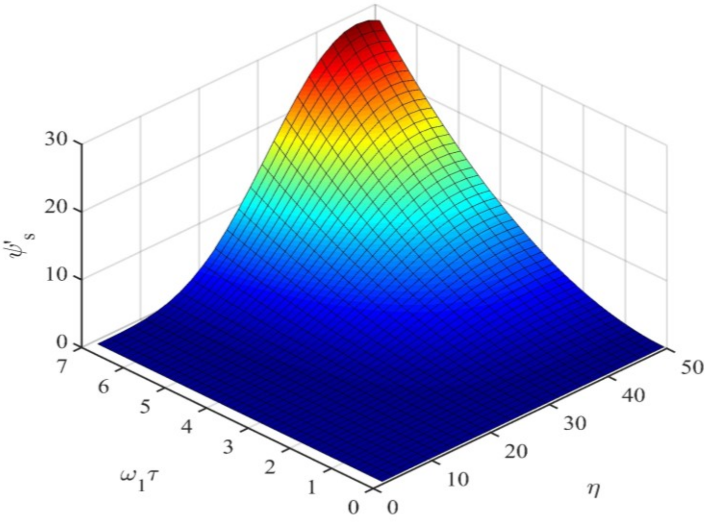

Figure 8-24 Interaction surface of the influence of load duration and overloading factor on $\boldsymbol{\psi'_s}$ for High Hardness Armour ($\boldsymbol{\sigma_0 = 1600MPa, r_e/L = 0.12, L = 150mm}$)

The interaction surface of the parameters such as pulse factor $\omega_1\tau$, load radius $\frac{r_e}{L}$ and overlocing factor on the magnitude of the EAEF are graphed in Figure 8-23-Figure 8-24.

8.7 CONCLUDING REMARKS

This chapter investigated the dynamic plastic response of localised blast loaded steel plates through dimensional analyses of the target and close-in blast loading. By implementing the piecewise blast function in the analysis, a set of 7 dimensionless functions are identified by applying the rank-nullity (Buckingham's Pi-) theorem. The functions were parametrised in terms of standoff/diameter ratio, and obtained in two stages, by a well-known preliminary numerical MMALE method in ABAQUS in conjunction with a regression analysis. The MMALE technique was based on the full interaction of the PE4 explosive products with the rigid structure, from which various loading parameters were obtained. The regression analysis performed on the scatter plots of the loading parameters identifies the form of dimensionless functions.

Preliminary results reveal the existence of a critical stand-off, beyond which the variation of the plate deformation, shifts from abrupt to smooth change, demonstrating a shift in the sensitivity of the plate response to the projection of the blast. With more proximal blast, the projection of the blast is focused on the central part of the plate, leading to large deformations, higher deformation gradients and potential rupture of the plate.

The dimensionless parameters studied here provide a spectrum of data that can render the same trend for the response of full-scale prototype plates possessing the same values of dimensionless parameters as the small-scale models to blast loads, without having to perform rigorous blast testing on the physical panel prototype.

A series of further FSI simulations was performed using deformable target surface. The numerical models were compared against the experimental data, showing good agreements in terms of permanent and maximum deformations. Although further investigations are required to predict the influence of the FSI on the damage model of the plates and accurate estimations accordingly, a commentary on the damage model of the plates was discussed in the context of the problem.

For experimental specimens with loading parameters that resulted in the rupture of the panels (Mode II failure), the dimensionless energy absorbing effectiveness factor was quantified numerically and utilised to predict the rupture of the plates for more distal blasts but increased charge heights (mass). This approach provides a pragmatic tool on prediction the threshold point of rupture, at which the transition of the deformed plates mode from mode I to higher modes occurs. geometrically similar ARMOX prototype panels, on which the load is generated by a cylindrical PE4 charge, assuming the material properties, such as visco-plasticity phenomenon, are impervious to scaling laws.

CHAPTER 9

Conclusions and recommendations for future work

9.1 INTRODUCTION

In light of the scope of this thesis, as outlined in Section 1.5, a literature review of the existing work on the subject was explored. The review signified the dearth of any available methods to describe the phenomenon of, and effects associated with, the localised blast load emanated from certain charge geometry, charge mass and stand-off on quadrangular plates-particularly high strength armour steel. The review also investigated the recent methods to capture the transient response of the plates, the significance of the localised blasts discussed in experimental and numerical studies pertaining to the performance of the high strength steel panels. The thesis also reviewed available theoretical models on the blast response of metallic plates, having various slenderness ratios, subjected to uniform blast.

Based on the literature survey, the scope of the first study entailed the findings from a series of experimental tests carried out in BISRU, which were supplemented by various numerical. It was found imperative to utilise the methods incorporating the FSI effects, such as MMALE, to predict accurate response of the structure numerically. Empirical methods were also performed to correlate between the findings of this thesis, available experimental studies, such as those on ARMOX 370T by [61].

The limitations highlighted in the literature, revealed a significant difference between the experimental/numerical results in this thesis and available empirical/theoretical models. Furthermore, the literature was found devoid of any theoretical models on quadrangular plates subjected to localised blast. This led to the various analytical studies attributed to the rigid-plastic and elastic-plastic plate constitutive equations, using the interactive yield surface of bending, combined bending and membrane or bending - transverse shear yield surfaces.

9.2 SUMMARY OF PRINCIPAL FINDINGS

9.2.1 On the characteristics of the localised blast load

The conclusions in this respect are as follows.

- The blast load function was assumed as a multiplicative decomposition of its spatial part and temporal part. The spatial part of the blast load was stipulated as a piecewise continuous function described by Eqn. (5-1), which is universal and adjustable, through alteration of its parameters, to replicate various loading scenarios from proximal (localised) to distal (global) blast loads. Various forms of the temporal part of the load were investigated in the context of the problem. The form of blast function corroborated with the numerical simulations and the findings in the literature [67], [208].

- A series of dimensional parameters that fully describe the blast load parameters (spatial and temporal functions) were quantified. The physics of the localised blast phenomenon, its highlighted effect on structure with respect to the plate geometry and stand-off distance was investigated. The correlation between the state variables was stipulated on the basis of a dimensional study.

- Past empirical analyses were extended to speculate the relationship between the permanent deformation of steel panels with the dimensionless impulse, considering a large scatter of data from experiments. It should be appreciated that, the empirical correlations, based on the inductive methods, are not universal and vary depending on the material type, blast test conditions, or set-up, of the explosive geometry and type. However, these models serve as a baseline approximation of the plate geometry for the design applications.

9.2.2 Blast testing on armour and mild steel

It can be concluded that

- Quasi-static tensile tests were performed on AR440T, the tensile stress strain curve gave the Young's modulus of $E \cong 200GPa$, yield stress of 1210MPa and rupture strain of 6%. Information for other materials used was taken from the literature.[18], [61], [132]

- The transient deformation of panels was captured numerically and validated by those from the DIC techniques. The martensitic high hardness armours (AR440T and AR500T) exhibited lower deformations than the mild steel or RHA type class 1 AR370T, due to the higher strength, the ability of energy dissipation increased.

- For the same blast threat, AR500T with areal density $\mu = 32kg/m^2$ and same geometry offers most reduction in permanent deformations and prevents rupture, when compared to mild steel or other armour steel type investigated earlier.

- None the panels exhibited rupture at stand-off beyond 25mm. The armour steel AR500T cracked due to 60g PE4 of 50mm diameter placed at 25mm, while AR440T exhibited rupture at a decreased mass of 50g. However, the results of [61] showed that hardness or ductility cannot be used to predict the rupture threshold of panels, as both AR370T and mild steel ruptured due to same impulse. However, the permanent deformation of AR370T was lower than the mild steel specimen.

9.2.3 On the fluid structure Interactions

The findings from the fluid structure interaction phenomenon are outlined as follows.

- The plate stiffness/rigidity, which is influenced by its characteristic thickness, inherently affects the magnitude of the imparted pressure to the target, in the case of localised blasts.

- Due to the superposition of the incident wave and the reflected wave at the fluid structure interface, a pressure of low magnitude builds up underneath the charge which travels along the plate characteristic dimensions. This pressure does not contribute to the maximum deformation of the plate but may be attributed to the change of curvature at certain distance from the target centre. However, the total impulse imparted to the rigid target plate may be reduced on the deformable clamped target, because of the contributions of the clamped boundaries to absorb the pressure build-up This occurs provided the quotient of the blast diameter to plate side length increases beyond 0.33. As the stand off on the target plates studied in this thesis was low, only negligible difference between the two impulses was observed.

- The pressure build-up due to the fluid structure interaction is often ignored in simplified models, viz., the pure Lagrangian and ConWep studies. Therefore, the CEL methods are essentially preferred due to accurate estimation of the state variables.

However, due to the computational expenses associated with the 3D MMALE methods, the 2D models may be set up to conveniently estimate the Mode I response [52], [138].

- The permanent and maximum deformation of the UEL, CEL and pure Lagrangian models were compared. The deformations of CEL methods were lower than the other methods, more concurrent with the experimental results, due not only to a reduction of transmitted impulse on flexible target, but also the implementation of FSI.

- The reduced form of load shape as a central uniform blast, pertaining to the Lagrangian models, considerably sacrifices the accuracy of the numerical solutions.

9.2.4 On the theoretical solutions of dynamic plastic collapse of the plates

The following points have been identified from the analytical work in this thesis.

- Using the constitutive framework of limit analysis, an expression for the static plastic collapse of the square plate, subject to the localised blast load was presented.

- This led to an investigation of the permanent deformation of the dynamically loaded square plates in the circumstances where the associated Kirchhoff-Love plate theory may be invoked. The apparition between the kinematically admissible velocity profiles was distinguished by the value of critical load amplification factor, having a stationary plastic hinge when $\eta \leq \eta_{crit}$ and travelling hinge provided $\eta \leq \eta_{crit}$. The associated permanent displacement was given in Eqn. (5-38) and (5-65) in each case, respectively.

- The analysis was extended, within bounds of rigid-plastic theory, to the large deformation of the membranes. The rigorous analyses revealed that the former case; i.e. stationary plastic hinge, would also occur provided the quotient of the central uniform blast load constant to plate length, $\omega_0 = \frac{r_e}{L} \leq 0.3$ regardless of the load magnitude, while the two necessary conditions to occurrence of an active hinge are given by the larger values of ω_0 and $\eta \geq \eta_{crit}$. The associated permanent displacement in each case is given in Eqns. (6-21) and (6-35), respectively.

- The reduced theoretical forms of the permanent deformations, which considered the membrane action only using each velocity profile pattern, was found sufficient to predict the large permanent deformations without the loss of accuracy. Excellent agreements were found between the theoretical models and the numerical and experimental models in the thesis. In dimensionless forms, the theoretical models gave an accurate fit to the large scatter of experimental data in the literature.

  - The influence of boundary conditions was investigated in the context of each analysis developed from constitutive expressions regarding the bending, combined bending and membrane, combined transverse shear and bending yield surfaces. The analyses of simply-supported and clamped boundaries provide upper and lower bound estimates for the most practical deign applications.
  - A commentary on the influence of visco-plasticity phenomenon was added. Further modal solutions implementing this phenomenon may be found, *a posteriori*, by replacing the corresponding loading parameters of the uniform blast with those of the localised one (viz., $V_0 = V_1\epsilon_1, \tau, W_f$), *mutatis mutandis*, in the expressions of strain or strain rate tensor from Ref. [105]. However, it turns out that the high strength armour steel material are insensitive to blast load up to strain rate of $3000s^{-1}$, thus, the derived theoretical expressions for membranes, as observed from the validation studies, predict the permanent deformation of the square plates with high degree of accuracy.
  - The theoretical solutions of class III thick plates $\nu \geq 5$, characterised by Mindlin-Reisner plate theory, converge to the cases of bending only. The range of slenderness ratio $\nu < 5$ is impractical in the design applications of protective plates against localised blasts. Thus, for moderately stocky plates, provided the membrane forces are insignificant, the classical Kirchhoff Love plate theory sufficiently estimates the permanent deformations.
  - Results for alternative pulse shape than rectangular pulse were presented in
  - The pulse shape played a significant role in the overall performance of the plate described by either aforementioned theories, provided the blast load regime is dynamic; however, the pulse load effect was virtually eliminated by considering Youngdahl's correlation parameters. The non-monotonic decay type of blast was not investigated, given the assessments of this type have been addressed in the literature [100].

- A study of nonlinear elastic systems was also conducted, which, combined with the rigid-perfectly plastic theory, signifies the deformation path of the elastic-plastic plates subject to various load conditions. It is anticipated that the mere FVK solutions provide useful information on the non-linear deformation of the membranes prior to point of stiffness degradation.

9.2.5 On the parameters affecting the blast load

The main findings are

- For experimental specimens with loading parameters that resulted in the rupture of the panels (Mode II failure), the dimensionless energy absorbing effectiveness factor was quantified numerically and utilised to predict the rupture of the plates for more distal blasts but increased charge heights (mass). This approach provides a pragmatic tool on the prediction of the rupture threshold, at which point the transition of the deformed plates mode from mode I to higher modes would occur. geometrically similar ARMOX prototype panels, on which the load is generated by a cylindrical PE4 charge, assuming the material properties, such as visco-plasticity phenomenon, are impervious to scaling laws. The energy absorbing effectiveness parameter is preferred over the SETF, ductility or hardness of the materials, as it provides an established correlation between the rupture threshold and material type.
- The dimensionless parameter accounting for the slenderness ratio, stand off and plate geometry [36] was revised to fit the larger data from experimental and numerical findings.
- The dimensional analysis identified a set of 14 dimensionless parameters that characterise the blast phenomenon and its effect on the isotropic, ductile plates.

9.3 LIMITATIONS OF THE STUDY AND A NOTE FOR FUTURE WORK

The scope of this thesis was, within reasonable bounds of accuracy, limited to simplifications in mathematical and numerical treatments. The limitations of this work have been addressed as follows hereunder. The limitations highlight the need for future investigations

9.3.1 On the dimensionless parameters characterising the blast load

The experimental and numerical work in this thesis were contingent upon consideration of PE4 charges, having cylindrical geometry. It is recommended that the various charge shapes and types (TNT, Composition B) are studied.

The influence of saturated impulse has not been investigated in this thesis. This phenomenon is referred to the critical pulse length beyond which no change in deformations occur. In other words, when the duration of the transverse rectangular pressure pulse load increases, the maximum and permanent deformation of the target plate would be affected by only part of the load, while the rest of the pulse makes no contribution to further increase in deformation [209], [210].

9.3.2 On the theoretical models

The classical constitutive framework of limit analysis was utilised effectively in the rapid assessment of the locally blast loaded plated structures. It is anticipated that the theoretical analyses in this thesis may be used for various practical application of blast loaded plates. For strain rate sensitive materials, it is suggested that the theoretical solutions retaining this phenomenon are investigated.

In the same spirit, the adiabatic shear phenomenon may be incorporated in the theoretical or numerical assessment of plates subjected to localised blasts.

Although various analyses in this thesis considered a special case of square plate, the exact theoretical analyses of rectangular plates may not be straightforward as the functional of the exponential function of the load shape yields an error function. Thus, further insights into the theoretical analysis of localised pressure pulse effects on rectangular plates are recommended.

In the circumstances of stiffened plates, assuming the stiffeners will behave as rigid elements, the theoretical solutions may be effectively altered by incorporating the strain energy (flexural strain energy and the strain energy at the plastic hinges), as well as the kinetic energy of the stiffeners, to the right and left-hand side of dynamic energy equilibrium Eqn. (6-5), respectively. An SDOF model of this analysis on uniform blast is presented by [98].

The foregoing analysis performed on the elastic response of thin, isotropic membranes may be extended to the composite materials such as PVB laminated glass, provided the full composite action may be considered a reasonable assumption prior to the failure point of the composite [211], [212]. To this end, the rule of mixture may be implemented to estimate the stiffness and Poisson's ratio of the system. The combined Young modulus, Poisson's ratio and mass per unit area mis given as $E = (2E_g h_g + E_p h_p)/(h_g + h_p)$ and Poisson's ratio $\nu_e = (2\nu_g h_g + \nu_p h_p)/(h_g + h_p)$, where E_g and E_p represent the modulus of the glass and PVB, respectively, h_g and h_p denote the corresponding thicknesses, while ν_g and ν_p represent the Poisson's ratios of glass and PVB, respectively [211].

While the expressions of elastic vibrations, considering only the first term of the truncated series of transverse displacement and Airy stress function ((6-75),(6-76), respectively) predicted the transient deformation of the plate with good estimate, it is interesting to investigate to which degree the truncation of the series would ensure the convergence of the theoretical predictions to the numerical/experimental measurements with high degree of accuracy.

9.3.3 Blast design and FSI

The state variables concerning the FSI in the studies by Refs. [31]–[33] concerned the uniform blast load. Similar studies in the circumstances of localised blasts are recommended for further study. The theoretical treatment may be effectively investigated in Cartesian or curvilinear coordinates. In a similar fashion, the numerical and analytical work on FSI may be extended to blast threats of multiple charges, such as the cases of reactive armour [213], [214].

The spring-back of the system was not investigated. The spring-back arises due to the elastic rebound of deformation, however, measuring spring-back analytically is difficult as the elastic and plastic zones are inter-spread in the structure.

Dimensional analysis and a comparison of the rupture performance of armour steel, composites and hybrid systems (Fibre Metal Laminates) due to various charge types, geometry and stand-off, by utilising the MMALE methods are recommended for future work.

9.4 CITATIONS

[1] A. Chen, L. A. Louca, and A. Y. Elghazouli, “Blast assessment of steel switch boxes under detonation loading scenarios,” *Int. J. Impact Eng.*, vol. 78, pp. 51–63, 2015.

[2] NATO, *Test Methodology for Protection of Vehicle Occupants against Anti-Vehicular Landmine Effects*, vol. 323, no. April. 2007.

[3] A. Ramasamy, A. M. Hill, S. D. Masouros, F. Gordon, J. C. Clasper, and A. M. J. Bull, “Evaluating the effect of vehicle modification in reducing injuries from landmine blasts. An analysis of 2212 incidents and its application for humanitarian purposes,” *Accid. Anal. Prev.*, vol. 43, no. 5, pp. 1878–1886, 2011.

[4] M. Y. Yahya, W. J. Cantwell, G. S. Langdon, and G. N. Nurick, “The blast behavior of fiber reinforced thermoplastic laminates,” *J. Compos. Mater.*, vol. 42, no. 21, pp. 2275–2297, 2008.

[5] K. Micallef, “The dynamic response of blast-loaded monolithic and composite plated structures: A thesis submitted for the degree of Doctor of Philosophy (Ph. D),” Imperial College London, 2013.

[6] U.S Detail Specification MIL-DTL-12560K (MR), “ARMOR PLATE, STEEL, WROUGHT, HOMOGENEOUS (FOR USE IN COMBAT-VEHICLES AND FOR AMMUNITION TESTING),” 2013.

[7] U.S Detail Specification MIL-DTL-32332 (MR), “ARMOR PLATE, STEEL, WROUGHT, ULTRA-HIGH-HARDNESS,” 2009.

[8] U.S Detail Specification MIL-DTL-46100E (MR), “ARMOR PLATE, STEEL, WROUGHT, HIGH-HARDNESS,” 2008.

[9] C. Choi, M. Callaghan, and B. Dixon, “Blast Performance of Four Armour Materials,” 2013.

[10] W. R. Whittington *et al.*, “Capturing the effect of temperature, strain rate, and stress state on the plasticity and fracture of rolled homogeneous armor (RHA) steel,” *Mater. Sci. Eng. A*, vol. 594, pp. 82–88, 2014.

[11] S. J. Cimpoeru, “The Mechanical Metallurgy of Armour Steels,” DST-Group-TR-3305, Melbourne, 2016.

[12] P. D. Smith and J. Hetherington, *Blast and Ballistic Loading of Structures*, 2011th ed. New York: Taylor & Francis, 1994.

[13] R. Rajendran and J. M. Lee, “Blast loaded plates,” *Mar. Struct.*, vol. 22, no. 2, pp. 99–127, 2009.

[14] M. . . Nettleton, *Gaseous Detonations: Their Nature, Effects and Control*, 1st ed. London: Chapman and Hall, 1987.

[15] M. H. Keshavarz and H. R. Nazari, “A simple method to assess detonation temperature without using any experimental data and computer code,” *J. Hazard. Mater.*, vol. 133, no. 1–3, pp. 129–134, 2006.

[16] M. H. Keshavarz and H. R. Pouretedal, “An empirical method for predicting detonation pressure of CHNOFCl explosives,” *Thermochim. Acta*, vol. 414, no. 2, pp. 203–208, 2004.

[17] M. H. Keshavarz, “Simple correlation for predicting detonation velocity of ideal and non-ideal explosives,” *J. Hazard. Mater.*, vol. 166, no. 2–3, pp. 762–769, 2009.

[18] T. Ngo, P. Mendis, A. Gupta, and J. Ramsay, “Blast loading and blast effects on structures - An overview,” *Electron. J. Struct. Eng.*, vol. 7, pp. 76–91, 2007.

[19] M. Larcher and F. Casadei, *Explosions in Complex Geometries - A Comparison of Several Approaches*,

vol. 1, no. 2. 2010.

[20] V. Aune, G. Valsamos, F. Casadei, M. Larcher, M. Langseth, and T. Børvik, “Numerical study on the structural response of blast-loaded thin aluminium and steel plates,” *Int. J. Impact Eng.*, vol. 99, pp. 131–144, 2017.

[21] N. Jacob, G. N. Nurick, and G. S. Langdon, “The effect of stand-off distance on the failure of fully clamped circular mild steel plates subjected to blast loads,” *Eng. Struct.*, vol. 29, no. 10, pp. 2723–2736, 2007.

[22] K. Micallef, A. Soleiman Fallah, D. J. Pope, M. Moatamedi, and L. A. Louca, “On dimensionless loading parameters for close-in blasts,” *Int. Jounral Multiphysics*, vol. 9, no. 2, pp. 171–194, 2015.

[23] DOD., *Unified Facilities Criteria (UFC): Structures to Resist the Effects of Accidental Explosions (UFC 3-340-02)*, no. December. Washington DC.: Department of Defence, 2008.

[24] A. Neuberger, S. Peles, and D. Rittel, “Scaling the response of circular plates subjected to large and close-range spherical explosions. Part II: Buried charges,” *Int. J. Impact Eng.*, vol. 34, no. 5, pp. 874–882, 2007.

[25] S. Chung Kim Yuen, G. S. Langdon, G. N. Nurick, E. G. Pickering, and V. H. Balden, “Response of V-shape plates to localised blast load: Experiments and numerical simulation,” *Int. J. Impact Eng.*, vol. 46, pp. 97–109, 2012.

[26] A. Neuberger, S. Peles, and D. Rittel, “Springback of circular clamped armor steel plates subjected to spherical air-blast loading,” *Int. J. Impact Eng.*, vol. 36, no. 1, pp. 53–60, 2009.

[27] N. Mehreganian, A. S. Fallah, G. K. Boiger, and L. A. Louca, “Reponse of armour steel square plates to localised air blast loading- A dimensional analysis,” *Int. J. Multiphys.*, vol. 11, no. 4, pp. 387–412, 2017.

[28] C. N. Kingery and N. Bulmash, “Air blast parameters from TNT spherical air burst and hemispherical surface burst, Report ARBL-TR-02555,” MD, 1984.

[29] Departments of the Army; the Navy; and the Air Force, “TM5-1300 Structure to resist the effects of accidental explosions.pdf,” *Army Manual*, vol. 5–1300. 1990.

[30] J. Shin, A. S. Whittaker, and D. Cormie, “TNT Equivalency for Overpressure and Impulse for Detonations of Spherical Charges of High Explosives,” *Int. J. Prot. Struct.*, vol. 6, no. 3, pp. 567–579, 2015.

[31] G. I. Taylor, “The pressure and Impulse of Submarine Explosion Waves on Plates,” *The Scientific Papers of Sir Geoffrey Ingram Taylor*, vol. III, no. 4. Cambridge University Press, Cambridge, UK, pp. 287–303, 1963.

[32] N. Kambouchev, R. Radovitzky, and L. Noels, “Fluid–Structure Interaction Effects in the Dynamic Response of Free-Standing Plates to Uniform Shock Loading,” *J. Appl. Mech.*, vol. 74, no. 5, p. 1042, 2007.

[33] N. Kambouchev, L. Noels, and R. Radovitzky, “Nonlinear compressibility effects in fluid-structure interaction and their implications on the air-blast loading of structures,” *J. Appl. Phys.*, vol. 100, no. 6, 2006.

[34] J. W. Hutchinson, “Energy and Momentum Transfer in Air Shocks,” *J. Appl. Mech.*, vol. 76, no. 5, p. 051307, 2009.

[35] N. Jones, *Structural Impact*, 1st ed. Cambridge: Cambridge University Press, 1997.

[36] A. S. Fallah, K. Micallef, G. S. Langdon, W. C. Lee, P. T. Curtis, and L. A. Louca, “Dynamic response of Dyneema® HB26 plates to localised blast loading,” *Int. J. Impact Eng.*, vol. 73, no. November, pp. 91–100, 2014.

[37] C. K. Youngdahl, “Influence of pulse shape on the final plastic deformation of a circular plate,” *Int. J. Solids Struct.*, vol. 7, no. 9, pp. 1127–1142, 1971.

[38] D. Karagiozova, G. S. Langdon, G. N. Nurick, and S. Chung Kim Yuen, “Simulation of the response of fibre-metal laminates to localised blast loading,” *Int. J. Impact Eng.*, vol. 37, no. 6, pp. 766–782, 2010.

[39] S. B. Menkes and H. J. Opat, “Broken beams - Tearing and shear failures in explosively loaded clamped beams,” *Exp. Mech.*, vol. 13, no. 11, pp. 480–486, 1973.

[40] M. D. Olson, G. N. Nurick, and J. R. Fagnan, “Deformation and rupture of blast loaded square plates—predictions and experiments,” *Int. J. Impact Eng.*, vol. 13, no. 2, pp. 279–291, 1993.

[41] R. G. Teeling-Smith and G. N. Nurick, “The deformation and tearing of thin circular plates subjected to impulsive loads,” *Int. J. Impact Eng.*, vol. 11, no. 1, pp. 77–91, 1991.

[42] G. N. Nurick and G. C. Shave, “The deformation and tearing of thin square plates subjected to impulsive loads - An experimental study,” *Int. J. Impact Eng.*, vol. 18, no. 1, pp. 99–116, 1996.

[43] G. N. Nurick, M. E. Gelman, and N. S. Marshall, “Tearing of blast loaded plates with clamped boundary conditions,” *Int. J. Impact Eng.*, vol. 18, no. 7–8, pp. 803–827, 1996.

[44] G. N. Nurick and A. M. Radford, “Deformation and tearing of clamped circular plates subjected to localised central blast loads,” *Recent Dev. Comput. Appl. Mech. a Vol. honour John B. Martin*, pp. 276–301, 1997.

[45] S. Chung Kim Yuen and G. N. Nurick, “The significance of the thickness of a plate when subjected to localised blast loads,” *Blast Impact Load. Struct.*, pp. 471–499, 2000.

[46] G. S. Langdon, S. C. K. Yuen, and G. N. Nurick, “Experimental and numerical studies on the response of quadrangular stiffened plates. Part II: Localised blast loading,” *Int. J. Impact Eng.*, vol. 31, no. 1, pp. 85–111, 2005.

[47] G. S. Langdon, S. C. K. Yuen, and G. N. Nurick, “The response of stiffened square plates subjected to localised blast loading,” in *Structures Under Shock and Impact*, vol. VII, N. Jones, C. Rajendran, and A. Brebbia, Eds. WIT Press, 2002.

[48] N. S. Rudrapatna, R. Vaziri, and M. D. Olson, “Deformation and failure of blast-loaded stiffened plates,” *Int. J. Impact Eng.*, vol. 24, no. 5, pp. 457–474, 2000.

[49] R. Rajendran and K. Narasimhan, “A shock factor based approach for the damage assessment of plane plates subjected to underwater explosion,” *J. Strain Anal. Eng. Des.*, vol. 41, no. 6, pp. 417–425, 2006.

[50] V. H. Balden and G. N. Nurick, “Numerical simulation of the post-failure motion of steel plates subjected to blast loading,” *Int. J. Impact Eng.*, vol. 32, no. 1–4, pp. 14–34, 2006.

[51] T. Wierzbicki and G. N. Nurick, “Large deformation of thin plates under localised impulsive loading,” *Int. J. Impact Eng.*, vol. 18, no. 96, pp. 899–918, 1996.

[52] B. McDonald, H. Bornstein, G. S. Langdon, R. Curry, A. Daliri, and A. C. Orifici, “Experimental response of high strength steels to localised blast loading,” *Int. J. Impact Eng.*, vol. 115, no. October 2017, pp. 106–119, 2018.

[53] G. S. Langdon, S. L. Lemanski, G. N. Nurick, M. C. Simmons, W. J. Cantwell, and G. K. Schleyer, “Behaviour of fibre-metal laminates subjected to localised blast loading: Part I-Experimental observations,” *Int. J. Impact Eng.*, vol. 34, no. 7, pp. 1202–1222, 2007.

[54] S. C. K. Yuen and G. N. Nurick, “Experimental and numerical studies on the response of quadrangular stiffened plates. Part I: Subjected to uniform blast load,” *Int. J. Impact Eng.*, vol. 31, no. 1, pp. 55–83, 2005.

[55] G. N. Nurick and J. B. Martin, “Deformation of thin plates subjected to impulsive loading—A review,” *Int. J. Impact Eng.*, vol. 8, no. 2, pp. 159–170, Jan. 1989.

[56] M. A. Wiehahn, G. N. Nurick, and H. C. Bowles, “Some insights into the mechanism of the deformation and tearing of thin plates at high strain rates incorporating temperature dependent material properties,” *Struct. under Shock Impact VI*, pp. 35–46, 2000.

[57] W. Grobbelaar and G. Nurick, “An investigation of Structures Subjected to Blast Loads Incorporating an Equation of State to Model the Material Behaviour of the Explosives,” in *7th International Symposium on Structural Failure and Plasticity (IMPLAST 2000)*, 2000, pp. 185–194.

[58] C. Geretto, S. Chung Kim Yuen, and G. N. Nurick, “An experimental study of the effects of degrees of confinement on the response of square mild steel plates subjected to blast loading,” *Int. J. Impact Eng.*, vol. 79, pp. 32–44, 2015.

[59] G. N. Nurick and J. B. Martin, “Deformation of thin plates subjected to impulsive loading - A review - Part II - Experimental results,” *Int. J. Impact Eng.*, vol. 8, no. 2, pp. 171–186, 1989.

[60] G. N. Nurick and J. B. Martin, “Deformation of thin plates subjected to impulsive loading-A review. Part I: Theoretical considerations,” *Int. J. Impact Eng.*, vol. 8, no. 2, pp. 159–170, 1989.

[61] G. S. Langdon, W. C. Lee, and L. A. Louca, “The influence of material type on the response of plates to air-blast loading,” *Int. J. Impact Eng.*, vol. 78, pp. 150–160, 2015.

[62] T. Borvik, O. S. Hopperstad, T. Berstad, and M. Langseth, “A computational model of viscoplasticity and ductile damage for impact and penetration,” *Eur. J. Mech. A/Solids*, vol. 20, no. 5, pp. 685–712, 2001.

[63] E. Irick, C. Heinol, T. Clayton, J. Hashemi, J. F. Cardenas-Garcia, and R. Sadhneni, “Numerical and Experimental Investigation of Adiabatic Shear Bands in Metals under Low-Velocity Impact Conditions,” *J. Mater. Eng. Perform.*, vol. 4, no. 6, pp. 709–716, 1995.

[64] P. Landau, S. Osovski, A. Venkert, V. Gärtnerová, and D. Rittel, “The genesis of adiabatic shear bands,” *Sci. Rep.*, vol. 6, pp. 4–9, 2016.

[65] Z. Rosenberg and Y. Ashuach, “On thermal softening and adiabatic shear failure of dynamically compressed metallic specimens in the Kolsky bar system,” *Philos. Trans. R. Soc. A Math. Phys. Eng. Sci.*, vol. 372, no. 2015, 2014.

[66] X. bin WANG, “Adiabatic Shear Localization for Steels Based on Johnson-Cook Model and Second- and Fourth-Order Gradient Plasticity Models,” *J. Iron Steel Res. Int.*, vol. 14, no. 5, pp. 56–61, 2007.

[67] D. Bonorchis and G. N. Nurick, “The influence of boundary conditions on the loading of rectangular plates subjected to localised blast loading - Importance in numerical simulations,” *Int. J. Impact Eng.*, vol. 36, no. 1, pp. 40–52, 2009.

[68] D. Bonorchis and G. N. Nurick, “The analysis and simulation of welded stiffener plates subjected to localised blast loading,” *Int. J. Impact Eng.*, vol. 37, no. 3, pp. 260–273, 2010.

[69] D. Bonorchis and G. N. Nurick, “The effect of welded boundaries on the response of rectangular hot-rolled mild steel plates subjected to localised blast loading,” *Int. J. Impact Eng.*, vol. 34, no. 11, pp. 1729–1738, 2007.

[70] T. Børvik, A. G. Hanssen, M. Langseth, and L. Olovsson, “Response of structures to planar blast loads - A finite element engineering approach,” *Comput. Struct.*, vol. 87, no. 9–10, pp. 507–520, 2009.

[71] S. Chung Kim Yuen, G. N. Nurick, G. S. Langdon, and Y. Iyer, “Deformation of thin plates subjected to impulsive load: Part III – an update 25 years on,” *Int. J. Impact Eng.*, vol. 107, pp. 1339–1351, 2017.

[72] H. Gharababaei and A. Darvizeh, “Experimental and analytical investigation of large deformation of thin circular plates subjected to localized and uniform impulsive loading,” *Mech. Based Des. Struct. Mach.*, vol. 38, no. 2, pp. 171–189, 2010.

[73] Y.-P. Zhao, “Suggestion of a new dimensionless number for dynamic plastic response of beams and plates,” *Arch. Appl. Mech.*, vol. 68, no. 7–8, pp. 524–538, 1998.

[74] Q. M. Li and N. Jones, “On dimensionless numbers for dynamic plastic response of structural members,” *Arch. Appl. Mech.*, vol. 70, no. 4, pp. 245–254, 2000.

[75] Y. Yuan and P. J. Tan, “Deformation and failure of rectangular plates subjected to impulsive

loadings," *Int. J. Impact Eng.*, vol. 59, pp. 46–59, 2013.

[76] N. Jacob, S. C. K. Yuen, G. N. Nurick, D. Bonorchis, S. A. Desai, and D. Tait, "Scaling aspects of quadrangular plates subjected to localised blast loads - Experiments and predictions," *Int. J. Impact Eng.*, vol. 30, no. 8–9, pp. 1179–1208, 2004.

[77] W. Fourney, U. Leiste, R. Bonenberger, and D. Goodings, "Mechanism of loading on plates due to explosive detonation," *Fragblast*, vol. 9, no. 4, pp. 205–217, 2005.

[78] K. Spranghers, I. Vasilakos, D. Lecompte, H. Sol, and J. Vantomme, "Identification of the plastic behavior of aluminum plates under free air explosions using inverse methods and full-field measurements," *Int. J. Solids Struct.*, vol. 51, no. 1, pp. 210–226, 2014.

[79] V. Aune, E. Fagerholt, K. O. Hauge, M. Langseth, and T. Børvik, "Experimental study on the response of thin aluminium and steel plates subjected to airblast loading," *Int. J. Impact Eng.*, vol. 90, pp. 106–121, 2016.

[80] L. Zhu, "Transient deformation modes of square plates subjected to explosive loadings," *Int. J. Solids Struct.*, vol. 33, no. 3, pp. 301–314, 1996.

[81] P. Hooper, "Blast performance of silicone-bonded laminated glass (PhD Thesis)," Imperial College London, 2011.

[82] K. Sato, Q. Yu, J. Hiramoto, T. Urabe, and A. Yoshitake, "A method to investigate strain rate effects on necking and fracture behaviors of advanced high-strength steels using digital imaging strain analysis," *Int. J. Impact Eng.*, vol. 75, pp. 11–26, 2015.

[83] J. P. Noble, B. D. Goldthorpe, P. Church, and J. Harding, "Use of the Hopkinson bar to validate constitutive relations at high rates of strain," *J. Mech. Phys. Solids*, vol. 47, no. 5, pp. 1187–1206, 1999.

[84] S. Coppieters, S. Cooreman, H. Sol, P. Van Houtte, and D. Debruyne, "Identification of the post-necking hardening behaviour of sheet metal by comparison of the internal and external work in the necking zone," *J. Mater. Process. Technol.*, vol. 211, no. 3, pp. 545–552, 2011.

[85] M. Joun, J. G. Eom, and M. C. Lee, "A new method for acquiring true stress-strain curves over a large range of strains using a tensile test and finite element method," *Mech. Mater.*, vol. 40, no. 7, pp. 586–593, 2008.

[86] M. Kamaya and M. Kawakubo, "A procedure for determining the true stress-strain curve over a large range of strains using digital image correlation and finite element analysis," *Mech. Mater.*, vol. 43, no. 5, pp. 243–253, 2011.

[87] L. Hamra, J. F. Demonceau, and V. Denoël, "Pressure-impulse diagram of a beam developing non-linear membrane action under blast loading," *Int. J. Impact Eng.*, vol. 86, pp. 188–205, 2015.

[88] A. S. Fallah and L. A. Louca, "Pressure-impulse diagrams for elastic-plastic-hardening and softening single-degree-of-freedom models subjected to blast loading," *Int. J. Impact Eng.*, vol. 34, no. 4, pp. 823–842, 2007.

[89] H. G. Hopkins and W. Prager, "The Load carrying capacity of circular plates," *J. Mech. nd Phys. Solids*, vol. 2, no. June, pp. 1–18, 1953.

[90] Z. Xue and J. W. Hutchinson, "A comparative study of impulse-resistant metal sandwich plates," *Int. J. Impact Eng.*, vol. 30, no. 10, pp. 1283–1305, 2004.

[91] Q. M. Li and N. Jones, "Foundation of Correlation Parameters for Eliminating Pulse Shape Effects on Dynamic Plastic Response of Structures," *J. Appl. Mech.*, vol. 72, no. 2, p. 172, 2005.

[92] A. D. Cox and L. W. Morland, "Dynamic plastic deformations of simply-supported square plates," *J. Mech. Phys. Solids*, vol. 7, no. 4, pp. 229–241, 1959.

[93] N. Jones, T. O. Uran, and S. A. Tekin, "The dynamic plastic behavior of fully clamped rectangular plates," *Int. J. Solids Struct.*, vol. 6, no. 12, pp. 1499–1512, 1970.

[94] N. Jones, “A theoretical study of the dynamic plastic behaviour of beams and plates with finite-deflections,” *Int. J. Solids Struct.*, vol. 7, no. 33, pp. 1007–1029, 1971.

[95] N. Jones, “Impulsive Loading of a Simply Supported Circular Rigid Plastic Plate,” *J. Appl. Mech.*, vol. 35, no. 1, p. 59, 1968.

[96] N. Jones, “The credibility of predictions for structural designs subjected to large dynamic loadings causing inelastic behaviour,” *Int. J. Impact Eng.*, vol. 53, pp. 106–114, 2013.

[97] N. Jones and N. Griffii, “An experimental study into the dynamic plastic bheaviour of wide beams and rectangular plates,” *Int. Jounral Mech. Sci.*, vol. 13, pp. 721–735, 1971.

[98] C. Zheng, X. S. Kong, W. G. Wu, and F. Liu, “The elastic-plastic dynamic response of stiffened plates under confined blast load,” *Int. J. Impact Eng.*, vol. 95, pp. 141–153, 2016.

[99] K. L. Komarov and Y. V. Nemirovskii, “Dynamic behaviour of rigid-plastic rectangular plates (Translated),” *Prikl. Mekhanika*, vol. 21, no. 7, pp. 683–690, 1986.

[100] Y. Yuan, P. J. Tan, K. A. Shojaei, and P. Wrobel, “Large deformation, damage evolution and failure of ductile structures to pulse-pressure loading,” *Int. J. Solids Struct.*, vol. 96, pp. 320–339, 2016.

[101] N. Jones, “Impact loading of ductile rectangular plates,” *Thin-Walled Struct.*, vol. 50, no. 1, pp. 68–75, 2012.

[102] N. Jones, “Pseudo-shakedown phenomenon for the mass impact loading of plating,” *Int. J. Impact Eng.*, vol. 65, pp. 33–39, 2014.

[103] F. L. Chen and T. X. Yu, “Membrane factor method for large deflection response of beams and plates to intense dynamic loading,” *WIT Trans. Built Environ.*, vol. 141, pp. 59–71, 2014.

[104] T. X. Yu and F. L. Chen, “The large deflection dynamic plastic response of rectangular plates,” *Int. J. Impact Eng.*, vol. 12, no. 4, pp. 605–616, 1992.

[105] N. Jones, “Dynamic inelastic response of strain rate sensitive ductile plates due to large impact, dynamic pressure and explosive loadings,” *Int. J. Impact Eng.*, vol. 74, pp. 3–15, 2014.

[106] G. S. Langdon and G. K. Schleyer, “Inelastic deformation and failure of profiled stainless steel blast wall panels. Part II: Analytical modelling considerations,” *Int. J. Impact Eng.*, vol. 31, no. 4, pp. 371–399, 2005.

[107] G. S. Langdon and G. K. Schleyer, “Inelastic deformation and failure of profiled stainless steel blast wall panels. Part I: Experimental investigations,” *Int. J. Impact Eng.*, vol. 31, no. 4, pp. 341–369, 2005.

[108] E. Nwankwo, A. Soleiman Fallah, G. S. Langdon, and L. A. Louca, “Inelastic deformation and failure of partially strengthened profiled blast walls,” *Eng. Struct.*, vol. 46, pp. 671–686, 2013.

[109] Q. M. Li, “Continuity conditions at bending and shearing interfaces of rigid, perfectly plastic structural elements,” *Int. J. Solids Struct.*, vol. 37, no. 27, pp. 3651–3665, 2000.

[110] N. Jones and N. Jones, “Bounds On The Dynamic Plastic Behaviour of Structures IncludingTransverse Shear Effects,” *Int. J. Impact Eng.*, vol. 3, no. 4, pp. 273–291, 1985.

[111] N. Jones, J. Gomes De Oliveira, and J. . de. Oliveira, “Dynamic Plastic Response of Circular Plates With Transverse Shear and Rotatory Inertia,” *J. Appl. Mech.*, vol. 47, no. March 1980, pp. 27–34, 1980.

[112] N. Jones and J. Gomes De Oliveira, “The Influence of Rotatory Inertia and Transverse Shear on the Dynamic Plastic Behavior of Beams,” *J. Appl. Mech.*, vol. 46, no. June 1979, pp. 303–310, 1979.

[113] J. G. De Oliveira and N. Jones, “A Numerical Procedure for the Dynamic Plastic Response of Beams with Rotatory Inertia and Transverse Shear Effects,” *J. Struct. Mech.*, vol. 7, no. 2, pp. 193–230, 1979.

[114] Q. M. Li and N. Jones, “Blast loading of fully clamped circular plates with transverse shear effects,”

Int. J. Solids Struct., vol. 31, no. 14, pp. 1861–1876, 1994.

[115] Q. M. Li and N. Jones, "Blast Loading of Fully Clamped Beams with Transverse Shear Effects," *Mech. Struct. Mach.*, vol. 23, no. 1, pp. 59–86, 1995.

[116] Q. M. Li and N. Jones, "Blast loading of a 'short' cylindrical shell with transverse shear effects," *Int. J. Impact Eng.*, vol. 16, no. 2, pp. 331–353, 1995.

[117] R. Zaera, A. Arias, and C. Navarro, "Analytical modelling of metallic circular plates subjected to impulsive loads," *Int. J. Solids Struct.*, vol. 39, no. 3, pp. 659–672, 2002.

[118] Q. M. Li and Y. G. Huang, "Dynamic plastic response of thin circular plates with transverse shear and rotatory inertia subjected to rectangular pulse loading," *Int. J. Impact Eng.*, vol. 8, no. 3, pp. 219–228, 1989.

[119] N. Mehreganian, L. A. Louca, G. S. Langdon, R. J. Curry, and N. Abdul-Karim, "The response of mild steel and armour steel plates to localised air-blast loading-comparison of numerical modelling techniques," *Int. J. Impact Eng.*, vol. 115, no. January, pp. 81–93, 2018.

[120] G. Cowper and P. Symonds, "Strain hardening and strain-rate effects in the impact loading of cantilever beam," Technical Report No. 28, Brown University Division of Applied Mathematics, 1957.

[121] S. Tanimura, T. Tsuda, A. Abe, H. Hayashi, and N. Jones, "Comparison of rate-dependent constitutive models with experimental data," *Int. J. Impact Eng.*, vol. 69, pp. 104–113, 2014.

[122] W. Q. Shen and N. Jones, "A failure criterion for beams under impulsive loading," *Int. J. Impact Eng.*, vol. 12, no. 1, pp. 101–121, 1992.

[123] V. Gyliene and V. Ostasevicius, "Cowper-Symonds material deformation law application in material cutting process using LS-DYNA FE code: Turning and Milling," *LS-DYNA® 8th Eur. User's …*, pp. 1–12, 2011.

[124] C. Hernandez, A. Maranon, I. A. Ashcroft, and J. P. Casas-Rodriguez, "A computational determination of the Cowper-Symonds parameters from a single Taylor test," *Appl. Math. Model.*, vol. 37, no. 7, pp. 4698–4708, 2013.

[125] G. N. N. Nurick, M. D. D. Olson, J. R. R. Fagnan, and A. Levin, "Deformation and tearing of blast-loaded stiffened square plates," *Int. J. Impact Eng.*, vol. 16, no. 2, pp. 273–291, 1995.

[126] W. Ramberg and W. R. Osgood, "Description of stress-strain curves by three parametes, technical note 902," Washington DC., 1943.

[127] Z. HUANG, Y. CHEN, and S.-L. BAI, "An Elastoplastic Constitutive Model for Porous Materials," *Int. J. Appl. Mech.*, vol. 05, no. 03, p. 1350035, 2013.

[128] G. R. Johnson and W. H. Cook, "Fracture characteristics of three metals subjected to various strains, strain rates, temperatures and pressures," *Eng. Fract. Mech.*, vol. 21, no. 1, pp. 31–48, 1985.

[129] K. Vedantam, D. Bajaj, N. S. Brar, and S. Hill, "Johnson - Cook strength models for mild and DP 590 steels," *AIP Conf. Proc.*, vol. 845 I, no. 2006, pp. 775–778, 2006.

[130] T. Cwik and B. Se, "Project report : Ballistic performance of Armox 370T and Armox 440 steels," no. June, 2015.

[131] SSAB, "Armox Blast Protection Plate," *SSAB Swedish Steel Ltd*, 2018. .

[132] P. Skoglund, M. Nilsson, and A. Tjernberg, "Fracture modelling of a high performance armour steel," *J. Phys. IV Fr.*, vol. 134, pp. 197–202, 2006.

[133] R. J. Curry and G. S. Langdon, "Transient response of steel plates subjected to close proximity explosive detonations in air," *Int. J. Impact Eng.*, vol. 102, pp. 102–116, 2017.

[134] J. Lapsien and D. Meiners, "Digital speckle techniques for measuring light deflection profiles of

inhomogeneous phase objects," *Appl. Opt.*, vol. 36, no. 28, pp. 7180–7187, 1997.

[135] T. J. Cloete, G. N. Nurick, and R. N. Palmer, "The deformation and shear failure of peripherally clamped centrally supported blast loaded circular plates," *Int. J. Impact Eng.*, vol. 32, no. 1–4, pp. 92–117, 2006.

[136] Dassault Systèmes Simulia, "Abaqus CAE User's Manual," *Abaqus 6.12*, p. 1174, 2012.

[137] G. Randers-Pehrson and K. A. Bannister, "Airblast Loading Model for DYNA2D and DYNA3D," Aberdeen, 1997.

[138] B. Zakrisson, B. Wikman, and H. K. Häggblad, "Numerical simulations of blast loads and structural deformation from near-field explosions in air," *Int. J. Impact Eng.*, vol. 38, no. 7, pp. 597–612, 2011.

[139] A. M. Remennikov, "A Review of Methods for Predicting Bomb Blast Effects on Buildings," *J. Battelf. Technol.*, vol. 6, no. 3, pp. 5–10, 2003.

[140] G. LeBlanc, M. Adoum, and V. Lapoujade, "External blast load on structures – Empirical approach," *5th Eur. LS-DYNA Users Conf.*, no. 2, 2005.

[141] E. L. Guzas and C. J. Earls, "Air blast load generation for simulating structural response," *Steel Compos. Struct.*, vol. 10, no. 5, pp. 429–455, 2010.

[142] M. Souli, A. Ouahsine, and L. Lewin, "ALE formulation for fluid-structure interaction problems," *Comput. Methods Appl. Mech. Eng.*, vol. 190, no. 5–7, pp. 659–675, 2000.

[143] R. van Loon, P. D. Anderson, F. N. van de Vosse, and S. J. Sherwin, "Comparison of various fluid-structure interaction methods for deformable bodies," *Comput. Struct.*, vol. 85, no. 11–14, pp. 833–843, 2007.

[144] Simulia, "ABAQUS Analysis user's Manual," *Cambridge University*. 2017.

[145] G. N. Nurick, S. Mahoi, and G. S. Langdon, "The response of plates subjected to loading arising from the detonation of different shapes of plastic explosive," *Int. J. Impact Eng.*, vol. 89, pp. 102–113, 2016.

[146] J. Trajkovski, R. Kunc, J. Perenda, and I. Prebil, "Minimum mesh design criteria for blast wave development and structural response-MMALE method," *Lat. Am. J. Solids Struct.*, vol. 11, no. 11, pp. 1999–2017, 2014.

[147] S. H. Tan, J. K. Poon, R. Chan, and D. Chng, "Retrofitting of Reinforced Concrete Beam-Column via Steel Jackets against Close-in Detonation," *12th Int. LS-Dyna Users Conf.*, no. 3, pp. 1–12, 2012.

[148] P. S. Symonds and W. T. Fleming, "Parkes revisited: On rigid-plastic and elastic-plastic dynamic structural analysis," *Int. J. Impact Eng.*, vol. 2, no. 1, pp. 1–36, 1984.

[149] G. B. Sinclair, J. R. Beisheim, and S. Sezer, "Practical convergence-divergence checks for stresses from FEA," *Proc. 2006 Int. ANSYS Conf.*, vol. 50, no. Reference 1, 2006.

[150] P. S. Symonds and T. X. Yu, "Counterintuitive behaviour in a problem of elastic-plastic beam dynamics," *J. Appl. Mech.*, vol. 52, no. 85, pp. 517–522, 1985.

[151] W. E. Baker, P. A. Cox, P. S. Westine, J. J. Kulesz, and R. A. Strehlow, *Explosion Hazards and Evaluation*. Amsterdam-Oxford-New York: ELSEVIER Scientific Publication Company, 1983.

[152] K. Micallef, A. S. Fallah, D. J. Pope, and L. A. Louca, "The dynamic performance of simply-supported rigid-plastic circular steel plates subjected to localised blast loading," *Int. J. Mech. Sci.*, vol. 65, no. 1, pp. 177–191, 2012.

[153] N. Mehreganian, L. A. Louca, and A. S. Fallah, "DYNAMIC PERFORMANCE OF SIMPLY-SUPPORTED RIGID-PLASTIC SQUARE PLATES SUBJECT TO LOCALISED BLAST LOADING (In press)," *J. Eng. Mech.*, 2018.

[154] WIERZBICKI T and FLORENCE AL, "Theoretical and Experimental Investigation of Impulsively Loaded Clamped Circular Viscoplastic Plates," *Int. J. Solids Struct.*, vol. 6, no. 5, pp. 553–568, 1970.

[155] a Florence, “Circular plate under a uniformly distributed impulse☆,” *Int. J. Solids Struct.*, vol. 2, no. 1, pp. 37–47, 1966.

[156] G. N. Nurick and V. . Balden, “Localised Blast Loaded Circular Plates: an Experimental and Numerical Investigation,” *Proc. IMPLAST 2010 Conf.*, vol. 12, no. 14, pp. 145–152, 2010.

[157] C. K. Youngdahl, “Correlation parameters for eliminating the effects of pulse shape on dynamic plate deformation,” *Trans. ASME J. Appl. Mech.*, vol. 37, no. 2, pp. 744–752, 1970.

[158] N. Jones and S.-B. Kim, “A Study on the Large Ductile Deformations and Perforation of Mild Steel Plates Struck by a Mass—Part II: Discussion,” *J. Press. Vessel Technol.*, vol. 119, no. 2, p. 185, 1997.

[159] G. W. Ma, X. Huang, and J. C. Li, “Simplified Damage Assessment Method for Buried Structures against External Blast Load,” *J. Struct. Eng.*, vol. 136, no. 5, pp. 603–612, 2010.

[160] S. Timoshenko, S.;Woinosky-Kreiger, *Theory of Plates and Shells*. New York: McGraw Hill, 1959.

[161] M. W. Braestrup, “Yield line theory and concrete plasticity,” *Mag. Concr. Res.*, vol. 60, no. 8, pp. 549–553, 2008.

[162] K. Micallef, A. S. Fallah, D. J. Pope, and L. A. Louca, “Dynamic Performance of Simply Supported Rigid Plastic Circular Thick Steel Plates Subjected to Localized Blast Loading,” *J. Eng. Mech.*, vol. 140, no. 1, pp. 159–171, 2014.

[163] S. C. K. Yuen and G. N. Nurick, “Deformation and Tearing of Uniformly Blast-Loaded Quadrangular Stiffened Plates,” in *Structural Engineering, Mechanics and Computation*, A. Zingoni, Ed. Oxford: Elsevier Science, 2001, pp. 1029–1036.

[164] A. D. Gupta, F. H. Gregory, R. L. Bitting, and S. Bhattacharya, “Dynamic analysis of an explosively loaded hinged rectangular plate,” *Comput. Struct.*, vol. 26, no. 1–2, pp. 339–344, 1987.

[165] M. Toolabi, A. S. Fallah, P. . Baiz, and L. . Louca, “Enhanced mixed interpolation XFEM formulations for discontinuous Timoshenko beam and Mindlin-Reissner plate,” *Int. J. Numer. Methods Eng.*, no. April 2018, pp. 1–24, 2018.

[166] P. S. Symonds and N. Jones, “Impulsive loading of fully clamped beams with finite plastic deflections and strain-rate sensitivity,” *Int. J. Mech. Sci.*, vol. 14, no. 1, pp. 49–69, 1972.

[167] N. Mehreganian, A S Fallah, and L. A. Louca, “Inelastic dynamic response of square membranes subjected to localised blast loading,” *Int. J. Mech. Sci.*, vol. 148, no. August, pp. 578–595, 2018.

[168] N. Jones and R. . Walters, “Large deflections of rectangular plates,” *J. Sh. Res.*, vol. 18, no. 2, pp. 125–131, 1983.

[169] K. Micallef, A. S. Fallah, P. T. Curtis, and L. A. Louca, “On the dynamic plastic response of steel membranes subjected to localised blast loading,” *Int. J. Impact Eng.*, vol. 89, pp. 25–37, 2016.

[170] N. Perrone and P. Bhadra, “A Simplified Method to Account for Plastic Rate Sensitivity With Large Deformations,” *J. Appl. Mech.*, vol. 46, no. 4, p. 811, 1979.

[171] N. Perrone and P. Bhadra, “Simplified Large Deflection Mode Solutions for Impulsively Loaded , Viscoplastic , Circular Membranes,” *J. Appl. Mech.*, vol. 51, no. Septembe, pp. 505–509, 1984.

[172] Q. M. Li and N. Jones, “Shear and adiabatic shear failures in an impulsively loaded fully clamped beam,” *Int. J. Impact Eng.*, vol. 22, no. 6, pp. 589–607, 1999.

[173] S. Vidoli, “Discrete approximations of the Föppl – Von Kármán shell model : From coarse to more refined models,” *Int. J. Solids Struct.*, vol. 50, no. 9, pp. 1241–1252, 2013.

[174] E. H. DOWELL and C. S. VENTRES, “Comparison of theory and experiment for nonlinear flutter of loaded plates,” *AIAA J.*, vol. 8, no. 11, pp. 2022–2030, 1970.

[175] E. H. . Dowell and O. Bendiksen, *Panel flutter. Encyclopedia of Aerospace Engineering*. John Wiley & Sons, 2010.

[176] P. Del Linz, X. Liang, P. A. Hooper, L. Z. Wang, and J. P. Dear, “An analytical solution for pre-crack

behaviour of laminated glass under blast loading," *Compos. Struct.*, vol. 144, pp. 156–164, 2016.

[177] Y. Yuan, P. J. Tan, and Y. Li, "Dynamic structural response of laminated glass panels to blast loading," *Compos. Struct.*, vol. 182, no. August, pp. 579–589, 2017.

[178] M. L. Dano and M. W. Hyer, "Thermally-induced deformation behavior of unsymmetric laminates," *Int. J. Solids Struct.*, vol. 35, no. 17, pp. 2101–2120, 1998.

[179] J. Dervaux, P. Ciarletta, and M. Ben Amar, "Morphogenesis of thin hyperelastic plates: A constitutive theory of biological growth in the Föppl-von Kármán limit," *J. Mech. Phys. Solids*, vol. 57, no. 3, pp. 458–471, 2009.

[180] Q. M. Li and H. Meng, "Pulse loading shape effects on pressure-impulse diagram of an elastic-plastic, single-degree-of-freedom structural model," *Int. J. Mech. Sci.*, vol. 44, no. 9, pp. 1985–1998, 2002.

[181] P. S. Symonds, "Elastic, Finite Deflection and Strain Rate Effects in a Mode Approximation Technique for Plastic Deformation of Pulse Loaded Structures.," *J. Mech. Eng. Sci.*, vol. 22, no. 4, pp. 189–197, 1980.

[182] T.-L. Teng, C.-C. Liang, and Liao-Ching-Cho, "Transient Dynamic Large-Deflection Analysis of Panel Structure under Blast Loading," *Japan Soc. Mech. Eng.*, vol. 339, no. 4, pp. 591–597, 1996.

[183] A. H. Nayfeh, *Introduction to Perturbation Techniques*, vol. 20. New York: Wiley-Interscience Publication, 1993.

[184] H.-D. D. Ta and H.-C. C. Noh, "Analytical solution for the dynamic response of functionally graded rectangular plates resting on elastic foundation using a refined plate theory," *Appl. Math. Model.*, vol. 39, no. 20, pp. 6243–6257, 2015.

[185] B. McDonald, H. Bornstein, A. Ameri, J. P. Escobedo-Diaz, and A. Orifici, "High strain rate and high temperature response of two armour steels: Experimental testing and constitutive modelling," in *Proceedings of the 12th International DYMAT Conference*, 2018, vol. 01022, pp. 1–6.

[186] N. Mehreganian, A. S. Fallah, and L. A. Louca, "Plastic dynamic response of simply supported thick square plates subject to localised blast loading," *Int. J. Impact Eng.*, vol. 126, no. December 2018, pp. 85–100, 2019.

[187] F. J. Zerilli and R. W. Armstrong, "Dislocation-mechanics-based constitutive relations for material dynamics calculations," *J. Appl. Phys.*, vol. 61, no. 5, pp. 1816–1825, 1987.

[188] D. J. Steinberg, S. G. Cochran, and M. W. Guinan, "A constitutive model for metals applicable at high-strain rate," *J. Appl. Phys.*, vol. 51, no. 3, pp. 1498–1504, 1980.

[189] F. Gálvez, D. Cendón, N. García, A. Enfedaque, and V. Sánchez-Gálvez, "Dynamic fracture toughness of a high strength armor steel," *Eng. Fail. Anal.*, vol. 16, no. 8, pp. 2567–2575, 2009.

[190] M. A. Iqbal, K. Senthil, P. Sharma, and N. K. Gupta, "An investigation of the constitutive behavior of Armox 500T steel and armor piercing incendiary projectile material," *Int. J. Impact Eng.*, vol. 96, no. May, pp. 146–164, 2016.

[191] A. C. Mackenzie, J. W. Hancock, and D. K. Brown, "On the influence of state of stress on ductile failure initiation in high strength steels," *Eng. Fract. Mech.*, vol. 9, no. 1, pp. 167–188, 1977.

[192] J. W. Hancock and A. C. Mackenzie, "On the mechanisms of ductile failure in high-strength steels subjected to multi-axial stress-states," *J. Mech. Phys. Solids*, vol. 24, no. 2–3, pp. 147–160, 1976.

[193] C. Fressengeas and V. Taupin, "A field theory of strain/curvature incompatibility for coupled fracture and plasticity," *Int. J. Solids Struct.*, vol. 82, pp. 16–38, 2016.

[194] H. Levanger, "Simulating Ductile Fracture in Steel using the Finite Element Method: Comparison of Two Models for Describing Local Instability due to Ductile Fracture," no. May, p. 135, 2012.

[195] T. Børvik, O. S. Hopperstad, and T. Berstad, "On the influence of stress triaxiality and strain rate on the behaviour of a structural steel. Part II. Numerical study," *Eur. J. Mech. A/Solids*, vol. 22, no. 1,

pp. 15–32, 2003.

[196] M. S. Mirza, D. C. Barton, and P. Church, “The effect of stress triaxiality and strain-rate on the fracture characteristics of ductile metals,” *J. Mater. Sci.*, vol. 31, no. 2, pp. 453–461, 1996.

[197] P. Zochowski and M. Zielenkiewicz, “Constitutive Modeling of High-Strength Steel Designed for Ballistic Protection,” in *DYMAT 2018*, 2018, vol. 01012, pp. 1–6.

[198] Basaran;Merden, “Stress State Dependent Damage Modeling with a Focus on the Lode Angel Influence,” RWTH Aachen university, 2011.

[199] B. Mcdonald *et al.*, “NUMERICAL MODELLING OF THE DEFORMATION AND RUPTURE OF ARMOUR STEELS UNDER BLAST LOADING,” in *Proceedings of the 12th International DYMAT Conference*, 2018, vol. 01022.

[200] A. Hillerborg, M. Modéer, and P. E. Petersson, “Analysis of crack formation and crack growth in concrete by means of fracture mechanics and finite elements,” *Cem. Concr. Res.*, vol. 6, no. 6, pp. 773–781, 1976.

[201] B. M. Dobratz, “Properties of chemical explosives and explosive simulants,” *Lawrence Livermore Natl. Lab.*, vol. 1, pp. 1–334, 1972.

[202] W. Johnson, *Crashworthiness of vehicles: an introduction to aspects of collision of motor cars, ships, aircraft and railway coaches*. London: Mechanical Engineering Publications, 1978.

[203] A. Ezra and R. . Fay, “An assessment of energy absorbing devices for prospective use in aircraft impact situations,” in *Dynamic response of structures : proceedings of a symposium held at Stanford University*, 1972, pp. 225–246.

[204] N. Jones, “Dynamic energy absorption and perforation of ductile structures,” *Int. J. Press. Vessel. Pip.*, vol. 87, no. 9, pp. 482–492, 2010.

[205] M. D. White and N. Jones, “A theoretical analysis for the dynamic axial crushing of top-hat and double-hat thin-walled sections,” *Proc. Inst. Mech. Eng. Part D J. Automob. Eng.*, vol. 213, no. 4, pp. 307–325, 1999.

[206] D. F. Haskell, “Deformation and Fracture of Tank Bottom Hull Plates Subjected to Mine Blast,” Aberdeen Proving Ground, Maryland, 1972.

[207] N. Jones, “Energy-absorbing effectiveness factor,” *Int. J. Impact Eng.*, vol. 37, no. 6, pp. 754–765, 2010.

[208] R. E. Bimha, “RESPONSE OF THIN CIRCULAR PLATES TO CENTRAL BLAST LOADING (MSc Thesis),” THe University of Cape Town, 1996.

[209] X. Bai, L. Zhu, and T. X. Yu, “Saturated impulse for pulse-loaded rectangular plates with various boundary conditions,” *Thin-Walled Struct.*, vol. 119, no. October 2016, pp. 166–177, 2017.

[210] L. Zhu and T. X. Yu, “Saturated impulse for pulse-loaded elastic-plastic square plates,” *Int. J. Solids Struct.*, vol. 34, no. 14, pp. 1709–1718, 1997.

[211] J. Wei and L. R. Dharani, “Fracture mechanics of laminated glass subjected to blast loading,” *Theor. Appl. Fract. Mech.*, vol. 44, no. 2, pp. 157–167, 2005.

[212] P. A. Hooper, R. A. M. Sukhram, B. R. K. Blackman, and J. P. Dear, “On the blast resistance of laminated glass,” *Int. J. Solids Struct.*, vol. 49, no. 6, pp. 899–918, 2012.

[213] M. Held, “Effectiveness of an ERA-sandwich with a large distance between sandwich and target,” *Propellants, Explos. Pyrotech.*, vol. 26, no. 1, pp. 33–37, 2001.

[214] X. dong Li, Y. shi Yang, and S. tao Lv, “A numerical study on the disturbance of explosive reactive armors to jet penetration,” *Def. Technol.*, vol. 10, no. 1, pp. 66–75, 2014.

APPENDIX A1. FIRST PHASE OF MOTION

The components of α_e function are defined as

$$\alpha_0 = \pi\left(b^2L^2 + \frac{1}{2}\pi^2\right)^2 \left(\left(1-(1+Lb)e^{-(Lb-br_e)} + br_e\right) + \frac{1}{2}b^2r_e^2\right) \tag{A. 1}$$

$$\alpha_{11} = L^2b^2\left(\frac{1}{2}(br_e-1)\pi^2 + b^2L^2(br_e+1)\right) \tag{A. 2}$$

$$\alpha_{12} = \frac{1}{\sqrt{2}}Lb^2\left(\frac{1}{2}\pi^2r_e + L^2b(br_e+2)\right) \tag{A. 3}$$

$$\alpha_{13} = ab^2L^2\left(\frac{1}{2}(Lb-1)\pi^2 + L^2b^2(Lb+1)\right) \tag{A. 4}$$

$$\alpha_{21} = \frac{1}{\sqrt{2}}ab^2L^2\left(b^2L^2 + 2Lb + \frac{1}{2}\pi^2\right) \tag{A. 5}$$

$$\alpha_{22} = -4b^2L^2\left(b^2L^2 + \frac{1}{2}\pi^2\right)^2 \tag{A. 6}$$

$$\alpha_{23} = \sqrt{2}b^2r_eL\left(b^2L^2 + \frac{1}{2}\pi^2\right)^2 \tag{A. 7}$$

$$\boldsymbol{f} = \pi\begin{bmatrix} \cos\left(\frac{\pi r_e}{\sqrt{2}L}\right) & \pi e^{-Lb}\sin\left(\frac{\pi}{\sqrt{2}}\right) \\ \pi\sin\left(\frac{\pi r_e}{\sqrt{2}L}\right) & \pi^{-2}\sin^2\left(\frac{\sqrt{2}}{4}\frac{\pi r_e}{L}\right) \\ e^{-Lb}\cos\left(\frac{\pi}{\sqrt{2}}\right) & \pi^{-1}\sin\left(\frac{\pi r_e}{\sqrt{2}L}\right) \end{bmatrix} \tag{A. 8}$$

The components of $\boldsymbol{\mathcal{A}}_{ij}$ are

$$\begin{aligned} a_{11} = (5.41\times10^9A_2E&\left(\left(-\frac{3}{4}\omega_{\mathrm{e}}^2t^2 + 16.48\right)\Gamma^3 + p_0\alpha_e(\omega_{\mathrm{e}}^2t^2 - 45.457)\Gamma^2\right. \\ &\left. + (409.60)p_0^2\mathrm{\alpha}_{\mathrm{e}}^2\Gamma - (18.204)p_0^3\mathrm{\alpha}_{\mathrm{e}}^3\right) \end{aligned} \tag{A. 9}$$

$$\begin{aligned} a_{12} = 3.38\times10^8A_2E\omega_{\mathrm{e}}t&\left(\left(-\left(\frac{39}{32}\right)\omega_{\mathrm{e}}^2t^2 - 63.19\right)\Gamma^3 + p_0\alpha_e(\omega_{\mathrm{e}}^2t^2 + 314.41)\Gamma^2\right. \\ &\left. - 503.47p_0^2\mathrm{\alpha}_{\mathrm{e}}^2\Gamma + \left(\frac{4096}{15}\right)p_0^3\mathrm{\alpha}_{\mathrm{e}}^3\right) \end{aligned} \tag{A. 10}$$

$$a_{13} = \left(-1.19 \times 10^8 A_2 E \left(\left(\omega_2^4 t^4 + \frac{8743}{150}\omega_1^2 t^2 + 703.93\right)\Gamma^3 - \frac{49664}{225}(\omega_1^2 t^2 - 40.968) p_0 \alpha_e \Gamma^2 + \frac{8192}{45}(\omega_\mathrm{e}^2 t^2 - 27.57) p_0^2 \alpha_\mathrm{e}^2 \Gamma + 30292.19 p_0^3 \alpha_\mathrm{e}^3\right) + 2.31 \times 10^9 A_1^3 \pi^2 p_0 \alpha_e \omega_\mathrm{e}^6\right) \quad \textbf{(A. 11)}$$

$$a_{21} = -\left(\frac{68}{525}\right)\Gamma^2\left(p_0\alpha_e - \left(\frac{503}{1428}\right)\Gamma\right) \quad \textbf{(A. 12)}$$

$$a_{22} = -\left(\frac{75}{128}\right)\omega_\mathrm{e} t\Gamma\left(\left(\omega_\mathrm{e}^2 t^2 - \frac{8029}{300}\right)\Gamma^2 + \left(\frac{1664}{25}\right)p_0\alpha_e\Gamma - \left(\frac{4096}{75}\right)p_0^2\alpha_\mathrm{e}^2\right) \quad \textbf{(A. 13)}$$

$$a_{23} = \left(\left(\frac{105}{8}\omega_\mathrm{e}^2 t^2 - \frac{3971}{23040}\right)\Gamma^3 - 15\left(\omega_\mathrm{e}^2 t^2 - \frac{421}{900}\right)p_0\alpha_e\Gamma^2 - \frac{256}{3}p_0^2\alpha_\mathrm{e}^2\Gamma + \left(\frac{4096}{45}\right)p_0^3\alpha_\mathrm{e}^3\right) \quad \textbf{(A. 14)}$$

$$a_{31} = \left(\left(-\left(\frac{5}{128}\right)\omega_\mathrm{e}^2 t^2 - \frac{3955}{4608}\right)\Gamma^2 + \left(\frac{47}{60}\right)p_0\alpha_e\Gamma + \left(\frac{32}{45}\right)p_0^2\alpha_\mathrm{e}^2\right) \quad \textbf{(A. 15)}$$

$$a_{32} = \frac{1}{3}t\left(p_0\alpha_e + \left(\frac{75}{256}\right)\Gamma\right)\omega_\mathrm{e}\Gamma \quad \textbf{(A. 16)}$$

$$a_{33} = \frac{1}{360}\left(p_0\alpha_e + \left(\frac{347}{256}\right)\Gamma\right)\Gamma \quad \textbf{(A. 17)}$$

The components of $\boldsymbol{\mathcal{G}}_{jk}$ are

$$g_{11} = \frac{\omega_\mathrm{e} t\Gamma^2}{1536}, \qquad g_{21} = \frac{1}{230400}\Gamma^2, \qquad g_{31} = -\frac{1}{3780}\Gamma \quad \textbf{(A. 18a-c)}$$

$$g_{12} = -\frac{24}{5}\omega_\mathrm{e}\left(p_0\alpha_e - \frac{3}{4}\Gamma\right)\Gamma, \qquad g_{22} = -\frac{1}{70}\Gamma^2\omega_\mathrm{e} t \quad \textbf{(A. 19a-c)}$$

$$g_{32} = \left(\left(\omega_\mathrm{e}^2 t^2 - \frac{2317}{225}\right)\Gamma^2 + \left(\frac{6536}{225}\right)\Gamma p_0\alpha_e - \left(\frac{1024}{45}\right)p_0^2\alpha_\mathrm{e}^2\right) \quad \textbf{(A. 20)}$$

$$g_{13} = -\left(\frac{1024}{3}\right)\omega_\mathrm{e} t\left(p_0^2\alpha_\mathrm{e}^2 - \left(\frac{113}{64}\right)\Gamma p_0\alpha_e + \left(\frac{1621}{2048}\right)\Gamma^2\right) \quad \textbf{(A. 21)}$$

$$g_{23} = \frac{225}{256}\omega_\mathrm{e}^2 t^2\left(\left(\omega_\mathrm{e}^2 t^2 + \frac{26741}{150}\right)\Gamma^2 - \left(\frac{9856}{25}\right)\Gamma p_0\alpha_e + \frac{8192}{45}p_0^2\alpha_\mathrm{e}^2\right)$$

$$g_{33} = 0 \quad \textbf{(A. 22a-b)}$$

In the first phase of motion, the expression of the transverse displacement using Poincaré-Lindstedt method is expressed as

$$
\begin{aligned}
W_1^{(2)} \;=\; & C_3 cos(\omega_e t) \\
& + \frac{1}{8L^4 A_1 \omega_e^2}\Bigg(A_1 C_0^3 E\{8cos(\omega_e t)^2 - cos(\omega_e t)^3 \;- 24\} \\
& + 15 C_0 A_1 \left(-\frac{8}{15}\overline{\omega_e}\omega_1 L^4 + C_0^2 E\right)\{cos(\omega_e t) + \omega_e t sin(\omega_e t)\} \\
& + \frac{8\alpha_e p_0 L^6}{\epsilon}\Bigg)
\end{aligned}
\qquad \textbf{(A. 23)}
$$

Where the integration constant C_3 is determined by invoking the kinematic continuity of the displacement and transverse velocity at the onset of loading (i.e. $W(x,y,0) = 0, \dot{W}(x,y,0) = 0$:

$$
C_3 = \frac{A_1 C_0 (4L^4 \omega_e \overline{\omega_e} + C_0^2 E)\epsilon - 4\alpha_e p_0 L^6}{4L^4 A_1 \omega_e^2 \epsilon} \qquad \textbf{(A. 24)}
$$

While the attributed frequency of vibration to eliminate the secular term may be determined as

$$
\overline{\omega_e} := \frac{15 C_0^2 E}{8L^4 \omega_e} \qquad \textbf{(A. 25)}
$$

APPENDIX A.2 SECOND PHASE OF MOTION

In the second phase of motion, the expression of second iteration of the transverse displacement field, with retention of the secular-term is given as:

$$
\begin{aligned}
W_2^{(2)} = & C_5 e^{-i\omega_{\mathrm{e}} t} + C_4 e^{i\omega_{\mathrm{e}} t} \\
& + \frac{1}{16 A_1 \omega_{\mathrm{e}}^2}\Gamma sin\left(\frac{1}{2}\omega_{\mathrm{e}}\tau\right)^3 \Bigg(12\omega_{\mathrm{e}} t cos\left(\frac{1}{2}\omega_{\mathrm{e}}(2t-\tau)\right) \\
& - 6 sin\left(\frac{1}{2}\omega_{\mathrm{e}}(2t-\tau)\right) - sin\left(\frac{3}{2}\omega_{\mathrm{e}}(2t-\tau)\right)\Bigg)
\end{aligned}
\qquad \textbf{(A. 26)}
$$

Where

$$
\begin{aligned}
C_4 = \frac{e^{-i\omega_e \tau}}{8 A_1 \omega_{\mathrm{e}}^2}\Bigg\{ & \Gamma sin\left(\frac{1}{2}\omega_e \tau\right)^6 + 3\left(i\omega_{\mathrm{e}}\tau - \frac{3}{4}\right)\Gamma sin\left(\frac{1}{2}\omega_{\mathrm{e}}\tau\right)^4 \\
& + \left(\frac{9}{8}\left(\frac{4}{3}\omega_{\mathrm{e}}\tau - i\right)\Gamma sin(\omega_{\mathrm{e}}\tau) - 8 A_1 C_0 \omega_{\mathrm{e}}^2 + \frac{3}{8} i \Gamma sin(2\omega_{\mathrm{e}}\tau)\right) sin\left(\frac{1}{2}\omega_{\mathrm{e}}\tau\right)^2 \\
& + 4 i A_1 C_0 \omega_{\mathrm{e}}^2 sin(\omega_{\mathrm{e}}\tau)\Bigg\}
\end{aligned}
\qquad \textbf{(A. 27)}
$$

The O.D.E constants of first iteration at final phase of motion are:

$$C_{11} = \frac{\omega_e}{\omega_3}\sin(\omega_e t_d)\cos(\omega_3 t_d) - \sin(\omega_3 t_d)\cos(\omega_e t_d) + \sin(\omega_3 t_d) \tag{A. 28}$$

$$C_{12} = -\frac{\omega_e}{\omega_3}\mathit{sin}(\omega_e t_d)\sin(\omega_3 t_d) - \cos(\omega_3 t_d)\cos(\omega_e t_d) + \cos(\omega_3 t_d) \tag{A. 29}$$

$$\begin{aligned} C_5 = \frac{e^{i\omega_e\tau}}{8A_1\omega_e^2}\Bigg\{ & -\Gamma \mathit{sin}\left(\frac{1}{2}\omega_e\tau\right)^6 + 3\left(i\omega_e\tau + \frac{3}{4}\right)\Gamma \mathit{sin}\left(\frac{1}{2}\omega_e\tau\right)^4 \\ & - \left(\frac{9}{8}\left(\frac{4}{3}\omega_e\tau + i\right)\Gamma\,\mathit{sin}(\omega_e\tau) + 8A_1C_0\omega_e^2 + \frac{3}{8}i\Gamma \mathit{sin}(2\omega_e\tau)\right)\mathit{sin}\left(\frac{1}{2}\omega_e\tau\right)^2 \\ & + 4iA_1C_0\omega_e^2\mathit{sin}(\omega_e\tau)\Bigg\} \end{aligned} \tag{A. 30}$$

$$\begin{aligned} C_{13} = \frac{1}{512A_1\omega_e C_5}\Bigg\{ & 576\Gamma\omega_e(\omega_e^2 - \omega_3^2)\left(\omega_e^2 t_d^2 - 2\right)\sin(3\omega_e t_d) - 2304\Gamma\omega_e^2 t_d\left(\omega_e^2 - \frac{35}{3}\omega_3^2\right)\sin\left(\frac{1}{2}\omega_e t_d\right)^2 \\ & - 1792\Gamma\omega_e^2 t_d(\omega_e^2 - \omega_3^2)\sin\left(\frac{3}{2}\omega_e t_d\right)^2 - 768\Gamma\omega_e(\omega_e^2 - 3\omega_3^2)\left(\omega_e^2 t_d^2 - 2\right)\sin(2\omega_e t_d) \\ & + 4608\Gamma\omega_e^2 t_d\left(\omega_e^2 - \frac{7}{3}\omega_3^2\right)\sin(\omega_e t_d)^2 - 192\Gamma\omega_e(\omega_e^2 + 15\omega_3^2)\left(\omega_e^2 t_d^2 - 2\right)\sin(\omega_e t_d) \\ & + 128(\omega_e^2 - \omega_3^2)t_d(\omega_e^2 - 9\omega_3^2)\left(\frac{3}{128}t_d^8\omega_e^8\Gamma - \left(\frac{1}{64}\right)\omega_e^6 t_d^6\Gamma + \omega_e^4 t_d^4\left(p_0\alpha_e + \frac{3}{8}\Gamma\right) \right. \\ & \left. - 2\omega_e^2 t_d^2\left(p_0\alpha_e - \frac{5}{16}\Gamma\right) + 16p_0\alpha_e\right)\Bigg\} \end{aligned} \tag{A. 31}$$

$$\begin{aligned} C_{14} = \frac{1}{256A_1C_5}\Bigg\{ & 576\Gamma\left(\omega_e^2 - \frac{35}{3}\omega_3^2\right)(\omega_e^2 t_d{}^2 - 2)\sin\left(\frac{1}{2}\omega_e t_d\right)^2 \\ & + 448\Gamma(\omega_e^2 - \omega_3^2)(\omega_e^2 t_d{}^2 - 2)\sin\left(\frac{3}{2}\omega_e t_d\right)^2 - 768\Gamma\omega_e t_d(\omega_e^2 - 3\omega_3^2)\sin(2\omega_e t_d) \\ & + 576\Gamma\omega_e t_d(\omega_e^2 - \omega_3^2)\sin(3\omega_e t_d) - 1152\Gamma\left(\omega_e^2 - \frac{7}{3}\omega_3^2\right)\left(\omega_e^2 t_d^2 - 2\right)\sin(\omega_e t_d)^2 \\ & - 192\Gamma\omega_e t_d(\omega_e^2 + 15\omega_3^2)\sin(\omega_e t_d) \\ & - 128(\omega_e^2 - \omega_3^2)t_d^2(3\omega_3 + \omega_e)\left(-\omega_e^6 t_d^6\Gamma + \frac{5}{32}\Gamma\omega_e^4 t_d^4 + p_0\alpha_e\omega_e^2 t_d^2 + 4p_0\alpha_e\right)(-3\omega_3 \\ & + \omega_e)\Bigg\} \end{aligned} \tag{A. 32}$$

$$C_5 = (\omega_e^4 - 10\omega_e^2\omega_3^2 + 9\omega_3^4) \tag{A. 33}$$

$$\begin{aligned} C_{15} = -\frac{EC_0^3}{4L^2\rho\omega_1^2}\Bigg(& \mathit{cos}(\omega_e t_d)^3 - \frac{1}{2}\mathit{cos}(\omega_e t_d)^2 - \frac{5}{4}\mathit{cos}(\omega_e t_d) - \frac{4\rho L^2\omega_e^2}{EC_0^2} + \frac{3}{4}\Bigg)(\mathit{cos}(\omega_e t_d) \\ & - 1) \end{aligned} \tag{A. 34}$$

$$C_{16} = -\frac{EC_0^3}{4L^2\rho\omega_e^2}\left(\mathit{cos}(\omega_e t_d)^3 - \frac{3}{2}\mathit{cos}(\omega_e t_d)^2 + \frac{3}{4}\,\mathit{cos}(\omega_e t_d) - \frac{4\rho L^2\omega_e^2}{EC_0^2} - \frac{1}{4}\right)\mathit{sin}(\omega_e t_d) \tag{A. 35}$$

APPENDIX A.3 VDLOAD FORTRAN SUBROUTINE [5]

```
  subroutine vdload(nblock, ndim, stepTime, totalTime,amplitude, curCoords, velocity, dirCos, jltyp, sname, value)
C
      include 'vaba_param.inc'
C
      dimension curCoords(nblock, ndim), velocity(nblock, ndim),dirCos(nblock, ndim, ndim), value(nblock)
C
      character*80 sname
C
C
C ******************
C input parameters
C ******************
C Ro: constant part, mm
C blastTime: duration of blast event, s
C Po: constant pressure under charge diameter, MPa
C W: parameter for temporal distribution, /s
C A: parameter for spatial distribution, MPa
C B: parameter for spatial distribution, /mm
C
      parameter (Ro = 25,blastTime = 0.00003, Po = 200, W = -135322,A = 661,B = -0.0506)
C
C
C *********************
C temporal distribution
C *********************
C assumes an exponential decay over time of the form P(t) = EXP(W*t)
C
       if (stepTime .LE. blastTime) then
           ampTime = EXP(W*stepTime)
       else
           ampTime = 0
       endif
```

```
C
C
C *********************
C spatial distribution
C *********************
C !assumes an exponential decay over space of the form P(r) = A*EXP(B*r)
C
                 do k = 1, nblock
C
C !works out radial distance from centre
C
      r = SQRT(((curCoords(k,1))**2) + ((curCoords(k,2))**2))
C
         if (r .LE. Ro) then
              value(k) = Po*ampTime
         else
              value(k) = (A*EXP(B*r))*ampTime
         end if
      enddo
C
C
       continue
C
     return
     end
C******************************************************************************************
```